

Study of the isotope-dependence
of molecular high-harmonic
generation in D₂ and H₂

Von der QUEST-Leibniz-Forschungsschule
der Gottfried Wilhelm Leibniz Universität Hannover
zur Erlangung des Grades

Doktor der Naturwissenschaften
(Dr. rer. nat.)

genehmigte Dissertation von

M. Sc. Marc Ruhmann

Referent: Prof. Dr. Manfred Lein
Leibniz Universität Hannover

Korreferent: Prof. Dr. Alejandro Saenz
Humboldt-Universität zu Berlin

Tag der Promotion: 12. Dezember 2018

Abstract

This thesis comprises a numerical study of high-order harmonic generation (HHG) in the hydrogen molecule H_2 and its heavier isotope D_2 . HHG refers to the emission of high-frequency radiation by an atom or molecule when it is subject to a strong laser field. It can be explained as a series of three steps: ionization, continuum travel of the freed electron and recombination of the electron with the parent ion, releasing its acquired energy as a high-energy photon. Our central focus lies on how the harmonic signal strength differs between the isotopologues, quantified by the ratio of the emitted harmonic intensities (harmonic ratio). The molecular analogue of the Lewenstein model predicts a dependence of the dipole moment, and consequently the harmonic intensity, on the vibrational autocorrelation function. This function measures the overlap of the vibrational ground state of the neutral molecule and the time-dependent state evolving on the Born-Oppenheimer potential energy curve of the ion while the electron is in the continuum. The duration of the time evolution is determined by the time of ionization and recombination of the participating electron. The heavier nuclear mass of D_2 leads to a slower vibration than in H_2 , which affects the time dependence of the autocorrelation and ultimately the intensity of the harmonic radiation. The analytical expression of the HHG dipole moment is typically simplified with the help of the saddle-point approximation, which leads to the peculiar result of complex-valued electron ionization and recombination times. We study the autocorrelation and in particular the ratio of autocorrelations of D_2/H_2 in the context of these complex times. We do so separately for the short and long trajectories, which are two distinct kinds of trajectories the electron follows during its continuum journey. The study consists of two parts. The first is purely theoretical where we compare autocorrelation ratios with harmonic ratios acquired by numerical solution of the time-dependent Schrödinger equation. The second consists of a comparison of the theoretical results with harmonic ratios determined by experiment. The theoretical comparison in the first part is done for two orientations of the molecular axis relative to the linearly polarized electric field of the driving laser pulse, parallel and perpendicular. Moreover, we employ two models of the autocorrelation function in the comparison. One uses real-valued times originating from the semiclassical three-step model and an LCAO-approximated dipole-transition matrix element. The other makes use of the complex-valued saddle-point times and an exact transition matrix element, calculated numerically via exact scattering states of the model potentials. The comparison with the experiment involves the study of the Stark effect as well as molecular alignment distributions. Additionally, also the PACER method (Probing Attosecond dynamics by Chirp-Encoded Recollision) is employed. That is, the molecular vibrational motion is reconstructed from the experimental observables on an attosecond time scale. Finally, the comparison between theory and experiment is carried out for the ammonia molecule NH_3 and its heavier counterpart ND_3 as well.

Keywords: High-harmonic generation, vibrational autocorrelation, time-dependent Schrödinger equation

Zusammenfassung

Diese Arbeit umfasst eine numerische Studie der Erzeugung hoher Harmonischer (HHG) im Wasserstoffmolekül H_2 und dem schwereren Isotop D_2 . HHG bezeichnet die Emission von hochfrequenter Strahlung durch ein Atom oder Molekül welches einem starken Laserfeld ausgesetzt ist. Es kann als ein dreistufiger Prozess verstanden werden: Ionisation, Bewegung des befreiten Elektrons im Kontinuum und Rekombination des Elektrons mit dem entstandenen Ion, wobei die erlangte Energie des Elektrons in Form eines hochenergetischen Photons freigesetzt wird. Das Ziel ist die Untersuchung der unterschiedlich starken harmonischen Signale der beiden Isotope, was durch das Verhältnis der Intensitäten der Harmonischen ausgedrückt werden kann (harmonisches Verhältnis). Das molekulare Analog des Lewenstein-Modells sagt eine Abhängigkeit des Dipolmoments, und somit der Intensität der Harmonischen, von der Vibrations-Autokorrelationsfunktion voraus. Diese Funktion misst den Überlapp zwischen dem Vibrationsgrundzustand des neutralen Moleküls und dem zeitabhängigen Zustand entwickelt auf der Born-Oppenheimer Potentialkurve des Ions während das Elektron im Kontinuum ist. Die Dauer der Zeitentwicklung ist durch die Ionisations- und Rekombinationszeit des teilnehmenden Elektrons bestimmt. Die schwerere Kernmasse von D_2 führt zu einer langsameren Vibration als in H_2 , was die Zeitentwicklung der Autokorrelation und letztendlich die Intensität der harmonischen Strahlung beeinflusst. Der analytische Ausdruck des HHG-Dipolmoments wird üblicherweise durch die Sattelpunktsnäherung vereinfacht, welches komplexwertige Ionisations- und Rekombinationszeiten des Elektrons zur Folge hat. Wir untersuchen die Autokorrelation und insbesondere das Verhältnis der Autokorrelationen von D_2 und H_2 hinsichtlich dieser komplexen Zeiten. Wir unterscheiden dabei explizit zwischen den kurzen und langen Trajektorien, welches zwei unterschiedliche Typen von Trajektorien sind, denen das Elektron im Kontinuum folgt. Unsere Studie besteht aus zwei Teilen. Der erste Teil ist eine rein theoretische Betrachtung, bei der wir Autokorrelationsverhältnisse mit harmonischen Verhältnissen aus numerischen Lösungen der zeitabhängigen Schrödingergleichung vergleichen. Der zweite Teil ist ein Vergleich der theoretischen Ergebnisse mit experimentellen harmonischen Verhältnissen. Der theoretische Vergleich im ersten Teil wird für zwei Orientierungen der Molekülachse zu dem linear polarisierten elektrischen Feld des Lasers durchgeführt, parallel und senkrecht. Darüber hinaus betrachten wir in dem Vergleich zwei Modelle der Autokorrelationsfunktion. Eines verwendet die reellwertigen Zeiten aus dem semiklassischen Drei-Stufen-Modell und ein Dipolübergangselement in LCAO-Näherung. Das andere benutzt die komplexwertigen Sattelpunktszeiten und ein exaktes Übergangselement, welches numerisch exakte Streulösungen der Modellpotentiale verwendet. Der Vergleich mit dem Experiment beinhaltet eine Studie des Stark-Effekts und molekularer Ausrichtungsverteilungen. Zusätzlich kommt auch die PACER-Methode zum Einsatz. Dies bedeutet, dass die Vibrationsbewegung des Molekülions aus den experimentellen Observablen auf der Attosekundenskala rekonstruiert wird. Der Vergleich zwischen Theorie und Experiment wird auch für das Ammoniakmolekül NH_3 und dem schwereren Gegenstück ND_3 durchgeführt.

Schlagworte: Erzeugung hoher Harmonischer, Vibrations-Autokorrelation, zeitabhängige Schrödingergleichung

Acknowledgements

First and foremost I want to express my gratitude to my supervisor *Prof. Dr. Manfred Lein* who gave me the opportunity to work on this thesis. I joined his research group as a master's student in November of 2012 and have enjoyed a friendly environment from the very beginning, which encouraged me to subsequently start my PhD studies. It was invaluable for the working atmosphere to always find an open door and be welcomed for a discussion when I needed help. I greatly appreciate the time he took to give me advice and answer my questions. I also want to thank him for allowing me to work on the institute's IT besides my scientific studies.

Special thanks also go to *Prof. Dr. Alejandro Saenz* for being the second examiner. I greatly appreciate that he takes the time to examine my work.

I also want to thank *Prof. Dr. Uwe Morgner* who kindly agreed to be the chairman of the examination board.

I want to thank *Florian Oppermann* with whom I shared an office for almost the entire time of my PhD studies. He has been a great colleague and I learned a lot in the numerous discussions we have had, the topics of which reached beyond our common interests in physics and IT. Our conversations helped me realize that a change of perspective is helpful also outside of scientific matters.

I thank the research group members for the nice atmosphere they created, in particular *Dr. Nikolay Shvetsov-Shilovski*, *Nicolas Eicke* and *Simon Brennecke* as well as the former members *Dr. Ingo Petersen* and *Dr. Jost Henkel*. Furthermore, I wish to thank *Dr. Jan Grelik* for introducing me to the institute's IT infrastructure. I also thank *Stina Scheer* for the company and chats during lunch breaks.

I am deeply indebted to my parents *Frauke and Jörg Ruhmann* who always supported me in pursuing my goals. I cannot thank them enough for affording me my university studies and for their unceasing faith in me. Times were not always easy in the last years and words cannot describe what it means to me that they were there to help me.

Atomic Units Unless stated otherwise, all quantities in this work are given in atomic units [1]. Specifically, the following physical constants are set to unity

Reduced Planck constant	\hbar
Electron mass	m_e
Elementary charge	e
Coulomb constant	$4\pi\epsilon_0$

Accordingly, the atomic units of length, time and energy are given by

Quantity	Expression	Approximate value
Length	$\frac{4\pi\epsilon_0\hbar^2}{me^2}$	$5.29 \cdot 10^{-11} \text{ m}$ (1 bohr)
Time	$\frac{16\pi^2\epsilon_0^2\hbar^3}{me^4}$	$2.42 \cdot 10^{-17} \text{ s}$ (24.2 as)
Energy	$\frac{e^2}{4\pi\epsilon_0a_0}$	$4.36 \cdot 10^{-18} \text{ J}$ (27.2 eV)

where a_0 is the bohr radius, which is equal to the atomic unit of length in the first row. The notation “a.u.” is omitted in the following.

Abbreviations

ADK	Ammosov-Delone-Krainov
BO	Born-Oppenheimer
CM	Center Of Mass
FC	Franck-Condon
FT	Fourier Transform
FWHM	Full Width at Half Maximum
HHG	High-Harmonic Generation
HO	Harmonic Order
LCAO	Linear Combination of Atomic Orbitals
LER	Low-Energy Region
PACER	Probing Attosecond dynamics by Chirp-Encoded Recollision
PT	Perturbation Theory
SAE	Single Active Electron
SFA	Strong-Field Approximation
SM	Simple Man’s
SPA	Saddle-Point Approximation
STFT	Short-Time Fourier Transform
TDSE	Time-Dependent Schrödinger Equation
WKB	Wentzel–Kramers–Brillouin

Contents

Abstract	3
Zusammenfassung	5
Acknowledgements	7
1. Introduction	15
1.1. Motivation	15
1.2. Outline	20
2. High-Harmonic Generation	21
2.1. Three-step model	22
2.1.1. First step: ionization	22
2.1.2. Second step: classical dynamics in the continuum	23
2.1.3. Third step: recombination	24
2.2. Strong-field approximation	27
2.2.1. Dipole moment	28
2.2.2. Spectrum	32
2.2.3. Length, velocity and acceleration formulations	33
2.2.4. Saddle-point approximation	33
3. Vibrational Autocorrelation Function	45
3.1. Relevance for harmonic ratio	46
3.2. Complex time-evolution	46
3.2.1. Path-independence	47
3.2.2. Relation between ionization time and tunnelling	48
3.2.3. Ratio of saddle-point factors	51
3.3. Basic properties	52
3.3.1. Classical times	52
3.3.2. Saddle-point times	56
3.4. Summary and Conclusion	60
4. Quantum Mechanical Model	61
4.1. Relevant physical properties of the molecular isotopes	61
4.2. Coordinates	62
4.3. Perpendicular orientation	65
4.4. Parallel orientation	66
4.5. Dipole-transition matrix element	67
4.5.1. Plane wave continuum	69

4.5.2.	Exact continuum	72
4.5.3.	Divergence of ionization matrix element in SPA	79
5.	Time-Frequency Study of Harmonic Signal	83
5.1.	Harmonic spectrum	83
5.2.	Gabor transform	84
5.2.1.	Short-time Fourier transform	84
5.2.2.	Extraction of harmonic ratios from the Gabor transform	86
5.3.	Results	88
5.3.1.	Harmonic ratios	89
5.4.	Discussion of results	94
5.4.1.	Perpendicular orientation	97
5.4.2.	Parallel orientation	98
5.5.	Summary and Conclusion	99
6.	Molecular Alignment	103
6.1.	Alignment in a strong laser pulse	103
6.2.	Theoretical model	105
6.2.1.	Field-free linear rigid rotor	105
6.2.2.	Nonresonant alignment of nonpolar linear molecules	106
6.2.3.	Nuclear spin statistics	108
6.2.4.	Case of Hydrogen	110
6.3.	Use in autocorrelation function	111
7.	Stark Effect	115
7.1.	Theory	115
7.1.1.	Time-independent perturbation theory	115
7.1.2.	DC Stark shift of energies	116
7.1.3.	AC Stark shift of energies	116
7.2.	Hydrogen molecular ion	119
7.2.1.	Parallel DC Stark shift as dressed state	119
7.2.2.	Perpendicular DC Stark shift	123
7.3.	Hydrogen molecule	124
7.3.1.	AC Stark shift	125
7.4.	Ionization potential	129
8.	Trajectory-Resolved High-Harmonic Spectroscopy	131
8.1.	Theoretical model	132
8.2.	PACER	134
8.2.1.	Results	135
8.3.	Stark effect	138
8.3.1.	DC effect in the ion	138
8.3.2.	Including the AC effect in the neutral molecule	139
8.4.	Orientation dependence of ionization	140
8.5.	Ammonia	141
8.5.1.	Model and Results	142
8.6.	Conclusion	145

9. Summary, Conclusion and Outlook	147
9.1. Summary and Conclusion	147
9.2. Outlook	149
A. Additional Information	151
A.1. H ₂ LCAO dipole transition matrix elements with plane waves	151
A.1.1. Velocity form	151
A.1.2. Length form	153
A.2. WKB approximation	153
A.2.1. Proof of WKB phase integral for the Coulomb potential	153
A.2.2. Eikonal approximation of WKB phase integral	154
A.3. Angle Average of LCAO dipole-transition matrix element in velocity form	155
A.4. Fixed parameters of PACER potential	155
A.5. Fit of H ₂ alignment distribution	156
A.6. Values of potential energy curves for small internuclear distances	157
A.7. Harmonic ratios	162
B. Numerical Implementation	165
B.1. Numerical algorithms	165
B.1.1. Solving the time-dependent Schrödinger equation	165
B.1.2. Absorbing mask at grid boundary	167
B.1.3. Solving the time-independent Schrödinger equation	167
B.1.4. Integration	169
B.2. Numerical implementations and parameters	170
B.2.1. Autocorrelation	170
B.2.2. Saddle-point times	172
B.2.3. TDSE	172
B.2.4. Dipole-transition matrix element	172
B.2.5. Alignment distribution	174
Bibliography	175
Curriculum Vitae	187
List of Publications	189

1. Introduction

The main topic of this thesis is the strong-field phenomenon of high-order harmonic generation (HHG) in the H_2 molecule. This chapter serves as a first introduction to the concepts of strong-field physics relevant for the treatment of HHG. In particular, section 1.1 presents the relevant theoretical landmarks that led to the studies presented in this work. Section 1.2 explains the purposes of the chapters.

1.1. Motivation

When a sufficiently intense laser pulse interacts with matter, specifically individual atoms or molecules (henceforth collectively just denoted as targets), a nonlinear response can be the consequence [2]. Nonlinearity in this context means a nonlinear electric field strength dependence of the induced polarization, a measure of how the electronic charge distribution around the atomic core is modified by the field. The physical mechanism behind this nonlinear response depends on the regime of laser parameters. There are two regimes that are commonly distinguished, the *perturbative regime* and the *strong-field regime*. In the former, the electric fields are still weak enough such that the interaction can be described using perturbation theory. Examples of phenomena that belong to this regime are, for example, single-photon ionization and low-order harmonic generation [3,4].

In the strong-field regime, the field strengths are comparable to or even greater than the inner-atomic Coulomb fields experienced by the bound electrons and it can no longer be considered a small perturbation of the field-free system. The advent of laser pulses with correspondingly high intensities, in excess of 10^{13} W/cm^2 , have made the strong-field regime experimentally accessible and have effectively opened up the research field of strong-field physics. Today they are the standard tool of physicists working in this field. The creation of ultrashort pulses, consisting of only a few cycles, as well as tailoring of their specific shape, have become increasingly possible in the last two decades, facilitating fine-grained control over experimental laser conditions. Today, pulse durations reach the sub-femtosecond timescale (1 femtosecond = 10^{-15} seconds) [5,6]. Considering that the dynamics of electrons bound in an atom typically unfolds on the attosecond timescale (1 attosecond = 10^{-18} seconds) means that manipulation of inner-atomic processes comes into the reach of technology [7].

The advances in such laser technologies have led to the discovery of many strong-field phenomena. The physical mechanism underlying most of these is the initial ionization of the target, commonly termed *strong-field ionization*. Examples of such phenomena are, among others, *multiphoton*

1. Introduction

ionization (MPI), which was first observed in 1965 [8–10], *high-order above-threshold ionization* (ATI), discovered in 1979 [11–13], *nonsequential double-ionization* (NSDI) [14,15] and *high-order harmonic generation* (HHG) [16–22]. In MPI, the electron absorbs multiple photons providing enough energy to transition into the continuum. The number of absorbed photons can be higher than the minimum number required to reach the continuum, which is the case of ATI. In NSDI two electrons are removed, where the second ionization event is caused by inelastic scattering of the first electron from the parent ion. HHG refers to the emission of radiation by the target with frequencies many times higher than the frequency of the laser pulse that initiates the process. Although it is nowadays commonly studied with gas targets as in the first reported measurement in 1987/88 [17,18], it was discovered in solids in 1977 [16]. The power spectrum of the emitted radiation features a *plateau* of approximately constant harmonic peaks at (usually) odd multiples of the laser frequency, followed by a sharp *cutoff*, i.e. a sudden decrease in intensity beyond a certain energy. HHG gives rise to very capable applications. The generated high harmonics may serve as the source of coherent attosecond pulse trains [23] or even isolated attosecond pulses [24], with frequencies up to the extreme ultraviolet and soft X-ray frequency range [25,26]. Furthermore, HHG can be utilized as a spectroscopy tool to study the generating target systems themselves, because rich structural and dynamical information is encoded in the harmonic spectrum [27–30].

The development of a thorough understanding of these phenomena is the goal of theoretical strong-field physics. As mentioned above, perturbation theory is generally not applicable in this regime. In order to describe strong-field effects, the electric field of the laser is treated classically, which is rooted in the fact that the field consists of a large number of photons and its interaction with a target does only negligibly change the state of the light. The coupling between the field and an electron is usually described in *dipole approximation*, i.e. it is assumed that the spatial variation of the electric field is negligible compared to the size of the target. The most accurate solution for such a system lies in numerically solving the time-dependent Schrödinger equation (TDSE). Unfortunately, an exact treatment, with all relevant degrees of freedom, is practically impossible for most targets. The reason for this is primarily the large number of spatial degrees of freedom (and also their extent due to the potentially large spreading of the wave function in the presence of intense fields). All but the simplest systems are of many-electron nature and finding the exact solution is, even with today’s computing power, a formidable task. This is especially relevant for molecules, which not only comprise a multitude of individual particles, but also lack spherical symmetry. The only mitigation to this problem is the introduction of approximations, the most prevalent of which is the *single-active electron* (SAE) approximation. As the name suggests, this reduces the computational complexity by assuming that only a single electron participates in the dynamics. It depends on the target system and the phenomenon to be studied whether the SAE is a useful practice, because multielectron effects are trivially absent. HHG and ATI are quite well describable as single-electron effects [31]. NSDI, however, is not. Calculations with more than one active electron usually have to be done with severe limits on the degrees of freedom, for example restricting two electrons to a single fixed direction. Such approximations often go along with approximating the exact Coulomb potential by a soft-core potential to avoid the singularity. This introduces an additional free parameter, the soft-core parameter, which can be adjusted to match, for example, the system’s ground-state energy to the real-world value. All things considered, it is necessary to find the right balance between a TDSE model that is sophisticated enough to capture the physical phenomenon at hand and suitable approximations that render the computational effort viable. It is often very helpful to

have a rough understanding of the phenomenon beforehand in order to realize this. This is especially important considering that the TDSE solution, once it has been acquired, has the status of a “theoretical measurement”. By itself it does not further the physical understanding, but needs to be interpreted in terms of intuitive models, similar to a real measurement made in a laboratory.

A theoretical breakthrough in such an intuitive understanding of strong-field phenomena was accomplished by the introduction of classical trajectories first by Corkum et al. in 1989 and 1993 [21, 32] and also Gallagher in 1988 [33] in order to describe the continuum travel of the electron after ionization. This model has become known as the *three-step model*, because its description of the process can be divided into three distinct and consecutive steps. The first is the ionization of the target due to removal of an electron. The second is the appearance of the electron in the continuum with zero velocity and its subsequent motion as a charged classical point particle in the electric field of the laser pulse only, i.e. the potential of the parent ion is neglected. The third is the return of the electron to the parent ion, either elastically scattering off the parent ion (ATI, see also [34, 35]), inelastically scattering off it (NSDI), or recombining with it and releasing its energy as a high-energy photon (HHG). The classical description of the continuum dynamics is naturally linked to the definition of *ionization and recombination times* that uniquely define a *trajectory* of the electron in the electric field. Two important kinds of trajectories emerge in such a study, the so-called *short* and *long* trajectories. For every harmonic energy up until the cutoff, there exists a unique short and long trajectory that contributes to that specific energy in the overall signal. The excursion time and distance to the parent ion of the short trajectories are smaller than for the long trajectories, giving rise to their names. Furthermore, the short trajectories produce an *up-chirp* and the long trajectories a *down-chirp*, meaning that the energy increases with excursion time for the short and decreases for the long trajectories. Since this model uses quantum mechanical as well as classical physics, it is often categorized as being *semiclassical* and due to its simplicity also called the *simple man’s model*. Despite this simplicity, it quantitatively explains the position of the high-harmonic cutoff with astonishing accuracy and proved very effective in the qualitative understanding.

It did not take long until the next theoretical milestone in strong-field physics appeared in 1994 [22]. What is nowadays known as the *Lewenstein model* is the full quantum mechanical counterpart of the three-step model. It is based on the *strong-field approximation* (SFA), whose concepts actually date back to the 1960s work of Keldysh [36] and later works by Faisal [37] and Reiss [38]. It shares a key assumption with the three-step model in that it neglects the influence of the parent ion on the electron. In quantum mechanical terms, this is equivalent to approximating the continuum states by *plane waves*, specifically *Volkov states*, which are the exact analytical solutions of the TDSE for an electron that interacts only with a time-dependent electric field. This, in turn, allows an analytical solution of the TDSE for the complete system, i.e. an electron initially bound by the target and under the influence of the strong laser field. It comes as no surprise that the Lewenstein model can be interpreted in terms of the quantum mechanical analogues of the same three steps as in the three-step model.

SFA-based transition amplitudes or dipole moments generally appear as multidimensional integrals over the electron momentum, the ionization time and also the recombination time, and can be interpreted as path integrals. The evaluation of these integrals is not possible

1. Introduction

analytically and theoretical studies in terms of the SFA therefore usually go along with another approximation, the *saddle-point approximation* [22]. By itself it is a purely mathematical tool that can be applied if the integrand is a product of a rapidly varying complex exponential and another slowly varying function. The idea is that the fast oscillations of the exponential mostly cancel themselves out in the integration and the dominant contributions come from the points where the exponent changes slowly, i.e. when its derivative vanishes. Applied to the HHG dipole moment, this leads to a set of equations for the *saddle points*, i.e. a set of values for the electron momentum, the ionization time and the recombination time, as a function of harmonic energy. In analogy to the three-step model, these values define trajectories, the *saddle-point trajectories*. In the context of path integrals they are the most relevant paths that give rise to the overall signal. A peculiarity of the so-called *saddle-point times* is that they are *complex-valued*, which is effectively caused by a nonzero ionization potential. This is related to the fact that the mechanism of ionization in the SFA is tunnelling [39], which is a purely quantum mechanical phenomenon with no classical analogue. The saddle-point times also allow a separation into short and long trajectories. In the limit of vanishing ionization potential, equivalent to a nonexistent tunnel barrier and therefore to the electron just appearing in the continuum, they coincide with the classical times from the three-step model. Overall, the SFA-based theoretical framework is the workhorse of today's strong-field physics and an indispensable tool in this field of research.

Despite its effectiveness, the SFA, by nature, cannot yield quantitatively accurate results in cases where the influence of the parent ions potential is comparable to or greater than that of the electric field of the laser. A typical example is a low-energy electron that moves in the vicinity of the ion, e.g. in low-order ATI or in the generation of low-order harmonics in HHG. Notable contributions to improve such a description were given by Smirnova et al. with the development of the *Eikonal-Volkov approximation* (EVA) starting in 2006 [40–42]. In the EVA, the laser field is included as usual, i.e. classically in dipole approximation, and the potential is treated in eikonal approximation. An introduction into this topic can be found in [42]. This led to more sophisticated theories such as the *analytical R-matrix* (ARM) theory by Torlina et al. in 2012 [43–45].

The study of HHG in *molecules* increasingly shifted into the focus of strong-field physicists in the beginning- to mid-1990s [46–48]. Due to the aforementioned complexity of molecular targets, early theoretical studies concentrated on diatomic molecules and in particular the hydrogen molecule H_2 or its even simpler molecular ion H_2^+ . The essential new degree of freedom is the internuclear distance vector, which specifies the distance between the nuclei and the orientation of the molecular axis with respect to the electric field vector of the driving laser. A common approximation in TDSE calculations in this context is fixing the positions of the nuclei in space, sometimes also called the *frozen-nuclei approximation*. This is closely related to the famous *Born-Oppenheimer* (BO) approximation that relies on the fact that the mass of an atomic nucleus is generally much larger than the mass of an electron and the nuclear motion therefore happens on a significantly slower timescale. Properties of HHG specific to molecules include the more efficient production of high harmonics due to charge resonance [47, 48], extended plateaus in the harmonic spectrum due to the electron recombining at a different nucleus than it ionized from [49] as well as due to two-electron interactions [50], the generation of even harmonics [51], and intramolecular interference structures in the harmonic spectrum [29, 52, 53]. The latter, for example, leads to a pronounced minimum (or maximum) in the harmonic spectrum, also

denoted as the *two-center interference minimum*.

An important contribution to the analytical treatment of molecular HHG was done by Lein in 2005 [54] with a modified version of the Lewenstein model for molecules, on the basis of H_2 . The resulting dipole moment is fundamentally the same as for the atomic case, the difference being the appearance of the *vibrational autocorrelation function*. This function measures the overlap between the initial vibrational state of the *neutral* molecule, i.e. the ground state in the neutral BO potential energy curve, and the same state evolved on the BO potential energy curve of the *ion*. The timespan of the evolution is given by the excursion time of the electron in the continuum, i.e. the difference between the recombination and the ionization time. The overlap initially decreases and typically shows an oscillatory behaviour for sufficiently long excursion times, corresponding to a vibration of the nuclei in the ion, which leaves a direct signature in the molecular dipole moment [55]. In particular, the *ratio* of harmonic spectra for different *isotopes* is primarily given by the ratio of the corresponding autocorrelations functions. The original publication [54] already exploited this property in order to extract the nuclear motion in the ion, a procedure nowadays commonly referred to as PACER (Probing Attosecond dynamics by Chirp-Encoded Recollision) [28]. It uses a fundamental characteristic of HHG, namely the mapping between a harmonic energy and the corresponding excursion time of a trajectory. This is equivalent to a pump-probe scheme [30], where the ionization corresponds to the pump, the continuum travel to a delay, and the recombination to the probe. The chirped nature of the trajectories means that a whole interval of pump-probe time delays is contained within a single HHG process. The time range and resolution depend on the laser parameters.

The autocorrelation picture has since been also applied to more complex molecules such as methane [28], water [56] and ammonia [57–59]. A common practice in such studies is the use of the classical times that originate from the three-step model, and the exclusion of the long trajectories. The classical times are convenient to work with because they are easily acquired numerically and the three-step model is often sufficiently accurate. However, the Lewenstein model gives rise to complex saddle-point times, which raises the question whether they provide an even better description of HHG in terms of the autocorrelation. Already in the seminal publication [54] it was noted that the autocorrelation ratio matches the experimental data only for a modified BO potential. Is the complex-valued nature of the saddle-point times the missing piece? In order to assess this, we extend the studies of the autocorrelation function in two ways. First, we use the full complex solutions for the saddle-point times in the time-evolution. Second, we include both the short and the long trajectories and consider them separately. The principal quantity in our studies is the harmonic ratio for the two hydrogen molecular isotopes D_2 and H_2 , i.e. the ratio of harmonic intensities emitted by these isotopes when they undergo HHG. This quantity is approximated by the modulus-squared ratio of the corresponding autocorrelations and we test the agreement in two ways. First, we compare autocorrelation ratios with harmonic ratios from numerical solutions of the TDSE. Second, we compare them with harmonic ratios determined by experiment. The models used in the TDSE calculations are two-dimensional, one dimension for the electron and the other for the internuclear distance. We therefore employ the single-active electron approximation but not the frozen-nuclei approximation. The inclusion of the nuclear degree of freedom is crucial for a meaningful comparison with the autocorrelation, otherwise any effects originating from different nuclear masses, i.e. different isotopes, would be absent. For the experimental comparison, the data was kindly shared with us by the group of Pengfei Lan from the Huazhong University of Science and Technology in Wuhan, China [59].

1.2. Outline

This thesis is organized in 9 chapters, this introduction being the first. The second chapter explains the theory of HHG and lays the theoretical foundation for the rest of the thesis. In this regard, section 2.1 presents the three-step model and the resulting classical times. The Lewenstein model is the subject of section 2.2, where we derive in detail the expression for the molecular HHG dipole moment of H_2 from first principles, based on the condensed derivation given in [54]. This derivation shows the origin and relevance of the vibrational autocorrelation function. Application of the saddle-point approximation yields the saddle-point times, which are studied in section 2.2.4.

The basic properties of the vibrational autocorrelation function itself are detailed in chapter 3. In particular, we present the differences between the classical and saddle-point times.

The fourth chapter presents two two-dimensional quantum-mechanical models of the H_2 molecule, one for parallel and one for perpendicular orientation. One dimension is for the electron, the other for the internuclear distance, describing the motion of the nuclei relative to one another (nuclear vibration). We exclusively consider linearly polarized light and the direction of motion of the electron coincides with the polarization direction of the electric field. These models serve two purposes. On the one hand we use them for numerical solutions of the TDSE, from which we can extract harmonic ratios. These ratios can then be compared to autocorrelation ratios. On the other hand they are the basis for the calculation of the dipole-transition matrix element that directly enters the autocorrelation. This matrix element requires the knowledge of the electronic ground state for a range of internuclear distances as well as continuum states for a range of electron momenta. It is calculated for both orientations and for two types of continuum states, plane waves and exact states. The plane-wave case follows from the SFA. The exact states are exact numerical scattering solutions of the electron-nuclear interaction potentials.

Chapter 5 is dedicated to the comparison between TDSE ratios and autocorrelation ratios. It presents the procedure of how we extract the harmonic ratios, for both the short and the long trajectories, from the TDSE solution, and presents the results of the comparison.

The chapters 6, 7 and 8 belong together and deal with the comparison of autocorrelation ratios against the experiment. The comparison itself is done in chapter 8. In the interpretation of the results, several questions arise concerning the influence of molecular alignment and the Stark effect on the harmonic ratios. These two effects are therefore studied beforehand in H_2 , separately in chapters 6 and 7, which present the basic theory and the relevant numerical results that are later needed in chapter 8. The experiment was also performed for ammonia, NH_3 , and chapter 8 presents a model and numerical results of autocorrelation ratios for this molecule as well.

2. High-Harmonic Generation

This chapter serves as an introduction to the strong-field phenomenon of high-order harmonic generation (HHG). The goal is to introduce the reader to the theoretical background that is necessary for the study of harmonic ratios, which is the main subject of this thesis. We are concerned with the single-atom or single-molecule response only and do not consider propagation effects that enter the picture when ensembles of systems are studied.

When an atomic or molecule is subject to a sufficiently strong laser field, radiation with frequencies many times higher than the fundamental laser frequency ω_0 can be observed. The physical mechanism behind this can be understood in terms of the *three-step model* [21]. In short, it consists of *ionization* of an electron from the target system, its subsequent *continuum travel* in the oscillating electric field of the laser, and its *recombination* once the field has changed sign, which opens the possibility for the electron to be driven back to the parent ion.

Between ionization and recombination, the electron follows *trajectories* that are characterized by their *ionization and recombination times*. These times are defined relative to the field maximum of the sinusoidal time-dependence of the electric field. The trajectories can be classified into distinct types, the most important of which are the *short trajectories* and the *long trajectories*. Considering these two, the whole harmonic generation process takes place within a single cycle of the driving field. The designations “short” and “long” refer to the duration of the electron continuum travel, i.e. the difference between the recombination and ionization time. The long trajectories start before the short ones and end after them. A more detailed description of the three-step model and these trajectories will be given below.

A typical power spectrum of the emitted radiation is shown in Figure 2.1. It consists of a *plateau* where the intensity of the harmonics stays approximately constant, followed by a sharp decline in intensity known as the *cutoff*. Closer inspection shows, given the driving field persists for sufficiently many cycles, that the intensity is concentrated at frequencies that are integer multiples of ω_0 , i.e. there are proper *harmonics*. This is a consequence of the process repeating identically every laser cycle, which leads to the Fourier spectrum having peaks at said integer multiples of ω_0 [30].

Furthermore, since the maxima of the driving field occur twice per optical cycle with alternating sign, the process is actually repeated every half-cycle (given that the initial state is not significantly depleted), but with a different sign of the induced dipole moment. If the target system possesses inversion symmetry, this repetition every half-cycle leads to there being only *odd* integer multiples of ω_0 . This again can be seen through a Fourier analysis. Such an inversion symmetry is naturally given in atoms, because of the spherical symmetry, and also in *homonuclear* molecules. The hydrogen molecule, which is the system that we are primarily

2. High-Harmonic Generation

concerned with in this work, therefore only exhibits odd harmonics. If the inversion symmetry is broken, the process results in *even-order* harmonics, as was for example studied in [51].

In the next section we will outline the three-step model as it was first used in the context of HHG by Corkum [21], followed a full quantum-mechanical treatment [22, 54].

2.1. Three-step model

The semiclassical three-step model, as it was first introduced to strong-field physics by Corkum, combines aspects of quantum-mechanical and classical physics to describe the emission of the high-harmonic radiation. In the original paper [21], the model is not only used to describe HHG, but also ATI and NSDI. We will concentrate on the HHG part in this work and recount the relevant concepts. Let the laser be linearly polarized and its electric field strength given by $E(t) = E_0 \cos(\omega_0 t)$. Additionally, let the target atom or molecule be located at the origin, $x = 0$.

2.1.1. First step: ionization

The first step in the process is the ionization of an electron from the target system. In strong-field ionization, two ionization regimes are commonly distinguished, quantified by the Keldysh parameter [36]

$$\gamma = \frac{\omega_0 \sqrt{2I_p}}{E_0},$$

with ionization potential I_p . One limiting case, $\gamma \gg 1$ (ω_0 large, E_0 small), is identified with *multiphoton ionization* (MPI), also known as the *vertical ionization channel* [39] and can be understood as the simultaneous absorption of multiple photons by the electron, giving it enough energy to transition into the continuum (a “vertical climb” up in energy). The other limiting case, $\gamma \ll 1$ (ω_0 small, E_0 large), is the regime of *tunnelling ionization*. The high electric field strength bends down the inner-atomic potential significantly (see the illustration in the left panel of Figure 2.2), thereby creating a finite potential barrier. Due to its slow oscillation, the barrier persists long enough for the electron to have a significant probability to tunnel out. In contrast to MPI, it is also called the *horizontal ionization channel*, motivated by the picture that part of the bound electrons wave function leaks out horizontally into the continuum. Both channels coexist but are of varying relevance depending on the value of γ [39].

Ionization in HHG usually falls into the tunnelling regime. The ionization rate $\Gamma_{\text{ADK}}(I_p, E(t))$ is then given by [30, 60]

$$\Gamma_{\text{ADK}}(I_p, E) = \Gamma_0(I_p, E) \exp\left(-\frac{2(2I_p)^{3/2}}{3|E|}\right). \quad (2.1)$$

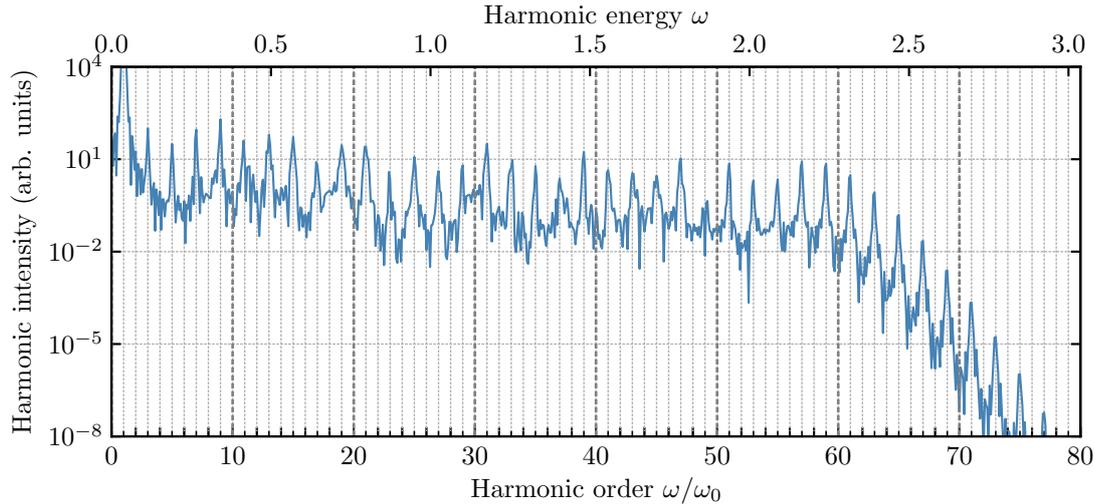


Figure 2.1.: Harmonic spectrum as it results from HHG, calculated with the perpendicular model of H_2 (see chapter 4), for a wavelength of 1200 nm and an intensity of $1 \cdot 10^{14} \text{ W/cm}^2$. The pulse consists of six cycles with two-cycle ramps in the beginning and end. Due to the multiple full laser cycles, the harmonic peaks are clearly visible. Shorter pulses generally imprint the laser frequency less clearly on the spectrum. The peaks are located at odd integer multiples of the fundamental laser frequency ω_0 . The classical cutoff law (2.9) predicts the cutoff to be at $\omega_c \approx 2.17$ (harmonic order 57), which agrees well with the plot.

It depends sensitively on the ionization potential I_p and the instantaneous electric field strength $E(t)$, due to the exponential function. The prefactor Γ_0 contains the contributions specific to the bound state of the system. The right panel in Figure 2.2 shows a plot of this rate for one cycle of the electric field for a specific set of laser parameters. It becomes apparent that there are temporarily localized bursts of ionization happening close to the maximum of the electric field.

2.1.2. Second step: classical dynamics in the continuum

Once the electron is liberated into the continuum, the probability of which can be obtained from Γ_{ADK} , it is in the second step treated as a classical point particle whose trajectory $x(t)$ is dictated by Newton's equation of motion

$$\ddot{x}(t) = -E_0 \cos(\omega_0 t). \quad (2.2)$$

The initial position and velocity, at $t = t_0$, are set to zero

$$x(t_0) = 0 \quad (2.3)$$

$$\dot{x}(t_0) = 0 \quad (2.4)$$

i.e. the electron appears at time of ionization t_0 with zero velocity at the origin, which is assumed to be the position of the parent ion. The subsequent motion can be easily determined

2. High-Harmonic Generation

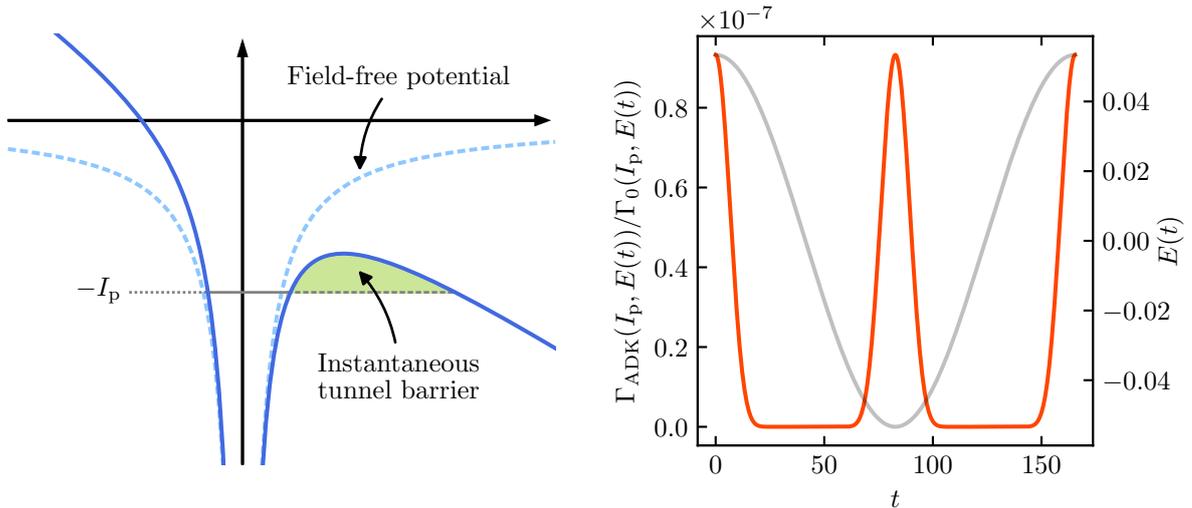


Figure 2.2.: **Left:** Illustration of the instantaneous tunnel barrier that is formed when an external electric field distorts the Coulomb potential of an atom. **Right:** ADK tunneling ionization rate for a single cycle of the electric field $E(t) = E_0 \cos(\omega_0 t)$, for the same wavelength and intensity as in Figure 2.1. The ionization potential is that of H_2 and the prefactor is set to one, $\Gamma_0 = 1$. Ionization is dominant close to the maxima of the electric field, which occur twice during one optical cycle.

by integration of equation (2.2) from t_0 to t

$$\dot{x}(t, t_0) = -\frac{E_0}{\omega_0} [\sin(\omega_0 t) - \sin(\omega_0 t_0)] \quad (2.5)$$

$$x(t, t_0) = \frac{E_0}{\omega_0^2} [\cos(\omega_0 t) - \cos(\omega_0 t_0)] + \frac{E_0}{\omega_0} \sin(\omega_0 t_0)(t - t_0). \quad (2.6)$$

We see that in addition to the oscillatory motion, the electron acquires a drift momentum $(E_0/\omega_0) \sin(\omega_0 t_0)$ that depends on the electric field phase $\omega_0 t_0$ at the time of ionization. This magnitude of this drift may be large enough such that the linear motion associated with it prevents the electron from returning to the parent. It turns out that the trajectories that start in a quarter cycle following a field maximum do eventually return to $x = 0$. The electron is then assumed to recombine with the parent ion, which constitutes the third and last step.

2.1.3. Third step: recombination

The recombination time t_r of a returning trajectory is defined as

$$x(t_r, t_0) = 0. \quad (2.7)$$

The kinetic energy of the electron at that instant then determines the energy of the emitted radiation ω

$$\omega = I_p + \frac{\dot{x}(t_r, t_0)^2}{2}, \quad (2.8)$$

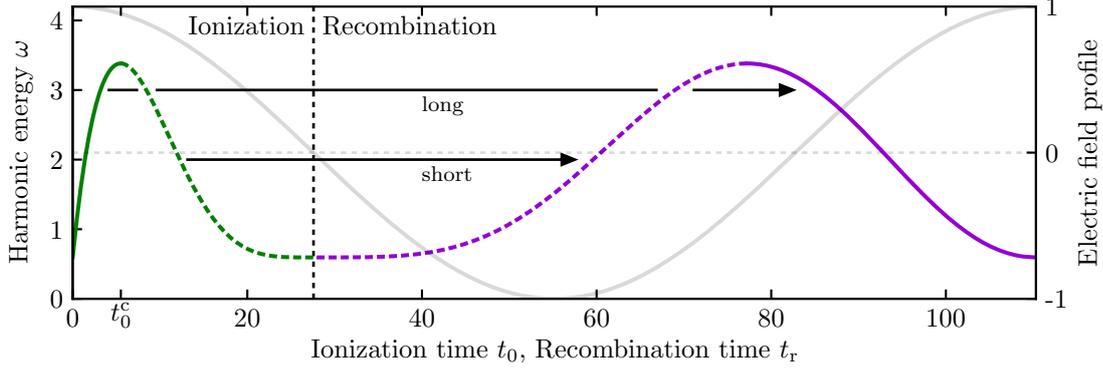


Figure 2.3.: Relation between the ionization time t_0 , the recombinations time t_r and the harmonic energy ω according to the semiclassical three-step model. The electric field profile is shown as a low-contrast curve. The wavelength is 800 nm and the intensity is $4 \cdot 10^{14} \text{ W/cm}^2$. The short (dashed lines) and long trajectories (solid lines) start in the first quarter cycle after a field maximum and recombine during the remaining three-quarters. A single trajectory, starting at t_0^c , gives rise to the highest harmonic energy and marks the boundary between short and long trajectories.

which follows from the conservation of energy. Figure 2.3 shows the ionization and recombination times, together with the corresponding harmonic energies. Only the trajectories that start in the first quarter cycle, $0 \leq t_0 \leq T/4$, are depicted. The ones starting after the second field maximum, $T/2 \leq t_0 \leq 3T/4$, are not shown.

One sees that the recombination times span the whole remaining three-quarter cycle after ionization. The highest possible return energy turns out to be

$$\max \left\{ \frac{\dot{x}(t_r, t_0)^2}{2} : 0 \leq t_0 \leq T/2 \right\} \approx 3.17U_p$$

with the *ponderomotive potential*, defined as the mean kinetic energy of the electron

$$\begin{aligned} U_p &= \frac{1}{T} \int_0^T dt \frac{\dot{x}(t, t_0)^2}{2} \Big|_{t_0=0} \\ &= \frac{E_0^2}{4\omega_0^2}. \end{aligned}$$

This defines the semiclassical *cutoff law* of HHG, i.e. the highest possible photon energy

$$\omega_c = I_p + 3.17U_p. \quad (2.9)$$

Only one trajectory reaches this maximum energy. Its time of ionization is $t_0^c \approx 0.05T$ after the field maximum, or $\omega_0 t_0^c \approx \pi/10$. This instant divides the trajectories into two types, which are called the *short trajectories* and *long trajectories*. The long trajectories start before t_0^c and the short trajectories after t_0^c . For every harmonic energy ω with $I_p \leq \omega < \omega_c$, there is a short and a long trajectory that contributes to that ω .

Figure 2.4 shows the harmonic energy plotted over the excursion time $\tau = t_r - t_0$ of the electron, including also the “very long trajectories”, i.e. trajectories that return to the origin multiple times with excursion times beyond one optical cycle. Note that all of these trajectories are

2. High-Harmonic Generation

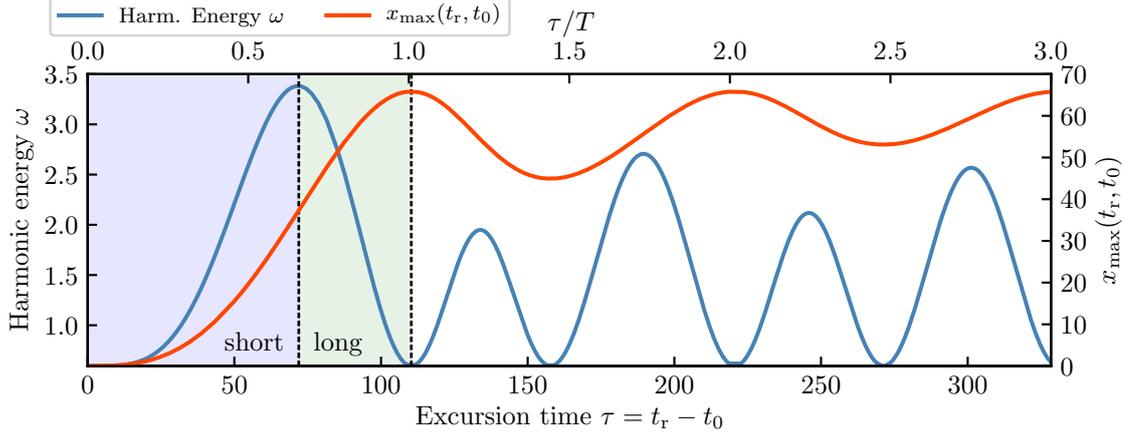


Figure 2.4.: Harmonic energy ω and maximum excursion distance x_{\max} plotted over the excursion time $\tau = t_r - t_0$, for trajectories starting in the first quarter cycle after the field maximum. The wavelength is 800 nm and the wavelength is $4 \cdot 10^{14}$ W/cm². The short and long trajectories corresponds to the first of multiple returns to the origin. Later returns have excursion times τ beyond one optical cycle. The maximum excursion distance $x_{\max}(t_r, t_0)$ is the largest distance to the origin a trajectory, starting at t_0 and recombining at t_r , experiences during the journey. It is a monotonically increasing function of τ for the short and long trajectories, with a maximum value of $2E_0/\omega_0$ (≈ 65.8 for the present laser parameters).

launched within a quarter cycle following the maximum of the laser field. Physically these are equivalent to short and long trajectories that do not recombine on the first return. They do not reach the cutoff energy, this is only possible on said first return.

Also shown in Figure 2.4 is the maximum excursion distance, $x_{\max}(t_r, t_0)$. It is largest distance to the origin that a trajectory with ionization time t_0 and recombination time t_r experienced during the excursion. We see that the long trajectories not only have a larger τ , but also a larger excursion distance to the parent ion. In fact, the curve for $x_{\max}(t_r, t_0)$ is monotonically increasing with τ for the short and long trajectories. The largest possible distance for any returning trajectory is

$$\max\{x_{\max}(t_r, t_0) : 0 \leq t_0 \leq T/2\} = \frac{2E_0}{\omega_0^2}.$$

Another characteristic that differs between the short and long trajectories is the change of frequency of the emitted radiation over time. In Figure 2.3 we see that the harmonic energy ω increases with the recombination time t_r for the short trajectories. In contrast, ω decreases with t_r for the long trajectories. This means that the short trajectories give rise to an *up-chirp*, while the long trajectories exhibit a *down-chirp* in the emitted radiation.

In the case of a single atom (in particular without phase matching effects relevant in experiments) the contributions of the long trajectories to the harmonic signal are usually larger than those of the short trajectories. The reason for this is the large ionization rate Γ_{ADK} (see Figure 2.2) close to the maximum of the driving field where the long trajectories start, compared to the time frame where the short trajectories start. The exponential dependence of Γ_{ADK} on the electric field strength has a significant influence in this respect. The larger ionization probability of the

long trajectories is counteracted by the increased wave packet spreading of the electron that is caused by the longer time it spends in the continuum, which decreases the recombination probability. These two effects, however, do not compensate and the long trajectories still give the larger contribution [61]. The situation is different for molecules, where the magnitude of the harmonic signal depends also on the vibrational autocorrelation function, which may suppress the contributions of the long trajectories below that of the short trajectories, see section 2.2.1 and chapter 3.

To arrive at the power spectrum, one needs to evaluate the expectation value of the dipole moment operator, $\langle \psi | \mathbf{r} | \psi \rangle$, where the state $|\psi\rangle = |\psi_g\rangle + |\psi_c\rangle$ is commonly assumed to be a superposition of the initial bound state, usually the ground state $|\psi_g\rangle$, and a continuum state $|\psi_c\rangle$ of the electron, which is a superposition of plane waves. This implies that no excited states are populated, a common assumption in HHG. The original work of the three-step model given in [21] also takes this approach, outlined in the following.

In [21] the depletion of $|\psi_g\rangle$ is neglected, which is another common assumption in the study of HHG. It not only simplifies the calculations because the ground state population is approximately constant, it also implies that the contributions of every half cycle are approximately equal (except for a change in sign of the dipole moment). The continuum state, $|\psi_c\rangle$, is constructed in an ad hoc manner. It is, as mentioned above, a superposition of plane waves that includes contributions from the short and long trajectories, added incoherently, for every harmonic order. Continuum-continuum transitions, $\langle \psi_c | \mathbf{r} | \psi_c \rangle$, are neglected, since the transition from the continuum to the initial ground state is the principal mechanism behind the harmonic generation process. To account for the different ionization probabilities of the trajectories, the individual plane waves are weighted by means of a position- and time-dependent normalization function, which acts as a wave-packet envelope. It is determined via Γ_{ADK} and the classical trajectories (2.5) and (2.6). The harmonic spectrum is reproduced well by this approach.

2.2. Strong-field approximation

The semiclassical three-step model presented in section 2.1 works well when studying the qualitative features of HHG. For a more detailed understanding, however, a full quantum mechanical treatment is necessary. Such a theory, on the basis of the *strong-field approximation*, was presented for atoms [22] shortly after the advent of three-step model and has become known as the *Lewenstein* model.

The theory was extended to diatomic molecules in [54] by studying the H_2 molecule, which revealed that the harmonic intensity depends von the vibrational dynamics in the ion via the *vibrational autocorrelation function*. This function measures the overlap between the initial vibrational wave packet in the ion, that is created by the ionization of an electron, and its time-evolved counterpart. It implies a dependence on the nuclear mass and therefore the isotope of a given molecular species. The next section presents this theory in detail, based on the original publication [54].

2. High-Harmonic Generation

2.2.1. Dipole moment

The goal is to solve the time-dependent Schrödinger equation (TDSE) for an H_2 molecule driven by an external laser, following the work made in [22,54]. Starting point is the Hamiltonian

$$H(\mathbf{r}_1, \mathbf{r}_2, R, t) = -\frac{\nabla_1^2}{2} - \frac{\nabla_2^2}{2} - \frac{1}{M} \frac{\partial^2}{\partial R^2} + V(\mathbf{r}_1, \mathbf{r}_2, R) + \mathbf{E}(t) \cdot (\mathbf{r}_1 + \mathbf{r}_2)$$

where $\mathbf{r}_1, \mathbf{r}_2$ are the coordinates of the two electrons and ∇_1, ∇_2 the corresponding derivatives. The internuclear distance is denoted by R and the electric field of the laser is given by $\mathbf{E}(t)$. The potential V includes the Coulomb interactions of all particles

$$V = V_{\mathbf{r}_1, \mathbf{r}_2} + V_R + V_{\mathbf{r}_1, p_1} + V_{\mathbf{r}_1, p_2} + V_{\mathbf{r}_2, p_1} + V_{\mathbf{r}_2, p_2}.$$

Given the assumptions below, the TDSE

$$i \frac{\partial \Psi(\mathbf{r}_1, \mathbf{r}_2, R, t)}{\partial t} = H \Psi(\mathbf{r}_1, \mathbf{r}_2, R, t)$$

can be solved with the ansatz

$$\Psi(\mathbf{r}_1, \mathbf{r}_2, R, t) = e^{-iE_0 t} \left(\Psi_0(\mathbf{r}_1, \mathbf{r}_2, R) + \int \frac{d^3 k}{(2\pi)^3} \phi(\mathbf{k}, R, t) \left[e^{i\mathbf{k} \cdot \mathbf{r}_1} \psi_R^+(\mathbf{r}_2) + e^{i\mathbf{k} \cdot \mathbf{r}_2} \psi_R^+(\mathbf{r}_1) \right] \right) \quad (2.10)$$

which consists of the Born-Oppenheimer (BO) ground state $\Psi_0(\mathbf{r}_1, \mathbf{r}_2, R) = \chi_0(R) \psi_R(\mathbf{r}_1, \mathbf{r}_2)$ of the neutral molecule (with energy E_0) and a superposition of BO states of the ion, where one of the two electrons is in the continuum. ψ_R^+ is the electronic BO ground state of the bound electron in H_2^+ .

It is assumed that

- in the neutral molecule only the BO ground state Ψ_0 is populated
- the ground state is not depleted by the interaction with the laser
- the ionized electron in the continuum does not interact with the remaining parent ion, i.e. its wave function is approximated by a plane wave
- once an electron has been moved to the continuum, the other one does not interact with the laser and remains in the ionic BO ground state

The left side of the TDSE yields

$$\begin{aligned} i e^{iE_0 t} \frac{\partial \Psi}{\partial t} &= E_0 \left(\dots \right) + i \int \frac{d^3 k}{(2\pi)^3} \frac{\partial \phi(\mathbf{k}, R, t)}{\partial t} \left[e^{i\mathbf{k} \cdot \mathbf{r}_1} \psi_R^+(\mathbf{r}_2) + e^{i\mathbf{k} \cdot \mathbf{r}_2} \psi_R^+(\mathbf{r}_1) \right] \\ &= E_0 \Psi_0(\mathbf{r}_1, \mathbf{r}_2, R) + i \int \frac{d^3 k}{(2\pi)^3} \left(-i E_0 \phi(\mathbf{k}, R, t) + \frac{\partial \phi(\mathbf{k}, R, t)}{\partial t} \right) \times \\ &\quad \times \left[e^{i\mathbf{k} \cdot \mathbf{r}_1} \psi_R^+(\mathbf{r}_2) + e^{i\mathbf{k} \cdot \mathbf{r}_2} \psi_R^+(\mathbf{r}_1) \right]. \end{aligned}$$

The right side gives

$$\begin{aligned} e^{iE_0t} H\Psi &= E_0\Psi_0(\mathbf{r}_1, \mathbf{r}_2, R) + \mathbf{E}(t) \cdot (\mathbf{r}_1 + \mathbf{r}_2)\Psi_0(\mathbf{r}_1, \mathbf{r}_2, R) \\ &+ \int \frac{d^3k}{(2\pi)^3} H\phi(\mathbf{k}, R, t) \left[e^{i\mathbf{k}\cdot\mathbf{r}_1}\psi_R^+(\mathbf{r}_2) + e^{i\mathbf{k}\cdot\mathbf{r}_2}\psi_R^+(\mathbf{r}_1) \right]. \end{aligned} \quad (2.11)$$

Application of H to the first term under the integral gives

$$\begin{aligned} H\phi(\mathbf{k}, R, t)e^{i\mathbf{k}\cdot\mathbf{r}_1}\psi_R^+(\mathbf{r}_2) &= \underbrace{\phi(\mathbf{k}, R, t)\frac{\mathbf{k}^2}{2}e^{i\mathbf{k}\cdot\mathbf{r}_1}\psi_R^+(\mathbf{r}_2)}_{-\nabla_1^2/2} - \frac{1}{M}\frac{\partial^2}{\partial R^2}\phi(\mathbf{k}, R, t)e^{i\mathbf{k}\cdot\mathbf{r}_1}\psi_R^+(\mathbf{r}_2) \\ &+ \underbrace{\phi(\mathbf{k}, R, t)e^{i\mathbf{k}\cdot\mathbf{r}_1}V_{\text{BO}}^+(R)\psi_R^+(\mathbf{r}_2)}_{-\nabla_2^2/2+V(\mathbf{r}_1, \mathbf{r}_2, R)} + \underbrace{\mathbf{E}(t) \cdot \mathbf{r}_1\phi(\mathbf{k}, R, t)e^{i\mathbf{k}\cdot\mathbf{r}_1}\psi_R^+(\mathbf{r}_2)}_{\mathbf{E}(t)\cdot(\mathbf{r}_1+\mathbf{r}_2)} \\ &= \left[\frac{\mathbf{k}^2}{2} - \frac{1}{M}\frac{\partial^2}{\partial R^2} + V_{\text{BO}}^+(R) + \mathbf{E}(t) \cdot \mathbf{r}_1 \right] \phi(\mathbf{k}, R, t)e^{i\mathbf{k}\cdot\mathbf{r}_1}\psi_R^+(\mathbf{r}_2). \end{aligned}$$

The contributions of \mathbf{r}_1 in $-\frac{\nabla_2^2}{2} + V(\mathbf{r}_1, \mathbf{r}_2, R)$ and from \mathbf{r}_2 in $\mathbf{E}(t) \cdot (\mathbf{r}_1 + \mathbf{r}_2)$ were neglected, in accordance with the above assumptions.

The second term under the integral in equation (2.11) has an analogous expression with the roles of \mathbf{r}_1 and \mathbf{r}_2 interchanged. The complete result of applying H to the ansatz takes the form

$$\begin{aligned} e^{iE_0t} H\Psi &= E_0\Psi_0(\mathbf{r}_1, \mathbf{r}_2, R) + \mathbf{E}(t) \cdot (\mathbf{r}_1 + \mathbf{r}_2)\Psi_0(\mathbf{r}_1, \mathbf{r}_2, R) \\ &+ \int \frac{d^3k}{(2\pi)^3} \left(\left[\frac{\mathbf{k}^2}{2} - \frac{1}{M}\frac{\partial^2}{\partial R^2} + V_{\text{BO}}^+(R) \right] \times \right. \\ &\quad \times \phi(\mathbf{k}, R, t) \left[e^{i\mathbf{k}\cdot\mathbf{r}_1}\psi_R^+(\mathbf{r}_2) + e^{i\mathbf{k}\cdot\mathbf{r}_2}\psi_R^+(\mathbf{r}_1) \right] \\ &\quad \left. + \phi(\mathbf{k}, R, t)\mathbf{E}(t) \cdot \left[\mathbf{r}_1e^{i\mathbf{k}\cdot\mathbf{r}_1}\psi_R^+(\mathbf{r}_2) + \mathbf{r}_2e^{i\mathbf{k}\cdot\mathbf{r}_2}\psi_R^+(\mathbf{r}_1) \right] \right). \end{aligned}$$

In order to get an equation for the ionic vibrational wave packets $\phi(\mathbf{k}, R, t)$ both sides of the TDSE are projected onto the ionic BO states $e^{i\mathbf{k}'\cdot\mathbf{r}}\psi_R^+$. Although the electronic BO ground states ψ_R^+ and ψ_R are real the asterisk indicating the complex-conjugate is kept for clarity. The term $E_0\Psi_0(\mathbf{r}_1, \mathbf{r}_2, R)$ appears on both sides and can be dropped. For the left side then holds

$$\begin{aligned} ie^{iE_0t}\frac{\partial\Psi}{\partial t} &\rightarrow i \int \frac{d^3k}{(2\pi)^3} \left(-iE_0\phi(\mathbf{k}, R, t) + \frac{\partial\phi(\mathbf{k}, R, t)}{\partial t} \right) \times \\ &\quad \times \left[(2\pi)^3\delta(\mathbf{k} - \mathbf{k}') + \underbrace{\int d^3r_1 \int d^3r_2 e^{-i\mathbf{k}'\cdot\mathbf{r}_1}\psi_R^{+*}(\mathbf{r}_2)e^{i\mathbf{k}\cdot\mathbf{r}_2}\psi_R^+(\mathbf{r}_1)}_{\approx 0} \right] \end{aligned}$$

where it was used that ψ_R^+ is normalized and $\int d^3r e^{i(\mathbf{k}-\mathbf{k}')\cdot\mathbf{r}} = (2\pi)^3\delta(\mathbf{k} - \mathbf{k}')$. The double integral over $\mathbf{r}_1, \mathbf{r}_2$ would be zero exactly if the exact continuum states were used instead of

2. High-Harmonic Generation

plane waves because of orthogonality of the continuum states and ψ_R^+ . Setting it to zero here is an approximation. Performing the integral over the δ -function simplifies the expression even further

$$ie^{iE_0t} \frac{\partial \Psi}{\partial t} \rightarrow E_0 \phi(\mathbf{k}', R, t) + i \frac{\partial \phi(\mathbf{k}', R, t)}{\partial t}.$$

Projection of the right side gives

$$\begin{aligned} e^{iE_0t} H\Psi &\rightarrow \chi_0(R) \mathbf{E}(t) \cdot \int d^3r_1 \int d^3r_2 e^{-i\mathbf{k}' \cdot \mathbf{r}_1} \psi_R^{+*}(\mathbf{r}_2) (\mathbf{r}_1 + \mathbf{r}_2) \psi_R(\mathbf{r}_1, \mathbf{r}_2) \\ &+ \int \frac{d^3k}{(2\pi)^3} \left[\frac{\mathbf{k}^2}{2} - \frac{1}{M} \frac{\partial^2}{\partial R^2} + V_{\text{BO}}^+(R) \right] \phi(\mathbf{k}, R, t) \times \\ &\times \left[(2\pi)^3 \delta(\mathbf{k} - \mathbf{k}') + \underbrace{\int d^3r_1 \int d^3r_2 e^{-i\mathbf{k}' \cdot \mathbf{r}_1} \psi_R^{+*}(\mathbf{r}_2) e^{i\mathbf{k} \cdot \mathbf{r}_2} \psi_R^+(\mathbf{r}_1)}_{\approx 0} \right] \\ &+ \mathbf{E}(t) \cdot \int \frac{d^3k}{(2\pi)^3} \phi(\mathbf{k}, R, t) \left[\int d^3r_1 \mathbf{r}_1 e^{i(\mathbf{k} - \mathbf{k}') \cdot \mathbf{r}_1} \right. \\ &\left. + \underbrace{\int d^3r_1 \int d^3r_2 e^{-i\mathbf{k}' \cdot \mathbf{r}_1} \psi_R^{+*}(\mathbf{r}_2) \mathbf{r}_2 e^{i\mathbf{k} \cdot \mathbf{r}_2} \psi_R^+(\mathbf{r}_1)}_{\approx 0} \right]. \end{aligned}$$

The two double integrals again vanish because of approximate orthogonality. Further simplifications yield

$$\begin{aligned} e^{iE_0t} H\Psi &\rightarrow \chi_0(R) \mathbf{E}(t) \cdot \left[\mathbf{d}_{\text{ion}}(\mathbf{k}', R) + \underbrace{\int d^3r_1 \int d^3r_2 e^{-i\mathbf{k}' \cdot \mathbf{r}_1} \psi_R^{+*}(\mathbf{r}_2) \mathbf{r}_2 \psi_R(\mathbf{r}_1, \mathbf{r}_2)}_{\approx 0} \right] \\ &+ \left[\frac{\mathbf{k}'^2}{2} - \frac{1}{M} \frac{\partial^2}{\partial R^2} + V_{\text{BO}}^+(R) \right] \phi(\mathbf{k}', R, t) + i \mathbf{E}(t) \cdot \nabla_{\mathbf{k}'} \phi(\mathbf{k}', R, t). \end{aligned}$$

Here it was used that $\int \frac{d^3k}{(2\pi)^3} \phi(\mathbf{k}, R, t) \int d^3r \mathbf{r} e^{i(\mathbf{k} - \mathbf{k}') \cdot \mathbf{r}} = i \nabla_{\mathbf{k}'} \phi(\mathbf{k}', R, t)$. The function \mathbf{d}_{ion} is the dipole-transition matrix element for ionization

$$\mathbf{d}_{\text{ion}}(\mathbf{k}, R) := \langle \mathbf{k} | \mathbf{r} | \psi_R \rangle = \int d^3r_1 \int d^3r_2 e^{-i\mathbf{k} \cdot \mathbf{r}_1} \psi_R^{+*}(\mathbf{r}_2) \mathbf{r}_1 \psi_R(\mathbf{r}_1, \mathbf{r}_2) \quad (2.12)$$

which is characteristic to the molecule at hand and describes the transition probability of the electron to the continuum. The other double integral is set to zero because it describes the dipole-transition matrix element for the inactive electron.

Equating both sides of the TDSE provides an equation for ϕ

$$\begin{aligned} \frac{\partial \phi(\mathbf{k}, R, t)}{\partial t} &= -i \left[\frac{\mathbf{k}^2}{2} - \frac{1}{M} \frac{\partial^2}{\partial R^2} + V_{\text{BO}}^+(R) - E_0 \right] \phi(\mathbf{k}, R, t) + \mathbf{E}(t) \cdot \nabla_{\mathbf{k}} \phi(\mathbf{k}, R, t) \\ &- i \chi_0(R) \mathbf{E}(t) \cdot \mathbf{d}_{\text{ion}}(\mathbf{k}, R). \end{aligned}$$

which is solved by

$$\begin{aligned} \phi(\mathbf{k}, R, t) = & -i \int_0^t dt' \mathbf{E}(t') \cdot U_R^+(t, t') \left[\mathbf{d}_{\text{ion}}(\mathbf{k} - \mathbf{A}(t) + \mathbf{A}(t'), R) \chi_0(R) \right] \times \\ & \times e^{-i \int_{t'}^t dt'' ([\mathbf{k} - \mathbf{A}(t) + \mathbf{A}(t'')]^2 / 2 - E_0)}. \end{aligned}$$

with $\mathbf{A}(t) = -\int^t dt' \mathbf{E}(t')$. The time-evolution in the ionic BO potential is given by U_R^+ [62]

$$i \frac{\partial U_R^+(t, t')}{\partial t} = H_R^+ U_R^+(t, t') \quad \text{with} \quad H_R^+ = -\frac{1}{M} \frac{\partial^2}{\partial R^2} + V_{\text{BO}}^+(R) \quad (2.13)$$

The dipole moment is defined as $\mathbf{D}(t) = -\langle \Psi(t) | \mathbf{r}_1 + \mathbf{r}_2 | \Psi(t) \rangle$. Inserting the ansatz for Ψ gives

$$\begin{aligned} -\mathbf{D}(t) = & \int dR |\chi_0(R)|^2 \underbrace{\int d^3 r_1 \int d^3 r_2 |\psi_R(\mathbf{r}_1, \mathbf{r}_2)|^2 (\mathbf{r}_1 + \mathbf{r}_2)}_{=0} \\ & + \left(2 \int \frac{d^3 k}{(2\pi)^3} \int dR \phi(\mathbf{k}, R, t) \chi_0^*(R) \left[\mathbf{d}_{\text{rec}}^*(\mathbf{k}, R) \right. \right. \\ & \left. \left. + \underbrace{\int d^3 r_1 \int d^3 r_2 e^{i\mathbf{k} \cdot \mathbf{r}_1} \psi_R^+(\mathbf{r}_2) \mathbf{r}_2 \psi_R^*(\mathbf{r}_1, \mathbf{r}_2)}_{\approx 0} \right] + \text{c.c.} \right) \\ & + \text{continuum-continuum transitions} \end{aligned}$$

The first double integral vanishes exactly because the electronic BO ground state of the neutral molecule has even symmetry and the second double integral again is the transition moment for the inactive electron. The function $\mathbf{d}_{\text{rec}}^*$ is the dipole-transition matrix element for recombination which is the complex-conjugate of the ionization element \mathbf{d}_{ion} , i.e. $\mathbf{d}_{\text{ion}} = \mathbf{d}_{\text{rec}}$. If the continuum-continuum transitions are neglected one gets

$$\mathbf{D}(t) = -2 \int \frac{d^3 k}{(2\pi)^3} \int dR \phi(\mathbf{k}, R, t) \chi_0^*(R) \mathbf{d}_{\text{rec}}^*(\mathbf{k}, R) + \text{c.c.}$$

Inserting the solution for ϕ and substituting $\mathbf{k} = \mathbf{p} + \mathbf{A}(t)$, where \mathbf{p} is the canonical momentum which is conserved in the continuum,

$$\begin{aligned} \mathbf{D}(t) = & 2i \int_0^t dt' \int \frac{d^3 p}{(2\pi)^3} \int dR \mathbf{d}_{\text{rec}}^*(\mathbf{p} + \mathbf{A}(t), R) \chi_0^*(R) \times \\ & \times \mathbf{E}(t') \cdot U_R^+(t, t') \left[\mathbf{d}_{\text{ion}}(\mathbf{p} + \mathbf{A}(t'), R) \chi_0(R) \right] e^{-i \int_{t'}^t dt'' ([\mathbf{p} + \mathbf{A}(t'')]^2 / 2 - E_0)} + \text{c.c.} \end{aligned}$$

We introduce the vibrational autocorrelation

$$\tilde{\mathcal{C}}(\mathbf{p}, t, t') := \int dR \mathbf{d}_{\text{rec}}^*(\mathbf{p} + \mathbf{A}(t), R) \chi_0^*(R) \mathbf{E}(t') \cdot U_R^+(t, t') \mathbf{d}_{\text{ion}}(\mathbf{p} + \mathbf{A}(t'), R) \chi_0(R)$$

and semiclassical action

$$S(\mathbf{p}, t, t') := \int_{t'}^t dt'' \left(\frac{[\mathbf{p} + \mathbf{A}(t'')]^2}{2} - E_0 \right). \quad (2.14)$$

2. High-Harmonic Generation

The integral over the first term in S is the *Volkov phase*, i.e. the phase that a free electron acquires over time in the laser field described by \mathbf{A} . It comes from neglecting the interaction between the electron and the parent ion during the time between ionization and recombination. This is the fundamental part of the strong-field approximation and is the origin of its name.

With these definitions, the dipole moment can be written in the more compact form

$$\mathbf{D}(t) = 2i \int_0^t dt' \int \frac{d^3p}{(2\pi)^3} \tilde{\mathbf{C}}(\mathbf{p}, t, t') e^{-iS(\mathbf{p}, t, t')} + \text{c.c.} \quad (2.15)$$

Fourier transformation results in

$$\tilde{\mathbf{D}}(\omega) = 2i \int dt \int_0^t dt' \int \frac{d^3p}{(2\pi)^3} \tilde{\mathbf{C}}(\mathbf{p}, t, t') e^{-i\tilde{S}(\mathbf{p}, t, t'; \omega)} \quad (2.16)$$

with

$$\tilde{S}(\mathbf{p}, t, t'; \omega) := S(\mathbf{p}, t, t') - \omega t, \quad (2.17)$$

where the complex conjugate in $\mathbf{D}(t)$ has been neglected, which is appropriate under the condition $\omega > 0$.

2.2.2. Spectrum

In high-harmonic generation, the subject of most interest is the spectrum of emitted radiation, which is proportional to the modulus-squared Fourier-transformed dipole acceleration $\ddot{\mathbf{D}}(t)$ [63, 64]

$$S_{\text{spec}}(\omega) \propto \left| \tilde{\ddot{\mathbf{D}}}(\omega) \right|^2 = \left| \int_{t_0}^{t_f} dt \ddot{\mathbf{D}}(t) e^{i\omega t} \right|^2$$

where it is assumed that the laser pulse is turned on and off between t_0 and t_f .

Applying integration by parts twice to $\tilde{\ddot{\mathbf{D}}}(\omega)$ relates it to the dipole moment $\mathbf{D}(t)$

$$\tilde{\ddot{\mathbf{D}}}(\omega) = \left(\dot{\mathbf{D}}(t) e^{i\omega t} - \mathbf{D}(t) (i\omega) e^{i\omega t} \right) \Big|_{t_0}^{t_f} + \int_{t_0}^{t_f} dt \mathbf{D}(t) (i\omega)^2 e^{i\omega t}. \quad (2.18)$$

Before the laser is turned on, $t < t_0$, the system is in its ground state and the dipole moment and velocity are identical to zero, $\mathbf{D}(t \leq t_0) = \dot{\mathbf{D}}(t \leq t_0) \equiv 0$. However, this does not need to be true after the laser pulse is turned off, $t > t_f$, where the total wave function is generally in a superposition of many different states, as can be seen by the ansatz (2.10), and thus can give rise to position and velocity components of the dipole. In other words, while the electron is no longer accelerated by the laser field, its wave function may still change over time and cause a varying charge distribution. Since these contributions are not of interest, the boundary terms in (2.18) can be neglected and the spectrum simply be written as

$$S_{\text{spec}}(\omega) \propto \omega^4 \left| \tilde{\mathbf{D}}(\omega) \right|^2.$$

It should be noted here that there may be recollisions shortly after the end of the laser pulse, which are also neglected by this approach.

2.2.3. Length, velocity and acceleration formulations

If the total wave function $\Psi(t)$ of the system is known *exactly*, the Ehrenfest theorem [65] assures that

$$\ddot{\mathbf{D}}(t) = \frac{\partial}{\partial t} \mathbf{P}_D(t) = \mathbf{A}_D(t) \quad (2.19)$$

with the dipole velocity \mathbf{P}_D and acceleration \mathbf{A}_D , for the single active electron, given in terms of $|\Psi(t)\rangle$

$$\begin{aligned} \mathbf{P}_D(t) &= -\langle \Psi(t) | \mathbf{p} | \Psi(t) \rangle \\ \mathbf{A}_D(t) &= \langle \Psi(t) | \nabla V + \mathbf{E}(t) | \Psi(t) \rangle. \end{aligned}$$

where V describes the interaction between the electron and the core. In the SFA, however, the wave function is only approximately known and equation (2.19) is not valid. Consequently, one should expect different results depending on which quantity is taken in the calculation of S_{spec} [66]. Following the literature, we refer to the different formulations as *length*, *velocity* and *acceleration forms*. Specifically, the different forms give rise to different recombination matrix elements \mathbf{d}_{rec}

$$\begin{aligned} \mathbf{d}_{\text{L}}^{\text{rec}} &= \langle \mathbf{k} | \mathbf{r} | \psi_R \rangle \\ \mathbf{d}_{\text{V}}^{\text{rec}} &= \langle \mathbf{k} | -i\nabla | \psi_R \rangle \\ \mathbf{d}_{\text{A}}^{\text{rec}} &= \langle \mathbf{k} | \nabla V | \psi_R \rangle. \end{aligned}$$

In section 2.2.2 it was shown that the spectrum S_{spec} can be written either in terms of the dipole moment or acceleration and if certain temporary boundary terms vanish, the difference is a simple factor ω^4 . If the time integration is taken over all times, the boundary terms can be set to zero and it holds that [66]

$$S_{\text{spec}} \propto \left| \tilde{\mathbf{A}}_D(\omega) \right|^2 = \omega^2 \left| \tilde{\mathbf{P}}_D(\omega) \right|^2 = \omega^4 \left| \tilde{\mathbf{D}}(\omega) \right|^2.$$

2.2.4. Saddle-point approximation

For HHG the primary interest lies in a linearly polarized electric field. In this case the components of the dipole moment perpendicular to the field can be neglected and the relevant quantities, such as \mathbf{A} , the transition elements \mathbf{d}_{ion} , $\mathbf{d}_{\text{rec}}^*$ and the canonical momentum \mathbf{p} , become scalar. The dipole moment then takes the form

$$\tilde{\mathbf{D}}(\omega) = 2i \int dt \int_0^t dt' E(t') \int \frac{dp}{2\pi} C(p, t, t') e^{-i\tilde{S}(p, t, t'; \omega)}. \quad (2.20)$$

with a redefined autocorrelation $C(p, t, t') := \tilde{C}(p, t, t')/E(t')$ (see beginning of chapter 3 for more details).

2. High-Harmonic Generation

Even in the case of linear polarization the evaluation of the multiple integrals in the dipole moment is computationally demanding. In order to reduce the effort, the saddle-point approximation [22] can be employed which transforms the integrals into finite sums over saddle-points of the action S . The resulting saddle-point equations have tuples of solutions (p_s, t_s, t'_s) (one for every frequency ω) that describe the electron trajectories (so-called saddle-point trajectories) that give the dominant contributions to the dipole moment. The approximation requires the phase factor $e^{-i\tilde{S}(p,t,t')}$ to vary much faster than the rest of the integrand, i.e. the autocorrelation $C(p, t, t')$. For this we introduce a suitable energy shift as outlined in the following.

The dipole moment (2.15) (and therefore the one in (2.20)) is invariant under energy shifts of the BO potentials, i.e. adding some constant energy to the potentials does not alter the value of $\tilde{D}(\omega)$. This can be seen easiest by rewriting the autocorrelation in terms of a finite sum

$$C(p, t, t') = \sum_{\nu} c_{\text{rec}}^{\nu*}(t, t') c_{\text{ion}}^{\nu}(t, t') e^{-iE_{\nu}^{+}(t-t')} \quad (2.21)$$

where the expansion coefficients $c_{\text{rec}}^{\nu}(t, t')$ and $c_{\text{ion}}^{\nu}(t, t')$ are defined such that

$$\begin{aligned} \sum_{\nu} c_{\text{ion}}^{\nu}(t, t') \chi_{\nu}^{+}(R) &= d_{\text{ion}}(p(t, t') + A(t'), R) \chi_0(R) \\ \sum_{\nu} c_{\text{rec}}^{\nu}(t, t') \chi_{\nu}^{+}(R) &= d_{\text{rec}}(p(t, t') + A(t), R) \chi_0(R) \end{aligned}$$

and E_{ν}^{+} are the eigenenergies of the BO potential $V_{\text{BO}}^{+}(R)$. Shifting the potential energy by some constant V_0 affects the total ground state energy E_0 in the action (2.14), (2.17) and the vibrational eigenenergies E_{ν}^{+} in (2.21). This gives rise to a factor $e^{iV_0(t-t')}$ and its inverse $e^{-iV_0(t-t')}$, respectively, which cancel out. It is therefore possible to choose a suitable zero-point of the energy such that the quality of the saddle-point approximation is improved. Defining the shifted BO potential $\mathcal{V}_{\text{BO}}^{+}$

$$\mathcal{V}_{\text{BO}}^{+}(R) = V_{\text{BO}}^{+}(R) + V_{\text{BO}}^{\text{shift}} \quad \text{with} \quad V_{\text{BO}}^{\text{shift}} = -(E_0 + I_p) \approx 0.57014, \quad (2.22)$$

the energy $-E_0$ in the action is replaced by the ionization potential I_p

$$\begin{aligned} \mathcal{S}(p, t, t') &:= \int_{t'}^t dt'' \left(\frac{[p + A(t'')]^2}{2} + I_p \right) \\ \tilde{\mathcal{S}}(p, t, t'; \omega) &:= \mathcal{S}(p, t, t') - \omega t. \end{aligned}$$

The vibrational eigenenergies E_{ν}^{+} are shifted up by $V_{\text{BO}}^{\text{shift}}$ accordingly. We apply the SPA to $\tilde{\mathcal{S}}$ and choose to do so for the momentum p first, followed by a combined SPA for t, t' .

Saddle-point equations and factors Setting the first derivatives of $\tilde{\mathcal{S}}$ with respect to p, t, t' equal to zero yields the following saddle-point equations.

Saddle-point momentum p

$$p_s(t_s, t'_s) = -\frac{1}{t_s - t'_s} \int_{t'_s}^{t_s} dt A(t) \quad (2.23)$$

Ionization time t'

$$\frac{[p_s(t_s, t') + A(t_s')]^2}{2} = -I_p \quad (2.24)$$

Recombination time t

$$\frac{[p_s(t_s, t') + A(t_s)]^2}{2} = \omega - I_p \quad (2.25)$$

These equations are almost identical to the ones encountered in the semiclassical three-step model in section 2.1. Equation (2.23) is the condition that the electron trajectory starts at the same location as it ends, which is analogous to the semiclassical model where this location is set to zero, see equations (2.3) and (2.7).

Furthermore, equation (2.25) tells us that the kinetic energy at the time of recombination (left hand side) should match the difference between the emitted harmonic energy ω and the ionization potential I_p . This is the conservation of energy and corresponds to equation (2.8).

The important difference to the semiclassical model can be seen in equation (2.24), where the initial kinetic energy of the electron is negative, $-I_p$, which is attributed to the fact that the electron must tunnel out through a potential barrier in order to enter the continuum [22, 61]. In the semiclassical model, tunneling is incorporated through the ionization rate (2.1), which influences the overall probability of a certain trajectory, but does not affect its ionization or recombination times. For $I_p = 0$, tunneling is not necessary and equations (2.24) and (2.4) coincide. The physically relevant case of nonzero I_p gives rise to complex-valued times t_s and t'_s .

The corresponding saddle-point factor for p reads

$$\begin{aligned} \Pi(t, t') &= \int \frac{dp}{2\pi} \exp\left(-\frac{i}{2} \frac{\partial^2 \tilde{\mathcal{S}}}{\partial p^2} (p - p_s)^2\right) \\ &= \int \frac{dp}{2\pi} \exp\left(-\frac{i}{2} (t - t') (p - p_s)^2\right) \\ &= \left(\frac{1}{2\pi i (t - t')}\right)^{1/2} \end{aligned} \quad (2.26)$$

where the exponent in the result counts the number of dimensions. In three dimensions for example, it would be $3/2$.

The saddle-point factor for t, t' is

$$\begin{aligned} \Lambda(t_s, t'_s) &= \int dt \int dt' \exp\left(-\frac{i}{2} \frac{\partial^2 \tilde{\mathcal{S}}}{\partial t^2} (t - t_s)^2\right) \times \\ &\quad \times \exp\left(-i \frac{\partial^2 \tilde{\mathcal{S}}}{\partial t \partial t'} (t - t_s)(t' - t'_s)\right) \exp\left(-\frac{i}{2} \frac{\partial^2 \tilde{\mathcal{S}}}{\partial t'^2} (t' - t'_s)^2\right) \end{aligned} \quad (2.27)$$

2. High-Harmonic Generation

where the derivatives of $\tilde{\mathcal{S}}$ are evaluated at the saddle-point times (t_s, t'_s) . With the help of equations (2.24) and (2.25) we can define the kinetic momenta of the electron at the saddle-point times of ionization and recombination as

$$\begin{aligned} k_{\text{ion}}^{\pm} &:= p_s(t_s, t'_s) + A(t'_s) = \pm \sqrt{-2I_p} \\ k_{\text{rec}}^{\pm}(\omega) &:= p_s(t_s, t'_s) + A(t_s) = \pm \sqrt{2(\omega - I_p)}. \end{aligned}$$

The second derivatives of $\tilde{\mathcal{S}}$ in $\Lambda(t_s, t'_s)$ can then be written as

$$\begin{aligned} \frac{\partial^2 \tilde{\mathcal{S}}}{\partial t^2}(t_s, t'_s; \omega) &= -(p_s(t_s, t'_s) + A(t_s)) \left(\frac{p_s(t_s, t'_s) + A(t_s)}{t_s - t'_s} + E(t_s) \right) \\ &= -k_{\text{rec}}^{\pm}(\omega) \left(\frac{k_{\text{rec}}^{\pm}(\omega)}{t_s - t'_s} + E(t_s) \right) \end{aligned} \quad (2.28)$$

$$\begin{aligned} \frac{\partial^2 \tilde{\mathcal{S}}}{\partial t'^2}(t_s, t'_s; \omega) &= -(p_s(t_s, t'_s) + A(t'_s)) \left(\frac{p_s(t_s, t'_s) + A(t'_s)}{t_s - t'_s} - E(t'_s) \right) \\ &= -k_{\text{ion}}^{\pm} \left(\frac{k_{\text{ion}}^{\pm}}{t_s - t'_s} - E(t'_s) \right) \end{aligned} \quad (2.29)$$

$$\begin{aligned} \frac{\partial^2 \tilde{\mathcal{S}}}{\partial t \partial t'}(t_s, t'_s; \omega) &= \frac{(p_s(t_s, t'_s) + A(t_s))(p_s(t_s, t'_s) + A(t'_s))}{t_s - t'_s} \\ &= \frac{k_{\text{rec}}^{\pm}(\omega) k_{\text{ion}}^{\pm}}{t_s - t'_s}. \end{aligned} \quad (2.30)$$

The existence of the integral in expression (2.27) is not clear a priori, but can be verified numerically. There exists a combination of signs in k_{ion}^{\pm} and $k_{\text{rec}}^{\pm}(\omega)$ such that the integral converges and the result is

$$\Lambda(t_s, t'_s) = 2\pi \left[\left(\frac{\partial^2 \tilde{\mathcal{S}}}{\partial t \partial t'} \right)^2 - \frac{\partial^2 \tilde{\mathcal{S}}}{\partial t^2} \frac{\partial^2 \tilde{\mathcal{S}}}{\partial t'^2} \right]^{-1/2}. \quad (2.31)$$

The saddle-point approximated expression for the Fourier-transformed dipole moment then reads

$$\tilde{D}_{\text{SPA}}(\omega) = 2i \sum_s E(t'_s) \Pi(t_s, t'_s) \Lambda(t_s, t'_s) C(p_s, t_s, t'_s) e^{-i\tilde{\mathcal{S}}(p_s, t_s, t'_s; \omega)} \quad (2.32)$$

where the sum goes over all tuples of solutions (p_s, t_s, t'_s) for a given ω .

Saddle-point times

In this section we want to study the solutions to equations (2.23) - (2.25). We employ the case of a linearly polarized electric field with constant intensity

$$E(t) = E_0 \cos(\omega_0 t) \quad \Rightarrow \quad A(t) := - \int^t dt' E(t') = -\frac{E_0}{\omega_0} \sin(\omega_0 t).$$

with peak amplitude E_0 and angular frequency ω_0 . This allows us to analytically solve equation (2.23)

$$p_s(t_s, t'_s) = -\frac{E_0}{\omega_0^2} \frac{\cos(\omega_0 t_s) - \cos(\omega_0 t'_s)}{t_s - t'_s}.$$

Hence, the problem reduces to solving the two equations (2.24) and (2.25)

$$\left[p_s(t_s, t'_s) - \frac{E_0}{\omega_0} \sin(\omega_0 t'_s) \right]^2 = -2I_p \quad (2.33)$$

$$\left[p_s(t_s, t'_s) - \frac{E_0}{\omega_0} \sin(\omega_0 t_s) \right]^2 = 2(\omega - I_p). \quad (2.34)$$

The energy of the emitted harmonic is ω . The expression in brackets on the left sides are the kinetic momenta at time of ionization (2.33) and recombination (2.34). Note that if t_s, t'_s are solutions, so are t_s^*, t'_s^* , i.e. the complex-conjugate times. A description of the properties of the saddle-point times can also be found in [61].

It should be noted that the features of the solutions described in this section have been studied only for a narrow range of parameters and therefore are not supported by a rigorous mathematical proof. While the descriptions may well apply to a wide range of parameters, it is not certain that it holds true for any set of such values. For example, any statement that involves large harmonic energies $\omega \rightarrow \infty$ is strictly speaking only tested for ω below a certain numerical limit.

Zero ionization potential Let us first, for simplicity, consider the case of a vanishing ionization potential $I_p = 0$. We then arrive at the classical case where the initial momentum of the electron is zero (2.33) and the return energy corresponds to the emitted harmonic energy ω (2.34). Figure 2.5 shows the solutions for a wavelength of 800 nm and intensity of $4 \cdot 10^{14}$ W/cm².

The times in Figure 2.5 should be understood as the limiting case of $I_p \rightarrow 0$. The saddle-point integral over t' in expression (2.27) does not converge for $I_p = 0$. The reason is the vanishing second derivatives of the action with respect to t' in expressions (2.29) and (2.30)

$$\frac{\partial^2 \tilde{\mathcal{S}}}{\partial t'^2}(t_s, t'_s; \omega) = \frac{\partial^2 \tilde{\mathcal{S}}}{\partial t \partial t'}(t_s, t'_s; \omega) = 0$$

because $k_{\text{ion}}^\pm = \pm \sqrt{-2I_p} = 0$.

There is a sharp energy threshold below which the saddle-point times t_s, t'_s are real and equal to the classical times. This boundary is what we define as the cutoff energy $\omega_c \approx 3.17U_p$. This is approximately 2.78 for the current parameters.

We call the range below that energy, $0 \leq \omega \leq \omega_c$, the plateau region. In that region, we can distinguish between two kinds of solutions, the short and long trajectories. The short trajectory is defined by having the lower excursion time $\tau_s = t_s - t'_s$ of the two. Correspondingly, the long trajectory has the higher value of τ_s . The long trajectories start before the short ones and

2. High-Harmonic Generation

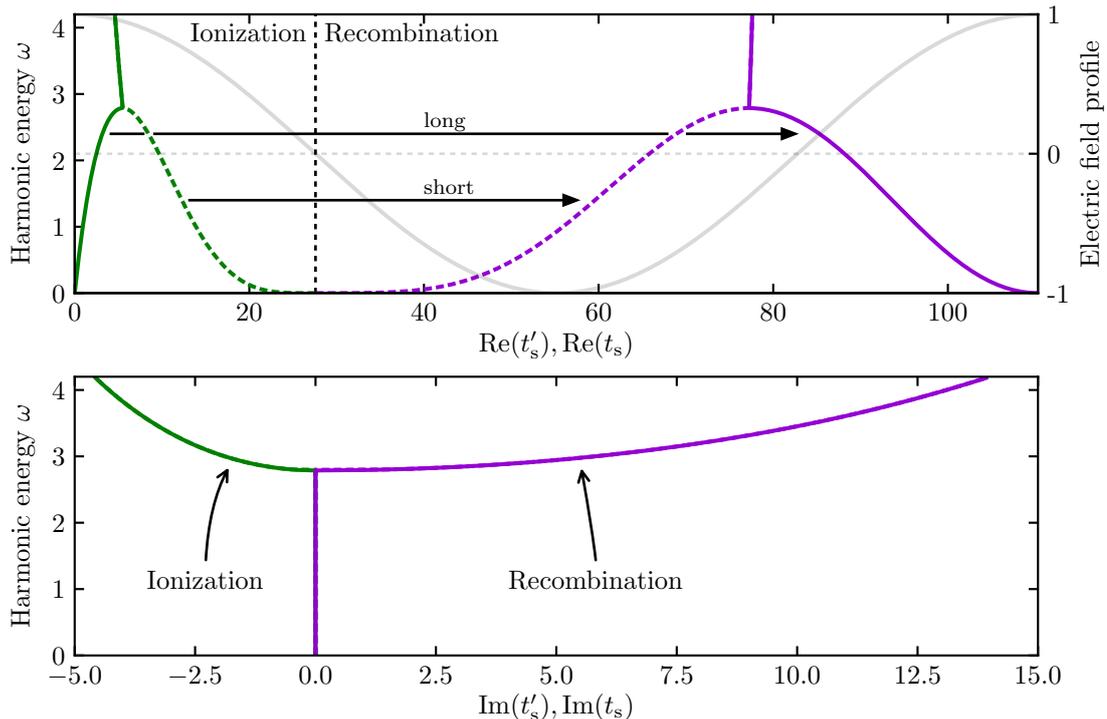


Figure 2.5.: Saddle-point solutions for a wavelength of 800 nm and intensity of $4 \cdot 10^{14} \text{ W/cm}^2$ and vanishing ionization potential $I_p = 0$. The period of the field is approximately 110. **Top:** Real part of ionization and recombination times for both short (dashed) and long (solid) trajectories. Also shown is the profile of the electric field $E(t)$. The vertical dashed line indicates the first quarter of the field period. **Bottom:** Imaginary part of the ionization and recombination times. Note that the times shown here are to be understood as the limiting case for $I_p \rightarrow 0$. The saddle-point integral over t' does not converge for $I_p = 0$ (see main text).

recombine after them. With the field maximum as reference, they both start within the first quarter of the field period and recombine in the last three quarters.

In the cutoff region, i.e. for $\omega > \omega_c$, there exist no real solutions. The short and long trajectories merge into just one complex trajectory. Otherwise it is not possible for the electron to reach kinetic energies higher than ω_c . Complex values for the ionization and recombination times are necessary to satisfy the saddle-point equations in this region. The imaginary part of the excursion time grows rapidly with increasing energy, while the real part has a nearly constant value of approximately $4.1/\omega$. For a wavelength of 800 nm, this is around 72 (see left panel in Figure 2.6).

The cutoff ω_c is clearly visible in Figure 2.5 as the energy where the real parts of the ionization and recombination times meet for the short and long trajectories, respectively. It is also the point where the imaginary parts deviate from zero. The right panel in Figure 2.6 demonstrates this for a fixed harmonic while the electric field intensity is varied. For a weak field, the harmonic lies in the cutoff-region where the excursion time is complex with an approximately constant real part. If the intensity is high enough, the harmonic enters the plateau region where the single complex solution becomes real and bifurcates into the short and long solutions.

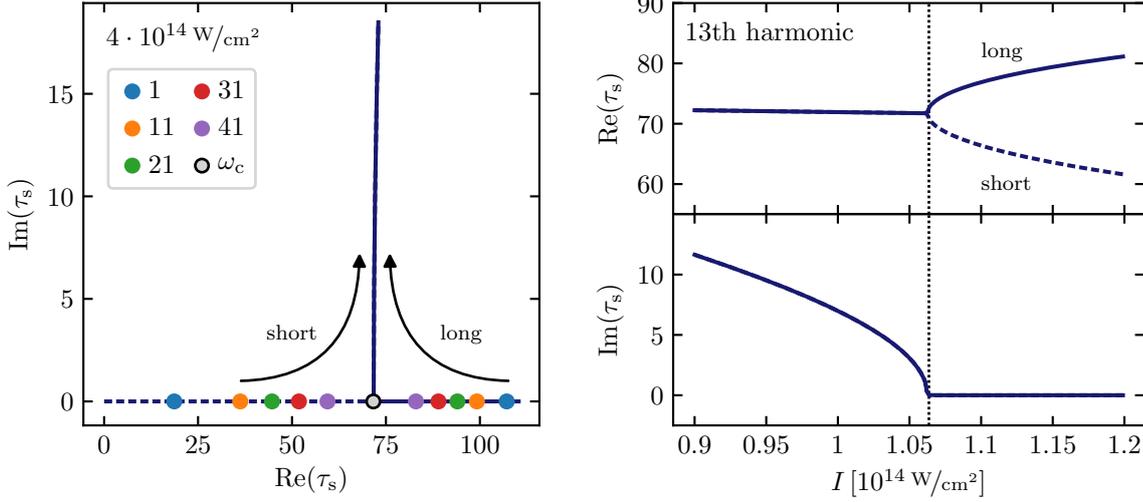


Figure 2.6.: Excursion time $\tau_s = t_s - t'_s$ for a wavelength of 800 nm and vanishing ionization potential, $I_p = 0$. **Left:** Real and imaginary part for an electric field intensity of $4 \cdot 10^{14} \text{ W/cm}^2$. The arrows indicate the direction of increasing harmonic energy ω . Once ω exceeds the cutoff energy ω_c , the saddle-point times become complex with approximately constant real part of τ_s . A selection of harmonic energies is shown as colored points. **Right:** Real and imaginary part as a function of field intensity for the 13th harmonic. Once the intensity is high enough for this harmonic to fall within the plateau region, the real part bifurcates into two branches corresponding to the short and long trajectory and the imaginary part becomes zero. The vertical dotted line indicates the intensity for which the harmonic energy equals the cutoff energy.

Nonzero ionization potential The physically relevant case is that of nonvanishing I_p . An example of such solutions for the same parameters of 800 nm and $4 \cdot 10^{14} \text{ W/cm}^2$ as before is shown in Figure 2.8 for the ionization potential of H_2 .

In contrast to the case of $I_p = 0$, there are no real solutions for the saddle-point times for any value of the harmonic energy ω . This is true independently of the electric field $E(t)$, see the more general equation (2.24). Below the cutoff, we can still identify short and long trajectories by taking the real part of the excursion time τ_s , i.e. $\text{Re}(\tau_s^{\text{short}}) < \text{Re}(\tau_s^{\text{long}})$.

The graphs of the solutions in Figure 2.8 share similarities to the ones for $I_p = 0$ in Figure 2.5. The real parts of ionization and recombination of both trajectories approach each other for increasing energy and in the transition to the cutoff-region they become less sensitive to the energy. Correspondingly, the real parts of the excursion time τ_s become less sensitive to the harmonic energy in that region too (see left panel in Figure 2.9). Furthermore, the imaginary parts show a rapid change with energy as for $I_p = 0$ as well.

The cutoff energy is more complicated to determine compared to $I_p = 0$, where the cutoff is the energy above which the saddle-point times become complex. It can be shown [22] that ω_c is approximately of the form

$$\omega_c \approx f_c(I_p/U_p)I_p + 3.17U_p \quad (2.35)$$

for some function f_c , which can be found numerically, see Figure 2.7. The correction to the classical expression $I_p + 3.17U_p$ can be attributed to the tunnelling of the electron and the

2. High-Harmonic Generation

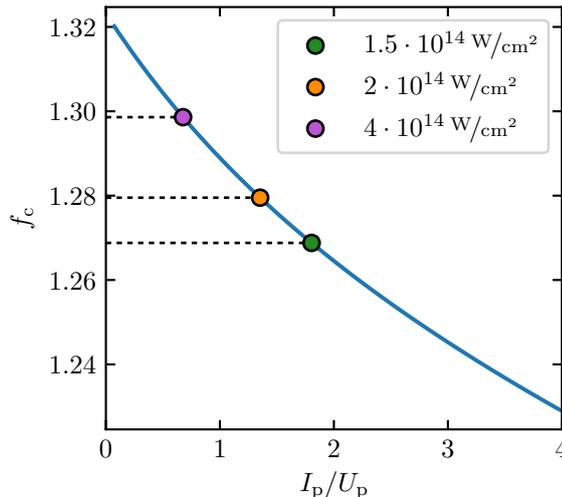


Figure 2.7.: Function f_c which enters the cutoff-law (2.35). The values were graphically extracted from FIG. 5 in [22]. For small but positive ionization potential, $0 < I_p \ll U_p$, the value is approximately 1.32. The colored dots show the value of H_2 for 800 nm and the given intensities.

spreading of its wave function in the continuum. For a more detailed description see [22].

In practice it suffices to think of a range of cutoff-energies. It is usually not necessary to identify a sharp boundary where the transition from the plateau- to the cutoff-region takes place. The conspicuous change in behaviour of the saddle-point solutions makes it possible to establish such a transition in a heuristic manner when referring to plots. This also holds for quantities that depend on the saddle-point times, since they inherit such a behaviour.

It seems that there is always an energy where the real part of the ionization time for the short trajectory intersects with that of the long trajectory. There are still two solutions above that energy, but the physical meaning of “short” and “long” loses its relevance. The solution that we identified as being short now has a greater real part of the excursion time than the long counterpart, since the real parts of the recombination times do not intersect. We can still distinguish between the two since the solutions should depend continuously-differentiable on the energy. In this regard, one starts by finding solutions for low energies and then keeping track of them while increasing the energy. The imaginary parts of the ionization times do not intersect and switching between former short and long trajectories would introduce a discontinuity.

Contrary to the real parts of the saddle-point solutions, the imaginary parts of the ionization times are larger than for the recombination times, at least below the cutoff. For energies above the cutoff, the imaginary part of the ionization time, for the long trajectory, at some energy becomes less than that of the recombination time (the solid lines intersect in the lower panel in Figure 2.8). Furthermore, the recombination times have an imaginary part close to zero, especially for the long trajectory.

We plot in the right panel of Figure 2.9 the dependence of the excursion time on the field intensity for a fixed harmonic. These graphs show a similar behaviour to the case of $I_p = 0$ as

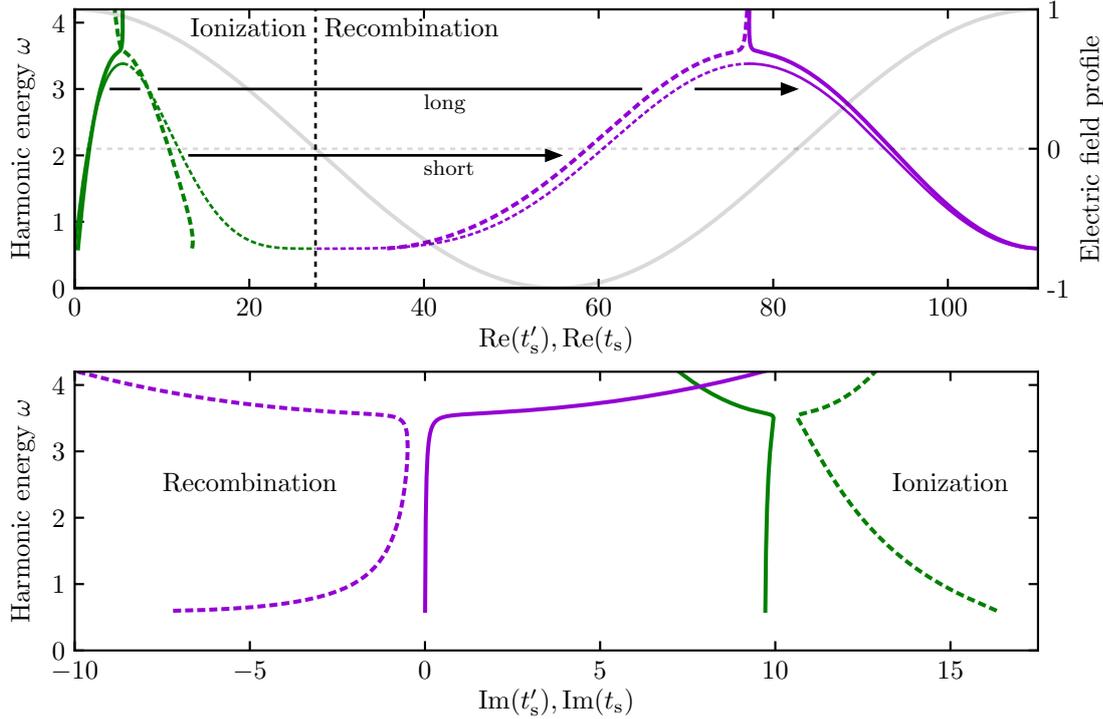


Figure 2.8.: Saddle-point solutions for a wavelength of 800 nm and intensity of $4 \cdot 10^{14} \text{ W/cm}^2$ for H_2 . The period of the field is approximately 110. **Top:** Real part of ionization and recombination times for both short (dashed) and long (solid) trajectories. The thin lines are the classical times. Also shown is the profile of the electric field $E(t)$. The vertical dashed line indicates the first quarter of the field period. **Bottom:** Imaginary part of the ionization and recombination times.

well. The real part is relatively insensitive to changes in field intensity when the harmonic is in the cutoff-region (low intensity) compared to when it falls within the plateau-region (high intensity). The opposite holds true for the imaginary part.

Experimental and theoretical studies of the phase of the harmonics generated by short and long trajectories and related phenomena (e.g. Quantum Path Interference) can be found in [61, 67–72].

Variation of ionization potential Having understood the general behaviour of the saddle-point times, we now turn our attention to how the times change when the ionization potential is varied. For this we concentrate on values of I_p around the value of H_2 , i.e. $I_p^{\text{H}} = 0.5944$. The relative change δt

$$\delta t(I_p, \omega) = \frac{\Delta t(I_p, \omega)}{t(I_p^{\text{H}}, \omega)} \quad \text{with} \quad \Delta t(I_p, \omega) = t(I_p, \omega) - t(I_p^{\text{H}}, \omega)$$

is plotted in Figure 2.10 for the ionization time t'_s and excursion time $\tau_s = t_s - t'_s$. We choose to plot τ_s here instead of t_s because we are ultimately interested in how the autocorrelation function changes with the ionization potential. In this context it is easiest to consider the

2. High-Harmonic Generation

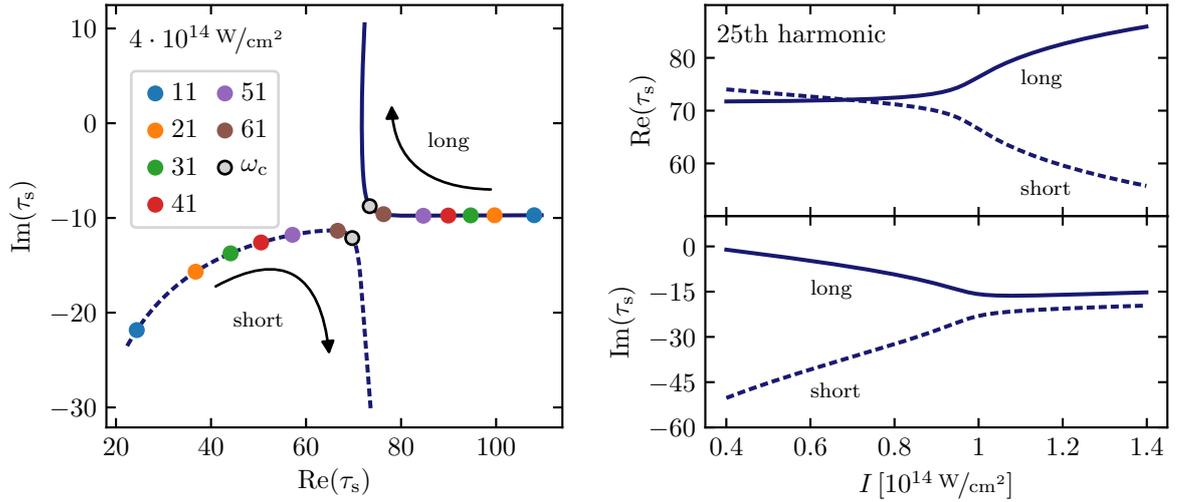


Figure 2.9.: Excursion time $\tau_s = t_s - t'_s$ for a wavelength of 800 nm for H_2 . **Left:** Real and imaginary part for an electric field intensity of $4 \cdot 10^{14} \text{ W/cm}^2$. The arrows indicate the direction of increasing harmonic energy ω . The excursion times for short and long trajectories approach each other for increasing energy. Similar to the case of vanishing I_p , beyond the cutoff the real part becomes less sensitive to the energy while the imaginary part changes rapidly. A selection of harmonic energies is shown as colored points and ω_c is calculated with expression (2.35). **Right:** Real and imaginary part as a function of field intensity for the 25th harmonic.

starting point of the vibrational dynamics, which is given by t'_s , and how long the time evolution takes place, given by τ_s .

The behaviour of the times as a function of ω is quite complicated. The transition from the plateau- to the cutoff-region manifests itself as peaks. We are primarily interested in how large δt becomes in the plateau-region. There the relative change is for the most part below 2.5%. The dependence of δt as a function of δI_p is linear in a good approximation, in particular for energies below and above the transition from the plateau to the cutoff.

The imaginary part of $\delta \tau_s$ exhibits a pole at $\omega \approx 4$ for the long trajectory. This originates from the intersection of $\text{Im}(t'_s)$ and $\text{Im}(t_s)$, visible in Figure 2.8.

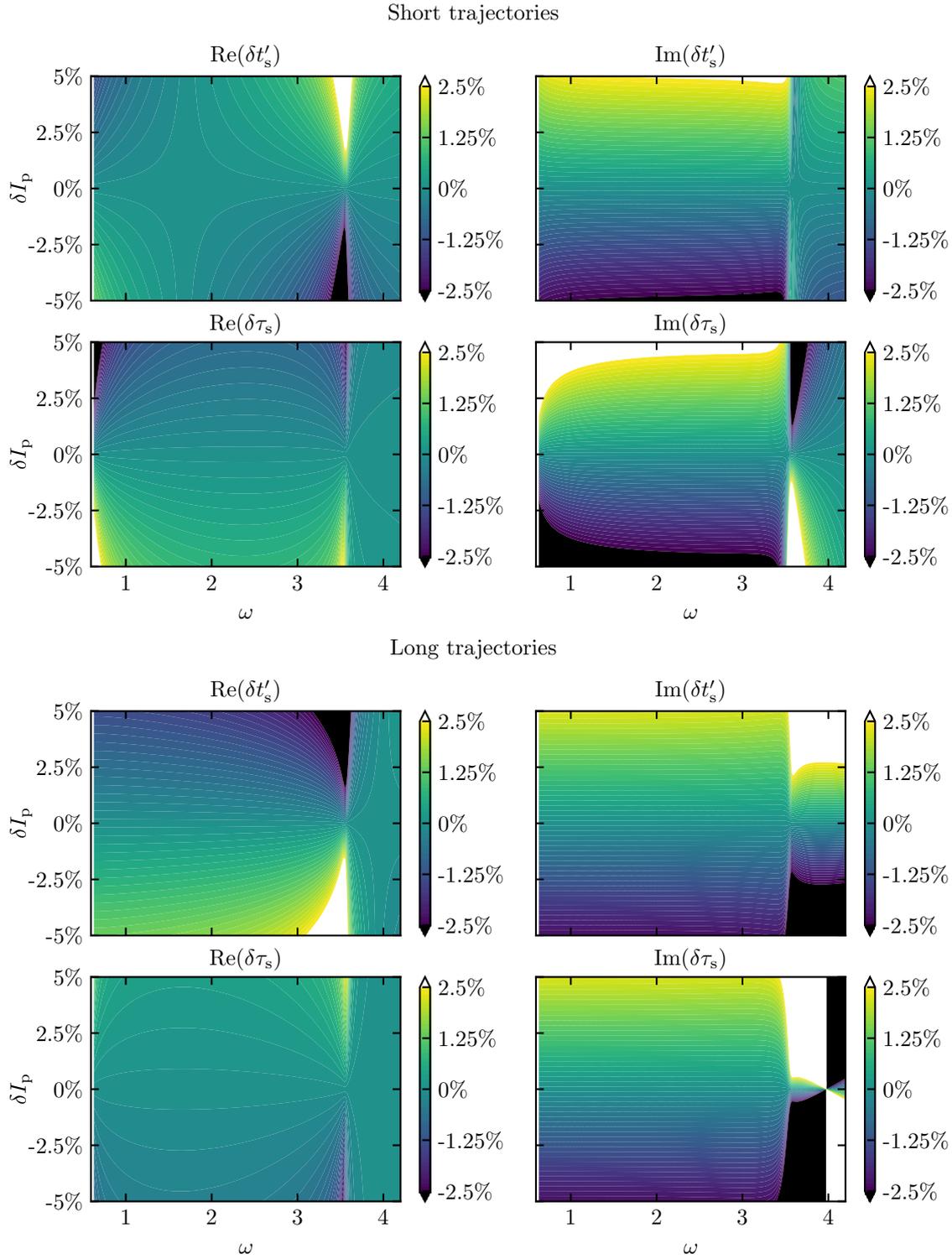


Figure 2.10.: Relative change δt of the saddle-point solutions of H_2 for the short (upper 4×4 grid) and long (lower 4×4 grid) trajectories. Shown is the dependence on harmonic energy ω and on the relative change of the ionization potential δI_p up to $\pm 5\%$. The electric field parameters are 800 nm and $4 \cdot 10^{14} \text{ W/cm}^2$. The ionization time t'_s is shown in the top row in each grid and the excursion time $\tau_s = t_s - t'_s$ in the bottom row. The real parts are on the left and the imaginary parts on the right. Values outside of the given range are colored white for the upper and black for the lower limit.

3. Vibrational Autocorrelation Function

This chapter is devoted to the study of the basic properties of the vibrational autocorrelation function

$$\tilde{C}(\mathbf{p}, t, t') = \int dR \mathbf{d}_{\text{rec}}^*(\mathbf{p} + \mathbf{A}(t), R) \chi_0^*(R) \mathbf{E}(t') \cdot \mathcal{U}_R^+(t, t') \mathbf{d}_{\text{ion}}(\mathbf{p} + \mathbf{A}(t'), R) \chi_0(R).$$

It appears in the expression of the dipole moment (2.15) and is an essential part of the SFA-based theory of HHG in H₂ that includes the nuclear dynamics. Here, \mathcal{U}_R^+ is the time-evolution operator for the shifted ionic BO potential $\mathcal{V}_{\text{BO}}^+$, \mathbf{d}_{ion} and \mathbf{d}_{rec} are the dipole-transition matrix elements for ionization and recombination, and $\chi_0(R)$ is the vibrational ground state of neutral H₂. For a linearly polarized electric field $\mathbf{E}(t)$ the components of \tilde{C} perpendicular to \mathbf{E} can be neglected. We define the autocorrelation along the direction of \mathbf{E} (see also section 2.2.4)

$$\begin{aligned} C(p, t, t') &= \frac{1}{E(t')} \mathbf{e}_{\mathbf{E}} \cdot \tilde{C}(\mathbf{p}, t, t') \\ &= \int dR \left[d_{\text{rec}}^*(p + A(t), R) \chi_0^*(R) \right] \mathcal{U}_R^+(t, t') \left[d_{\text{ion}}(p + A(t'), R) \chi_0(R) \right]. \end{aligned} \quad (3.1)$$

with a constant unit vector $\mathbf{e}_{\mathbf{E}}$ and $\mathbf{E}(t) = E(t)\mathbf{e}_{\mathbf{E}}$. The matrix elements in the direction of $\mathbf{e}_{\mathbf{E}}$ are denoted by d_{rec} and d_{ion} . This is the general expression used in all our numerical calculations and whenever we refer to the autocorrelation we implicitly mean this form.

Expression (3.1) can be rewritten in a different form, which is useful for practical evaluation. We have already used it in equation (2.21), but repeat it here for completeness

$$C(p, t, t') = \sum_{\nu} c_{\text{rec}}^{\nu*}(t, t') c_{\text{ion}}^{\nu}(t, t') e^{-i\mathcal{E}_{\nu}^+(t-t')}, \quad (3.2)$$

with shifted ionic vibrational eigenenergies \mathcal{E}_{ν}^+ and expansion coefficients $c_{\text{ion}}^{\nu}(t, t')$, $c_{\text{rec}}^{\nu}(t, t')$ such that

$$\begin{aligned} \sum_{\nu} c_{\text{ion}}^{\nu}(t, t') \chi_{\nu}^+(R) &= d_{\text{ion}}(p(t, t') + A(t'), R) \chi_0(R) \\ \sum_{\nu} c_{\text{rec}}^{\nu}(t, t') \chi_{\nu}^+(R) &= d_{\text{rec}}(p(t, t') + A(t), R) \chi_0(R). \end{aligned}$$

The ionic vibrational eigenstates are given by χ_{ν}^+ .

3.1. Relevance for harmonic ratio

The main interest in the autocorrelation function stems from its role in the harmonic ratio of different isotopes of the molecule. The saddle-point-approximated dipole moment (2.32) can be separately evaluated for short and long trajectories via choice of the saddle-point times t_s, t'_s for a given ω

$$\tilde{D}_{\text{SPA}}(p_s, t_s, t'_s; \omega) = 2iE(t'_s)\Pi(t_s, t'_s)\Lambda(t_s, t'_s)C(p_s, t_s, t'_s)e^{-i\tilde{S}(p_s, t_s, t'_s; \omega)}.$$

The saddle-point factor for p is given by $\Pi(t, t')$, see expression (2.26), and for t, t' by $\Lambda(t, t')$, expression (2.31). The modulus-squared of \tilde{D}_{SPA} gives the spectrum of the emitted harmonic radiation.

Define, for a function $f(p, t, t'; \omega, I_p)$, its modulus-squared ratio, evaluated at the saddle-point times for D_2 in the numerator and for H_2 in the denominator

$$\mathcal{R}[f](\omega) := \frac{\left| f\left(p_s(t_s^{\text{D}}(\omega), t_s^{\text{D}}(\omega)), t_s^{\text{D}}(\omega), t_s^{\text{D}}(\omega); \omega, I_p^{\text{D}}\right) \right|^2}{\left| f\left(p_s(t_s^{\text{H}}(\omega), t_s^{\text{H}}(\omega)), t_s^{\text{H}}(\omega), t_s^{\text{H}}(\omega); \omega, I_p^{\text{H}}\right) \right|^2}.$$

The ratio of harmonic intensities is then given by

$$\mathcal{R}[\tilde{D}_{\text{SPA}}](\omega) = \mathcal{R}[E\Pi\Lambda](\omega) \times \mathcal{R}[C](\omega) \times \mathcal{R}[\exp(-i\tilde{S})](\omega), \quad (3.3)$$

where \times represents multiplication of real numbers. Here it becomes clear that the ratio of the modulus-squared vibrational autocorrelations for the different isotopes directly enters the ratio of harmonic intensities.

The autocorrelation, by definition, describes the nuclear dynamics of the ion during the continuum travel of the electron. Experimental [28, 29, 56, 57] as well as theoretical [54, 58] results of harmonic spectra show that heavier isotopes may produce more intense harmonics. This can be explained by the appearance of the modulus-squared autocorrelation in $\mathcal{R}[C](\omega)$, which decreases faster for the lighter isotope (see section 3.3), leading to a smaller value of the spectral intensity. Extraction of the nuclear dynamics from the harmonic spectra is called PACER, see chapter 8.

3.2. Complex time-evolution

In contrast to the real ionization and recombination times originating from the semiclassical three-step model (section 2.1), the use of the complex saddle-point times (section 2.2.4) in calculations of the autocorrelation function changes the nature of the time evolution. For instance, the time-evolution operator is no longer unitary and the norm of the wave function therefore not conserved. There also arises the question of which path through the complex plane is to be taken.

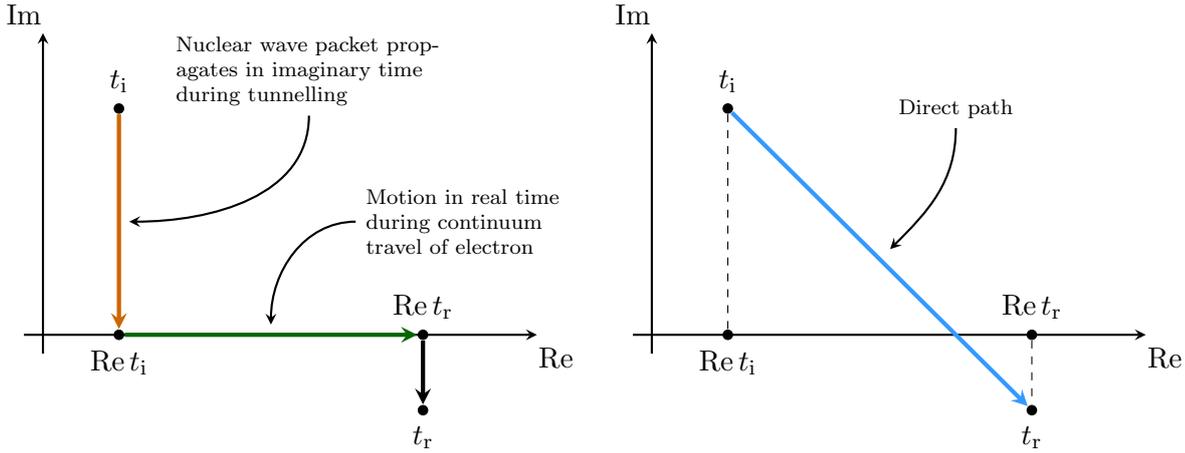


Figure 3.1.: Illustration of ionization and recombination time in the complex plane. **Left:** Stepwise evolution from t_i to t_r . This picture is more representative of the short trajectory than the long trajectory because for the latter $\text{Im } t_r$ is usually much smaller than illustrated here and also positive, see Figure 2.8. **Right:** Direct path

Figure 3.1 shows an illustration of a pair of saddle-point times (t_i, t_r) in the complex plane and a stepwise path which allows a physical interpretation. The first step, $t_i \rightarrow \text{Re } t_i$, can be identified with the tunnelling of the electron, see section 3.2.2. While the electron is tunnelling out, the nuclei already undergo a motion in imaginary time. The subsequent real path from $\text{Re } t_i$ to $\text{Re } t_r$ corresponds to the travel time of the electron in the continuum during which the nuclei evolve in real time. The last step, $\text{Re } t_r \rightarrow t_r$, completes the process with the recombination. The absolute value of the imaginary part of t_r is usually small compared to the ionization time when the harmonic energy lies in the plateau region, see Figure 2.8.

3.2.1. Path-independence

Time-independent potential Without any modifications such as the Stark shift (7.2.1), the ionic vibrational potential is time-independent and the time-evolution operator $\mathcal{U}_R^+(t, t')$ in expression (3.1) is given by the operator exponential

$$\mathcal{U}_R^+(t, t') = \exp(-i\mathcal{H}_R^+(t - t'))$$

with Hamiltonian

$$\mathcal{H}_R^+ = -\frac{1}{M} \frac{\partial^2}{\partial R^2} + \mathcal{V}_{\text{BO}}^+(R).$$

\mathcal{U}_R^+ does therefore not depend separately on t and t' , but only on the travel time $t - t'$. In particular, it does not matter at which point in the complex plane the evolution starts or ends, as long as $t - t'$ is the same.

3. Vibrational Autocorrelation Function

Time-dependent potential A general statement about the path-independence in case of a time-dependent potential is a much harder problem to solve compared to the case of a time-independent potential. It would be desirable to have a mathematical proof to assure a unique continuation of the solution to the TDSE into the complex plane. Unfortunately, there does not seem to exist such a theorem that applies to the Schrödinger equation. We therefore rely on numerical verification to show that the autocorrelation is path-independent. It is an open question whether the path-independence holds generally.

3.2.2. Relation between ionization time and tunnelling

In the limit of a small Keldysh parameter, i.e. the tunnelling regime relevant for HHG, the modulus squared of the action phase factor $e^{-i\mathcal{S}}$ along the imaginary part of the saddle-point ionization time is related to the ADK tunnelling rate [39, 60]

$$\exp(2 \operatorname{Im} \mathcal{S}(p_s(t_s, t'_s), \operatorname{Re} t'_s, t'_s)) \approx \Gamma(I_p, E(\operatorname{Re} t'_s)) \quad \text{with} \quad \Gamma(I_p, E) = \exp\left(-\frac{2[2I_p]^{3/2}}{3|E|}\right) \quad (3.4)$$

This holds because the imaginary part of the *recombination* time, in the plateau region, is usually small compared to the other components of the saddle-point times, a notable exception being the short trajectories at low harmonic energies (lower panel of Figure 2.8). This means that the ionization dynamics of HHG can be reasonably well described with the dynamics encountered in ATI. The general idea is that, because the recombination time t_s is nearly real, the momentum p_s is nearly real as well. This can be seen in equation (2.25), where a vanishing imaginary part of t_s necessarily leads to a zero imaginary part of p_s , which corresponds to the case of just ionization. A more comprehensive analysis of the comparison between ionization in HHG and ATI can be found in the supplementary material of [73].

As a consequence, the action along the remaining integration path after ionization, $\operatorname{Re} t'_s \rightarrow t_s$, only has a small imaginary part and the approximation in (3.4) can be made for the whole integration of $\tilde{\mathcal{S}}$

$$\exp\left(2 \operatorname{Im} \tilde{\mathcal{S}}(p_s(t_s, t'_s), t_s, t'_s)\right) \approx \Gamma(I_p, E(\operatorname{Re} t'_s)). \quad (3.5)$$

This leads to the approximation

$$\mathcal{R}[\exp(-i\tilde{\mathcal{S}})] \approx \mathcal{R}[\Gamma'] \quad (3.6)$$

with $\Gamma'(t'_s; I_p) := \sqrt{\Gamma(I_p, E(\operatorname{Re} t'_s))}$. This ratio accounts for the different ionization probabilities of the isotopes. A comparison is shown in Figure 3.2. Apart from low plateau energies of the short trajectories, the approximation in (3.6) works well. In terms of harmonic ratios, equation (3.6) is most reliable within a large plateau region, because then $\operatorname{Re} t_s$ is small in a wide energy range. More care must be taken for small cutoff energies, when the plateau region is narrow. In this case it might be more appropriate to use $\mathcal{R}[\exp(-i\tilde{\mathcal{S}})]$ instead of $\mathcal{R}[\Gamma']$.

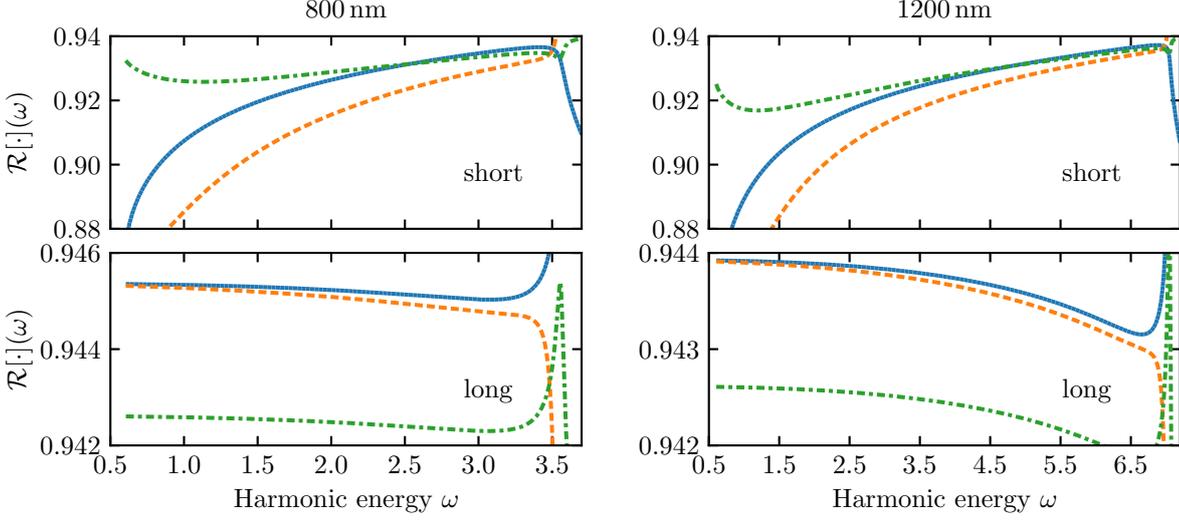


Figure 3.2.: Comparison of the ratios \mathcal{R} of $\exp(-i\tilde{\mathcal{S}}(p_s(t_s, t'_s), t_s, t'_s))$ (blue, solid) and $\exp(-i\mathcal{S}(p_s(t_s, t'_s), \text{Re } t'_s, t'_s))$ (orange, dashed), with the ratio of the ADK rate Γ' (green, dash-dotted). The approximations work best when $\text{Im } t_s$ is small, which is the case for the long trajectories and for high plateau energies of the short trajectories. The intensity is $4 \cdot 10^{14} \text{ W/cm}^2$. **Left:** 800 nm **Right:** 1200 nm **Top:** short trajectories **Bottom:** long trajectories.

Expansion coefficients after tunnelling

The connection between the tunnelling of the electron and the saddle-point ionization time manifests itself also in the expansion coefficients of the neutral vibrational wave packet after the purely imaginary time evolution from t'_s to $\text{Re } t'_s$ (see Figure 3.1). This can be seen as follows.

One approach [57, 58] to include the influence of tunnelling on the neutral vibrational ground state is to modify the Franck-Condon factors $c_{\text{FC}}^\nu = \langle \chi_\nu^+ | \chi_0 \rangle$ by multiplying them with the square-root of the ADK tunnelling rate Γ , i.e. the tunnelling amplitude. The electric field used in the amplitude is usually taken to be the peak field strength. This is an approximation which strictly holds only for trajectories starting close to the maximum of the field (i.e. the long trajectories) and makes the resulting coefficients independent of the harmonic order. A more accurate approach is to use the instantaneous electric field at the moment of ionization t'_s . The new coefficients, for a certain harmonic order corresponding to ionization time t'_s , then take the form

$$c_{\text{Tunnel}}^\nu = c_{\text{FC}}^\nu \sqrt{\Gamma(I_p(\nu), E(\text{Re } t'_s))} \quad (3.7)$$

$$= c_{\text{FC}}^\nu \exp\left(-\frac{[2I_p(\nu)]^{3/2}}{3|E(\text{Re } t'_s)|}\right) \quad (3.8)$$

where $I_p(\nu) = E_\nu^+ - E_0$. Taylor-expanding the tunnelling factor to first order in $I_p(\nu) - I_p$ yields

$$\exp\left(-\frac{[2I_p(\nu)]^{3/2}}{3|E(\text{Re } t'_s)|}\right) = \exp\left(-\frac{[2I_p]^{3/2}}{3|E(\text{Re } t'_s)|}\right) \exp\left(-\frac{\sqrt{2I_p}(I_p(\nu) - I_p)}{|E(\text{Re } t'_s)|}\right) \dots \quad (3.9)$$

3. Vibrational Autocorrelation Function

Applying the time-evolution operator, corresponding to the imaginary part of the ionization time, to the neutral ground state gives

$$\begin{aligned} \mathcal{U}_R^+(-i \text{Im } t'_s) |\chi_0\rangle &= \sum_{\nu} c_{\text{FC}}^{\nu} \exp(-i \mathcal{E}_{\nu}^+(-i \text{Im } t'_s)) |\chi_{\nu}^+\rangle \\ &\approx \sum_{\nu} c_{\text{FC}}^{\nu} \exp\left(-\frac{\sqrt{2I_p}(I_p(\nu) - I_p)}{|E(\text{Re } t'_s)|}\right) |\chi_{\nu}^+\rangle \end{aligned} \quad (3.10)$$

where in the first step $|\chi_0\rangle$ was expanded in vibrational eigenstates of the ion, $|\chi_{\nu}^+\rangle$, on which \mathcal{U}_R^+ acts by multiplication with a phase factor. In the second step the shifted ionic eigenenergies $\mathcal{E}_{\nu}^+ = E_{\nu}^+ - (E_0 + I_p) = I_p(\nu) - I_p$ were used, together with the definition of the Keldysh time to approximate the imaginary part of the ionization time [74]

$$\text{Im } t'_s \approx \tau_K = \frac{\sqrt{2I_p}}{|E(\text{Re } t'_s)|}. \quad (3.11)$$

The weight factor of the expansion coefficients occurring in (3.10) equals the first order term in (3.9) and therefore

$$\sum_{\nu} c_{\text{FC}}^{\nu} \sqrt{\Gamma(I_p(\nu), E(\text{Re } t'_s))} |\chi_{\nu}^+\rangle \approx \sqrt{\Gamma(I_p, E(\text{Re } t'_s))} \mathcal{U}_R^+(-i \text{Im } t'_s) |\chi_0\rangle \quad (3.12)$$

which means that the approach in (3.8) to describe the influence of tunnelling on the vibrational wave packet is approximately equivalent to a time-propagation in complex time.

Another approach for including tunnelling [58, 75] is to replace the ionization potential for a specific vibrational state $I_p(\nu)$ with the difference of the BO potentials $I_p(R) = V_{\text{BO}}^+(R) - V_{\text{BO}}(R)$

$$\begin{aligned} c_{\text{Tunnel},R}^{\nu} &= \langle \chi_{\nu}^+ | \sqrt{\Gamma(I_p(R), E(\text{Re } t'_s))} | \chi_0 \rangle \\ &= \int dR \chi_{\nu}^{+*}(R) \sqrt{\Gamma(I_p(R), E(\text{Re } t'_s))} \chi_0(R). \end{aligned} \quad (3.13)$$

The two approaches in (3.8) and (3.13) are related, which can be seen by using (3.12) and writing \mathcal{U}_R^+ as an exponential

$$\begin{aligned} \frac{c_{\text{Tunnel}}^{\nu}}{\sqrt{\Gamma(I_p, E(\text{Re } t'_s))}} &\approx \langle \chi_{\nu}^+ | \exp(-i \mathcal{H}_R^+(-i \text{Im } t'_s)) | \chi_0 \rangle \\ &\approx \langle \chi_{\nu}^+ | \exp(-i(T_R + \mathcal{V}_{\text{BO}}^+)(-i \text{Im } t'_s)) | \chi_0 \rangle \end{aligned} \quad (3.14)$$

with the shifted Hamiltonian $\mathcal{H}_R^+ = T_R + \mathcal{V}_{\text{BO}}^+$ and nuclear kinetic energy T_R . The neutral ground-state energy E_0 occurring in the definition of the BO-shift $V_{\text{BO}}^{\text{shift}} = -(E_0 + I_p)$ in (2.22) enters $\mathcal{V}_{\text{BO}}^+ = V_{\text{BO}}^+ + V_{\text{BO}}^{\text{shift}}$ in the exponential and can be written as the result of applying the Hamiltonian $H_R = T_R + V_{\text{BO}}$ of the *neutral* molecule to the state $|\chi_0\rangle$ on the right. This then gives

$$\frac{c_{\text{Tunnel}}^{\nu}}{\sqrt{\Gamma(I_p, E(\text{Re } t'_s))}} \approx \langle \chi_{\nu}^+ | \exp(-i(H_R^+ - H_R - I_p)(-i \text{Im } t'_s)) | \chi_0 \rangle$$

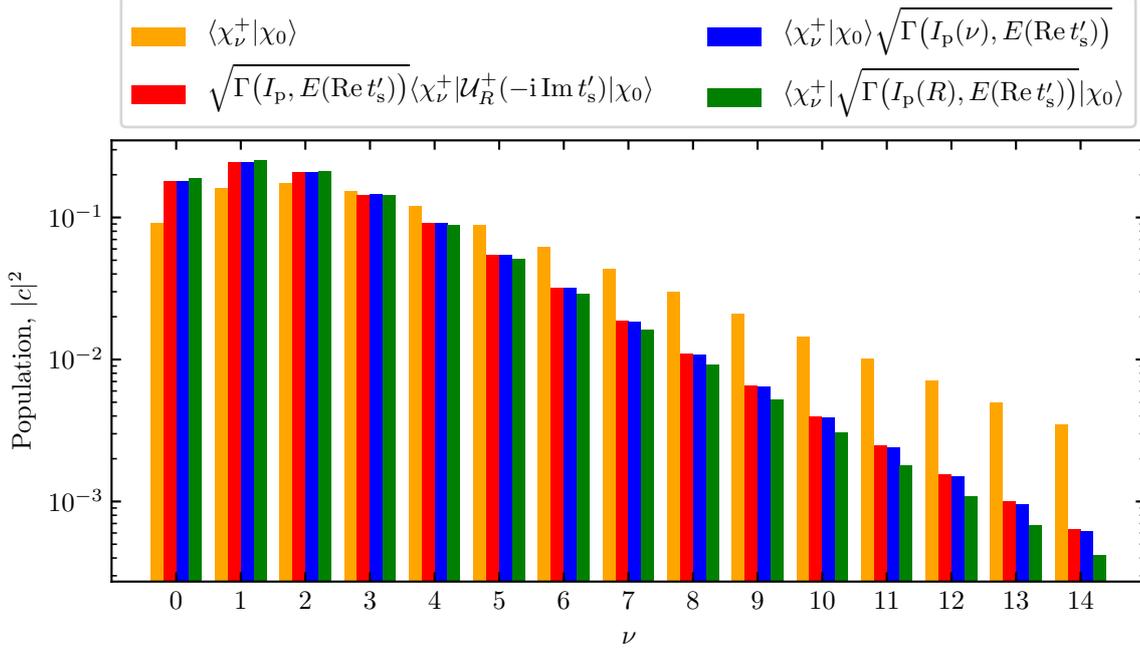


Figure 3.3.: Comparison of the modulus squared of the expansion coefficients for the bound eigenstates of H_2 , for the various cases described in the text. Shown is the case for a wavelength of 1200 nm and an intensity of $4 \cdot 10^{14} \text{ W/cm}^2$, with the ionization time corresponding to the 95th harmonic and the short trajectory. The corresponding wave functions are normalized.

with $H_R^+ = T_R + V_{\text{BO}}^+$. Using the definition of $I_p(R)$ yields

$$\begin{aligned} \frac{c_{\text{Tunnel}}^\nu}{\sqrt{\Gamma(I_p, E(\text{Re } t'_s))}} &\approx \langle \chi_\nu^+ | \exp(-i(I_p(R) - I_p)(-i \text{Im } t'_s)) | \chi_0 \rangle \\ &\approx \frac{1}{\sqrt{\Gamma(I_p, E(\text{Re } t'_s))}} \langle \chi_\nu^+ | \sqrt{\Gamma(I_p(R), E(\text{Re } t'_s))} | \chi_0 \rangle \end{aligned} \quad (3.15)$$

and therefore

$$c_{\text{Tunnel}}^\nu \approx c_{\text{Tunnel},R}^\nu.$$

In (3.15) the definition of the Keldysh time in (3.11), together with the reverse Taylor expansion in (3.9) was used to write the overlap in terms of Γ .

A direct comparison of the different coefficients can be seen in Figure 3.3.

3.2.3. Ratio of saddle-point factors

The harmonic ratio in equation (3.3) also contains the ratio $\mathcal{R}[E\Pi\Lambda]$ of the electric field $E(t'_s)$ and the saddle-point factors $\Pi(t_s, t'_s)$, expression 2.26, and $\Lambda(t_s, t'_s)$, expression 2.31. An example of this ratio is shown in Figure 3.4. It has not much influence in the plateau region and can usually be neglected.

3. Vibrational Autocorrelation Function

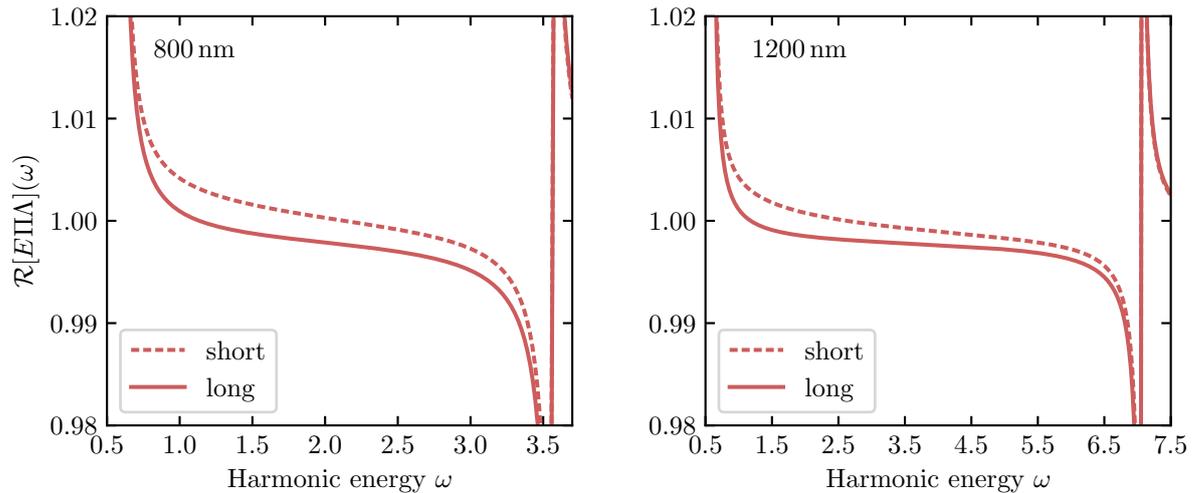


Figure 3.4.: Ratio $\mathcal{R}[EII\Lambda](\omega)$ of the electric field $E(t'_s)$ and the saddle point factors $\Pi(t_s, t'_s)$, expression (2.26), and $\Lambda(t_s, t'_s)$, expression 2.31. It is close to unity for both short and long trajectories in the plateau region and therefore of less importance for the harmonic ratio than the ratio of the ionization probabilities $\mathcal{R}[\exp(-i\tilde{S})]$, see Figure 3.2. The laser intensity is $4 \cdot 10^{14} \text{ W/cm}^2$. **Left:** 800 nm **Right:** 1200 nm.

3.3. Basic properties

In this section we want to show some generic examples of graphs of the autocorrelation function. For this we use it in its simplest form, with ionization d_{ion} and recombination d_{rec} matrix elements set to unity

$$C_{d=1}(\tau) = \int dR \chi_0^*(R) \mathcal{U}_R^+(\tau) \chi_0(R), \quad (3.16)$$

which corresponds to the overlap of the neutral vibrational ground state of H_2/D_2 with its time-evolved counterpart. An illustration of the physical picture is shown in Figure 3.5. The value at the $\tau = 0$ is $C_{d=1}(0) = 1$, because χ_0 is normalized.

3.3.1. Classical times

In the semiclassical three-step model, the continuum dynamics of the electron is treated as that of a classical point particle (see section 2.1), giving rise to real-valued ionization and recombination times. For these times the autocorrelation exhibits a simple and qualitatively predictable behaviour in the beginning of the time-evolution. Neutral H_2 has a equilibrium distance of approximately 1.4, while for H_2^+ it is 2. The vibrational wave packet will therefore initially move towards larger internuclear distances as time passes. This reduces the overlap (3.16) and $|C_{d=1}(\tau)|^2$ is monotonically decreasing. At some later instant of time the wave packet reaches a turning point in the ionic potential well, because its energy is not large enough to escape from it. The direction of motion is reversed at that point accordingly, ultimately resulting in an oscillation that leads to local maxima of $|C_{d=1}(\tau)|^2$. Figure 3.6 shows the

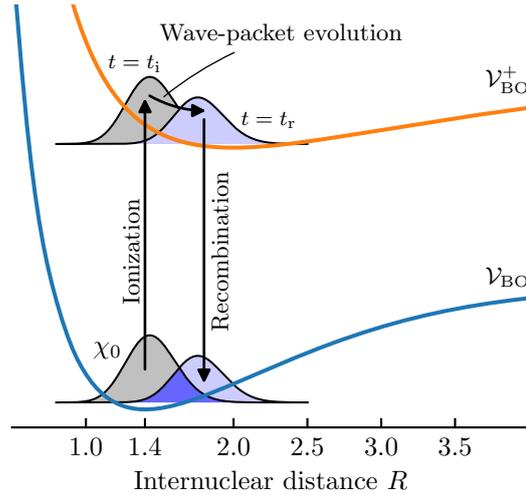


Figure 3.5.: Illustration of the vibrational dynamics of HHG in H₂/D₂. Ionization launches a vibrational wave packet on the ionic BO potential energy curve. During the continuum travel of the electron, the wave packet undergoes a time-evolution. The overlap between the initial and the evolved state at the time of return gives the value of the autocorrelation (depicted as shaded area between the wave packets on the lower curve).

evolution of $|C_{d=1}(\tau)|^2$ for H₂ and D₂. The initial decrease and the next maximum starting at approximately $\tau = 500$ (750) for H₂ (D₂) are clearly visible. Interference of the wave packet with itself produces additional oscillations for longer times and the dynamic becomes more complicated.

The BO potential $\mathcal{V}_{\text{BO}}^+$ is the same for both isotopes and the only difference is that D₂ has a higher nuclear mass than H₂. The larger inertia causes a slower separation of the nuclei and a corresponding slower initial decrease of the autocorrelation. The ratio $|C_{d=1}^{\text{D}}(\tau)|^2 / |C_{d=1}^{\text{H}}(\tau)|^2$ is therefore increasing at first. Accordingly, the maxima are delayed as well. This is the primary mechanism that gives rise to a ratio of harmonic intensities greater than unity between D₂ and H₂.

The dependence of $|C_{d=1}|^2$ on electron travel time τ that can be seen in Figure 3.6 is without regard for short and long trajectories. To give a reference, the transition, in terms of travel time, between short and long trajectories is shown in Figure 3.7 for a selection of wavelengths. For 800 nm it is at approximately 71.7.

It is also instructional to plot $|C_{d=1}|^2$ as a function of harmonic energy ω . The semiclassical three-step model provides a mapping between electron travel time τ and ω , see equation (2.8). The 3D plot in Figure 3.8 shows how $|C_{d=1}|^2$ varies with ω and τ for the short and long trajectories. The laser parameters are a wavelength of 800 nm and intensity of $4 \cdot 10^{14}$ W/cm². Also plotted are the corresponding projections that show the dependence on τ and ω separately. The curve in the C - τ plane is the same as in Figure 3.6. Here it ends at $\tau \approx 110$, which is the period of a 800 nm cycle and the duration of the longest long trajectory. This duration still falls within the initial decrease of the autocorrelation and the values of $|C_{d=1}|^2$ for the short trajectories are therefore strictly larger than those for the long trajectories.

3. Vibrational Autocorrelation Function

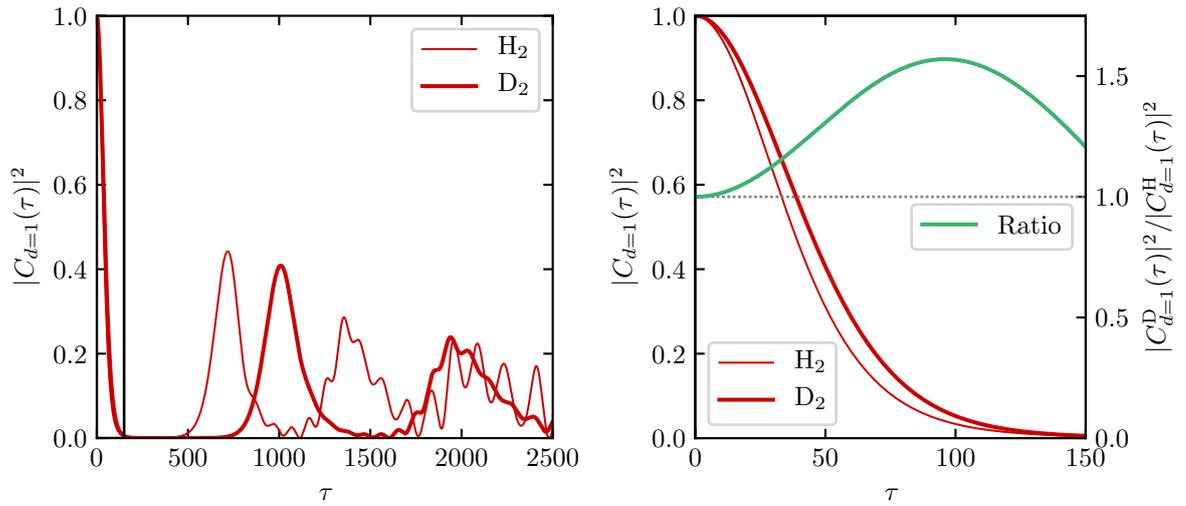


Figure 3.6.: Modulus-squared of the real-time vibrational autocorrelation function with matrix elements set to unity, for H_2 (thin lines) and D_2 (thick lines). **Left:** Long-term time-evolution **Right:** Beginning of evolution as marked by the rectangle in the left panel. The higher nuclear mass of D_2 means a slower separation of the nuclei. This causes a less rapid initial decrease and delayed maxima compared to H_2 and leads to an initially increasing ratio $|C_{d=1}^D(\tau)|^2 / |C_{d=1}^H(\tau)|^2$.

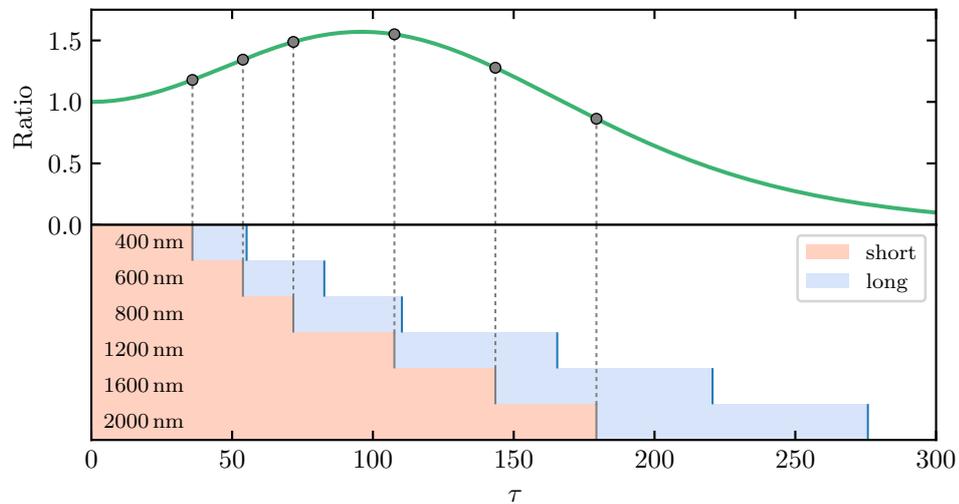


Figure 3.7.: Ranges of classical electron travel times for a selection of wavelengths (lower panel). The shortest short trajectory has a travel time of $\tau = 0$. This means the autocorrelation ratio (upper panel) always exhibits the same behaviour in the beginning of the time-evolution. In contrast, the interval of travel times for the long trajectories shifts to ever higher values for increasing wavelengths.

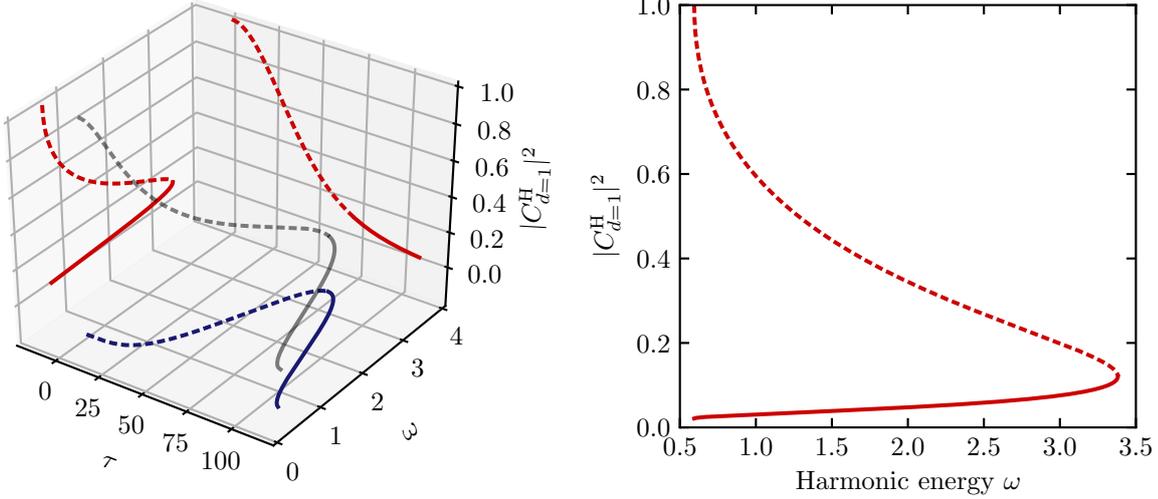


Figure 3.8.: **Left:** Dependence of classical $|C_{d=1}^H|^2$ of H_2 on electron travel time τ and harmonic energy ω (low contrast black), for short (dashed lines) and long (solid lines) trajectories. The wavelength is 800 nm and the intensity equals $4 \cdot 10^{14} \text{ W/cm}^2$. The projections on the C - ω and C - τ planes show the variations separately. Note that ω and τ are not independent from one another, but are related by a mapping originating from the classical equations of motion. This mapping can be seen as the projection on the τ - ω plane. **Right:** Projection on the C - ω plane, also visible in the left panel.

Ratio The right panel in Figure 3.6 shows the ratio of $|C_{d=1}^H|^2$ for D_2 and H_2 as a function of electron travel time τ . We now want to study the ratio as a function of harmonic energy ω . This is the quantity that directly relates to the ratio of harmonic spectra, see section 3.1. The different ionization potentials of the isotopes mean that a certain travel time τ maps to slightly different harmonic energies ω . Figure 3.9 shows the ratios for 800 nm and 1200 nm and for an intensity of $4 \cdot 10^{14} \text{ W/cm}^2$. For the sake of simplicity we will henceforth call the ratio of the autocorrelation for the short trajectories “short ratio” and for the long trajectories “long ratio”.

In Figure 3.9 the short ratio is smaller than the long ratio in case of the lower wavelength. The situation is reversed for the higher wavelength. This is rooted in the fact that the transition from short to long trajectories happens at a time τ that grows with increasing wavelength (see Figure 3.7). Hence, the long ratio will fall below the short ratio once the wavelength is sufficiently large and the transition time has passed the maximum ratio. After that maximum, the ratio is monotonically falling with τ and will rise again when the autocorrelation for D_2 exhibits its next maximum. This happens at $\tau \approx 750$ and requires much higher wavelengths. Furthermore, for 800 nm the long ratio is quite insensitive to a change in ω compared to the short ratio and is slightly falling above $\omega = 1.5$ (left panel of Figure 3.9). This is because the electron travel times for the long ratio are (for this specific set of laser parameters) situated around the maximum in Figure 3.7 where the ratio changes little.

The ratio will always approach unity for $\tau \rightarrow 0$ since the autocorrelation (3.16) does so, independent of the isotope. Because the short trajectories are positively chirped, i.e. ω grows with τ , their low-energy ratio does only weakly depend on the laser parameters. This is different for the long trajectories where the interval of electron travel times τ is shifted to larger τ when the wavelength increases. The reason why the short ratio is larger than the long ratio for the

3. Vibrational Autocorrelation Function

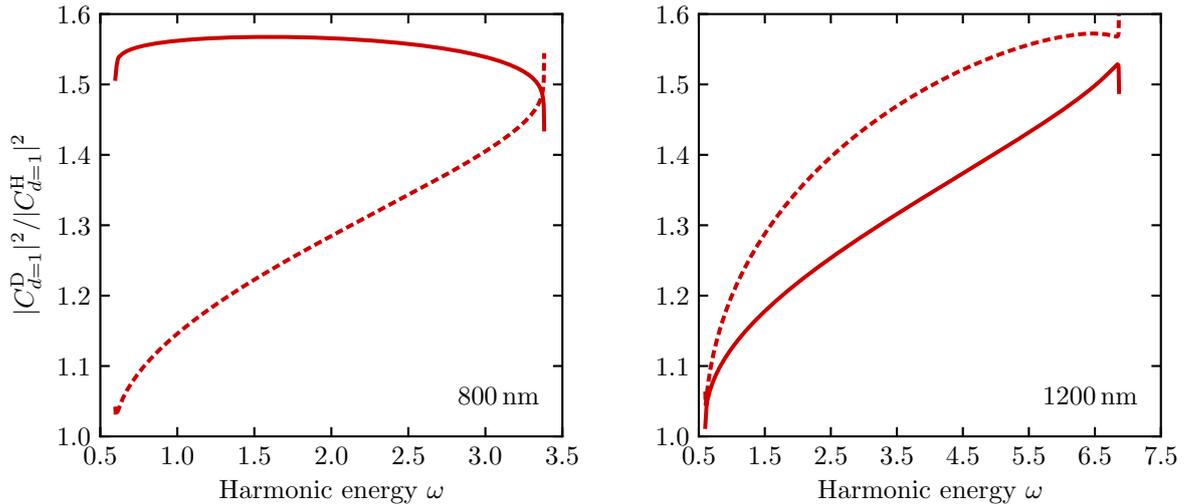


Figure 3.9.: Ratio of classical autocorrelations $|C_{d=1}^D|^2/|C_{d=1}^H|^2$ as a function of harmonic energy ω for 800 nm and 1200 nm. The intensity is $4 \cdot 10^{14} \text{ W/cm}^2$. The short trajectories yield a lower ratio in case of the low wavelength. For the high wavelength, the situation is reversed.

higher wavelength in Figure 3.9 is therefore that the long ratio decreases significantly while the short ratio changes only marginally when the wavelength is increased. This explains also why the long ratio is increasing with ω for the higher wavelength. For 1200 nm, the transition time between short and long lies just after the maximum ratio, which implies that long trajectories with shorter travel times have larger ratios. Combined with the fact that the long trajectories are negatively chirped, ω falls with τ , the ratio increases with ω . For 800 nm the transition time is located just before the maximum where the ratio changes little with τ .

The spike-like features that occur at the beginning and end of the curves in Figure 3.9 originate from the large slopes that the autocorrelation exhibits at low and high energy (see Figure 3.8). A certain travel time corresponds to slightly different harmonic energies for the two isotopes, because of slightly different ionization potentials. The ratio will therefore be significantly affected if one the autocorrelations changes its value quickly.

3.3.2. Saddle-point times

We now want to study the properties of $|C_{d=1}|^2$ when its time evolution is calculated with complex saddle-point times. The left panel of Figure 3.10 shows what the graph of $|C_{d=1}|^2$ looks like as a function of the complex-valued electron travel time $\tau_s = t_s - t'_s$. The projection on the $C\text{-Re}(\tau_s)$ plane shares similarities with the classical case, which can also be seen in the top right panel. Apart from a slight upwards shift and the conspicuous cutoff spikes, both cases show the same trend. The lowest-energy short trajectory has a nonzero travel time, which is why the dashed curve does not start at $\text{Re}(\tau_s) = 0$.

As already mentioned in section 3.2.1, the two-dimensional nature of the complex saddle-point times requires choosing a path from the start time t'_s to the end time t_s of the time-evolution.

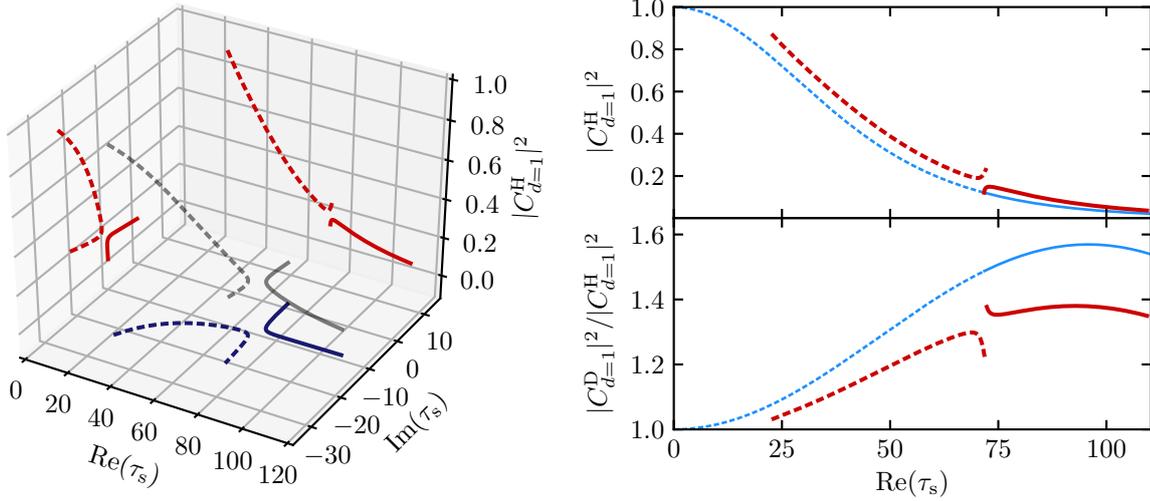


Figure 3.10.: Modulus-squared vibrational autocorrelation $|C_{d=1}|^2$ of H_2 calculated with saddle-point times, for short (dashed) and long (solid) trajectories. The wavelength is 800 nm with an intensity of $4 \cdot 10^{14} \text{ W/cm}^2$. **Left:** Dependence on real- and imaginary parts of electron travel time τ_s , including projections to show the dependences separately. The projection on $\text{Re}(\tau_s)$ - $\text{Im}(\tau_s)$ plane is the same graph as in the left panel of Figure 2.9. **Right Top:** Projection on the C - $\text{Re}(\tau)$ plane. **Right Bottom:** Ratio $|C_{d=1}^D|^2 / |C_{d=1}^H|^2$. For comparison the classical graphs are shown as thin blue lines as well.

In the classical case there is only one possible path and for every pair t'_s, t_s the intermediate values of $C_{d=1}$ during the evolution from t'_s to t_s are the same. In terms of the modulus-squared, this means that $|C_{d=1}|^2$ and the ratio always follow the curves in Figure 3.6 until $\tau_s = t_s - t'_s$ is reached and the evolution stops. The situation is different in the saddle-point case where $C_{d=1}$ generally assumes different values between t'_s and t_s because of the different paths. As a consequence, the evolution of $C_{d=1}$ cannot be as easily understood as for the classical times. It should be noted here that in case of a time-dependent potential, the time-evolution in the autocorrelation generally depends on the absolute values of t'_s, t_s and the intermediate values of $C_{d=1}$ are not the same for all trajectories in the classical case as well.

In the bottom right panel of Figure 3.10 we show $|C_{d=1}^D|^2 / |C_{d=1}^H|^2$. The classical and the saddle-point ratio show the same trend, with the latter being noticeably smaller. Both curves have a local maximum at $\text{Re}(\tau_s) \approx 95$ but the maximum is smaller by approximately 0.2 in the saddle-point case. This is a significant difference. The larger inertia of the nuclei in D_2 has less impact on the harmonic ratio when the saddle-point times are used to model their dynamics.

To get a better understanding of the long-term behaviour, we plot in the left panel of Figure 3.11 the graph of $|C_{d=1}|^2$ for a much larger wavelength of 10000 nm. This increases the travel times of the trajectories sufficiently to cover the first maximum. It can be seen that it occurs at approximately the same $\text{Re}(\tau_s)$ as for the classical times.

Considered as a function of ω , the saddle-point autocorrelation $|C_{d=1}|^2$ can be seen in the right panel of Figure 3.11. For comparison the classical case is shown as well. Both cases again share similarities, the most significant difference being that the saddle-point curves are shifted upwards. The cutoff is clearly visible as the energy where the curves exhibit a kink. It lies

3. Vibrational Autocorrelation Function

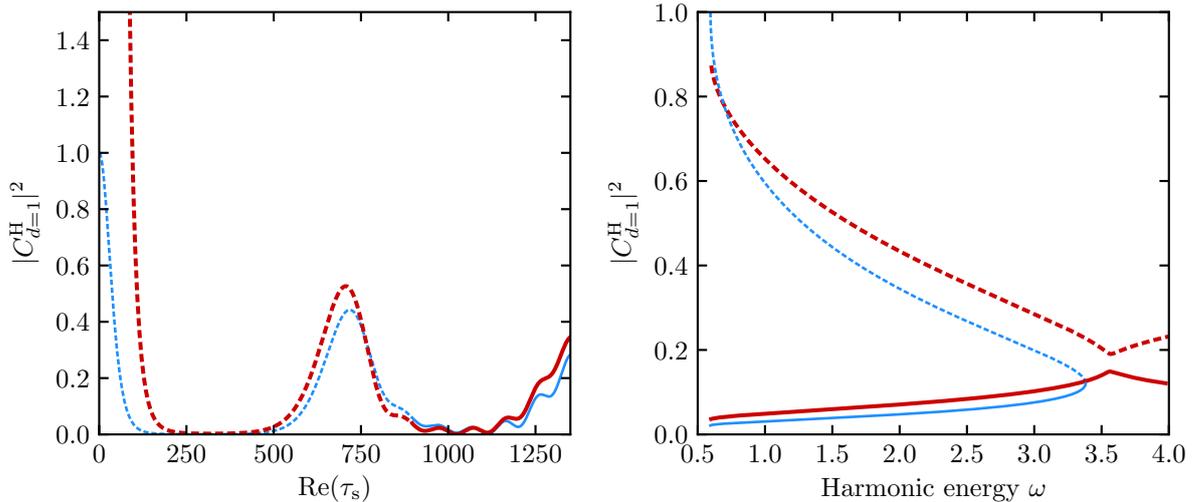


Figure 3.11.: Comparison between saddle-point (dark-red, thick) and classical (blue, thin) graphs of $|C_{d=1}^H|^2$ of H_2 , for short (dashed) and long (solid) trajectories. **Left:** $|C_{d=1}^H|^2$ for 10000 nm and $4 \cdot 10^{14} \text{ W/cm}^2$ as a function of $\text{Re}(\tau_s)$. This demonstrates that there exist maxima in $|C_{d=1}^H|^2$ in the saddle-point case as well. Because of the nonzero imaginary part, $|C_{d=1}^H|^2$ can become greater than 1. This happens in particular in the low-energy region of the short trajectories since the modules of $\text{Im}(t'_s)$ and $\text{Im}(t_s)$ takes on large values there, compare Figure 2.8. Shown are only values for harmonic energies below the cutoff. This is why the transition at $\text{Re}(\tau_s) \approx 896$ from the short to the long trajectories appears continuous here. It normally shows a discontinuity similar to the one in the upper right panel of Figure 3.10. **Right:** $|C_{d=1}^H|^2$ as a function of harmonic energy for 800 nm and $4 \cdot 10^{14} \text{ W/cm}^2$.

at a slightly larger harmonic energy, as we already know from the study of the saddle-point solutions, see section 2.2.4.

In Figure 3.12 we show the evolution of $|C_{d=1}^H|^2$ for a specific pair t'_s, t_s that corresponds to the 15th harmonic of H_2 , for the stepwise and direct paths (Figure 3.1). Note that such curves exist for every point on the curves in left panel of Figure 3.10, which shows the autocorrelation for a whole range of harmonic energies. It also serves as a demonstration of path-independence since both paths yield the same value at $t = t_s$.

Ratio We already established that the qualitative behaviour of the saddle-point autocorrelation is comparable with the classical case. The most notable difference is the lower ratio in the bottom right panel of Figure 3.10. It can therefore be expected that the overall trend, if the ratio is considered as a function of harmonic energy ω , is similar as well. Figure 3.13 confirms this. The arguments presented in section 3.3.1 to understand the graphs in the plateau region can be applied here as well.

Also shown in Figure 3.13 are the ratios with the imaginary part of the recombination time neglected in the time evolution, $\text{Im } t_s = 0$. It generally only weakly alters the plateau region of the ratio, because of small values of $|\text{Im } t_s|$ (see the lower panel of Figure 2.8). The long ratios are generally less affected than the short ratios, because the long trajectories have a particularly small $|\text{Im } t_s|$ and the difference to the full time evolution is barely visible. The

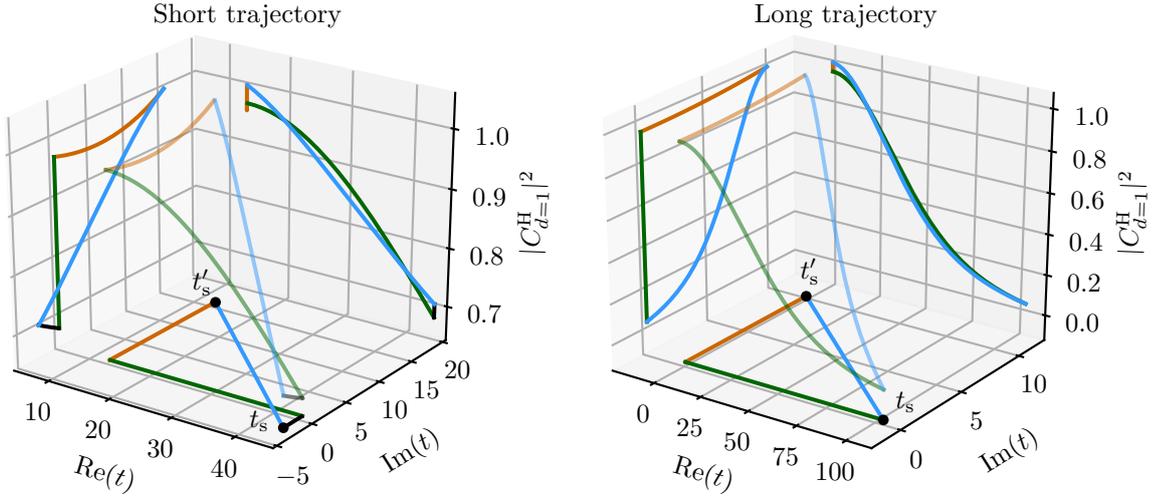


Figure 3.12.: Complex time-evolution of $|C_{d=1}^H|^2$ for a specific pair of saddle-point times t'_s, t_s belonging to the 15th harmonic of H_2 , i.e. the evolution starts at t'_s and the value at t_s lies on the curve in the left panel of Figure 3.10. Shown is the evolution along the two paths given in Figure 3.1, i.e. stepwise and direct. Because of path-independence both paths yield the same value at t_s . **Left:** Short trajectory **Right:** Long trajectory. Note that $\text{Im}(t_s)$ is quite small for the long trajectory and not visible on this scale. The laser parameters are 800 nm and $4 \cdot 10^{14} \text{ W/cm}^2$.

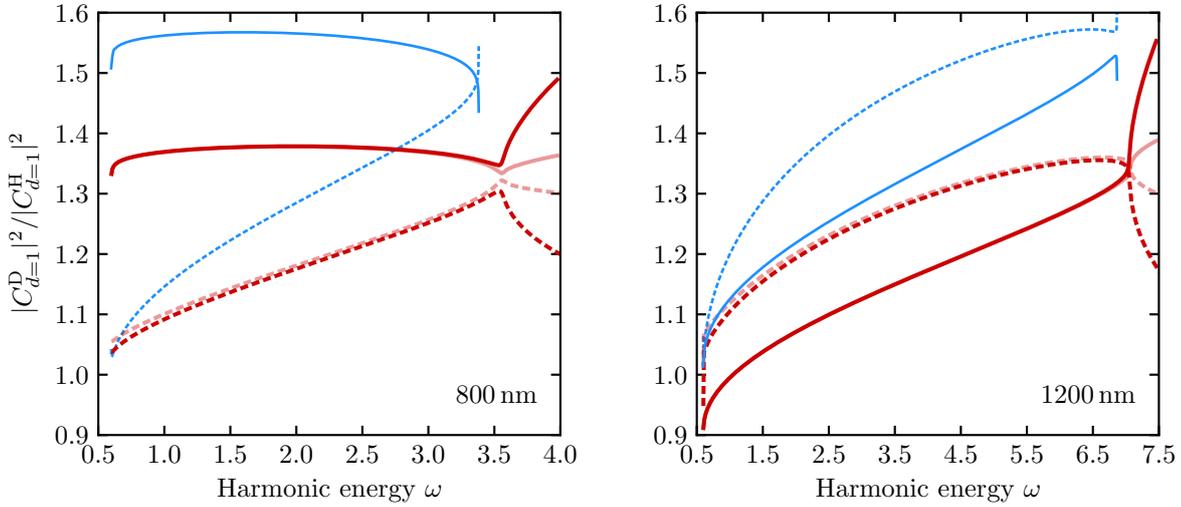


Figure 3.13.: Ratio of saddle-point autocorrelations $|C_{d=1}^D|^2 / |C_{d=1}^H|^2$ (dark-red, solid) as a function of harmonic energy ω for 800 nm and 1200 nm with an intensity of $4 \cdot 10^{14} \text{ W/cm}^2$. Plotted are also the corresponding classical ratios (blue, thin) for comparison. Both cases exhibit a lower short ratio for the lower wavelength and a higher short ratio for the higher wavelength. The reason is the same position for the first local maximum in the bottom right panel of Figure 3.10. Also shown is the ratio with $\text{Im } t_s = 0$ (low contrast curves).

3. Vibrational Autocorrelation Function

situation is different beyond the cutoff energy, where $|\text{Im } t_s|$ becomes large.

3.4. Summary and Conclusion

The modulus-squared saddle-point-approximated harmonic ratio for two isotopes, $\mathcal{R}[\tilde{D}_{\text{SPA}}]$, can be written as the product of three separate ratios, expression (3.3). These are the ratio of the saddle-point factors, $\mathcal{R}[E\Pi\Lambda]$, of the vibrational autocorrelation, $\mathcal{R}[C]$, and of the action phase factor $\mathcal{R}[\exp(-i\tilde{S})]$. Of these three, $\mathcal{R}[C]$ and $\mathcal{R}[\exp(-i\tilde{S})]$ are the important ones, i.e. they influence the harmonic ratio significantly in the plateau region. The heavier isotope D_2 has a lower ionization probability (and rate) than H_2 , thus giving a corresponding ratio smaller than unity. This is described by $\mathcal{R}[\exp(-i\tilde{S})]$, which can be adequately approximated by the ratio of ADK tunnelling rates, $\mathcal{R}[\Gamma']$, see section 3.2.2.

The dynamics of the nuclei enters the harmonic ratio via $\mathcal{R}[C]$, which is its most important ingredient. The overall qualitative features of $\mathcal{R}[C]$, i.e. the autocorrelation ratio calculated with complex-valued saddle-point times, can be understood by studying the autocorrelation with real-valued times that come from the (semi)classical three-step model, see Figures 3.10, 3.11 and 3.13. The differences between the classical and the saddle-point case are of a quantitative nature, hidden in the intricate complex-time evolution. The effect of this is a lower ratio for the saddle-point times. The imaginary part of the recombination time is negligible for the ratio in the plateau region.

In summary we conclude that the saddle-point autocorrelation ratio, while sharing similarities with the classical one, is noticeably shifted. It therefore gives rise to a shifted harmonic ratio and a more detailed study, with the recombination transition matrix element included, is justified. This is the subject of chapter 5.

4. Quantum Mechanical Model

In this chapter we present two quantum mechanical models to describe high-harmonic generation of the H_2 molecule in a strong linearly polarized laser field. One model is for parallel orientation of the laser polarization to the internuclear axis, the other for perpendicular orientation. Both models are two-dimensional, one dimension for the active electron and one for the internuclear distance. We are not interested in multielectron effects and therefore set one of the electrons to be inactive. It interacts neither with the laser field nor with the active electron or nuclei. This reduces the computational complexity significantly.

4.1. Relevant physical properties of the molecular isotopes

In this section we introduce the physical properties of the H_2 and D_2 molecules relevant for our studies. The masses of the real nuclei are [76]

$$\begin{aligned}m_n^{\text{proton}} &= 1836.152\ 673\ 89 \\m_n^{\text{deuteron}} &= 3670.482\ 967\ 85.\end{aligned}$$

An overview of the lowest exact BO potential energy curves for H_2 and H_2^+ is given in Figures 4.1 and 4.2. When we refer to the *BO potential* or *vibrational potential*, we implicitly mean the *ground-state* potential energy curve. For the neutral molecule, we denote it by V_{BO} , this is the $X^1\Sigma_g^+ 1s\sigma_g$ state. For the ion, it is denoted by V_{BO}^+ , which is the $1s\sigma_g$ state. Since these are defined in BO approximation, they are independent of the isotope. The equilibrium distances, i.e. the position of the minimum of the potential energy well, of the neutral, R_0 , and ion, R_0^+ , are

$$\begin{aligned}R_0 &\approx 1.401 \\R_0^+ &\approx 1.997.\end{aligned}$$

These are numerically determined for the curves V_{BO} and V_{BO}^+ . Our notion of the ionization potential is given by the *vertical ionization potential*. For H_2 and D_2 it is

$$\begin{aligned}I_{\text{p}}^{\text{H}} &= V_{\text{BO}}^+(R_0) - E_0^{\text{H}} \approx 0.5944 \\I_{\text{p}}^{\text{D}} &= V_{\text{BO}}^+(R_0) - E_0^{\text{D}} \approx 0.5973,\end{aligned}$$

where E_0^{H} and E_0^{D} are the total ground-state energies of H_2 and D_2 , respectively, i.e. the energies of the vibrational ground states of V_{BO} . Their values are

$$\begin{aligned}E_0^{\text{H}} &\approx -1.16454 \\E_0^{\text{D}} &\approx -1.16743.\end{aligned}$$

4. Quantum Mechanical Model

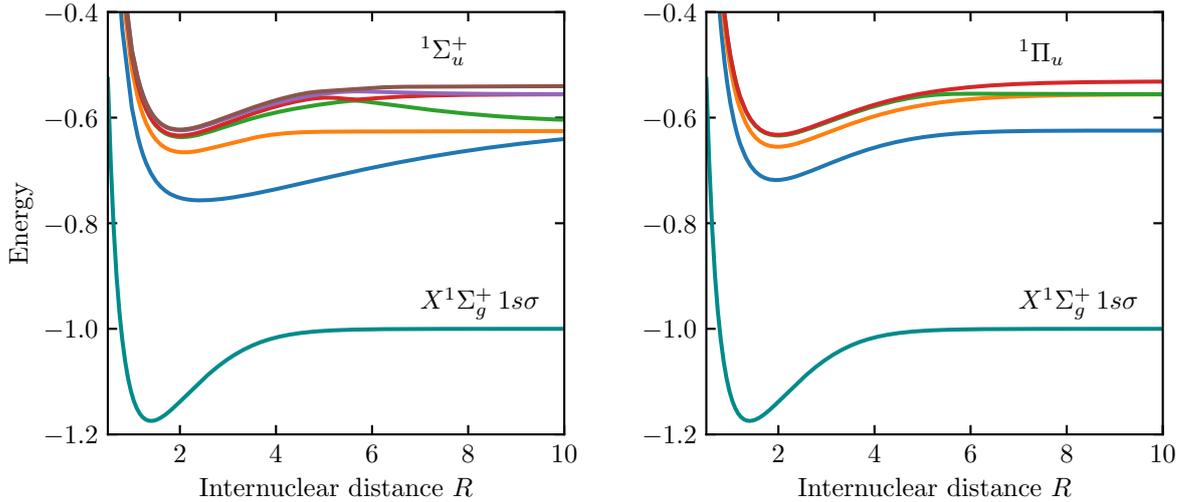


Figure 4.1.: **Left:** H₂ Born-Oppenheimer potential energy curves for the ground state and the next six lowest ¹Σ_u⁺ states [77]. **Right:** H₂ Born-Oppenheimer potential energy curves for the ground state and the next four lowest ¹Π_u states. [78]

An illustration of the definition of I_p is given in the right panel of Figure 4.2.

4.2. Coordinates

For completeness we also introduce position coordinate for the inactive electron in the beginning. This position will later be fixed in the middle between the two nuclei, i.e. at their center of mass, when the single-active-electron approximation is adopted. The contribution of the inactive electron to the system is indirect via the potential energy (see next sections). So we are initially considering a system of four particles which in the laboratory reference frame have position coordinates \mathbf{r}_1 , \mathbf{r}_2 for the two nuclei and \mathbf{r}_a and \mathbf{r}_i for the active and inactive electron, respectively. The transformation to the molecular frame, so-called *Jacobi coordinates* [79], takes the form

$$\begin{aligned}\mathbf{R}_{\text{CM}} &= \frac{1}{2m_n + 2}(m_n\mathbf{r}_1 + m_n\mathbf{r}_2 + \mathbf{r}_a + \mathbf{r}_i) \\ \mathbf{R} &= \mathbf{r}_1 - \mathbf{r}_2 \\ \mathbf{r} &= \mathbf{r}_a - \frac{m_n\mathbf{r}_1 + m_n\mathbf{r}_2}{2m_n} = \mathbf{r}_a - \frac{\mathbf{r}_1 + \mathbf{r}_2}{2} \\ \mathbf{s} &= \mathbf{r}_i - \frac{m_n\mathbf{r}_1 + m_n\mathbf{r}_2}{2m_n} = \mathbf{r}_i - \frac{\mathbf{r}_1 + \mathbf{r}_2}{2}\end{aligned}$$

where m_n is the mass of one nucleus. The internuclear distance coordinate \mathbf{R} describes vibration and rotation of the two nuclei. The active electron coordinate \mathbf{r} is defined as the distance of the electron to the nuclear center of mass. The position for the inactive electron, \mathbf{s} , is defined analogously. \mathbf{R}_{CM} is the total center of mass of the molecule. Technically, these are not genuine Jacobi coordinates since both electron coordinates are defined relative to the nuclear center of

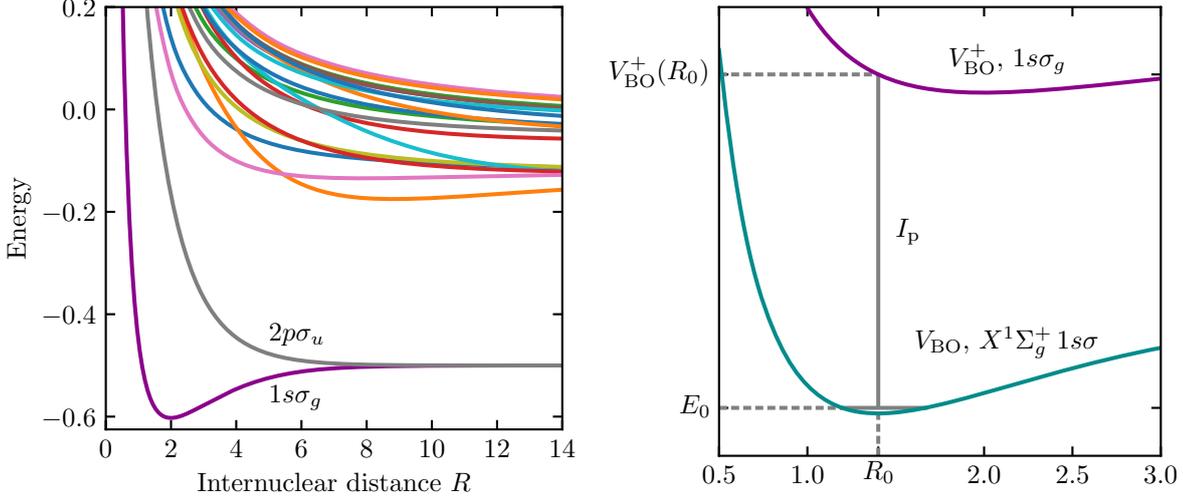


Figure 4.2.: **Left:** Collection of Born-Oppenheimer potential energy curves for H_2^+ . The two energetically lowest states $1s_g$ and $2p\sigma_u$ are separated from higher states by an energy gap. **Right:** Illustration of how the vertical ionization potential I_p is defined. It is the difference between the ionic potential energy at the neutral equilibrium distance $V_{\text{BO}}^+(R_0)$ and the vibrational ground-state energy of the neutral molecule, E_0 . The potential energy curves are the same for all isotopes, which means the difference between the isotopes lies in the value of E_0 . The ionization potentials consequently differ by the difference in E_0 . Note that the upper curve in the right panel is the same as the lowest curve in the left panel. The lower curve in the right panel is the lowest curve in the panels of Figure 4.1.

mass. As a consequence, the kinetic energy is not diagonal in this frame but contains mixed term of the electron momenta (see below). This does not complicate the calculations in this work because, as already mentioned, the inactive electron coordinate is fixed later on.

The transformation back to laboratory frame reads

$$\begin{aligned} \mathbf{r}_1 &= \mathbf{R}_{\text{CM}} + \mathbf{R}/2 - \frac{\mathbf{r} + \mathbf{s}}{2m_n + 2} \\ \mathbf{r}_2 &= \mathbf{R}_{\text{CM}} - \mathbf{R}/2 - \frac{\mathbf{r} + \mathbf{s}}{2m_n + 2} \\ \mathbf{r}_a &= \mathbf{R}_{\text{CM}} + \mathbf{r} - \frac{\mathbf{r} + \mathbf{s}}{2m_n + 2} \\ \mathbf{r}_i &= \mathbf{R}_{\text{CM}} + \mathbf{s} - \frac{\mathbf{r} + \mathbf{s}}{2m_n + 2} \end{aligned}$$

Interaction with the laser The transformation of the length-gauge laser-interaction potential in dipole approximation is

$$(\mathbf{r}_a + \mathbf{r}_i - \mathbf{r}_1 - \mathbf{r}_2) \cdot \mathbf{E}(t) = (\mathbf{r} + \mathbf{s}) \cdot \mathbf{E}(t). \quad (4.1)$$

Here we see that neither the center of mass \mathbf{R}_{CM} nor the internuclear separation \mathbf{R} couple to the electric field $\mathbf{E}(t)$. Physically this makes sense, the molecule as a whole is uncharged and is not acted upon by the electric field. Furthermore, the individual nuclei couple identically to the field and their separation is therefore not changed by it. This is a consequence of the dipole approximation that neglects the spatial dependence of the laser field.

4. Quantum Mechanical Model

Kinetic energy The kinetic energies of all particles in the laboratory frame takes the form

$$T = -\frac{1}{2m_n}\nabla_1^2 - \frac{1}{2m_n}\nabla_2^2 - \frac{1}{2}\nabla_a^2 - \frac{1}{2}\nabla_i^2.$$

Transformed to the molecular frame

$$T = -\frac{1}{2(2m_n + 2)}\nabla_{\text{CM}}^2 - \frac{1}{2\mu_n}\nabla_R^2 - \frac{1}{2\mu_e}\nabla_r^2 - \frac{1}{2\mu_e}\nabla_s^2 - \frac{1}{2m_n}\nabla_r\nabla_s \quad (4.2)$$

with reduced masses

$$\mu_n = \frac{m_n}{2} \quad \text{and} \quad \mu_e = \frac{2m_n}{2m_n + 1}.$$

Here it can be seen that the center-of-mass motion decouples from the intramolecular dynamics and the total state can be written as a product

$$|\psi_{\text{total}}\rangle = |\psi_{\text{CM}}\rangle|\psi\rangle.$$

The center of mass, and correspondingly the molecule as a whole, does not couple to the electric field, see (4.1). The state $|\psi_{\text{CM}}\rangle$ is that of a free particle and we can simply drop it, only considering the intramolecular state $|\psi\rangle$.

Dipole acceleration The total induced dipole moment of the molecule, in the laboratory frame, is given by

$$\mathbf{D}(t) = \langle\psi_{\text{total}}(t)|\mathbf{r}_1 + \mathbf{r}_2 - \mathbf{r}_a + \mathbf{r}_i|\psi_{\text{total}}(t)\rangle$$

where the expectation value is calculated for the total time-dependent wave function in the laboratory frame and with respect to all particle coordinates. Using equation (4.1) we see that in the molecular frame this reduces to

$$\mathbf{D}(t) = -\langle\psi(t)|\mathbf{r} + \mathbf{s}|\psi(t)\rangle$$

under the assumption that the center-of-mass state $|\psi_{\text{CM}}\rangle$ is normalized. The dipole acceleration is the second time derivative of $\mathbf{D}(t)$. With the help of the Ehrenfest theorem [65] this can be written as

$$\ddot{\mathbf{D}}(t) = \frac{1}{\mu_e}\langle\psi_{\text{total}}(t)|(\nabla_r + \nabla_s)V(\mathbf{r}, \mathbf{s}, t)|\psi_{\text{total}}(t)\rangle \quad (4.3)$$

where $V(\mathbf{r}, \mathbf{s}, t)$ is the total potential under which the electrons move, i.e. the interaction with the core and the electric field of the laser (compare with section 2.2.3). This form has the advantage that it is only sensitive to regions where the interaction with the core is significant. In particular, parts of the wave function located far from the core, where the potential is flat, are automatically weighted less.

In the gradient of V above, the interaction with the laser gives rise to a term proportional to $\mathbf{E}(t)$. Such a term introduces only the spectrum of the laser, which is not of interest. It is therefore appropriate to omit this contribution in V .

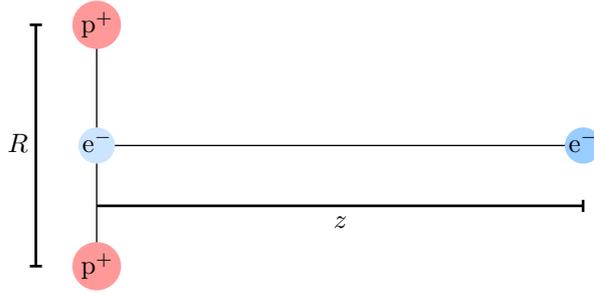


Figure 4.3.: Illustration of the perpendicular model. The electric field, and the electron motion that is coupled to it, is oriented perpendicular to the internuclear axis along which the two nuclei vibrate. Note that the position of the inactive electron in the middle between the nuclei is purely illustrative and does not reflect its physical state.

Treatment of the inactive electron Adopting the single-active-electron approximation, we assume that the inactive electron stays in the electronic BO ground state at all times and does not participate in the dynamics initiated by the electric field of the laser. Correspondingly, we set the kinetic-energy term in (4.2) equal to zero

$$\frac{1}{2\mu_e}\nabla_s \equiv 0.$$

The mixed kinetic term $\nabla_r\nabla_s/2m_n$ is neglected. The inactive electron contributes indirectly in that the electron-core interaction potentials $V_{\perp,\parallel}$ (introduced in the following) are defined relative to the ionic BO potential V_{BO}^+ . In particular, $V_{\perp,\parallel}$ do not contain interaction terms for the inactive electron and the term including ∇_s in the dipole acceleration (4.3) is zero.

From now on when we talk about an electron, the active one is implicitly meant except where otherwise stated.

4.3. Perpendicular orientation

Since we are only interested in linearly polarized laser fields, we consider a model that treats the internuclear distance as well as the electron position one-dimensionally, such that the electron is able to move along the polarization direction and the nuclei are allowed to move along the direction given by the orientation of the molecule relative to the field. An illustration of this model [80] is shown in Figure 4.3. The electron, with one-dimensional position coordinate z , is constrained to the direction perpendicular to the internuclear axis. The nuclei are allowed to vibrate, described by the internuclear separation coordinate R . This orientation avoids two-center interference minima in the spectra [52, 53] and therefore allows isotope-dependent harmonic ratios to be studied independently of such an interference effect.

The Hamiltonian for this system in the molecular frame and after separation of the center-of-mass motion takes the form

$$H_{\perp} = -\frac{1}{2\mu_n}\frac{\partial^2}{\partial R^2} - \frac{1}{2\mu_e}\frac{\partial^2}{\partial z^2} + V_{\perp}(z, R) + V_{\text{BO}}^+(R) + E(t)z \quad (4.4)$$

4. Quantum Mechanical Model

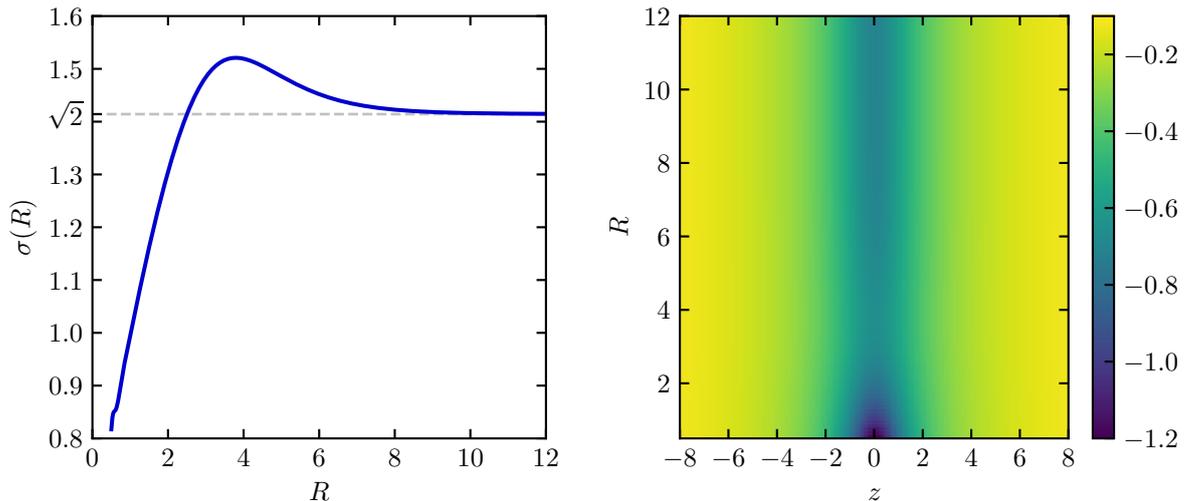


Figure 4.4.: **Left:** Perpendicular soft-core parameter $\sigma(R)$. **Right:** Perpendicular electronic-nuclear interaction potential $V_{\perp}(z, R)$. Since the electron is moving perpendicular to the internuclear axis, it sees only one potential well. Note that $V_{\perp}(0, R) = -1/\sigma(R)$. The asymptotic potential $V_{\perp}(z, R \rightarrow \infty) = 1/\sqrt{z^2 + 2}$ reproduces the correct asymptotic energy of $\lim_{R \rightarrow \infty} [V_{\text{BO}}(R) - V_{\text{BO}}^+(R)] = -1/2$ [81], which is also the ground-state energy of the hydrogen atom.

where $V_{\text{BO}}^+(R)$ is the BO ground-state potential of the ion, H_2^+ .

The electronic-nuclear interaction potential reads

$$V_{\perp}(z, R) = -\frac{1}{\sqrt{z^2 + \sigma^2(R)}}. \quad (4.5)$$

There is only a single potential well for the active electron in $V_{\perp}(z, R)$ because of the perpendicular arrangement. The electron always has the same distance to both of the nuclei. The depth of the well depends on the separation R which enters the potential via the soft-core parameter $\sigma(R)$. This parameter is chosen such that the BO ground-state potential energy curve of H_{\perp} equals the exact one for H_2 , i.e. $V_{\text{BO}}(R)$. This is where the otherwise nonparticipating inactive electron has its indirect contribution: the potential $V_{\perp}(z, R)$ is defined relative to $V_{\text{BO}}^+(R)$ and is adjusted to match $V_{\text{BO}}(R)$ in BO approximation. A plot of $\sigma(R)$ and $V_{\perp}(z, R)$ is shown in Figure 4.4.

4.4. Parallel orientation

For this orientation we can also reduce the dimensionality, for the same reasons as for the perpendicular case. The one-dimensional electron coordinate is denoted by x , the internuclear distance by R as before. An illustration is given in Figure 4.5.

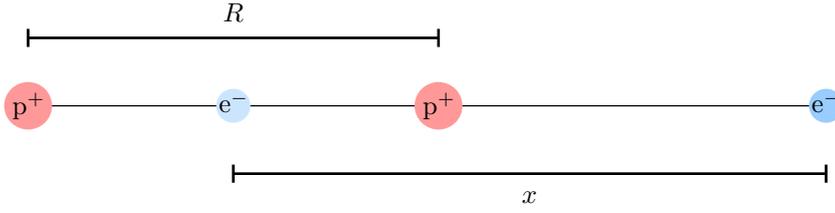


Figure 4.5.: Illustration of the parallel model. The electron motion is oriented parallel to the internuclear axis along which the two nuclei vibrate. Similar to Figure 4.3, the position of the inactive electron in the middle between the nuclei is purely illustrative and does not reflect its physical state.

The Hamiltonian H_{\parallel} is analogue to H_{\perp} and in the molecular frame reads

$$H_{\parallel} = -\frac{1}{2\mu_n} \frac{\partial^2}{\partial R^2} - \frac{1}{2\mu_e} \frac{\partial^2}{\partial x^2} + V_{\parallel}(x, R) + V_{\text{BO}}^+(R) + E(t)x. \quad (4.6)$$

The reduced masses are the same as in the perpendicular case, namely $\mu_n = m_n/2$ and $\mu_e = 2m_n/(2m_n + 1)$. In contrast to H_{\perp} the electron sees two potential wells. The corresponding electronic-nuclear interaction potential is chosen similar to ref. [54]

$$V_{\parallel}(x, R) = -\frac{Z_{\text{eff}}(x + \frac{R}{2})}{\sqrt{(x + \frac{R}{2})^2 + \varepsilon(R)^2}} - \frac{Z_{\text{eff}}(x - \frac{R}{2})}{\sqrt{(x - \frac{R}{2})^2 + \varepsilon(R)^2}}.$$

The effective nuclear charge Z_{eff} is meant to describe the screening effect of the inactive electron by means of a Gaussian function, $Z_{\text{eff}}(x) = \frac{1}{2}(1 + e^{-4\ln(2)x^2}) = \frac{1}{2}(1 + 2^{-4x^2})$, with a FWHM of 1. The screening of one nucleus by the inactive electron is the smaller the closer the active electron is to that nucleus, i.e. $Z_{\text{eff}}(x \rightarrow 0) = 1$. On the other hand, if the active electron is far away, the remaining ion carries a total charge of 1 and one could say that this charge is equally shared by both nuclei, i.e. $Z_{\text{eff}}(x \rightarrow \infty) = \frac{1}{2}$.

As in the perpendicular case, the soft-core parameter $\varepsilon(R)$ is chosen to match the $V_{\text{BO}}(R)$ potential curve in BO approximation. Figure 4.6 shows $\varepsilon(R)$ and $V_{\parallel}(x, R)$.

4.5. Dipole-transition matrix element

In this section the dipole-transition matrix element is investigated for the parallel and perpendicular models described above, which is an essential part of the vibrational autocorrelation (3.1). Primary interest lies in the recombination step because it is the main ingredient in calculating the harmonic spectrum [82, 83]. The ionization step, which is the reversed process, is of less importance for the structure of the spectrum as it mostly determines the yield.

We distinguish between length/velocity *gauge* and length/velocity *form*. The former concerns the (physically equivalent) gauges of the laser-matter-interaction and determines if the ionization matrix element is calculated with the position or momentum operator. The latter affects the

4. Quantum Mechanical Model

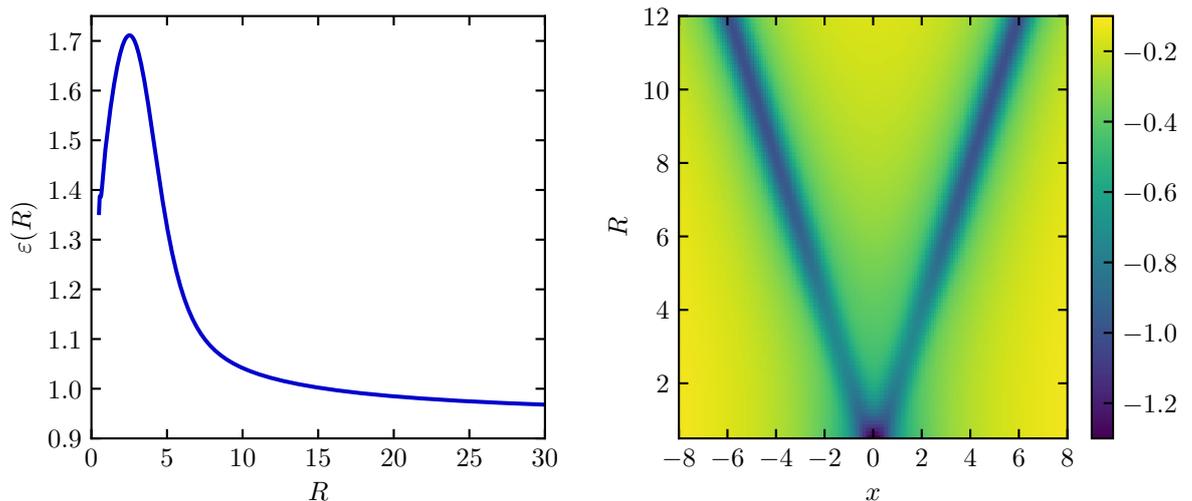


Figure 4.6.: **Left:** Parallel soft-core parameter $\varepsilon(R)$. **Right:** Parallel electronic-nuclear interaction potential $V_{\parallel}(x, R)$. In this orientation the electron sees two potential wells.

recombination matrix element, as discussed in section 2.2.3, and the forms are equivalent when the state of the system is known exactly.

We are interested in two different descriptions of the continuum wave function. The first are plane waves used in the SFA and the second are exact scattering solutions. Both cases are discussed in the following. Regarding plane waves, it was pointed out in section 2.2.3 that it makes a difference as to which form of the matrix element is used because they are not exact solutions for a nonvanishing potential. To address this, we will consider both the length and velocity forms. The acceleration form ranks close to the velocity form when accuracy is concerned, but is more demanding to calculate [66]. Specifically, we concern ourselves with the following two integrals

$$d_L(k, R) = \langle \psi_k^c | x | \psi_R \rangle = \int dx \psi_k^{c*}(x) x \psi_R(x) \quad (4.7)$$

$$d_V(k, R) = \langle \psi_k^c | k | \psi_R \rangle = \int dx \psi_k^{c*}(x) (-i\nabla) \psi_R(x) \quad (4.8)$$

where ψ_k^c is a general continuum wave function. In the SFA these are $\psi_k^c(x) = e^{ikx}$, expression (2.12). The electronic BO states ψ_R are the one-dimensional ground states of the electronic-nuclear interaction potential for constant R .

In general, the matrix element needs to be calculated only once for a molecular target and is independent of the isotope. Since there are no analytical expressions for ψ_R for the model potentials above, the evaluation is done numerically. It is helpful to compare the results with an approximate model where ψ_R is given in LCAO approximation. These are given in the appendix, section A.1.

Physically the cases of k and $-k$ should be equivalent because H_2 is a homonuclear diatomic molecule. In our model the electron is constrained to one dimension and can be thought of to

move from the left to the right for positive k and in the opposite direction for negative k . This means the continuum states should satisfy

$$\psi_{-k}^c(-x) = \psi_k^c(x).$$

We therefore know for a general dipole moment operator \hat{d}

$$\begin{aligned} d(-k, R) &= \int_{-\infty}^{\infty} dx \psi_{-k}^{c*}(x) \hat{d} \psi_R(x) \\ &= \int_{\infty}^{-\infty} d(-x) \psi_{-k}^{c*}(-x) (-\hat{d}) \psi_R(-x) \\ &= -d(k, R) \end{aligned} \quad (4.9)$$

because $\psi_R(-x) = \psi_R(x)$ for the same symmetry reasons. The operator \hat{d} is antisymmetric under the transformation $x \rightarrow -x$ in both length and velocity form. We conclude that the matrix element is antisymmetric under reversion of the electron momentum. As a side note, changing the sign of the internuclear distance leaves d invariant because $R \rightarrow -R$ amounts to an exchange of the identical nuclei.

4.5.1. Plane wave continuum

This is the realm of the SFA where the influence of the core potential upon the continuum electron is neglected. The matrix elements are given by

$$\begin{aligned} d_L(k, R) &= \int dx e^{-ikx} x \psi_R(x) \\ d_V(k, R) &= \int dx e^{-ikx} (-i\nabla) \psi_R(x). \end{aligned}$$

Changing the sign of k in e^{-ikx} is equivalent to taking the complex-conjugate. The states ψ_R can be and are chosen real-valued in position representation. This gives for d_L and d_V

$$\begin{aligned} d_L^*(k, R) &= \int dx e^{ikx} x \psi_R(x) & d_V^*(k, R) &= \int dx e^{ikx} (i\nabla) \psi_R(x) \\ &= d_L(-k, R) & &= -d_V(-k, R) \\ &= -d_L(k, R) & &= d_V(k, R) \end{aligned}$$

where the last equalities come from (4.9). d_L is therefore purely imaginary and d_V is real. Consequently, $\arg(d_L(k, R)) = \pm\pi/2$ and $\arg(d_V(k, R)) = 0, \pm\pi$.

Perpendicular orientation

We first consider the perpendicular orientation, i.e. the electronic BO states ψ_R are the one-dimensional eigenstates of V_{\perp} for constant R . The single potential well in this orientation is equivalent to an atom. Interference effects [53] originating from the multiple nuclei are absent.

4. Quantum Mechanical Model

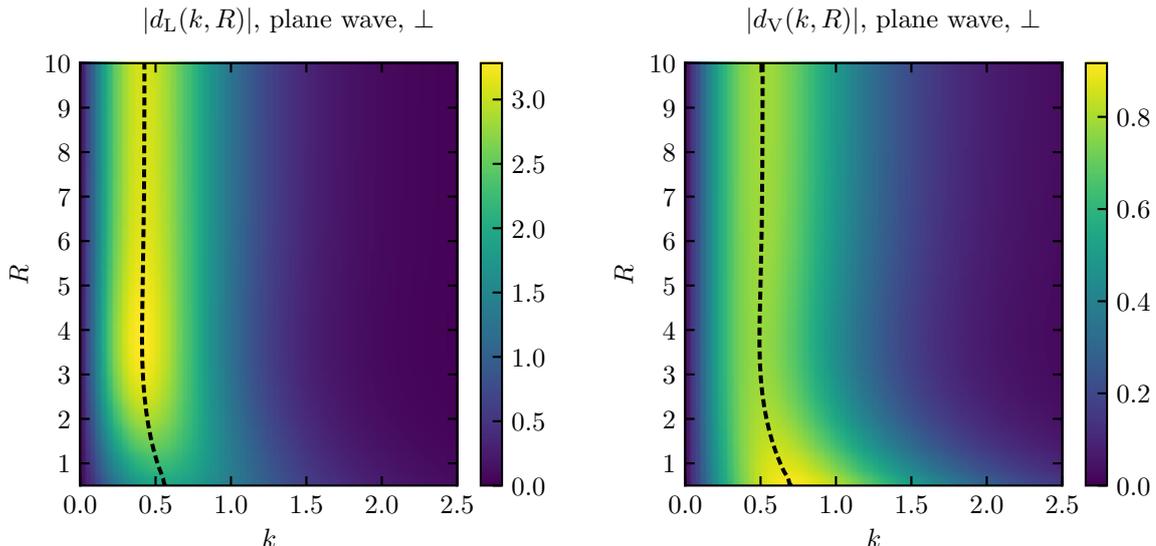


Figure 4.7.: Absolute values of the matrix elements for *perpendicular* orientation, calculated with *plane waves*. This case is physically equivalent to an atom and no interference features due to multiple nuclei are visible. Instead there is a single maximum as a function of k , which as a function of R inherits the shape from the reciprocal of $\sigma(R)$ in Figure 4.4. **Left:** $|d_L(k, R)|$ **Right:** $|d_V(k, R)|$

The absolute values of the matrix elements are shown in Figure 4.7, d_L on the left, d_V on the right.

As expected, there are no interference features visible in both panels of Figure 4.7, instead there is a single maximum as a function of k . This is qualitatively similar to the LCAO case in Figure A.2 in section A.1 in the appendix. The position and value of the maximum of both d_L and d_V are nonconstant functions of R , inheriting the shape of the reciprocal soft-core parameter $\sigma(R)$ of V_\perp shown in Figure 4.4. The position of the maximum is shown as a black dashed line and for large R , it can be reasonably well described in LCAO approximation since the nuclei can be considered separated. This gives $k_L^{\max}(R \gg 0) \approx 1/\sqrt{5} \approx 0.45$ and $k_V^{\max}(R \gg 0) \approx 1/\sqrt{3} \approx 0.58$, see appendix A.1.

Parallel orientation

Here we study the parallel orientation, i.e. ψ_R are the one-dimensional eigenstates of V_\parallel for constant R . This orientation reveals the molecular structure since there are two potential wells. It is well known [52, 53] that the two (independent) nuclear centers together with the recombining plane wave of the electron are equivalent to a double-slit setup. This causes interference patterns in the recombination matrix element, which are imprinted onto the harmonic spectrum. Depending on the angle θ between the wave vector \mathbf{k} of the returning electron and the internuclear axis \mathbf{R} , there is an effective internuclear separation $|\mathbf{R}| \cos(\theta)$ that corresponds to the separation of the slits. If an odd number of half wavelengths $\lambda/2 = \pi/|\mathbf{k}|$ matches this effective separation the interference is destructive and the harmonic radiation with frequency $\omega = |\mathbf{k}|^2/2 + I_p$ is suppressed. This is commonly known as the *two-center interference*

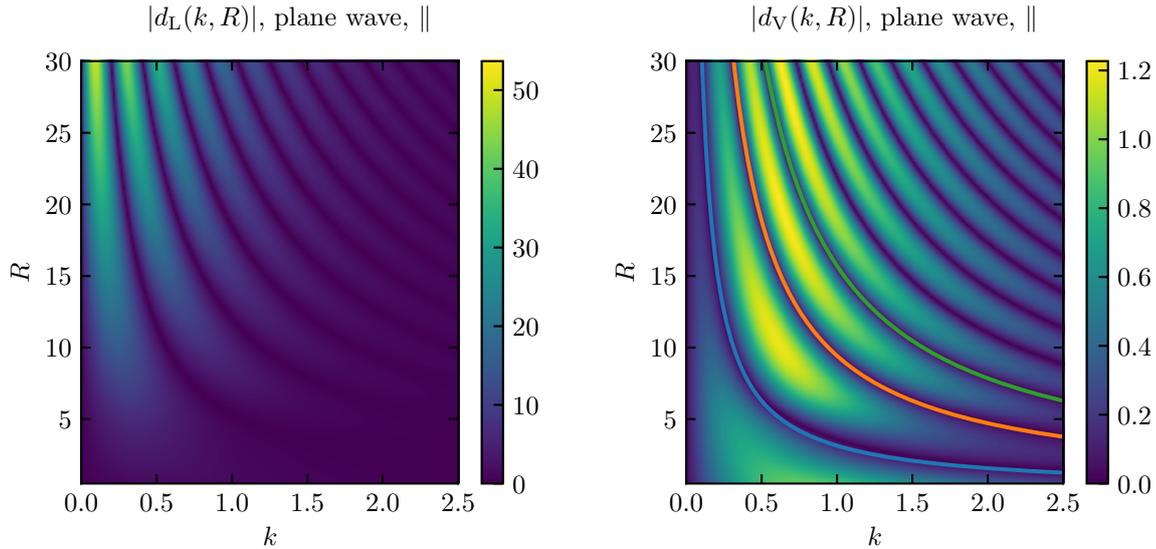


Figure 4.8.: Absolute values of the matrix elements for *parallel* orientation, calculated with *plane waves*. Internuclear interference (see main text) causes more intricate features compared to the perpendicular case in Figure 4.7. **Left:** $|d_L(k, R)|$ **Right:** $|d_V(k, R)|$. The first three two-center interference minima ($m = 0, 1, 2$ in expression (4.10)) are shown as well. It fits the minima of $|d_V(k, R)|$ quite well and is more accurate for large R .

minimum. Correspondingly, if a multiple of full wavelengths matches the effective separation, the emitted radiation is enhanced. Since this reasoning is based on a plane-wave formulation for the continuum electron, the different formulations of the matrix element are not equivalent and yield different results [66]. The velocity form is preferable in this respect.

The present case of parallel orientation means the angle is equal to zero, $\theta = 0$, and the effective separation is equal to the true internuclear separation R . One should therefore expect that the velocity-form recombination matrix element exhibits roots approximately at

$$kR = (2m + 1)\pi \quad \text{for } m = 0, 1, 2, \dots \quad (4.10)$$

This approximation improves with increasing $|k|$ because in this case the plane-wave description of the continuum electron becomes more appropriate. It also improves for increasing R since the electron can then be taken to interact independently with both nuclei. The interference minima coincide with the roots of d , which means that crossing a curve describing such a minimum within the k - R -plane leads to a jump in the phase of π .

The absolute values of both forms are shown in Figure 4.8. Shown is a relatively large range of internuclear distances to demonstrate the many orders of interference minima, which can clearly be seen. The dominant part of the nuclear dynamics in the ion H_2^+ is taking place in the well of the ionic potential curve, however, below $R \approx 4$.

4. Quantum Mechanical Model

4.5.2. Exact continuum

Approximating the continuum states of the electron by plane waves is one of the key elements of the SFA. However, neglecting the influence of the core potential is problematic because the long-range nature of the Coulomb potential means that the electron is never affected by the laser-field only. Effects such as two-center interference [82], which depend on the interaction between electron the core, cannot be accurately described with this approach. The soft-core potentials V_{\perp} and V_{\parallel} introduced above possess this long-range tail as well and the same shortcomings are present.

In this section we want to go beyond the plane-wave approximation for the continuum electron and use numerically exact, field-free scattering states in the recombination matrix element. This improves the accuracy of the results obtained from the vibrational autocorrelation function (3.1) since it explicitly depends on the matrix element. The scattering states that we are using have been applied before, see [84,85].

Length and velocity form

Using an exact continuum state ψ_k^c , i.e. a scattering solution of the electronic-nuclear interaction potential, in expressions (4.7) and (4.8), means that both participating states are exact eigenstates of their respective Hamiltonian. In particular, it follows that

$$\begin{aligned} d_V(k, R) &= \langle \psi_k^c | -i\nabla | \psi_R \rangle \\ &= -i \langle \psi_k^c | [x, H] | \psi_R \rangle \\ &= i \left(\frac{k^2}{2} - E(R) \right) d_L(k, R). \end{aligned} \tag{4.11}$$

From the first to the second line it was used that the momentum operator is related to the commutator $[x, H]$. The Hamiltonian H is the field-free version of H_{\perp} , expression (4.4), or H_{\parallel} , expression (4.6), in BO approximation. From the second to the third line, after expanding the definition of the commutator, $[x, H] = xH - Hx$, the Hamiltonian acted to the left and right to yield the eigenenergies $k^2/2$ of ψ_k^c and $E(R) = V_{\text{BO}}(R) - V_{\text{BO}}^+(R)$ of ψ_R .

We see that the phases of d_V and d_L are related by a shift of $\pi/2$. The absolute value differs by the energy difference of the continuum and bound state. Note that $k^2/2 - E(R)$ is positive and therefore nonzero for all k, R . Thus, d_V and d_L have the same roots. For large R it holds that $E(R) \approx -1/2$ and the matrix elements differ by a factor of approximately $(k^2 + 1)/2$ in magnitude.

Because of this, explicit study of the matrix element for both forms is not necessary. However, doing independent calculations for either form serves as an additional check that the numerical data is valid. In the following we show plots of both cases to have a complete reference.

Procedure

Starting point is the solution to the one-dimensional time-independent Schrödinger equation in *WKB approximation* [86]. For a given asymptotic (i.e. $x \rightarrow \pm\infty$) kinetic momentum k then holds

$$\psi_k^{\text{WKB}}(x) = \frac{N}{\sqrt{|p_k(x)|}} \exp\left(\pm i \int^x dx' p_k(x')\right) \quad (4.12)$$

with the expression for the classical momentum

$$p_k(x) = \sqrt{k^2 - 2V(x)}. \quad (4.13)$$

The constant N provides normalization. The first term in the square root is twice the total energy of the state. Since the potential $V(x)$ vanishes for $x \rightarrow \pm\infty$, the total energy asymptotically equals the kinetic energy $k^2/2$. With the help of the special case of zero potential, $\psi_k^{\text{WKB}}(x) \propto \exp(\pm i k|x|)$, we see that the \pm -sign can be interpreted as the sign of k .

For nonzero potential, the WKB approximation is valid in regions where $V(x)$ changes little, compared to the total energy, on length scales comparable to the de-Broglie wavelength $2\pi/k$. The basic idea is that under these conditions the wave function is close to that of a free particle, i.e. for a constant potential. To account for the slow but nevertheless nonconstant spatial dependence of the potential, the amplitude and phase of the wave function are allowed to depend on the position x . One then arrives at the expressions (4.12) and (4.13).

The general idea to determine the exact numerical scattering states is the following. We know that expression (4.12) is a good approximation of the exact solution for large values of $|x|$ and can therefore use it as an initial value at a numerical grid boundary sufficiently far from the potential well. The complete wave function is then determined by numerically integrating the Schrödinger equation over the rest of the grid.

Although the exact scattering states are to be calculated for the soft-core potentials V_{\perp} and V_{\parallel} , we choose to use the exact Coulomb potential $V(x) = -1/|x|$ in expressions (4.12) and (4.13) to determine the initial values at the boundary. This has the advantage that the integral can be evaluated analytically and the introduced error should be negligible by the fact that asymptotically the soft-core potentials coincide with the Coulomb potential (also for the parallel orientation where the potential is a sum of two shifted Coulomb potentials). The WKB phase integral then reads

$$\begin{aligned} \frac{1}{\text{sgn}(k)} \phi_k^{\text{WKB}}(x) &= \int_0^x dx' \sqrt{k^2 + \frac{2}{|x'|}} \\ &= x \sqrt{k^2 + \frac{2}{|x|}} + \frac{\text{sgn}(x)}{|k|} \ln \left(1 + k^2|x| + |kx| \sqrt{k^2 + \frac{2}{|x|}} \right), \end{aligned} \quad (4.14)$$

assuming that the electron starts its journey at the origin. See A.2.1 in the appendix for the proof of this expression. The momentum $p_k(x)$ in the amplitude in (4.12) is set to be constant, which is asymptotically correct. Note that $\phi_{-k}^{\text{WKB}}(x) = -\phi_k^{\text{WKB}}(x)$.

4. Quantum Mechanical Model

To get a better physical intuition about expression (4.14), it is helpful to approximate the square root for $|x| \rightarrow \infty$. One then arrives at

$$\phi_k^{\text{WKB}}(x) \approx \phi_k^{\text{Coulomb}}(x) + \text{sgn}(x)\phi_{\text{shift}}(k)$$

with

$$\begin{aligned} \phi_k^{\text{Coulomb}}(x) &= kx + \frac{\text{sgn}(x)}{k} \ln(2|kx|) \\ \phi_{\text{shift}}(k) &= \frac{1}{k} \left[1 + \ln(|k|) \right]. \end{aligned} \quad (4.15)$$

This is equivalent to the *Eikonal approximation*, which further approximates the WKB expression for potentials that are small compared to the total energy of the state. For a more detailed derivation, see A.2.2 in the appendix. The first term, $\phi_k^{\text{Coulomb}}(x)$, is the well-known asymptotic phase in the Coulomb potential [87], which corresponds to a plane wave with momentum k that is corrected by a contribution due to the Coulomb tail. The second term, $\phi_{\text{shift}}(k)$, is a global constant phase shift.

The transmitted part, i.e. on the side of the potential well opposite to where the incident wave is coming from, of the scattering state in the asymptotic region is set to

$$\psi_k^c(x) = \exp\left(i\phi_k^{\text{boundary}}(x)\right) \quad \text{for} \quad |x| \gg 0 \quad (4.16)$$

with the phase

$$\phi_k^{\text{boundary}}(x) = \phi_k^{\text{WKB}}(x) - \text{sgn}(x)\phi_{\text{shift}}(k). \quad (4.17)$$

Here, the expression for $\phi_k^{\text{WKB}}(x)$ is the one in (4.14). Asymptotically expression (4.17) is equal to $\phi_k^{\text{Coulomb}}(x)$, which is the usual expression found in the literature. [42, 84, 85].

For our purpose we need the *outgoing solution*, i.e. the wave function is asymptotically a superposition of an incident wave and a scattered wave travelling outwards from the scattering center [88]. There exists also an *incoming solution*, which is a superposition of an incident and inwards travelling wave. Specifically, for $k > 0$ and outgoing type, we set the wave function as in (4.16) at the *positive* end of the grid, i.e. $x \gg 0$. Once the numerical solution ψ_k^c is known on the whole grid, it needs to be properly normalized, i.e. multiplied by a number $\mathcal{T}(k)$, such that for $x \ll 0$

$$\mathcal{T}(k)\psi_k^c(x) = \exp\left(i\phi_k^{\text{boundary}}(x)\right) + \mathcal{R}(k) \exp\left(i\phi_{-k}^{\text{boundary}}(x)\right). \quad (4.18)$$

The terms on the right-hand side correspond to the aforementioned incident (left term) and outgoing scattered (right term) wave. Note that also $\phi_{-k}^{\text{boundary}}(x) = -\phi_k^{\text{boundary}}(x)$. The modulus-squared of the functions $\mathcal{T}(k)$ and $\mathcal{R}(k)$ can then be interpreted as *transmission coefficient* and *reflection coefficient*, respectively, and it can be numerically verified that $\mathcal{T}^2(k) + \mathcal{R}^2(k) = 1$.

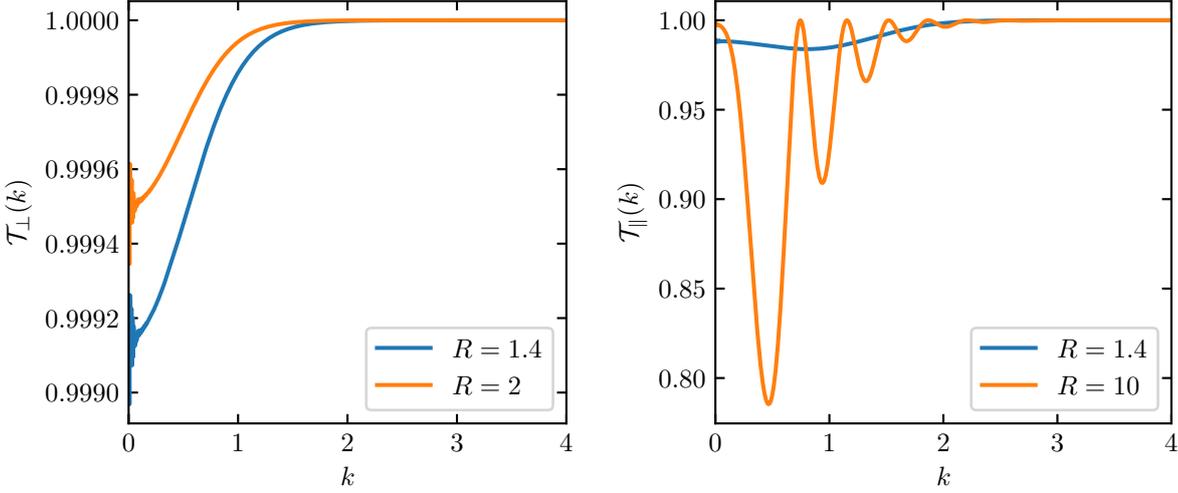


Figure 4.9.: Transmission coefficient $\mathcal{T}^2(k)$ for the indicated internuclear distances R . The reflection coefficient $\mathcal{R}^2(k)$ is given by $1 - \mathcal{T}^2(k)$. Due to numerical difficulties for small asymptotic momenta k , the solution is not accurate in that region (see main text). This can be seen in the left panel, where artifacts are visible. **Left:** Perpendicular orientation. **Right:** Parallel orientation.

Using expression (4.18) at two different points in the asymptotic region, say x_1, x_2 with $x_1 \neq x_2$, it is easy to see that

$$\mathcal{T}(k) = \frac{\exp\left(i\phi_{-k}^{\text{boundary}}(x_2)\right) \exp\left(i\phi_k^{\text{boundary}}(x_1)\right) - x_1 \leftrightarrow x_2}{\exp\left(i\phi_{-k}^{\text{boundary}}(x_2)\right) \psi_k^c(x_1) - x_1 \leftrightarrow x_2}$$

$$\mathcal{R}(k) = \frac{\exp\left(i\phi_k^{\text{boundary}}(x_1)\right) \psi_k^c(x_2) - x_1 \leftrightarrow x_2}{\exp\left(i\phi_{-k}^{\text{boundary}}(x_2)\right) \psi_k^c(x_1) - x_1 \leftrightarrow x_2}$$

where $x_1 \leftrightarrow x_2$ stands for the preceding term with x_1 and x_2 interchanged. Numerically, x_1 and x_2 are chosen as the two neighbouring points at the grid boundary. The function $\mathcal{T}^2(k)$ for some internuclear distances is shown in Figure 4.9.

Accuracy

With respect to numerical accuracy, the calculation of the exact scattering states is difficult for low asymptotic momenta k . As mentioned above, the WKB approximation is valid when the potential varies slowly, over a wavelength $2\pi/k$, compared to the total energy $k^2/2$. This loosely defines what qualifies as the asymptotic region. To make this a little more clear, consider (for $x > 0$) the change of the Coulomb potential over the distance $2\pi/k$ relative to $k^2/2$

$$r(k, x) = \frac{1/x - 1/(x + 2\pi/k)}{k^2/2} = \frac{4\pi}{k^3 x(x + 2\pi/k)}.$$

4. Quantum Mechanical Model

This serves as a measure of accuracy in the sense that if $r(k, x)$ is small, so is the error when adopting the WKB approximation. Requiring a fixed error $r(k, x_b) = a$ for small k leads to

$$\begin{aligned} x_b &= \frac{1}{k} \left(-\pi + \sqrt{\pi^2 + \frac{4\pi}{ka}} \right) \\ &\approx \frac{1}{k} \left[-\pi + \sqrt{\frac{4\pi}{ka}} \left(1 + \frac{1}{2} \frac{ka\pi}{4} \right) \right] \\ &= \sqrt{\frac{\pi}{a}} \left(\frac{2}{k^{3/2}} + \frac{\pi}{4} \frac{1}{k^{1/2}} \right) - \frac{\pi}{k} \end{aligned}$$

We see that for fixed a , x_b grows with a leading term of $k^{-3/2}$ as $k \rightarrow 0$, although the term proportional to $-k^{-1}$ dampens the growth in some intermediate region. Otherwise for fixed k and $a \rightarrow 0$, the position x_b grows as $a^{-1/2}$.

Numerically, this means that large grids need to be used to adequately calculate the dipole matrix element for small k . Failure to do so usually manifests itself in artifacts as can be seen in the left panel of Figure 4.9. Another example is the absolute value of the matrix element for $k \rightarrow 0$. We know by means of equation (4.9) that $d(k \rightarrow 0, R) \rightarrow 0$. However, in numerical results, the absolute value of d tends to some constant value greater than 0 which depends on the grid boundary.

The behaviour of the absolute value of the matrix element could possibly be inferred from the Wigner-threshold law, that, among other processes, describes the low-energy cross section of photoionization. This cross section depends on the modulus-squared of the corresponding matrix element, see for example [89,90] and references therein. However, our studies of HHG in this work are not concerned with low harmonic energies. Primary interest lies in the plateau region of the harmonic emission, well above the threshold harmonic energy given by the ionization potential $I_p \approx 0.6$. We can therefore neglect the numerical inaccuracies of the matrix element for small k .

Perpendicular orientation

Generally, the qualitative behaviour of the absolute value of the transition matrix element is similar to the plane-wave case. In case of perpendicular orientation, this means we still arrive at a single maximum as a function of k . This can be seen in the left panels of Figures 4.10 (length form) and 4.11 (velocity form). The difference is quantitative, such as the position and value of the maximum (black dashed line). In velocity form that maximum lies at higher k than in length form, which can be understood by means of equation (4.11).

Compared to plane waves, low internuclear distances have more weight relative to higher distances. This is especially apparent in the velocity form, but is also the case for the length form. Recombination for small R is therefore enhanced. This is plausible, because at small internuclear distances the electron-core interaction is especially strong. The electron approaches closer to a more concentrated positive charge of the nuclei when its distance to the internuclear axis decreases. Hence, the difference to plane waves should be more pronounced.

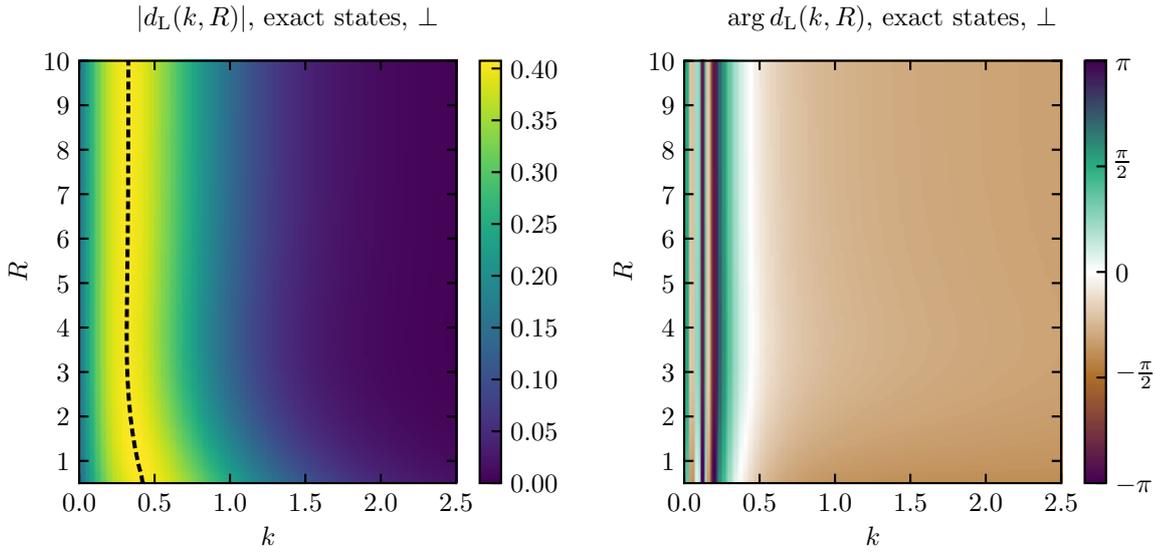


Figure 4.10.: Length-form dipole-transition matrix element for *perpendicular* orientation, calculated with *exact scattering states*. **Left:** Absolute value, it is qualitatively similar to the plane-wave case with a single R -dependent maximum as a function of k (black dashed line). For large R the maximum lies at $k \approx 0.327$. **Right:** Phase, it diverges for $|k| \rightarrow 0$, which results in jumps of 2π . For large $|k|$, the scattering states approach plane waves and the phase of the matrix element therefore approaches $\pi/2$ for negative k and $-\pi/2$ for positive k .

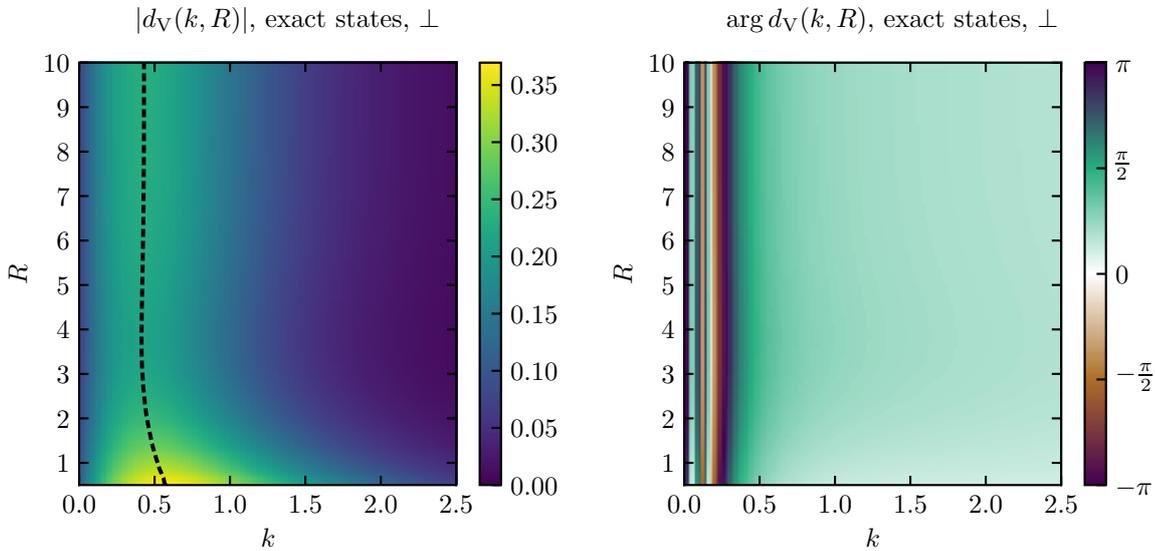


Figure 4.11.: Velocity-form dipole-transition matrix element for *perpendicular* orientation, calculated with *exact scattering states*. **Left:** Absolute value, it is qualitatively similar to the plane-wave case with a single R -dependent maximum as a function of k (black dashed line). For large R the maximum lies at $k \approx 0.43$. **Right:** Phase, it diverges as $|k| \rightarrow 0$, which causes jumps of 2π . For $|k| \rightarrow \infty$, the phase approaches the phase of the plane-wave case, which is 0 for positive k and $\pm\pi$ for negative k .

4. Quantum Mechanical Model

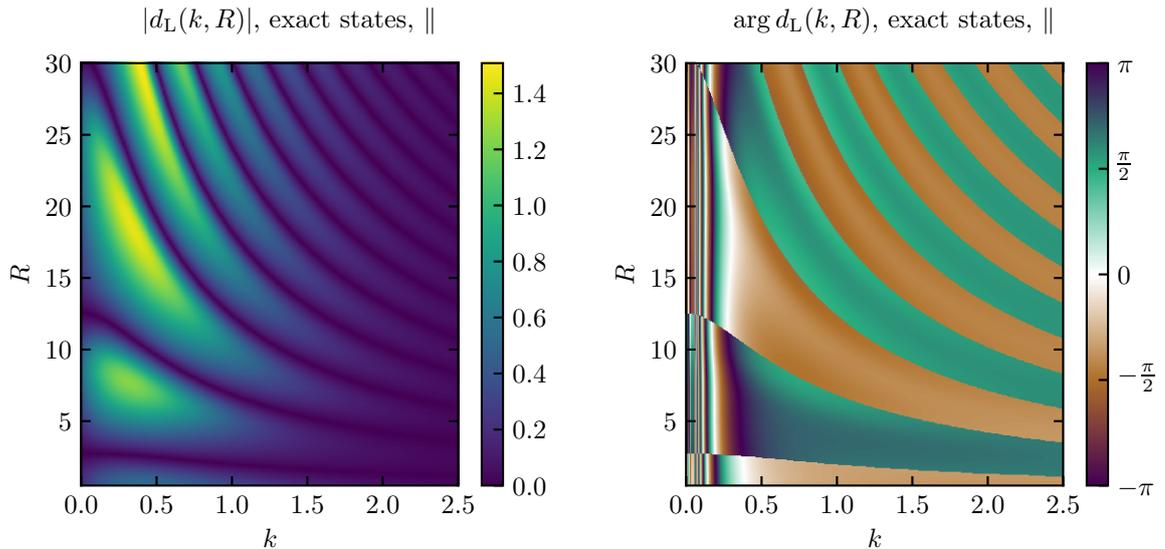


Figure 4.12.: Length-form dipole-transition matrix element for *parallel* orientation, calculated with *exact scattering states*. **Left:** Absolute value, the interference minima lie at different positions compared to the plane-wave matrix element in Figure 4.8. **Right:** Phase, it diverges for $|k| \rightarrow 0$, which causes jumps of 2π . Additionally, there are jumps of π at the positions of the interference minima, which coincide with the roots. For large $|k|$ the phase shows the behaviour of the plane-wave case, which are jumps between $\pm\pi/2$. This can be seen particularly well for large R in the upper-right corner.

The most notable difference to the plane-wave case is the phase of d , which is no longer constant within a halfplane of positive or negative k (right panels of Figures 4.10 and 4.11). It diverges for $|k| \rightarrow 0$ and (slowly) approaches the plane-wave phase of $\pm\pi/2$ (length-form) and $0, \pm\pi$ (velocity-form) for $|k| \rightarrow \infty$. The rapidly varying phase for small $|k|$ is not well represented by the numerical data. This is another manifestation of the increasing numerical effort necessary as $|k|$ tends to zero.

Parallel orientation

In this orientation the quantitative difference between plane waves and exact scattering states becomes especially apparent, see Figures 4.12 and 4.13. Qualitatively, the absolute value is similar. It shows a series of interference minima (left panels). The crucial distinction is that the minimum curves are at different positions compared to the plane-wave case. This is expected since the electron-core interaction is the physical mechanism behind the interference effects and is specifically what the exact states are meant to address. The term $k^2/2$ in equation (4.11), that relates d_V and d_L , gives more relative weight to the interference structures of d_V at large k , visible as a higher contrast in the left panel of Figure 4.13.

The phase is a complicated function of k and R . The interference minima lie at the roots of d (as for plane waves) and corresponding jumps of π thus occur. Analogous to the perpendicular orientation, the phase diverges for $|k| \rightarrow 0$ and approaches the phase of the plane-wave case for $|k| \rightarrow \infty$. Note that d_L and d_V are related by equation (4.11) and the roots of d_L and d_V thus

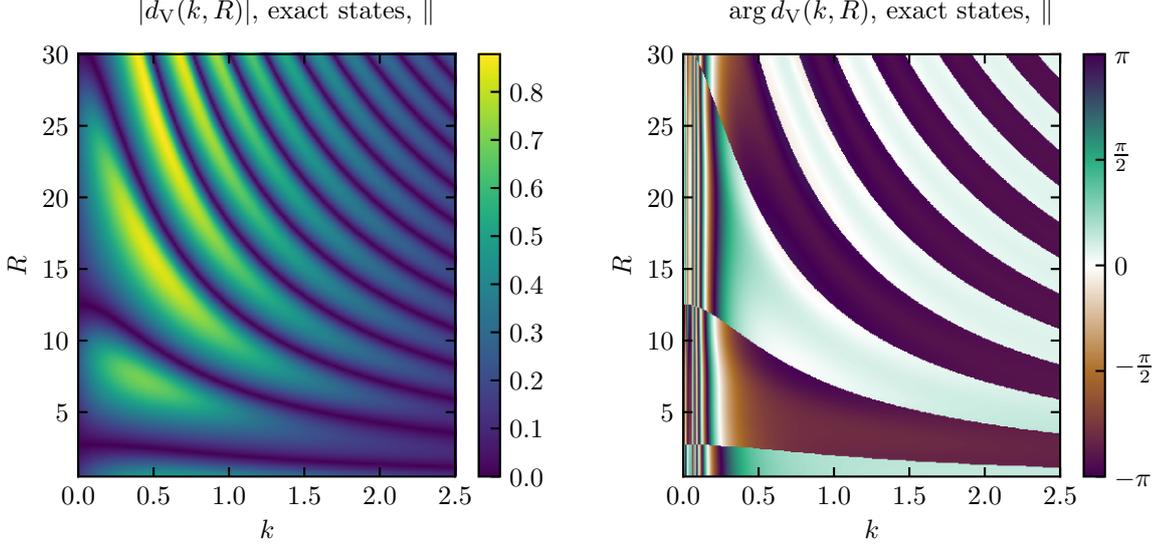


Figure 4.13.: Velocity-form dipole-transition matrix element for *parallel* orientation, calculated with *exact scattering states*. **Left:** Absolute value, the interference minima lie at different positions compared to the plane-wave matrix element in Figure 4.8. **Right:** Phase, it diverges for $|k| \rightarrow 0$, which causes jumps of 2π . Additionally, there are jumps of π at the positions of the interference minima, which coincide with the roots. For large $|k|$ the phase shows the behaviour of the plane-wave case, i.e. jumps between 0 and $\pm\pi$. This can be seen particularly well for large R in the upper-right corner.

coincide. The interference minima are therefore located at the same positions.

Figure 4.14 compares the positions of the first 10 interference minima with equation (4.10). The approximation (4.10) is based on plane waves as continuum states. We see that the curves in Figure 4.14 agree increasingly well for large $|k|$.

4.5.3. Divergence of ionization matrix element in SPA

The ionization step in HHG, as described by the length-gauge matrix element d_{ion} , presents a problem in saddle-point approximation. Specifically, the function $d_{\text{ion}}(k, R)$ has a singularity at k_{ion}^{\pm} , as can be seen in the following.

For electron positions far from the core, i.e. $x \rightarrow \pm\infty$, the electronic-nuclear interaction potential, which we denote by V here, goes to zero for any R (and any orientation)

$$\lim_{x \rightarrow \pm\infty} V(x, R) = 0.$$

The electronic BO states ψ_R are therefore asymptotically given by (we take $\mu_e \approx 1$ because $m_n \gg 1$)

$$\psi_R(x) \xrightarrow{x \rightarrow \pm\infty} e^{\mp\sqrt{2|E(R)|}x}$$

4. Quantum Mechanical Model

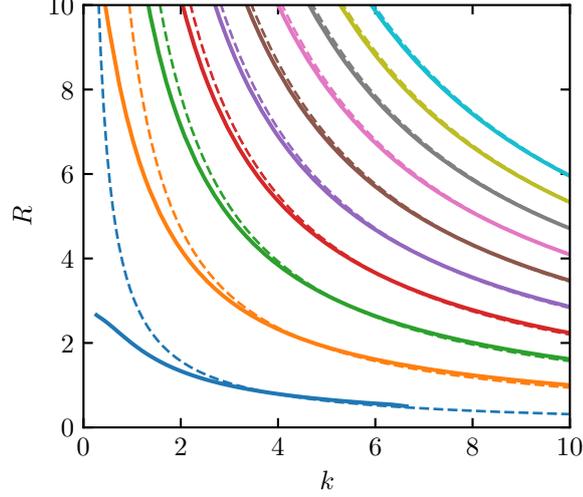


Figure 4.14.: Position of the lowest 10 interference minima of the transition matrix element for the parallel orientation, counted starting at 0 and increasing from lowest to highest internuclear distance R . The curves for the exact matrix element are shown as thick solid lines. For comparison, the minima according to equation (4.10), $kR = (2m + 1)\pi$, $m = 0, 1, 2, \dots$, are shown as thin dashed lines. The exact minima approach (4.10) for large $|k|$ and R .

with $E(R) = V_{\text{BO}}(R) - V_{\text{BO}}^+(R)$. In order to show that $d_{\text{ion}}(k_{\text{ion}}^{\pm}, R)$ is undefined, we study the asymptotic behaviour of the integrand of d_{ion} . If we set the continuum state to be a plane wave $\psi_k^c = \exp(ikx)$ we arrive at the asymptotic integrand (see expression (4.7))

$$f_x^{\pm}(k, R) = \exp(-ikx)x \exp\left(\mp\sqrt{2|E(R)|}x\right).$$

where f_x^+ holds for $x \rightarrow +\infty$ and f_x^- for $x \rightarrow -\infty$. Let us first consider the case of $k_{\text{ion}}^+ = i\sqrt{2I_p}$

$$f_x^{\pm}(k_{\text{ion}}^+, R) = x \exp\left(\left[\sqrt{2I_p} \mp \sqrt{2|E(R)|}\right]x\right).$$

We see that for any R

$$f_x^-(k_{\text{ion}}^+, R) = x \exp\left(\left[\sqrt{2I_p} + \sqrt{2|E(R)|}\right]x\right) \xrightarrow{x \rightarrow -\infty} 0.$$

In contrast, the behaviour of $f_x^+(k_{\text{ion}}^+, R)$ depends on the value of R . There exists a $R_{\text{thr}} \approx 1.43$ (for $I_p \approx 0.6$) such that $I_p \geq |E(R)|$ for $R \geq R_{\text{thr}}$ and $I_p < |E(R)|$ otherwise. It follows that

$$f_x^+(k_{\text{ion}}^+, R \geq R_{\text{thr}}) = x \exp\left(\left[\sqrt{2I_p} - \sqrt{2|E(R \geq R_{\text{thr}})|}\right]x\right) \xrightarrow{x \rightarrow +\infty} \infty$$

and consequently $d_{\text{ion}}(k_{\text{ion}}^+, R \geq R_{\text{thr}}) \rightarrow \infty$. The value of R_{thr} is close to the equilibrium distance $R_0 \approx 1.4$, where the vibrational ground state χ_0 yields a significant probability.

The situation is similar for $k_{\text{ion}}^- = -i\sqrt{2I_p}$. Here we have

$$f_x^{\pm}(k_{\text{ion}}^-, R) = x \exp\left(-\left[\sqrt{2I_p} \pm \sqrt{2|E(R)|}\right]x\right)$$

and therefore

$$f_x^+(k_{\text{ion}}^-, R) = x \exp\left(-\left[\sqrt{2I_p} + \sqrt{2|E(R)|}\right]x\right) \xrightarrow{x \rightarrow +\infty} 0$$

while in the other limit

$$f_x^-(k_{\text{ion}}^-, R \geq R_{\text{thr}}) = x \exp\left(\left[\sqrt{2|E(R \geq R_{\text{thr}})|} - \sqrt{2I_p}\right]x\right) \xrightarrow{x \rightarrow -\infty} -\infty.$$

Hence, $d_{\text{ion}}(k_{\text{ion}}^-, R \geq R_{\text{thr}}) \rightarrow -\infty$.

The argument also applies for the exact scattering states. For large x the Coulomb phase-correction is proportional to $\ln(2|kx|)$, expression (4.15), which in any case grows slower for $|x| \rightarrow \infty$ than the phase linear in x which causes the singularity.

The problem of the ill-defined ionization matrix element has direct consequences for the vibrational autocorrelation function (see chapter 3), which is therefore also ill-defined. The saddle-point approximation simply fails to appropriately describe the ionization step. This does not a priori mean, however, that the *ratio* of vibrational autocorrelations, which is the physical relevant quantity of interest, loses its significance as well. It may be that, although the autocorrelations by themselves diverge, their ratio stills contains information about how the ionization step differs between the isotopes. A suitable regularization procedure of the integrals might help in extracting such information. Unfortunately, the problem is aggravated by the fact that d_{ion} is not a global factor, but is involved in the functional dependence of the autocorrelation integrand. Furthermore, the evaluation of the autocorrelation integral is only possible numerically, which makes a prospective regularization a formidable task.

Another way to deal with the singularity, which is the way we choose to overcome the problem, is to neglect the ionization matrix element altogether. This is equivalent to setting it identically to 1, $d_{\text{ion}} \equiv 1$. The R - and isotope-dependent ionization-amplitude is consequently not accessible. However, the structure of the harmonic spectrum is largely independent of how the electron was promoted to the continuum [52, 83], rendering the ionization step less important than the recombination step. Leaving out d_{ion} should therefore be seen as an additional approximation of the SFA-SPA-based model of HHG.

5. Time-Frequency Study of Harmonic Signal

The purpose of this chapter is to compare vibrational autocorrelation ratios with harmonic ratios calculated via solutions of the TDSE. For this we use the parallel and perpendicular models from chapter 4. The central focus lies on the autocorrelation ratios that are calculated with the complex saddle-point times, see section 2.2.4. The theoretical background and basic properties of the autocorrelation function can be found in chapters 2 and 3.

5.1. Harmonic spectrum

In HHG, the quantity of interest is the power spectrum of the emitted harmonic radiation. Once the exact wave function $\psi(t)$ has been found numerically via the TDSE, the dipole acceleration (see also section 4.2)

$$D_{\text{acc}}(t) = \frac{1}{\mu_e} \left\langle \psi(t) \left| \frac{\partial V(x, R)}{\partial x} \right| \psi(t) \right\rangle$$

is related to the spectrum by its modulus-squared Fourier transform, as explained in section 2.2.2.

$$S_{\text{spec}}(\omega) \propto \left| \tilde{D}_{\text{acc}}(\omega) \right|^2 = \left| \int_{t_0}^{t_f} dt D_{\text{acc}}(t) e^{i\omega t} \right|^2, \quad (5.1)$$

with suitably chosen start time t_0 and end time t_f . Since we are only interested in linearly polarized electric fields, the dipole acceleration above is taken to be a scalar quantity. The harmonic ratio can then be calculated by

$$\mathcal{R}_{\text{spec}}(\omega) = \frac{S_{\text{spec}}^{\text{D}}(\omega)}{S_{\text{spec}}^{\text{H}}(\omega)},$$

where $S_{\text{spec}}^{\text{D}}$ and $S_{\text{spec}}^{\text{H}}$ are the spectra for D_2 and H_2 , respectively. Examples of such spectra, for the parallel orientation, together with the harmonic ratio $\mathcal{R}_{\text{spec}}$ resulting from it, is shown in Figure 5.1. The laser pulse is a single cycle starting at full amplitude, i.e. $E(t) = E_0 \cos(\omega_0 t)$ with $t \in [t_0, t_f] = [0, 2\pi/\omega]$.

In the left panel, the low contrast curves are the spectra as calculated with expression (5.1). The high contrast curves show the same data smoothed by means of a moving average. The ratio of the smooth curves is shown in the right panel. The two-center interference minima in the spectra occur at slightly different energies for the two isotopes and give rise to the peak in the ratio at $\omega \approx 2$.

5. Time-Frequency Study of Harmonic Signal

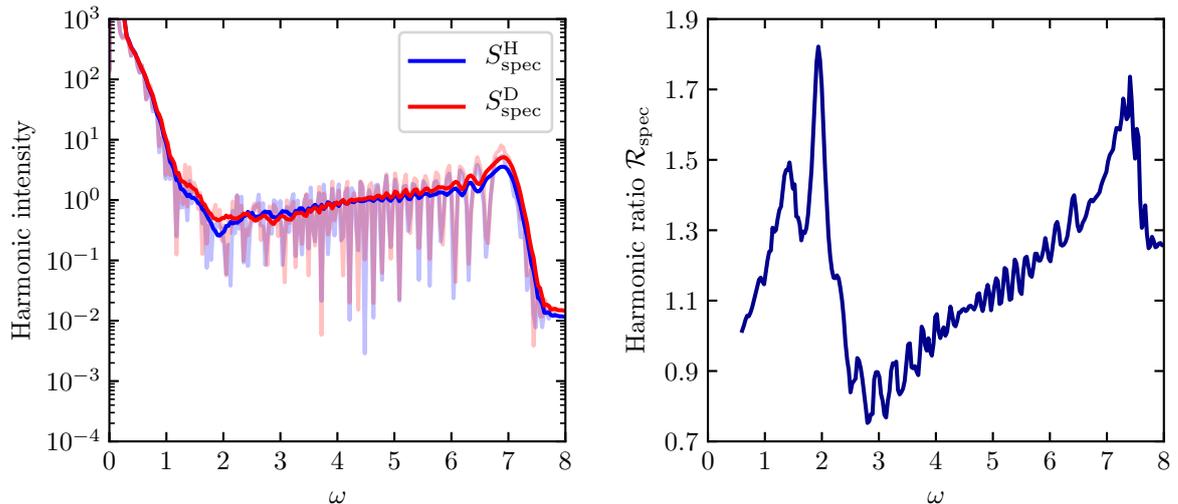


Figure 5.1.: **Left:** Example of harmonic spectra for D₂ and H₂ (low contrast curves). The driving laser field is a single cycle starting at full amplitude, i.e. $E(t) = E_0 \cos(\omega_0 t)$ with $t \in [0, 2\pi/\omega_0]$. The wavelength is 1200 nm with an intensity of $4 \cdot 10^{14} \text{ W/cm}^2$. A smoothed spectrum, calculated by a moving average over an energy range of approximately 0.42, is given by the high contrast curves. **Right:** Ratio of the smoothed spectra (D₂ vs. H₂).

There are drawbacks to obtaining the ratio directly from the harmonic spectra. The most prominent, concerning our purpose, is that the contributions from short and long trajectories cannot be distinguished. Only their combined signal, and therefore the interference between them, enters the spectrum. Additionally, in a pulse that is longer than the single cycle considered here, contributions from different cycles interfere as well. It is therefore more useful to use a *short-time Fourier transform* that allows for a time-resolved spectral analysis of the harmonic signal.

5.2. Gabor transform

5.2.1. Short-time Fourier transform

A Short-time Fourier transform (STFT) is defined as the Fourier transform of the product of the signal to be analyzed and a suitable window function $f_{\text{win}}(t)$ [91]

$$S_{\text{STFT}}[f_{\text{win}}](\omega, t) = \int dt' D_{\text{acc}}(t') f_{\text{win}}(t' - t) e^{i\omega t'}.$$

For any window position t , the function f_{win} selects a certain temporal range while suppressing the rest. The overall Fourier transform is therefore only sensitive to the frequency components within that range. Moving the position of the window over the whole signal then gives information not only about the frequency content, but also at which instants these frequencies occur.

The temporal width of the window needs to be chosen appropriately. The spectral and temporal resolutions of a STFT obey the familiar uncertainty relation between energy and time. A wide window increases the sample length for the Fourier transform and therefore the spectral resolution, but it simultaneously decreases the ability to attribute the frequencies to a certain moment in time. In contrast, a narrow window increases the temporal resolution since it restricts the signal content to a small time interval, but it decreases the sample length and consequently the spectral resolution. As the window width approaches zero, less and less full periods of ever higher frequencies no longer fit into the window and cannot be resolved. Note that this is a general principle that underlies any time-frequency analysis [92].

A *Gabor transform* is a STFT with the special case of a Gaussian window

$$f_{\text{win}}^G(t) = \frac{1}{\sqrt{2\pi}\sigma} \exp\left(-\frac{t^2}{2\sigma^2}\right),$$

which is the case that we use in this work. Define

$$G = |S_{\text{STFT}}[f_{\text{win}}^G]|^2.$$

The width of the window is given by σ . In our calculations we set σ equal to

$$\sigma_{I_p} = \frac{1}{\sqrt{8 \ln(2)}} \frac{2\pi}{I_p}$$

with $I_p \approx 0.6$ for all isotopes. This is chosen such that the lowest order harmonic, with energy I_p , fits into the FWHM of the Gaussian window. It turns out that the harmonic ratio \mathcal{R}_G (introduced below), in the plateau region, depends only weakly on σ around σ_{I_p} and the exact value is therefore not relevant, which from a physical standpoint is sensible.

A typical Gabor transform G of a HHG signal is shown in Figure 5.2, for a two-cycle laser field. Within these two cycles, the first, the third and the fifth quarter-cycles, which start at full amplitude, launch trajectories that can recombine. They lead to what we denote as “branches”, consisting of a contribution from the short (left part) and long (right part) trajectories.

The first branch is the most suitable to extract harmonic ratios from, because it contains the least interference. The later branches are weaker and also contain contributions from trajectories of earlier cycles that have excursion times longer than the long trajectories (see chapter 2). This gives rise to complicated interference patterns, as can be seen in the second and third branch in Figure 5.2.

The maximum of G for the first branch is shown as solid lines in Figure 5.2. It agrees well with the real part of the saddle-point return times that are given by the dashed lines. This agreement generally improves with increasing ponderomotive potential U_p .

Another typical feature of G for HHG is a strong contribution at low energies, visible as the yellow horizontal stripe for ω close to zero. This is caused by the slow oscillation of the wave function as it follows the laser field.

5. Time-Frequency Study of Harmonic Signal

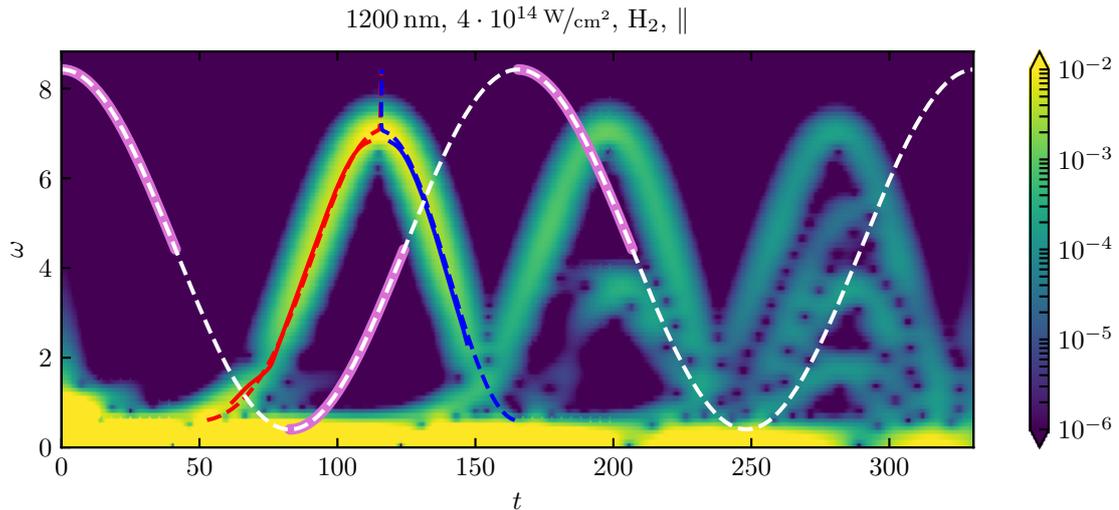


Figure 5.2.: Gabor transform G for a two-cycle laser field (white dashed line) with a wavelength of 1200 nm and an intensity of $4 \cdot 10^{14} \text{ W/cm}^2$, for the parallel orientation of H_2 (see chapter 4). The three highlighted quarter-cycles that start at full amplitude give rise to three branches consisting of contributions from the short and long trajectories. The position of the maximum $t_{\text{max}}^{\text{H}}(\omega)$ of G for the first branch is shown as solid lines, red for the short and blue for the long trajectories. Additionally, the dashed lines show the real parts of the saddle-point return times, which agree well with the position of the maximum. The effect of the two-center interference minimum can be seen as a small oscillation of the maximum at $\omega \approx 2$ and $t \approx 75$.

5.2.2. Extraction of harmonic ratios from the Gabor transform

The Gabor transform G can be thought of as a “local spectrum” that includes only the frequency components within the temporal window of width σ . We know from chapter 2 that the short and long trajectories both contribute to a certain emitted harmonic energy ω at specific return times t_{r} within a cycle. When viewed as a function of t for fixed ω , $G(\omega, t)$ exhibits a local maximum at $t \approx t_{\text{r}}$ (Figure 5.2), which suggests that the value of this maximum may be a measure of the harmonic signal strength of the corresponding trajectory. The harmonic ratio should then be given by

$$\mathcal{R}_G(\omega) = \frac{G^{\text{D}}(\omega, t_{\text{max}}^{\text{D}}(\omega))}{G^{\text{H}}(\omega, t_{\text{max}}^{\text{H}}(\omega))}, \quad (5.2)$$

where G^{D} and G^{H} stand for the Gabor transforms of D_2 and H_2 , respectively. The position of the maximum of $G^{\text{D,H}}$ is given by $t_{\text{max}}^{\text{D,H}}$. As explained above, this is a function of ω and in Figure 5.2 given by the red/left (short trajectories) and blue/right (long trajectories) solid lines.

A priori, it is not clear the ratio in expression (5.2) is a physically reasonable quantity. Harmonic ratios, by definition, are ratios of harmonic intensities, i.e. ratios of the full harmonic spectra. The autocorrelation ratio that appears in expression (3.3) and that we want to compare the TDSE ratios to, is no exception. However, the Gabor transform G contains only part of the signal for a given window position and might be an inappropriate quantity for such a comparison.

In order to verify the suitability of expression (5.2), a test TDSE calculation can be carried

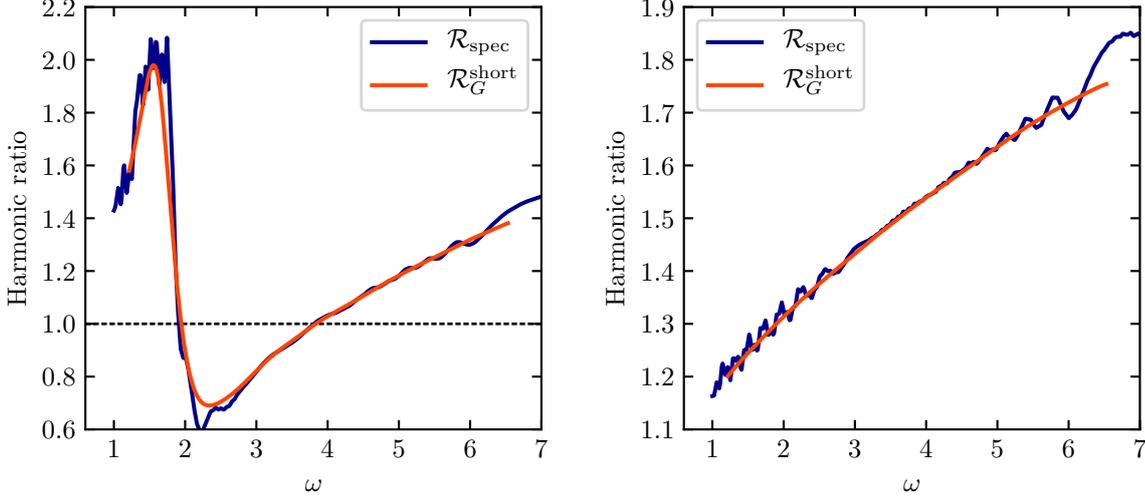


Figure 5.3.: Comparison of harmonic ratios $\mathcal{R}_{\text{spec}}$ and \mathcal{R}_G to verify the suitability of \mathcal{R}_G . The laser parameters are a wavelength of 1200 nm with an intensity of $4 \cdot 10^{14}$ W/cm², with a single cycle starting at full amplitude, i.e. $E(t) = E_0 \cos(\omega_0 t)$ with $t \in [0, 2\pi/\omega_0]$. The extent of the grid in the calculation of $\mathcal{R}_{\text{spec}}$ is chosen such that the absorber starts at E_0/ω_0^2 , gradually suppressing the wave function to zero as it reaches the grid boundary at $\approx 1.1E_0/\omega_0^2$. The dipole accelerations that enter $S_{\text{spec}}^{\text{D,H}}$ are multiplied by a quadratic window function that is zero at t_0 and t_f and one at $t_0 + (t_f - t_0)/2$. This suppresses the artificial high-frequency components at t_0 and t_f that result from the sudden turn-on and -off of the laser field. Furthermore, the spectra $S_{\text{spec}}^{\text{D,H}}$ are smoothed over an energy range of approximately 0.11 before the calculation of $\mathcal{R}_{\text{spec}}$ in order to slightly reduce the interference structures. The grid dimensions in the calculation of \mathcal{R}_G are large enough to accommodate the long trajectories also. **Left:** Parallel orientation **Right:** Perpendicular orientation.

out, with a numerical grid size in the electrons dimension intentionally chosen too small such that the long trajectories are prevented from returning to the parent ion [93]. From chapter 2 we know that the transition between the short and long trajectories happens at a time of approximately $0.05T$ (T is the laser period) after the field maximum. This corresponds to a maximum distance of approximately $1.1E_0/\omega_0^2$ (compare Figure 2.4), which is chosen as the extent of the numerical grid. All long trajectories are therefore absorbed at the grid boundary and the full spectrum, as calculated by expression (5.1), contains only the contributions of the short trajectories. The corresponding ratio $\mathcal{R}_{\text{spec}}$ should then coincide with the Gabor ratio \mathcal{R}_G for the short trajectory subbranch t_{max} , calculated with a grid size that is large enough to accommodate also the long trajectories. The result of such a test is shown in Figure 5.3.

The calculation in Figure 5.3 is done for a single cycle. The numerical grid parameters for the calculation of $\mathcal{R}_{\text{spec}}$ and \mathcal{R}_G are identical except for the aforementioned smaller electron dimension in case of $\mathcal{R}_{\text{spec}}$. The agreement between $\mathcal{R}_{\text{spec}}$ and \mathcal{R}_G is remarkable. Apart from interference structures in case of $\mathcal{R}_{\text{spec}}$, the curves coincide very well. This proves that \mathcal{R}_G is a suitable measure of the harmonic ratio and that, in particular, the lost phase information in the modulus-squared of G is irrelevant for the ratio. It is reasonable to assume that this also holds for the long trajectories, whose harmonic ratios cannot be verified by this procedure.

The Gabor ratio has the advantage that it does not contain interferences that result from trajectories recombining at different times during the laser cycle, most notably the interference between short and long trajectories. This naturally leads to smoother harmonic ratios $\mathcal{R}_G(\omega)$.

5. Time-Frequency Study of Harmonic Signal

It does, however, still contain interferences between trajectories that recombine at similar times, i.e. when differences in return times are smaller than the Gabor window width. This may lead to peaks and oscillations in $\mathcal{R}_G(\omega)$ for some laser parameters and does not yield useful ratios.

It is generally not possible to calculate $\mathcal{R}_G(\omega)$ for harmonic energies as low as I_p . The low-energy region of G is often complicated because of interferences. In particular, the short subbranch usually allows for lower energies to be studied than the long subbranch. This is primarily caused by the overlap of the long subbranch of one laser half-cycle with the short subbranch of the subsequent half-cycle. This can be seen in the example of Figure 5.2, where the curve of t_{\max} for the long trajectories stops at $t \approx 150$. Such an overlap introduces oscillations of G . Furthermore, the broad contributions in G at $\omega \approx 0$ also cause interferences at low energy. We collectively call such low-energy interferences ‘‘LER’’ in the following. As a consequence, settings with low ponderomotive potentials are generally less favorable for calculating \mathcal{R}_G because the accessible energy range is quite small.

5.3. Results

In this section we compare Gabor ratios $\mathcal{R}_G(\omega)$, equation (5.2), with autocorrelation ratios $\mathcal{R}[C](\omega)$, see (3.3). The general form of C is that from expression (3.1), with ionization element set to unity (see section 4.5.3)

$$C(p, t, t') = \int dR d_{\text{rec}}^*(p + A(t), R) \chi_0^*(R) \mathcal{U}_R^+(t, t') \chi_0(R).$$

We concentrate on two cases. In the first, the values of the recombination time t and ionization time t' are taken from the saddle-point approximated SFA (section 2.2.4). The recombination matrix element is taken with exact continuum states and in length-form, $d_L^{\text{exact}}(k, R)$, as introduced in section 4.5.2. The kinetic return momentum, according to equation (2.25), is given by $p_s(t_s, t'_s) + A(t_s) = \sqrt{2(\omega - I_p)} =: k_{\text{rec}}(\omega)$. The time-evolution operator \mathcal{U}_R^+ is only a function of the excursion time, $\tau_s(\omega) = t_s(\omega) - t'_s(\omega)$. We then arrive at

$$C_{\text{SPA}}(\omega) = \int dR d_{\text{rec}}^{\text{exact}}(k_{\text{rec}}(\omega), R) \chi_0^*(R) \mathcal{U}_R^+(\tau_s(\omega)) \chi_0(R). \quad (5.3)$$

In the second case, the times come from the semiclassical three-step model (section 2.1) and the recombination element is calculated with plane waves, LCAO-approximated electronic ground state and in velocity form (see appendix section A.1). Additionally, the heuristic relation $\tilde{k}_{\text{rec}}(\omega) := \sqrt{2\omega}$ is used as the return momentum. It has been shown that this improves the agreement in terms of the two-center interference when plane waves are used [53, 82, 94]. Physically it can be interpreted as an additional energy gain of I_p when the electron enters the potential well of the core. The autocorrelation then takes the form

$$C_{\text{SM}}(\omega) = \int dR \cos\left(\frac{\tilde{k}_{\text{rec}}(\omega) R \cos(\theta)}{2}\right) \chi_0^*(R) \mathcal{U}_R^+(\tau(\omega)) \chi_0(R). \quad (5.4)$$

The angle θ is measured between the molecular axis and the return direction of the electron, i.e. the polarization direction of the laser. For perpendicular orientation it is $\theta = \pi/2$ and for parallel orientation $\theta = 0$.

The autocorrelation ratio, $\mathcal{R}[C](\omega)$, is in both cases multiplied with the ratio of the ionization probabilities, $\mathcal{R}[\Gamma](\omega)$, see expression (3.3) and section 3.2.2. The ratio of the saddle-point factors, $\mathcal{R}[E\Pi\Lambda](\omega)$, is neglected, as was shown in section 3.2.3. The autocorrelation ratios are therefore of the form

$$\mathcal{R}_c[C](\omega) := \mathcal{R}[C](\omega)\mathcal{R}[\Gamma](\omega).$$

All Gabor ratios \mathcal{R}_G in this section are calculated with a single-cycle electric field starting at full amplitude, i.e. $E(t) = E_0 \cos(\omega_0 t)$ with $t \in [0, 2\pi/\omega_0]$. The ratio is then calculated for the single branch that appears in G . This is sufficient for our purpose since this first branch (see Figure 5.2) is the most suitable, as explained above, and any interaction with the electric field longer than one period only adds more branches that we are not interested in.

When we speak of the ‘‘autocorrelation ratios’’ in the following sections, we implicitly mean both $\mathcal{R}_c[C_{\text{SPA}}]$ and $\mathcal{R}_c[C_{\text{SM}}]$. With ‘‘Gabor ratio’’ we mean \mathcal{R}_G .

5.3.1. Harmonic ratios

In order to familiarize the reader with the Gabor as well as autocorrelation ratios defined above, we show in this section such ratios for selected laser parameters. A study of which autocorrelation ratio, i.e. either $\mathcal{R}_c[C_{\text{SPA}}]$ or $\mathcal{R}_c[C_{\text{SM}}]$, reproduces \mathcal{R}_G better is done in the next section. The reader is advised to read chapter 3 first to see what the graphs of the autocorrelation and its ratio look like without a transition matrix element.

Figures 5.4 and 5.5 show examples of harmonic ratios for a wavelength of 1200 nm and an intensity of $4 \cdot 10^{14}$ W/cm². For this particular set of laser parameters the Gabor ratios \mathcal{R}_G can be adequately extracted for both the short and long trajectories. As will become clear later, it is often difficult for both kinds of trajectories to be studied simultaneously for a single set of laser parameters, because interference structures of G may distort the ratio significantly. The oscillations of \mathcal{R}_G in the right panel of Figure 5.5 are an example of that. Characteristic for the parallel orientation is the two-center interference minimum in the harmonic spectrum which, in case of the *first* minimum, causes a maximum in the harmonic ratio that lies between $\omega = 1$ and $\omega = 2$. Overall, we see that the qualitative features of \mathcal{R}_G such as the position of said two-center maximum and, in this case, an increasing ratio with harmonic energy, agree well with the autocorrelation ratios. The LER interferences manifest themselves as oscillations which can be seen particularly well in the right panels (long trajectories) below $\omega \approx 2$. Here, the low-contrast thin solid curves represent \mathcal{R}_G along the real part of the saddle-point recombination time, $\text{Re } t_s(\omega)$. In the plateau region both ratios, i.e. \mathcal{R}_G along $t_{\text{max}}(\omega)$ and along $\text{Re } t_s(\omega)$, agree well. Since $t_{\text{max}}(\omega)$ can typically not be reliably determined in the LER region, the ratio \mathcal{R}_G along $\text{Re } t_s(\omega)$ is the only straightforward way to access this energy region. The long ratio \mathcal{R}_G often exhibits a sharp incline or decline for low energies because of these interferences (see the right panel of Figure 5.4).

The intensity of Figures 5.4 and 5.5 is rather high and the ground state is significantly depleted during the action of the laser pulse. The ground state populations at the end of the pulse range

5. Time-Frequency Study of Harmonic Signal

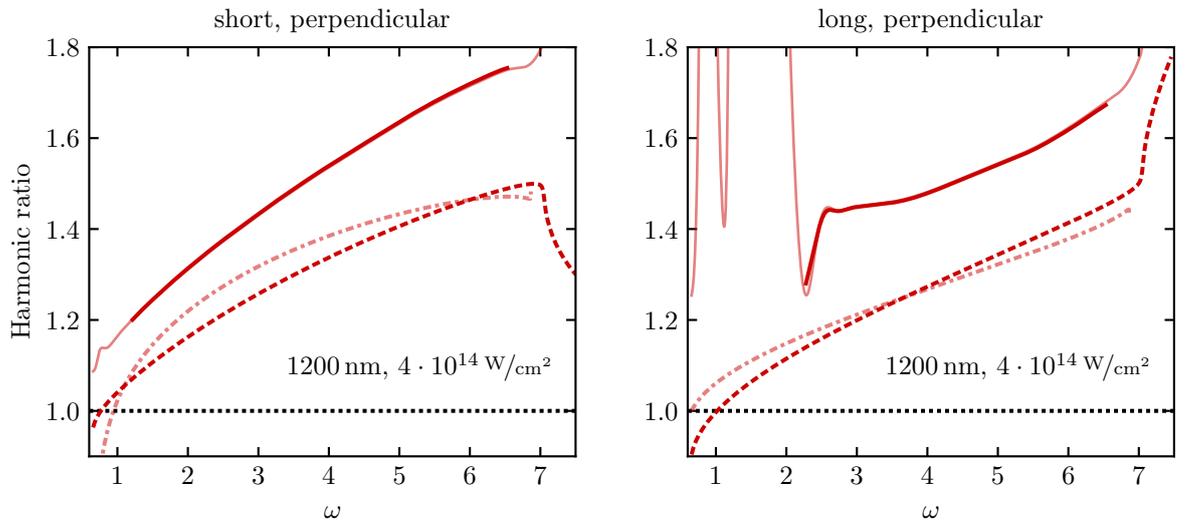


Figure 5.4.: Example of harmonic ratios for the *perpendicular* orientation, \mathcal{R}_G (high-contrast solid line), $\mathcal{R}_c[C_{SPA}]$ (high-contrast dashed line) and $\mathcal{R}_c[C_{SSM}]$ (low-contrast dashed-dotted line). The low-contrast thin solid line is \mathcal{R}_G with $G(\omega, \text{Re } t_s)$, i.e. evaluated along the real part of the saddle-point return time (see the dashed lines in Figure 5.2 for an example). If no interferences distort the branch in the plateau region, it agrees well with the maximum of G , given by $t_{\max}(\omega)$. Here it also serves as a good demonstration of the oscillations that appear at low energies. The wavelength is 1200 nm with an intensity of $4 \cdot 10^{14}$ W/cm². **Left:** short trajectories **Right:** long trajectories.

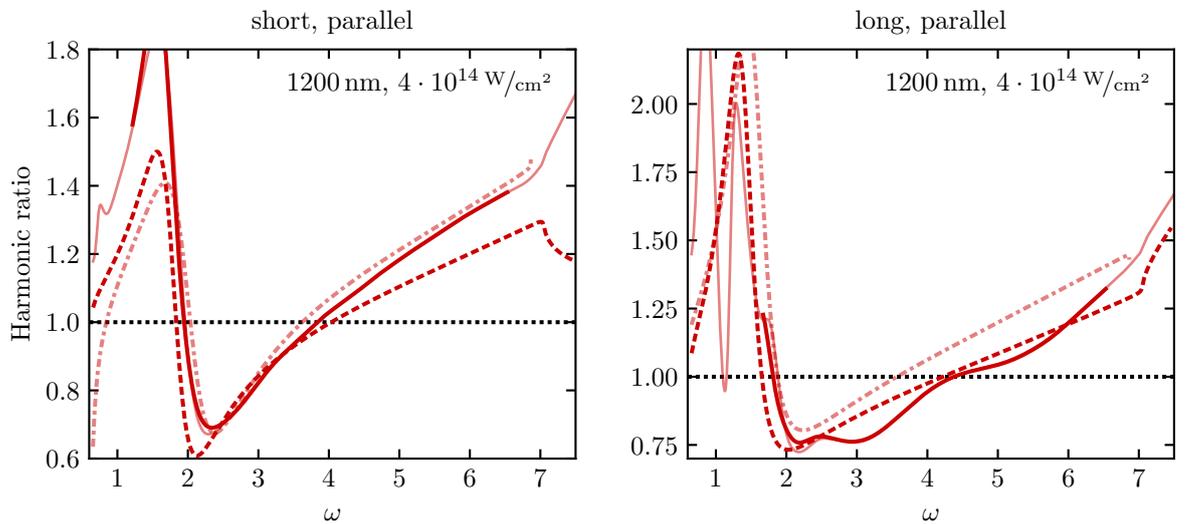


Figure 5.5.: Example of harmonic ratios for the *parallel* orientation, see the caption of Figure 5.4 for the types of curves shown. Because of two-center interference, the ratios exhibit a peak between $\omega = 1$ and $\omega = 2$.

between $P_{\text{gr}} \approx 10\%$ and 13% , with D_2 having a population slightly higher than H_2 , as expected, and the parallel orientation slightly lower than the perpendicular orientation. Such a depletion is not included in the SFA theory of section 2.2. In order to determine if it has a noticeable influence on the harmonic ratio, we checked the time-dependence of $(1 - P_{\text{gr}}^{\text{D}}(t))/(1 - P_{\text{gr}}^{\text{H}}(t))$ during the first quarter cycle of the pulse, i.e. the time span where the trajectories are launched. This quantity has its lowest value for the parallel orientation and the shortest short trajectory at around 0.97, with all other trajectories having values closer to unity. This shows that both isotopes experience similar depletion of their ground states and this should not influence the harmonic ratio significantly. Furthermore, it can approximately be interpreted as the ratio of the ionization rates and is consistent with (the right panel of) Figure 3.2.

Figures 5.6 and 5.7 show the ratios for a fixed intensity of $6 \cdot 10^{13} \text{ W/cm}^2$ and varying wavelengths, ranging from 2000 nm to 3000 nm. For such high wavelengths, the electron excursion times reach well beyond the first maximum of the autocorrelation ratio (see Figure 3.7) and cause the long ratio to be less than unity. For this intensity, the short ratio exhibits pronounced high values at low energies. This originates from an interference structure that distorts the short subbranch of G . This is not related to two-center interference because it occurs for both orientations (compare the left panels of Figures 5.6 and 5.7). It can be observed in the intensity range from $5 \cdot 10^{13} \text{ W/cm}^2$ to $1 \cdot 10^{14} \text{ W/cm}^2$ where it prevents a meaningful comparison with the autocorrelation ratios. It is absent for $2 \cdot 10^{14} \text{ W/cm}^2$ and above and its origin is not known. In contrast, the long ratio is free from such features and the agreement with the autocorrelation ratios in Figures 5.6 and 5.7 increases with wavelength. In particular, the shape of all three curves agree remarkably well for high wavelengths. For intensities below $5 \cdot 10^{13} \text{ W/cm}^2$ (not shown) the harmonic signal becomes weak and the both the short- and long ratios suffer from interference-induced oscillations. The beginning of such oscillations are already discernible in the right panel of Figure 5.7. A higher intensity of $8 \cdot 10^{13} \text{ W/cm}^2$ is shown in Figures A.7 and A.8 in appendix section A.7. There the mentioned interference structure causes pronounced maxima in the short ratio.

A typical feature of the two-center maximum of \mathcal{R}_G is that it takes on higher values than the corresponding maxima of the autocorrelation ratios. A good example is also the short ratio for $8 \cdot 10^{13} \text{ W/cm}^2$ in the appendix, where it lies outside the vertical scale while the autocorrelation maxima are within the scale. It is therefore better to compare only the energy at which it occurs (which is done below) and not its value.

Figure 5.8 shows the harmonic ratios for the perpendicular orientation and for a higher intensity of $3 \cdot 10^{14} \text{ W/cm}^2$. The wavelengths reach from 900 nm to 1300 nm, which corresponds to approximately the same range of cutoff energies as in Figure 5.6. Here the short ratio \mathcal{R}_G is not distorted by interference and it follows approximately the same curve for low energies, independent of wavelength. This agrees well with the same behaviour of the autocorrelation ratio, which was discussed in Figure 3.7. Furthermore, for these wavelengths, the range of long excursion times lies around the position of the first maximum of the autocorrelation ratio (see again Figure 3.7) and the long ratio is therefore comparable in absolute value to the short ratio.

The values of \mathcal{R}_G in Figure 5.8 are noticeably higher than $\mathcal{R}_c[\text{C}_{\text{SPA}}]$ and $\mathcal{R}_c[\text{C}_{\text{SM}}]$ for both kinds of trajectories and especially for the long trajectories there is poor agreement. In Figure 5.9, that presents the parallel orientation, the agreement is better. Here, \mathcal{R}_G is not too high

5. Time-Frequency Study of Harmonic Signal

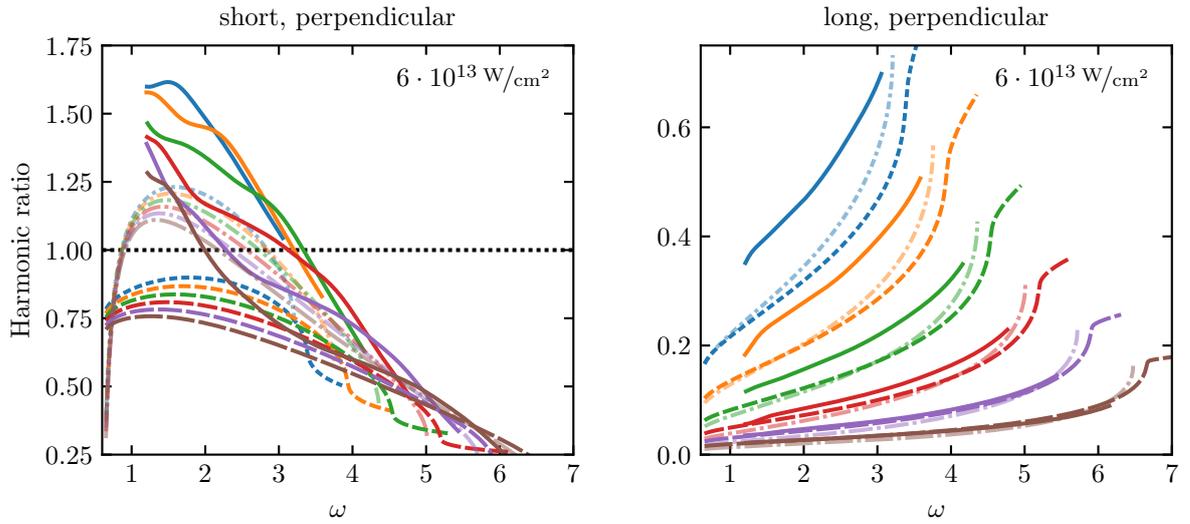


Figure 5.6.: Harmonic ratios for the *perpendicular* orientation, a fixed intensity of $6 \cdot 10^{13} \text{ W/cm}^2$ and wavelengths of 2000 nm, 2200 nm, 2400 nm, 2600 nm, 2800 nm and 3000 nm. Shown are \mathcal{R}_G (high-contrast solid line), $\mathcal{R}_c[C_{\text{SPA}}]$ (high-contrast dashed line) and $\mathcal{R}_c[C_{\text{SM}}]$ (low-contrast dotted-dashed line). Same-color curves belong to the same wavelengths; additionally, the length of the dashes indicate the wavelength. The high ratios at low energies in case of the short trajectories originate from an interference structure of G that also gives rise to the maxima in Figures A.7 and A.8 in the appendix. Such interferences render a comparison with autocorrelation ratios infeasible in the intensity range below approximately $2 \cdot 10^{14} \text{ W/cm}^2$.

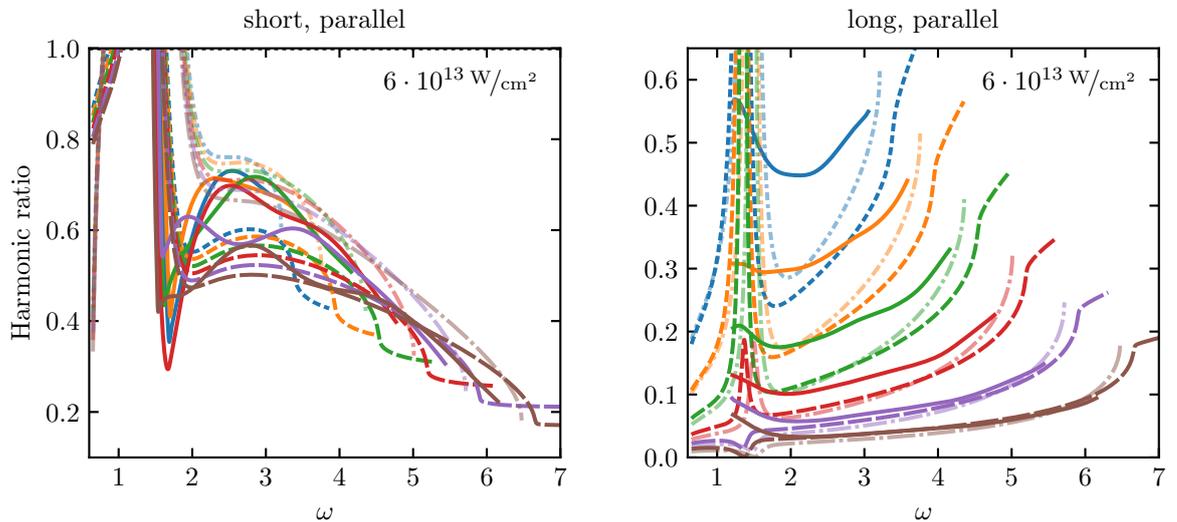


Figure 5.7.: Harmonic ratios for the *parallel* orientation with the same laser parameters as in Figure 5.6.

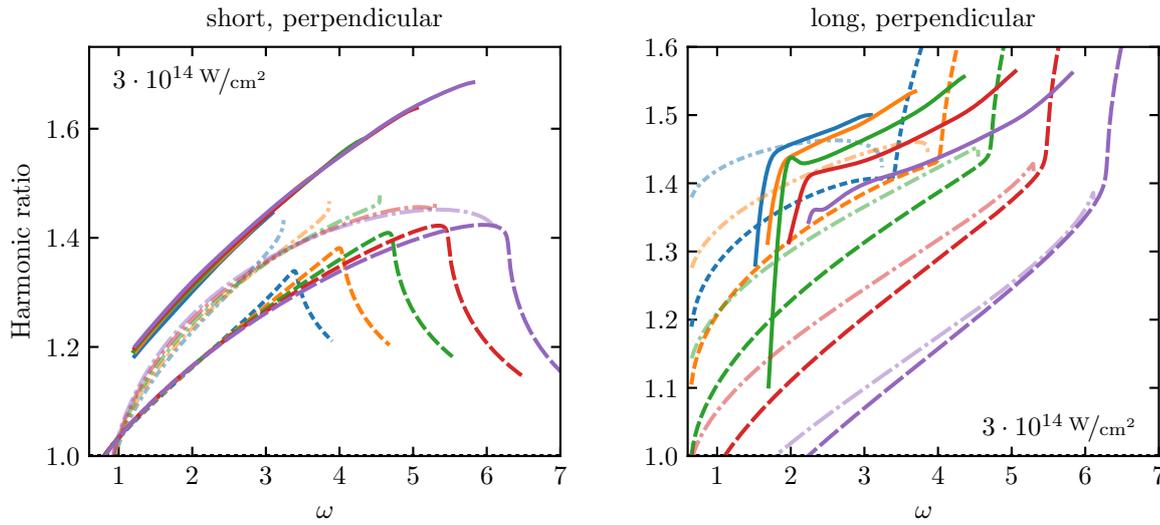


Figure 5.8.: Harmonic ratios for the *perpendicular* orientation, a fixed intensity of $3 \cdot 10^{14} \text{ W/cm}^2$ and wavelengths of 900 nm, 1000 nm, 1100 nm, 1200 nm and 1300 nm. Shown are \mathcal{R}_G (high-contrast solid line), $\mathcal{R}_c[C_{\text{SPA}}]$ (high-contrast dashed line) and $\mathcal{R}_c[C_{\text{SM}}]$ (low-contrast dotted-dashed line). Same-color curves belong to the same wavelengths and the length of the dashes indicate the wavelength. For this intensity \mathcal{R}_G for the short trajectories is free from interference maxima and reproduces qualitatively the behaviour of the autocorrelation ratios. However, \mathcal{R}_G is noticeably higher for both kinds of trajectories. In case of the long trajectories, LER interference is visible below $\omega \approx 2.5$.

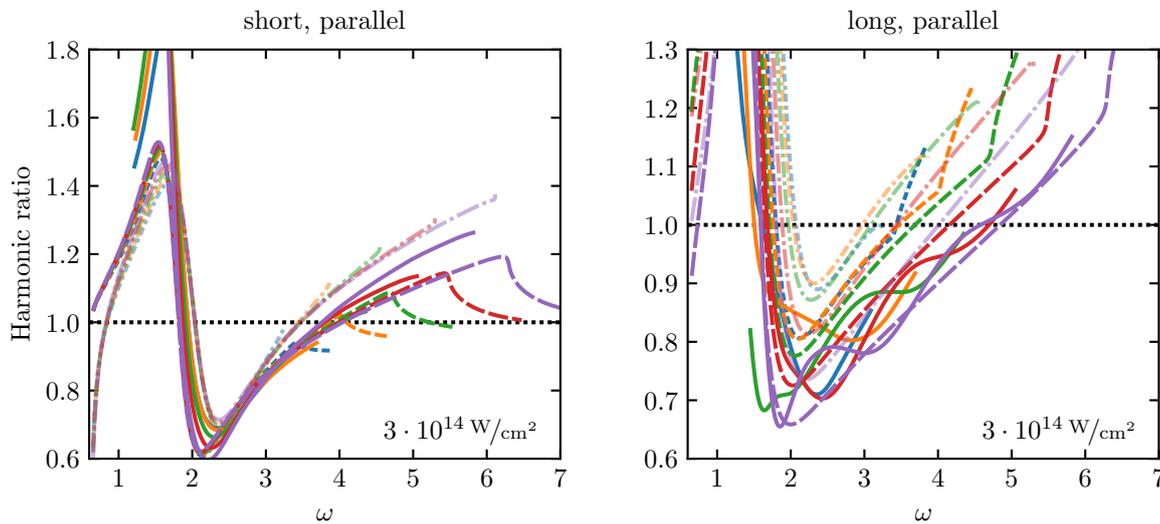


Figure 5.9.: Harmonic ratios for the *parallel* orientation with the same laser parameters as in Figure 5.8. \mathcal{R}_G agrees well with the autocorrelation ratios for the short trajectories. The long ratio \mathcal{R}_G exhibits oscillations but is also in reasonable agreement.

5. Time-Frequency Study of Harmonic Signal

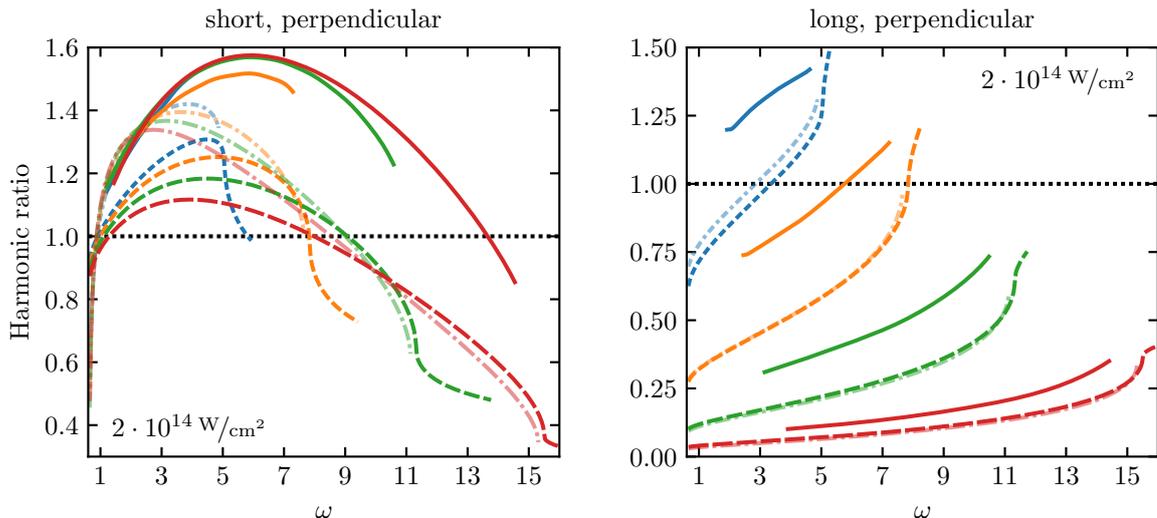


Figure 5.10.: Harmonic ratios for the *perpendicular* orientation, a fixed intensity of $2 \cdot 10^{14} \text{ W/cm}^2$ and wavelengths of 1400 nm, 1800 nm, 2200 nm, 2600 nm. Shown are \mathcal{R}_G (high-contrast solid line), $\mathcal{R}_c[C_{\text{SPA}}]$ (high-contrast dashed line) and $\mathcal{R}_c[C_{\text{SM}}]$ (low-contrast dotted-dashed line). Same-color curves belong to the same wavelengths and the length of the dashes indicate the wavelength. Similar to the lower intensity in Figure 5.6 the long \mathcal{R}_G agrees well with the autocorrelation ratios for high wavelengths. The short \mathcal{R}_G is noticeably higher, similar to Figure 5.8.

and for the short trajectories fits the autocorrelation ratios well. The long ratio \mathcal{R}_G exhibits oscillations but is also in reasonable agreement.

In order to test higher ponderomotive potentials, we show in Figure 5.10 the ratios for the perpendicular orientation and for a similar intensity of $2 \cdot 10^{14} \text{ W/cm}^2$, with higher wavelengths from 1400 nm to 2600 nm. It is apparent that the agreement of the long ratio for the perpendicular orientation increases with wavelength, similar to Figure 5.6. This suggests that the long ratio \mathcal{R}_G is well reproduced by the autocorrelation ratios when the electron excursion times reach beyond the first maximum, where the ratio becomes small. The short ratio \mathcal{R}_G is again noticeably higher than the autocorrelation ratios. For the parallel orientation, Figure 5.11, we see the appearance of another maximum that stems from the *second* two-center interference minimum of the autocorrelations. It is often much higher and broader for \mathcal{R}_G than for the autocorrelation ratios, see the left panel of Figure 5.11.

Finally, in Figures 5.12 and 5.13 the ratios are shown for a fixed wavelength of 800 nm and intensities from 4 to $8 \cdot 10^{14} \text{ W/cm}^2$. Similar to the short wavelengths in Figures 5.8 and 5.9, there is good agreement. The LER interference affects the long ratio significantly.

5.4. Discussion of results

In this section we compare the individual autocorrelation ratios, $\mathcal{R}_c[C_{\text{SPA}}]$ and $\mathcal{R}_c[C_{\text{SM}}]$, with the Gabor ratio \mathcal{R}_G . This is done separately for the parallel and perpendicular orientation. In order to quantify the agreement it is useful to introduce a measure. Define, for two functions f

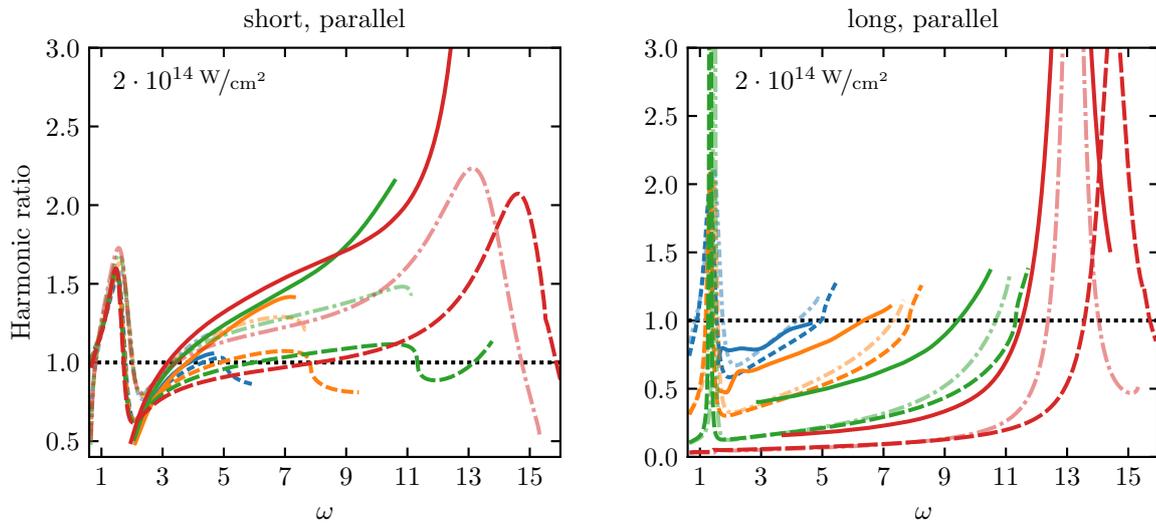


Figure 5.11.: Harmonic ratios for the *parallel* orientation with the same laser parameters as in Figure 5.10. The second two-center interference minimum in G typically gives rise to a broad and large maximum of \mathcal{R}_G .

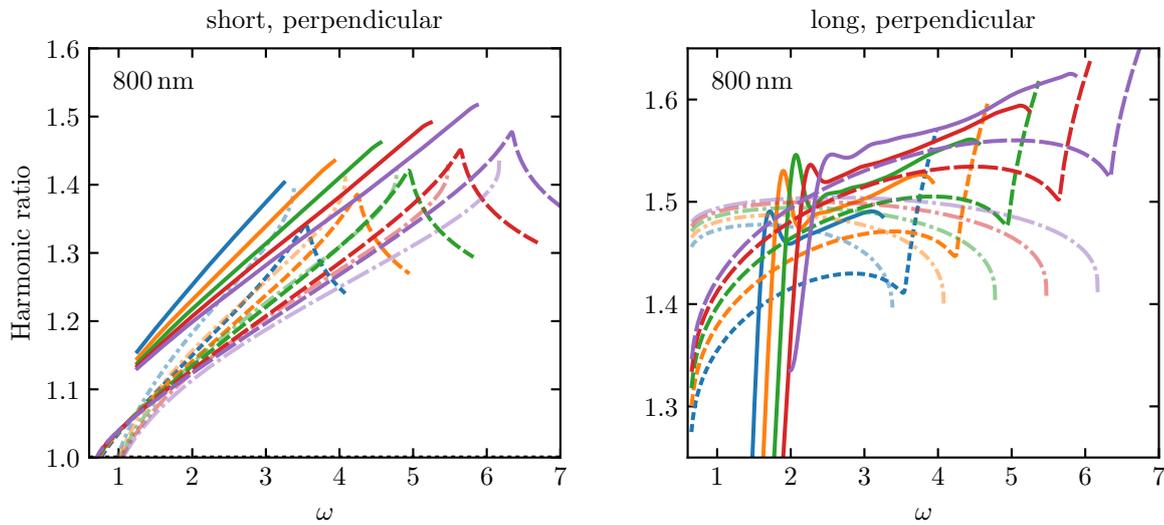


Figure 5.12.: Harmonic ratios for the *perpendicular* orientation, a fixed wavelength of 800 nm and intensities of 4, 5, 6, 7 and $8 \cdot 10^{14} \text{ W/cm}^2$. Shown are \mathcal{R}_G (high-contrast solid line), $\mathcal{R}_c[C_{\text{SPA}}]$ (high-contrast dashed line) and $\mathcal{R}_c[C_{\text{SM}}]$ (low-contrast dotted-dashed line). Same-color curves belong to the same intensities and the length of the dashes indicate the intensity. For this low wavelength the agreement of the short ratio is noticeably better than for higher wavelengths.

5. Time-Frequency Study of Harmonic Signal

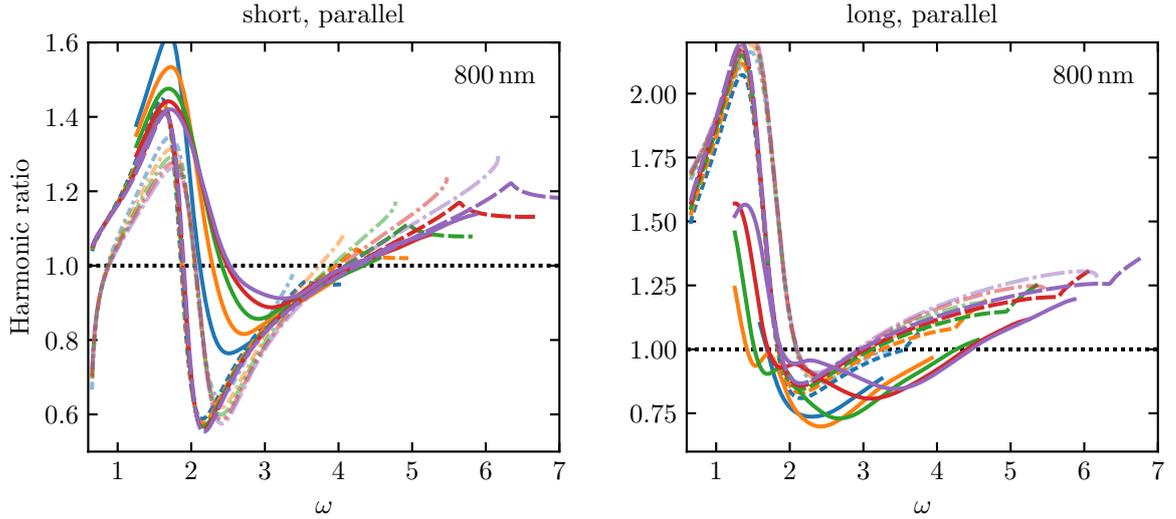


Figure 5.13.: Harmonic ratios for the *parallel* orientation with the same laser parameters as in Figure 5.12.

and g , that depend on the harmonic energy ω , the following absolute and relative deviation measures

$$\Delta\{f, g\} := \sqrt{\frac{1}{N} \sum_n^N (f(\omega_n) - g(\omega_n))^2},$$

$$\delta\{f, g\} := \sqrt{\frac{1}{N} \sum_n^N \left(\frac{f(\omega_n) - g(\omega_n)}{|f(\omega_n)| + |g(\omega_n)|} \right)^2},$$

where the functions are sampled at N harmonic energies ω_n . For our purpose, one function will be equal to \mathcal{R}_G and the other to either $\mathcal{R}_c[C_{\text{SPA}}]$ or $\mathcal{R}[C_{\text{SM}}]$. In particular, we consider the ratio as well as its derivative

$$\begin{aligned} \Delta\mathcal{R}[C] &:= \Delta\{\mathcal{R}_G, \mathcal{R}_c[C]\} & \delta\mathcal{R}[C] &:= \delta\{\mathcal{R}_G, \mathcal{R}_c[C]\} \\ \Delta\partial\mathcal{R}[C] &:= \Delta\left\{\frac{d\mathcal{R}_G}{d\omega}, \frac{d\mathcal{R}_c[C]}{d\omega}\right\} & \delta\partial\mathcal{R}[C] &:= \delta\left\{\frac{d\mathcal{R}_G}{d\omega}, \frac{d\mathcal{R}_c[C]}{d\omega}\right\} \end{aligned}$$

Every one of these 4 measures has its merit. $\Delta\mathcal{R}$ simply gives the average difference between two ratios, which can be easily compared with pictures of the ratios themselves. For ratios with values between 1 and 2 (which is the typical scenario for short wavelengths) one can readily draw conclusions from $\Delta\mathcal{R}$. If the ratio close to zero, which happens for long wavelengths, $\delta\mathcal{R}$ may be interesting as well. Using the derivatives of the ratios in $\Delta\partial\mathcal{R}$ and $\delta\partial\mathcal{R}$ gives a measure that is not sensitive to a shift, i.e. if the ratios are equal up to a constant, it yields zero. Since \mathcal{R}_G may behave erratic, a case study is often required and all measures need to be considered for a complete picture.

In order to avoid LER interferences, all measures shown in the following are calculated for $\omega \geq 2.5$. The upper bound is $\omega \approx 0.95\omega_c$ with the cutoff energy ω_c given by expression (2.9).

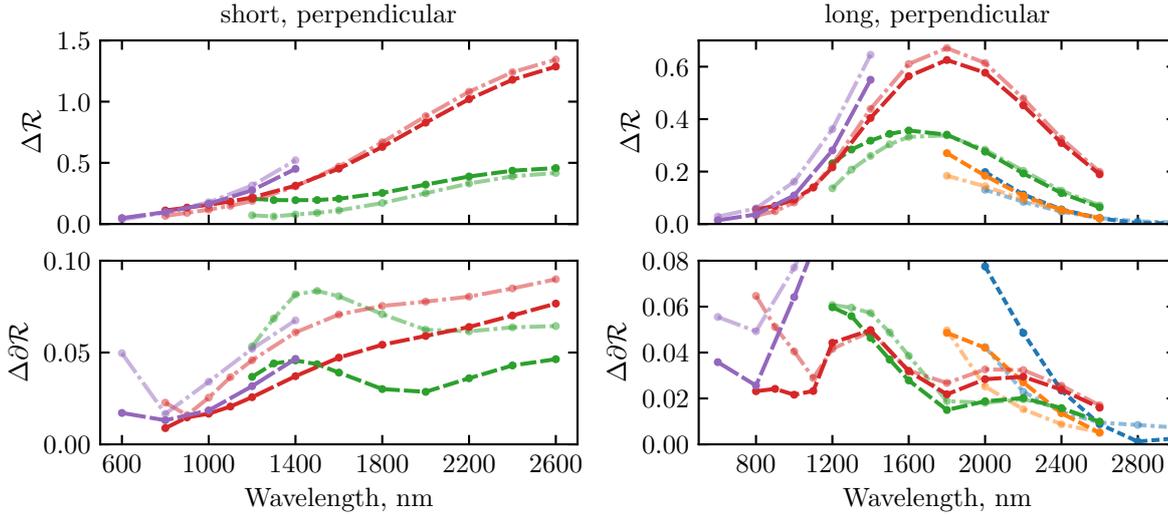


Figure 5.14.: Absolute deviations $\Delta\mathcal{R}$ and $\Delta\partial\mathcal{R}$ as a function of wavelength for intensities of $6 \cdot 10^{13} \text{ W/cm}^2$ (blue), $8 \cdot 10^{13} \text{ W/cm}^2$ (orange), $2 \cdot 10^{14} \text{ W/cm}^2$ (green), $4 \cdot 10^{14} \text{ W/cm}^2$ (red) and $6 \cdot 10^{14} \text{ W/cm}^2$ (purple). Shown are $\Delta\mathcal{R}[C_{\text{SPA}}]$, $\Delta\partial\mathcal{R}[C_{\text{SPA}}]$ (high-contrast dashed line) and $\Delta\mathcal{R}[C_{\text{SM}}]$, $\Delta\partial\mathcal{R}[C_{\text{SM}}]$ (low-contrast dotted-dashed line). The dash-length indicates the wavelength. $\Delta\mathcal{R}$ tends to zero for the long trajectories while it increases for the short trajectories. $\Delta\partial\mathcal{R}$ also tends to zero for the long trajectories while it stays approximately constant for the short trajectories.

5.4.1. Perpendicular orientation

The perpendicular orientation is generally easier to study than the parallel orientation, where the two-center interference maxima distort the ratio noticeably. In Figures 5.14 and 5.15 the absolute and relative deviations are plotted as a function of wavelength for intensities of 2, 4 and $6 \cdot 10^{14} \text{ W/cm}^2$. For the long trajectories, also 6 and $8 \cdot 10^{13} \text{ W/cm}^2$ are shown.

We see that for the short trajectories the deviation increases with wavelength, in absolute as well as relative terms. See for example the ratios in the left panel of Figure 5.10, where \mathcal{R}_G is noticeably higher than the autocorrelation ratios. For the higher intensity $4 \cdot 10^{14} \text{ W/cm}^2$ (ratios not shown) the discrepancy is even larger. For low wavelengths (and high intensities such that the cutoff energy is not too small), the agreement is better, see Figure 5.12. In terms of the deviation of the derivative, $\Delta\partial\mathcal{R}$ as well as $\delta\partial\mathcal{R}$ are small for low wavelengths, as for example evidenced by the left panel of Figure 5.12, where the ratios are approximately linear. For high wavelengths $\Delta\partial\mathcal{R}$ and $\delta\partial\mathcal{R}$ are approximately constant, i.e. while the short ratio \mathcal{R}_G is significantly higher than the autocorrelation counterparts, the shape of the curves match reasonably for increasing wavelength (see also the left panel of Figure 5.10).

For the long trajectories, the deviations $\Delta\mathcal{R}$ and $\delta\mathcal{R}$ are also small for low wavelengths and initially increase with it. Above a certain wavelength, that slightly depends on the intensity, the absolute deviation $\Delta\mathcal{R}$ decreases with wavelength. This is the trend that we observed in the right panels of Figures 5.6 and 5.10. For such high wavelengths the ratio itself becomes small and the relative deviation is large, as can be seen in the upper-right panel of Figure 5.15. For the lowest intensity of $6 \cdot 10^{13} \text{ W/cm}^2$ and longest tested wavelength of 3000 nm, the

5. Time-Frequency Study of Harmonic Signal

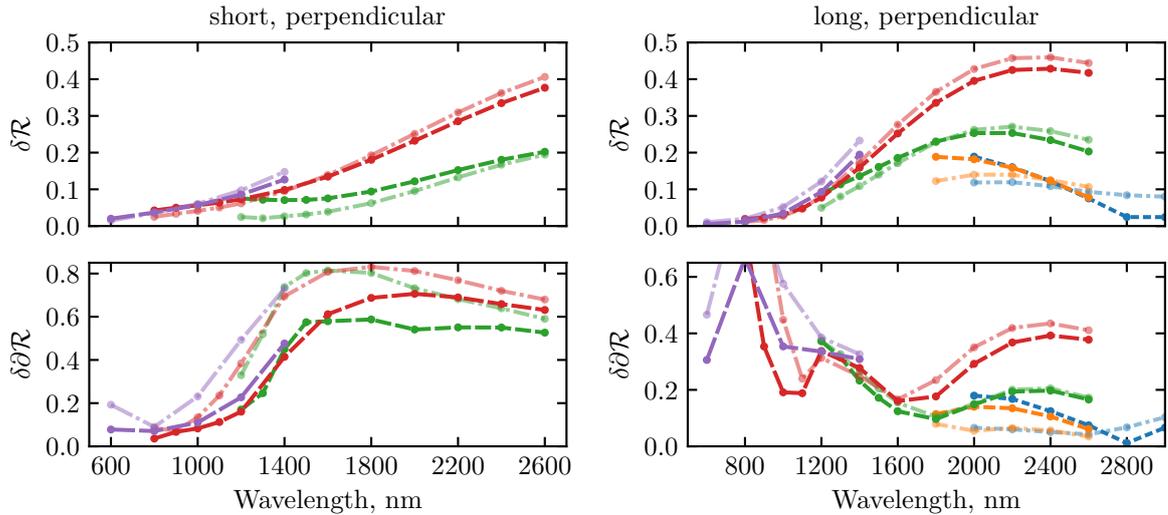


Figure 5.15.: Same setting as in Figure 5.14 but for the relative deviations $\delta\mathcal{R}$ and $\delta\partial\mathcal{R}$.

agreement is nearly perfect and also $\delta\mathcal{R}$ is small (lowest curves in the right panel of Figure 5.6). Presumably $\delta\mathcal{R}$ also tends to zero for the higher intensities. A small but discernible trend is visible in the upper-right panel of Figure 5.15. This was not tested, however. An interesting scenario would be laser parameters where the autocorrelation reaches the vibrational period. The erratic behaviour of the derivative deviations $\Delta\partial\mathcal{R}$ and $\delta\partial\mathcal{R}$ at low wavelengths stems from LER interferences that reach above $\omega = 2.5$ (which is the lower energy boundary considered in the measures) for high intensities. Apart from that, $\Delta\partial\mathcal{R}$ and $\delta\partial\mathcal{R}$ behave similarly to $\Delta\mathcal{R}$ and $\delta\mathcal{R}$ for high wavelengths.

5.4.2. Parallel orientation

The deviation measures defined above are often not useful for the parallel orientation. The height of the two-center maxima, in particular the second one, of \mathcal{R}_G may be significantly higher than the autocorrelation counterparts (see for example the left panel of Figure 5.11) and this effect dominates the graphs of the measures. However, for the cases where the second maximum is not relevant, a good agreement as it can be seen in Figures 5.7 and 5.9 is reflected in low deviation measures (note here that the first two-center maximum of the ratio is not contained in the measures because it lies below $\omega = 2.5$).

Instead, it is better to compare the positions of these maxima. In order to do this we evaluate \mathcal{R}_G along $\text{Re } t_s$, which gives us access to low energies. One has to keep in mind that this region is prone to interference and an exact agreement of the maximum positions cannot be expected. However, a general trend may still be visible if considered as a function of wavelength. Figure 5.16 shows such a plot for the short trajectories and the first maximum. For the long trajectories the maximum could not be reliably determined.

Indeed, the position of the maximum of \mathcal{R}_G follows the same trend as the autocorrelation

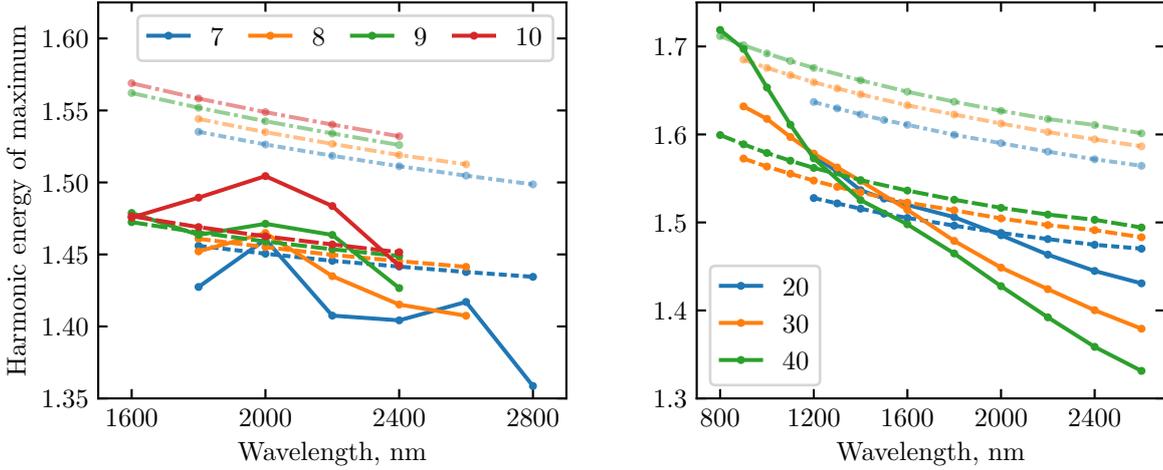


Figure 5.16.: Harmonic energy of the *first* short-trajectory two-center maximum as a function of wavelength (parallel orientation). Shown are the harmonic ratios \mathcal{R}_G (high-contrast solid line), $\mathcal{R}_c[C_{\text{SPA}}]$ (high-contrast dashed line), $\mathcal{R}_c[C_{\text{SM}}]$ (low-contrast dotted-dashed line). The numbers in the legend indicate the intensity in units of 10^{13} W/cm^2 . In both respective panels the length of the dashes indicate the intensity. **Left:** low intensities **Right:** high intensities.

counterparts, i.e. it decreases with wavelength. This is to be expected because a higher wavelength entails a longer excursion time of the electron, giving the nuclei more time to separate. The higher internuclear distance that results from this corresponds to lower harmonic energies of the two-center minimum, see Figures 4.8 and 4.14. Analogously, a short trajectory with fixed harmonic energy has a decreasing excursion time for increasing intensity (see Figure 2.9). This gives the nuclei less time to separate and the internuclear distance is smaller, giving a higher energy. This is also seen for \mathcal{R}_G for the low intensities in the left panel. For the high intensities in the right panel the order is reversed for high wavelengths. This may be due to LER interference. Also seen in Figure 5.16 is that $\mathcal{R}_c[C_{\text{SPA}}]$ reproduces the position of the maximum better than $\mathcal{R}_c[C_{\text{SM}}]$ for most laser parameters.

In Figure 5.17 we show the position of the second two-center maximum of the ratios for both the short and long trajectories. The discrepancy between the ratios is larger than for the first maximum. The absolute position of \mathcal{R}_G is better reproduced by $\mathcal{R}_c[C_{\text{SM}}]$ than $\mathcal{R}_c[C_{\text{SPA}}]$. For the short trajectories, left panel, the position increases with wavelength for $3 \cdot 10^{14} \text{ W/cm}^2$ and decreases with wavelength for $4 \cdot 10^{14} \text{ W/cm}^2$ in case of \mathcal{R}_G . This trend can also be seen for $\mathcal{R}_c[C_{\text{SPA}}]$, which is small but discernible in that scale.

5.5. Summary and Conclusion

When one is interested in HHG, the typical quantity of interest is the power spectrum S_{spec} of the emitted radiation, as it can be calculated from the dipole acceleration with expression (5.1). This quantity, however, does not allow to separate the contributions from the short and long

5. Time-Frequency Study of Harmonic Signal

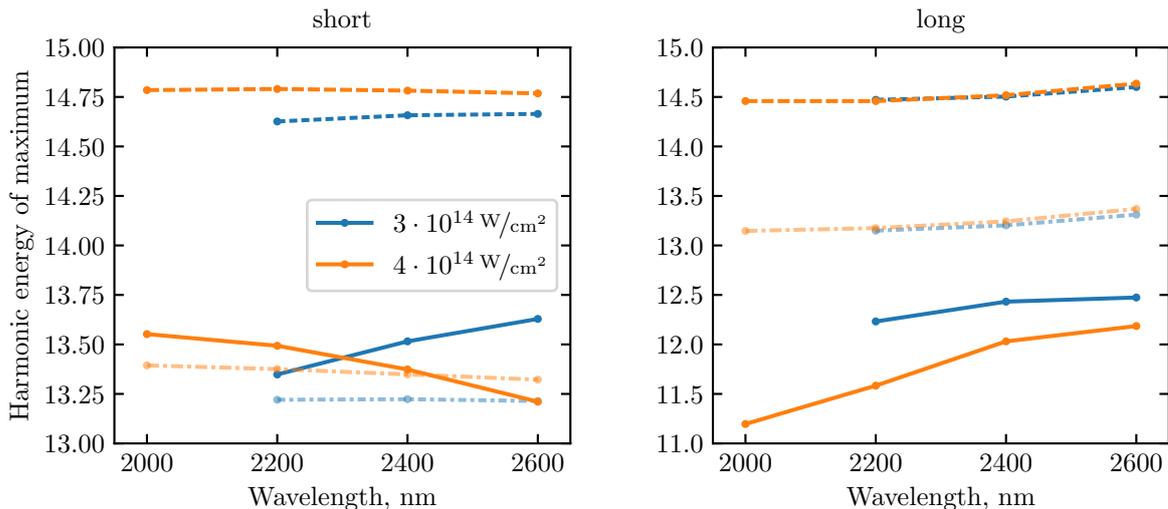


Figure 5.17.: Harmonic energy of the *second* two-center maximum as a function of wavelength for the parallel orientation. Shown are the harmonic ratios \mathcal{R}_G (high-contrast solid line), $\mathcal{R}_c[C_{\text{SPA}}]$ (high-contrast dashed line), $\mathcal{R}_c[C_{\text{SM}}]$ (low-contrast dotted-dashed line). **Left:** short trajectories **Right:** long trajectories.

trajectories, which are inextricably contained within S_{spec} . In order to study both contributions separately, a time-frequency study with the help of a short-time Fourier transform (section 5.2.1) can be carried out. A special type of such a transform is the Gabor transform G . In section 5.2.2 it was shown that it can be used to calculate trajectory-resolved ratios \mathcal{R}_G of harmonic intensities.

The Gabor ratio \mathcal{R}_G is often prone to interference-related oscillations. In particular, the low-energy region of G is complicated due to interference structures which were denoted as “LER interference”. It hampers the study of low harmonic energies and settings with low cutoff energies are therefore not accessible. Typically, the short ratio \mathcal{R}_G can be studied for lower harmonic energies than the corresponding long ratio. For some settings, also higher plateau energies may be inaccessible, an example being the short ratio \mathcal{R}_G for intensities below $2 \cdot 10^{14} \text{ W/cm}^2$ (see Figures 5.6, 5.7 and A.7, A.8). Where this particular interference structure originates from, and if it is specific to our setting, is not known.

The goal of the calculation of \mathcal{R}_G was a comparison with ratios of vibrational autocorrelations of two different types. One, $\mathcal{R}_c[C_{\text{SM}}]$ from expression (5.4), uses the classical excursion times from the well-established three-step model, a LCAO recombination matrix element and a heuristically corrected electron return momentum. The other, $\mathcal{R}_c[C_{\text{SPA}}]$ from expression (5.3), uses the complex-valued times from the saddle-point approximated SFA theory, an exact recombination matrix element and the correct electron return momentum as it follows from the saddle-point equations. This comparison was done to test if the more elaborate approach of $\mathcal{R}_c[C_{\text{SPA}}]$ offers an improved description of the harmonic ratios over $\mathcal{R}_c[C_{\text{SM}}]$.

The first observation is that $\mathcal{R}_c[C_{\text{SM}}]$ works remarkably well considering its simplicity and it often yields comparable results to the more exact approach of $\mathcal{R}_c[C_{\text{SPA}}]$. The differences lie in the details. A good summary for the perpendicular orientation can be seen in Figures 5.14 and

5.15. These show the deviation measures, defined in the beginning of section 5.4, for a selection of laser parameters. The absolute, $\Delta\mathcal{R}$, as well as the relative, $\delta\mathcal{R}$, deviations behave very similar for both $\mathcal{R}_c[C_{SM}]$ and $\mathcal{R}_c[C_{SPA}]$. For long wavelengths and high intensities $\mathcal{R}_c[C_{SPA}]$ yields slightly lower $\Delta\mathcal{R}$ and $\delta\mathcal{R}$ and therefore a better agreement with the Gabor ratio \mathcal{R}_G . In particular, the derivative of the harmonic ratio as a function of harmonic energy is often better reproduced by $\mathcal{R}_c[C_{SPA}]$, as evidence by $\Delta\partial\mathcal{R}$ and $\delta\partial\mathcal{R}$ in the lower panels in the Figures. Examples of this can also be seen in the left panel of Figures 5.10 or 5.12. In this respect the saddle-point approach is preferable.

Apart from interference-induced oscillations, \mathcal{R}_G often takes on significantly larger values than the autocorrelation counterparts. The discrepancy increases with intensity and affects the short trajectories in particular. For the long trajectories, increasing the wavelength reduced the absolute deviation for all tested intensities and for both orientations. The wavelengths then fall in the regime of small autocorrelation ratios well below unity (Figure 3.7).

The maxima of \mathcal{R}_G due to two-center interference in the parallel orientation may be much higher and broader than for $\mathcal{R}_c[C_{SM}]$ and $\mathcal{R}_c[C_{SPA}]$. The second of such maxima in particular may be noticeably different between the Gabor and autocorrelation ratios while the first is usually in better agreement. A comparison of the position of these maxima shows that the first is better reproduced by $\mathcal{R}_c[C_{SPA}]$ and the second by $\mathcal{R}_c[C_{SM}]$.

In conclusion we can say that $\mathcal{R}_c[C_{SPA}]$ does offer an improvement over $\mathcal{R}_c[C_{SM}]$. It is not universally better for all tested laser parameters, but even in the cases where $\mathcal{R}_c[C_{SM}]$ is closer to \mathcal{R}_G than $\mathcal{R}_c[C_{SPA}]$ is the latter not far off. In particular, qualitatively the ratio is better reproduced by the saddle-point approach. There is, however, a noticeable discrepancy between the Gabor and both autocorrelation ratios. Finding out the origin of this justifies further studies.

6. Molecular Alignment

This chapter comprises the theoretical background needed to calculate alignment distributions of diatomic molecules in strong laser pulses. Such distributions are needed for the comparison of autocorrelation ratios with experimental data, which is done in chapter 8.

Although it may not be intended in experiments on high-harmonic generation, the molecular ensemble under consideration can undergo an alignment process due to the influence of the strong driving laser pulse. Because of the sensitivity of the harmonic spectrum to the angle between the internuclear axis and the returning electron momentum [52, 53] as well as the addition of contributions originating from different molecules, the macroscopic harmonic signal may significantly depend on the degree of alignment. It is therefore sensible to gauge the extent to which alignment plays a role in the specific conditions under study.

In case of polar molecules, i.e. molecules with a permanent dipole moment, the ensemble can already be aligned with a static electric field [95], depending on the strength of that dipole moment. The alignment of nonpolar molecules, in contrast, relies on inducing a temporal dipole moment. This is a second-order effect in the electric field quantified by the *polarizability*. The pulse intensities encountered in experiments on HHG ($10^{13} \text{ W/cm}^2 - 10^{15} \text{ W/cm}^2$) correspond to electric fields for which this becomes relevant.

It is possible to induce rotational dynamics where neither electronic nor vibrational transitions are resonantly excited. Specifically for the hydrogen molecule, the vibrational constant is $\omega_0 \approx 4395 \text{ cm}^{-1}$ [96]. The electronic transitions have energy differences even higher (see Figure 4.1 and consider that $0.1 \text{ a.u.} \approx 2.2 \cdot 10^4 \text{ cm}^{-1}$). Compare this to the photon energy of a 800 nm laser pulse of 12500 cm^{-1} . We will consider this nonresonant regime in more detail in section 6.2.2.

In the next section we will first introduce the two major regimes of alignment dynamics taking place in strong laser pulses. After that the relevant case for HHG is investigated in more detail.

6.1. Alignment in a strong laser pulse

Strong-field experiments are usually carried out with pulsed lasers. Due to the large electric fields involved, it is possible to align molecules which do not have a permanent dipole moment, which is the case for the hydrogen molecule. A linearly polarized laser will cause a linear molecule to align its molecular axis along the axis of polarization. This is because of the larger

6. Molecular Alignment

polarizability in the direction of the molecular axis, α_{\parallel} , than perpendicular to it, α_{\perp} . This is conventionally measured in terms of the *polarizability anisotropy* defined as $\Delta\alpha = \alpha_{\parallel} - \alpha_{\perp}$. The higher the value of $\Delta\alpha$ the more the molecule tends to be aligned by the laser pulse. The presence of the pulse introduces an interaction potential into the Hamiltonian of the field-free system which depends on α_{\parallel} and α_{\perp} (See 6.2.2). Depending on the pulse duration two limiting cases can be distinguished, generally named the *adiabatic* and *impulsive* (or *dynamic*) limit.

The adiabatic limit holds if the pulse envelope has a temporal width large compared to the rotational period of the molecular species. In this case the rotational motion can adiabatically follow the changing laser intensity and the degree of alignment shows a profile close to the shape of the envelope. This means that an initially randomly aligned ensemble smoothly enters a state of alignment, with the maximum degree of alignment occurring at the peak of the envelope. It then smoothly changes back to the isotropic angular distribution. In this case the interaction potential can be considered quasi-static and allows the use of the time-independent Schrödinger equation with the instantaneous value of the potential. The solutions are called *pendular* states and approximate the solutions of the time-dependent Schrödinger equation at the respective times.

In the impulsive limit the pulse envelope changes on a time scale much shorter than the rotational period of the molecule. The ensemble cannot follow the rapidly varying laser intensity (often referred to as a “kick”) and is left in a time-dependent coherent superposition of field-free eigenstates which persists after the end of the pulse. In other words, the laser populates a wide range of angular momentum eigenstates. This superposition undergoes a field-free time evolution after the pulse which leads to recurring instants of high degree of alignment, so-called *revivals*, as the different components of the state move in and out of phase. This process lasts as long as the coherent superposition persists. Eventually, the ensemble will go back into its initial isotropic distribution.

A comparison between both cases can be seen in Figure 6.1 where the degree of alignment (for the definition see section 6.2.2) of nitrogen N_2 is shown for two different sets of laser parameters. The rotational period of N_2 is $T_{\text{rot}} \approx 8.4$ ps. The half- and full-period revival peaks are clearly visible. In this case also quarter-period revivals are present due to a disproportion of even- and odd-numbered angular momentum states in the initial ensemble (see section 6.2.3).

For the hydrogen molecule the rotational period in the ground state, with a rotational constant $B_0 \approx 60.8 \text{ cm}^{-1}$ [97], is

$$T_{\text{rot}}^{\text{H}_2} = \frac{h}{2B_0} \approx 274 \text{ fs}$$

which is approximately one order of magnitude larger than a typical pulse duration in strong-field experiments of 30 fs. Since high-harmonic generation is a subcycle process we are interested in the alignment distribution during the short, nonadiabatic laser interaction. The rotational dynamics after the pulse, which is often exploited in experiments to achieve a high degree of field-free alignment, is irrelevant in the present context.

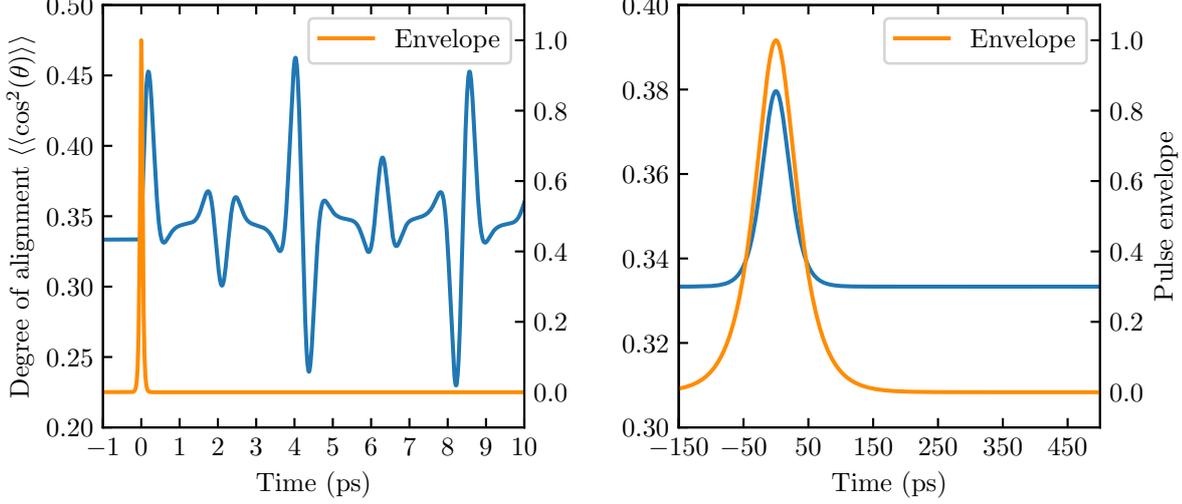


Figure 6.1.: Comparison of the degree of alignment $\langle\langle \cos^2(\theta) \rangle\rangle$ between impulsive (left panel) and adiabatic (right panel) alignment limits for N_2 with a temperature of 50 K. The pulse envelope has the form $\text{sech}(2 \ln(1+\sqrt{2})t/\tau)$. The rotational constant is $B_0 = 1.989 \text{ cm}^{-1}$ [98], giving a rotational period of $T_{\text{rot}} \approx 8.4 \text{ ps}$. The laser parameters in the impulsive limit are $\tau = 50 \text{ fs}$, $2.5 \cdot 10^{13} \text{ W/cm}^2$ and in the adiabatic limit $\tau = 50 \text{ ps}$, $2.5 \cdot 10^{12} \text{ W/cm}^2$. For details of the calculation see section 6.2.2. Inspired by Fig.1 of [98].

6.2. Theoretical model

In this section we want to give the technical details of how to model the laser-induced alignment of a molecular ensemble. We will restrict our considerations to linear (diatomic) molecules and a linearly polarized electric field of the laser pulse. In section 6.2.1 the linear rigid rotor is introduced which is the foundation for the alignment consideration in section 6.2.2.

6.2.1. Field-free linear rigid rotor

In Born-Oppenheimer approximation the time-independent Schrödinger equation of the two nuclei in the center-of-mass frame of the molecule allows separation into radial and angular parts (analogue to the case of the hydrogen atom) [96,99]. The angular equation takes the form

$$\frac{\hat{j}^2}{2I} Y(\theta, \phi) = E Y(\theta, \phi)$$

with the squared angular-momentum operator in spherical coordinates

$$\hat{j}^2 = - \left(\frac{1}{\sin(\theta)} \frac{\partial}{\partial \theta} \left(\sin(\theta) \frac{\partial}{\partial \theta} \right) + \frac{1}{\sin^2(\theta)} \frac{\partial^2}{\partial \phi^2} \right)$$

whose representation stems from the Laplace operator (i.e. θ is the polar angle and ϕ the azimuthal angle). The moment of inertia $I = \mu R_0^2$ depends on the reduced mass μ of the two nuclei and is taken at the constant equilibrium internuclear separation $R = R_0$. By fixing R , no vibration and in particular no stretching during rotation is allowed. This is why it

6. Molecular Alignment

is called a *rigid rotor*. The solutions to this equation are the familiar *spherical harmonics* $Y(\theta, \phi) = Y_j^m(\theta, \phi)$. The eigenenergies

$$E_J = B_0 J(J + 1) \quad (6.1)$$

are independent of $M = -J, -J+1, \dots, J$ and therefore the J th state is $(2J+1)$ -fold degenerate. The *rotational constant* B_0 is defined in terms of the moment of inertia

$$B_0 = \frac{1}{2I}$$

and therefore specific to the molecule. It is the single characteristic input of the rigid rotor. Since it depends on the fixed internuclear distance R_0 it completely determines the rotational motion as long as the internuclear distance of the molecule can be approximated by its equilibrium distance. It differs in higher vibrational states. Also, when high rotational states J are excited additional higher-order terms need to be added to the energy (6.1), i.e. $E_J = B_0 J(J + 1) + D_0 J^2(J + 1)^2 + \dots$. This can be shown by introducing a centrifugal force via adding a corresponding potential. This extends the model to the *nonrigid rotor* which we are not concerned with in this work.

6.2.2. Nonresonant alignment of nonpolar linear molecules

There is quite extensive literature on molecular alignment available [98, 100–107] covering a wide range of different aspects on the subject. We are interested in alignment distributions during the action of the laser pulse, i.e. what is the probability that the molecular ensemble is aligned at a certain angle θ . The theory presented here can primarily be found in [98, 102] with background information from [107].

Multiple different processes of aligning molecules exist. In the case of high intensities (where perturbation theory is no longer applicable) one can distinguish between *resonant* and *nonresonant* alignment. In the first case the frequency of the driving field is set near the energy of an electronic or vibrational transition, i.e. Rabi oscillations are initiated. This produces rotational wave packets in the participating electronic or vibrational states which can ultimately lead to alignment (see e.g. [101]).

Our focus is on the nonresonant case, where the driving frequency is detuned from vibrational and electronic transitions and energy transfer takes place via Raman scattering. Under such conditions a nonpolar, homonuclear diatomic molecule experiences an interaction potential of the form

$$V_{\text{int}}(\theta, t) = -\frac{1}{2}E(t)^2(\Delta\alpha \cos^2(\theta) + \alpha_{\perp}) \quad (6.2)$$

with the aforementioned polarizability anisotropy $\Delta\alpha = \alpha_{\parallel} - \alpha_{\perp}$ and perpendicular polarizability α_{\perp} . The angle θ is measured between the internuclear axis and the electric field vector. We assume a linearly polarized field with amplitude $E(t) = E_0 f(t) \cos(\omega t)$ and pulse envelope $f(t)$. This contribution is of second-order in the electric field. For a molecule with a permanent

dipole moment a first-order potential of the form $-dE(t) \cos(\theta)$ with dipole moment d would be present.

If the pulse duration is much longer than the period of the carrier wave one usually uses an averaged potential instead of (6.2)

$$V_{\text{int}}^{\text{av}}(\theta, t) = -\frac{E_0^2 f(t)^2}{4} (\Delta\alpha \cos^2(\theta) + \alpha_{\perp})$$

which only contains the time-dependence of the pulse envelope $f(t)$. This expression is then used as an additional potential in the Schrödinger equation of the rigid rotor

$$i \frac{\partial |\psi(\theta, t)\rangle}{\partial t} = \left(B_0 \hat{J}^2 + V_{\text{int}}^{\text{av}}(\theta, t) \right) |\psi(\theta, t)\rangle, \quad (6.3)$$

where the values of the polarizabilities are taken at the equilibrium distance R_0 . In the nonrigid case the α 's depend on R . The solution of (6.3) is expanded in terms of field-free states

$$|\psi_{J_i M_i}\rangle(t) = \sum_{J \geq |M_i|} F_{J_i J}(t) |JM_i\rangle. \quad (6.4)$$

This accounts for the population of possibly many angular momentum eigenstates J . Since M is conserved in a linearly polarized field the expansion only includes states with the same magnetic quantum number $M = M_i$ as the initial rotational state. The initial angular momentum quantum number is denoted by J_i . Inserting the ansatz (6.4) into (6.3) and projecting onto field-free states gives a system of coupled equations for the coefficient functions $F_{J_i J}(t)$

$$i \frac{\partial F_{J_i J}(t)}{\partial t} = B_0 \left\{ (J(J+1) - f(t)^2 \omega_{\perp}) F_{J_i J}(t) - f(t)^2 \Delta\omega \sum_{J'} F_{J_i J'}(t) \langle J' M_i | \cos^2(\theta) | J M_i \rangle \right\} \quad (6.5)$$

where the polarizabilities have been rescaled $\omega_{\perp, \parallel} := \alpha_{\perp, \parallel} E_0^2 / 4B_0$. In addition, the orthonormality of the spherical harmonics was used $\langle J' M | J M \rangle = \delta_{J' J}$. The initial condition is $F_{J_i J}(t_0) = \delta_{J_i J}$.

The equations (6.5) are further simplified by taking into account that the matrix elements $\langle J' M_i | \cos^2(\theta) | J M_i \rangle$ take on nonvanishing values only for $J' = J - 2, J, J + 2$ [108]. We then arrive at

$$i \frac{\partial F_{J_i J}(t)}{\partial t} = -B_0 \left\{ f(t)^2 (\omega_{\perp} + \Delta\omega \Lambda_J^M) - J(J+1) F_{J_i J}(t) + \Delta\omega f(t)^2 \left[\Lambda_{J+}^M F_{J_i, J+2}(t) + \Lambda_{J-}^M F_{J_i, J-2}(t) \right] \right\} \quad (6.6)$$

with $\Lambda_{J, \pm}^M := \langle J \pm 2, M_i | \cos^2(\theta) | J M_i \rangle$ and Λ_J^M analogous with $J' = J$.

The system of equations (6.6) can be solved numerically, for details see section B.2.5 in the appendix. Once the coefficient functions $F_{J_i J}$ have been obtained the alignment distribution can be calculated. For an ensemble of molecules in thermodynamic equilibrium the system is

6. Molecular Alignment

initially in a mixed state of different $|J_i M_i\rangle$ with coefficients given by the Boltzmann distribution. Therefore, the final alignment distribution takes the form

$$\sigma(\theta, t) = \frac{1}{Z_r} \sum_{J_i} \mathcal{W}_{J_i} \sum_{M_i=-J_i}^{J_i} |\psi_{J_i M_i}(\theta, t)|^2 \quad (6.7)$$

with

$$\mathcal{W}_J = e^{-B_0 J(J+1)/k_B T}. \quad (6.8)$$

The temperature is given by T and k_B is Boltzmann's constant. The rotational partition function

$$Z_r = \sum_J (2J+1) e^{-B_0 J(J+1)/k_B T}$$

sums up all Boltzmann factors, including the degeneracy in terms of M , of the field-free rigid rotor.

Note that the rotational wave packets $\psi_{J_i M_i}(\theta, t)$ are normalized

$$\int_0^{2\pi} d\phi \int_0^\pi \sin(\theta) d\theta |\psi_{J_i M_i}(\theta, t)|^2 = 1,$$

with azimuthal angle ϕ .

The degree of alignment, as shown in Figure 6.1, is conventionally defined as the expectation value of the squared cosine

$$\langle\langle \cos^2(\theta) \rangle\rangle(t) = \frac{1}{Z_r} \sum_{J_i} \mathcal{W}_{J_i} \sum_{M_i=-J_i}^{J_i} \langle \psi_{J_i M_i} | \cos^2(\theta) | \psi_{J_i M_i} \rangle(t) \quad (6.9)$$

As will be shown in section 6.2.3, an additional statistical weight is needed to account for an unbalanced ratio of even and odd J states in the initial molecular ensemble. This imbalance stems from the nuclear spins of the constituent atoms of the molecule.

6.2.3. Nuclear spin statistics

Homonuclear diatomic molecules have a center of symmetry (inversion center) in the middle between the two nuclei. A rotation around that center of 180° may be seen as an exchange of both nuclei [109], given that the rest of the wave function is symmetric under such a rotation. In this case, the total wave function ψ_{total} (including the spin) has to fulfil the exchange symmetry condition, according to the Pauli principle, under rotation. This means a change of sign if the nuclei are fermions and no sign change in case of bosons. Writing ψ_{total}

$$\psi_{\text{total}} = \psi_{\text{pos}} \times \psi_{\text{spin}}$$

as a product of position and (total) spin wave functions, it becomes clear that the Pauli principle may impose different symmetry requirements on the rotational part of ψ_{pos} , depending on the total nuclear spin.

The hydrogen molecule H_2 is a good example to demonstrate this. The hydrogen nucleus, i.e. a single proton, is a fermion with a spin of $1/2$. Hence, ψ_{total} is antisymmetric under exchange of the nuclei. The total spin of both protons can take on the values 1 (parallel) or 0 (antiparallel). The former is called ortho-hydrogen and the latter para-hydrogen.

In case of ortho-hydrogen, the total spin function ψ_{spin} is symmetric under exchange of the nuclei. In the ground state, the electronic part of ψ_{pos} is symmetric under rotation. This forces the rotational part of ψ_{pos} to be antisymmetric and therefore to only contain states of odd quantum numbers J . Accordingly, in case of para-hydrogen, the rotational part is symmetric and thus only contains states with even-numbered J , because the spin function is antisymmetric.

A total spin of 1 can be realized by three different (symmetric) states (triplet states). In contrast, a total spin of 0 is only possible in a single (antisymmetric) state (singlet state). In thermodynamic equilibrium there are therefore three times as many states with total spin 1 than 0. This adds an additional statistical weight of $3/1$ in favor of odd-numbered J to the Boltzmann distribution in (6.7) and (6.9).

In general, for a molecule with inversion center and nuclear spin I , the ratio of statistical weights for symmetric and antisymmetric nuclear spin states, in thermodynamic equilibrium, is given by [109]

$$\frac{\text{symmetric}}{\text{antisymmetric}} = \frac{I + 1}{I}. \quad (6.10)$$

For hydrogen ($I = 1/2$) this gives the aforementioned ratio of $3/1$ in favor of ortho-hydrogen.

Of relevance to the present work is also the case of the heavier isotope deuterium D_2 . Here the nucleus is made up of a proton and neutron with a combined nuclear spin of $I = 1$. According to (6.10) the ratio is $2/1$ for symmetric nuclear spin states. Because of the bosonic nature of the nucleus, the total wave function is of positive symmetry under exchange of the nuclei. The electronic part of the position wave function is also of positive symmetry (as for H_2). This means that states with even-numbered J are more prevalent.

As a side note, the quarter-period revivals in the example of impulsive alignment of nitrogen N_2 (in the left panel of Figure 6.1) are a consequence of such a statistical imbalance and are absent if equal weights are chosen. The nuclear spin of nitrogen is $I = 1$, which ultimately leads to the same ratio as for deuterium D_2 .

In the end the total alignment distribution (6.7) is modified to

$$\sigma(\theta, t) = \frac{1}{Z_r} \sum_{J_i} \mathcal{G}_{J_i} \mathcal{W}_{J_i} \sum_{M_i=-J_i}^{J_i} |\psi_{J_i M_i}(\theta, t)|^2. \quad (6.11)$$

with additional weights \mathcal{G}_J . The rotational partition function Z_r is modified accordingly. The same modification of the weighting also applies to the degree of alignment in (6.9).

6. Molecular Alignment

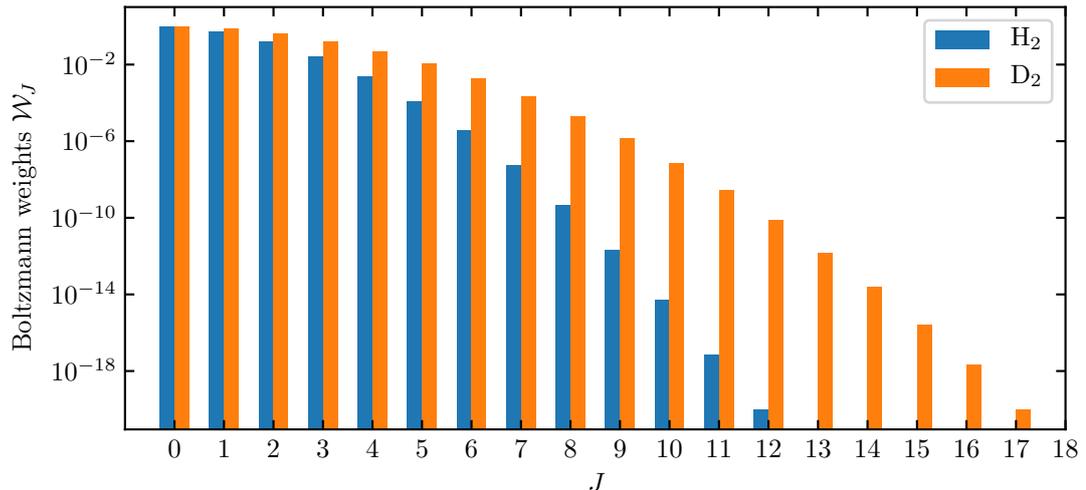


Figure 6.2.: Boltzmann weights \mathcal{W}_J for H_2 and D_2 at a temperature of 293.15 K

6.2.4. Case of Hydrogen

In this section we want to study in a little more detail the case of the hydrogen molecule H_2 and its heavier isotope D_2 . We are interested in the alignment distribution (6.11). As was explained in the previous section 6.2.3 we have to account for the nuclear spin which introduces the following isotope-dependent statistical weights

$$\mathcal{G}_J^{\text{H}_2} = \begin{cases} 1, & J \text{ even} \\ 3, & J \text{ odd} \end{cases} \quad \text{and} \quad \mathcal{G}_J^{\text{D}_2} = \begin{cases} 2, & J \text{ even} \\ 1, & J \text{ odd} \end{cases}.$$

The rotational constants are [97]

$$B_0^{\text{H}_2} = 60.84 \text{ cm}^{-1} \quad \text{and} \quad B_0^{\text{D}_2} = 30.44 \text{ cm}^{-1}.$$

According to the Boltzmann coefficients (6.8) the ensemble temperature T has critical influence on the total alignment distribution. The contribution of higher rotational states grows with increasing temperature. In the limit of a cold ensemble $T \rightarrow 0$ only the lowest rotational state $J = 0$ is initially populated. Figure 6.2 shows the Boltzmann weights for H_2 and D_2 at room temperature of about 293 K. The effect on the alignment distribution can be seen in Figure 6.3 which compares the results for both isotopes at two different intensities and temperatures at the peak of a 30 fs laser pulse of sech-shape (see Figure description).

The results shown in Figure 6.3 can be intuitively understood. First, all curves have their maximum at $\theta = 0, \pi$ (both are equivalent orientations for symmetry reasons in diatomic molecules). This is the orientation along the electric field vector. Second, the heavy isotope D_2 experiences less alignment than H_2 because of the higher moment of inertia which requires more torque to gain a certain rotational energy in a fixed time span. Third, a higher intensity leads to a more pronounced alignment of both isotopes since the field exerts a larger torque on the molecules. Equivalently, the interaction potential (6.2) has a deeper well. Last, a lower

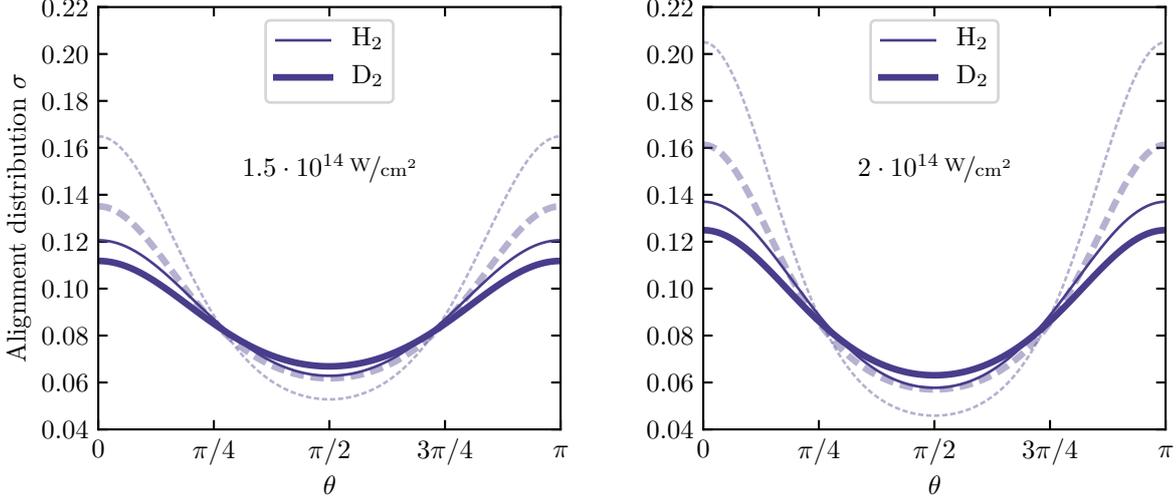


Figure 6.3.: Alignment distribution σ of H_2 (thin curves) and D_2 (bold curves) at the peak of a pulse with electric field envelope $\text{sech}(2 \ln(1 + \sqrt{2})t/\tau)$ with $\tau = 30$ fs. The left panel shows the distribution for the low intensity $1.5 \cdot 10^{14} \text{ W/cm}^2$ and the right panel for the high intensity $2 \cdot 10^{14} \text{ W/cm}^2$. Additionally, two different temperatures are compared, 10^{-15} K (low contrast, dashed) and 293.15 K (high contrast, solid).

temperature leads to more alignment. Because more molecules are initially in the same state with low rotational energy, it is more likely to align a larger portion of them.

We can conclude that, for the particular intensities studied here, at low temperatures there is a significant difference in alignment between the two isotopes. This difference decreases with increasing temperature.

6.3. Use in autocorrelation function

The general approach to including the molecular alignment distribution $\sigma(\theta, t)$ into the autocorrelation is by considering it as a weighting function for the angle dependence that originates from the recombination matrix element. For a linearly polarized electric field the angle-averaged autocorrelation, with the ionization element set identically to one, $d_{\text{ion}} \equiv 1$, and the recombination element given by the angle dependence as resulting from a LCAO approximation, $d_{\text{rec}} \approx \cos(kR \cos(\theta)/2)$, takes the form

$$C(\omega) = 2\pi \int_0^\pi d\theta \sin(\theta) \sigma(\theta, t_s(\omega)) C_\theta(\omega) \quad (6.12)$$

where the factor 2π comes from the integration over the azimuthal angle. Note that such a constant factor is not relevant for the ratio of autocorrelations. The autocorrelation for a specific angle θ is

$$C_\theta(\omega) = \int dR \cos\left(\frac{k(\omega)R \cos(\theta)}{2}\right) \chi_0^*(R) U_R^+(\tau_s(\omega)) \chi_0(R).$$

6. Molecular Alignment

The electron excursion time $\tau_s(\omega) = t_s(\omega) - t'_s(\omega)$ is determined by the saddle-point ionization and recombination times $t'_s(\omega)$ and $t_s(\omega)$, respectively. For the return momentum we use the relation $k(\omega) = \sqrt{2(\omega - I_p)}$, i.e. no heuristic modification as in chapter 5. The angle θ is measured between the internuclear axis and the electric field vector. The direction of the electron return momentum is taken to coincide with the electric field direction. χ_0 is the vibrational ground state of the neutral hydrogen molecule H_2 and U_R^+ is the time-evolution operator in the ground-state potential energy curve of the ion H_2^+ .

The time-dependence of $\sigma(\theta, t)$ presents a problem in expression (6.12). The saddle-point times are complex, which means the values of $\sigma(\theta, t)$ need to be known for complex arguments t . While there might be a continuation into the complex plane, the fact that $\sigma(\theta, t)$ is only known numerically makes this a formidable task. Taking the real part of the times is an option, but it is not clear if this is appropriate. Another approach is to assume that the major contribution to the macroscopic harmonic signal comes from the maximum of the pulse envelope. This is questionable given that the envelope may be an important parameter in experimental setups (see chapter 8). However, when the autocorrelation is evaluated within a single cycle of full amplitude, it is inherently agnostic with regard to the overall pulse shape. It is therefore plausible to choose the maximum of the envelope t_{\max} as the relevant point in time for alignment, as has been done for example in [29]. This approach implies that there are trajectories which are most relevant in the sense that they have recombination times close to t_{\max} and therefore contribute the most. This enables us to use the alignment distribution at that time, $\sigma_{\max}(\theta) := \sigma(\theta, t_{\max})$, to estimate the influence of the alignment on the harmonic signal. Expression (6.12) then reads

$$C(\omega) = 2\pi \int_0^\pi d\theta \sin(\theta) \sigma_{\max}(\theta) C_\theta(\omega). \quad (6.13)$$

In practice it is convenient to approximate $\sin(\theta)\sigma_{\max}(\theta)$ by a fit of the form

$$\sin(\theta)\sigma_{\max}(\theta) \approx \sum_{\substack{n=1 \\ n \text{ odd}}}^N \lambda_n \sin(n\theta) + \sum_{\substack{n=1 \\ n \text{ even}}}^N \mu_n \cos(n\theta) - \sum_{\substack{n=1 \\ n \text{ even}}}^N \mu_n. \quad (6.14)$$

This has the advantage that if there are no dependencies of χ_0 and U_R^+ on the angle θ , the complete angle average

$$\eta(\omega, R) := \int_0^\pi d\theta \sin(\theta) \sigma_{\max}(\theta) \cos\left(\frac{k(\omega)R \cos(\theta)}{2}\right) \quad (6.15)$$

can be evaluated analytically. The autocorrelation in this case

$$C(\omega) = 2\pi \int dR \eta(\omega, R) \chi_0^*(R) U_R^+(\tau_s(\omega)) \chi_0(R)$$

is then easy to work with since $\eta(\omega, R)$ is readily evaluated with the fit-parameters λ_n, μ_n as input. These parameters are determined once for a given distribution $\sigma_{\max}(\theta)$. Even if the analytical evaluation of $\eta(\omega, R)$ is not possible because of further angle dependencies, it is still beneficial to use an analytic expression for $\sin(\theta)\sigma_{\max}(\theta)$. As for the number of terms necessary in (6.14), a number of $N = 3$ turns out to be adequate. See appendix A.5 for a more detailed description.

In case of a constant alignment distribution, i.e. a randomly aligned ensemble of molecules, the function η simplifies to (see appendix section A.3)

$$\begin{aligned}\eta_{\text{random}}(\omega, R) &\propto \int_0^\pi d\theta \sin(\theta) \cos\left(\frac{k(\omega)R \cos(\theta)}{2}\right) \\ &\propto \frac{\sin(k(\omega)R/2)}{k(\omega)R/2}.\end{aligned}\tag{6.16}$$

7. Stark Effect

It is well known that an atomic or molecular system experiences a modification of its eigenenergies and -states when subject to an external electric field. This phenomenon is called the *Stark effect* or *Stark shift*. In high-harmonic generation, the electric field of the strong laser pulse may have significant influence on the eigenstates of the system. For example, the ionic BO potential is distorted by the laser during the continuum travel of the electron and therefore changes the nuclear motion compared to the field-free potential. This in turn changes the time-dependent vibrational autocorrelation, see chapter 3.

This chapter deals with the theory of the Stark effect and its application to the hydrogen molecule and hydrogen molecular ion. It is the foundation for the study of experimental harmonic ratios that we are concerned with in chapter 8.

7.1. Theory

7.1.1. Time-independent perturbation theory

The modification of the eigenenergies due to the electric field are usually described using standard nondegenerate time-independent perturbation theory. In general, a perturbing potential W is added to the unperturbed Hamiltonian H_0 [110]

$$H(\lambda) = H_0 + \lambda W,$$

where the parameter λ measures the strength of the perturbation. This introduces corrections to the eigenenergy $E_n^{(0)}$ of a particular nondegenerate state $|\phi_n\rangle$ of H_0 , given by

$$E_n(\lambda) = E_n^{(0)} + \lambda E_n^{(1)} + \lambda^2 E_n^{(2)} + O(\lambda^3)$$

with

$$E_n^{(1)} = \langle \phi_n | W | \phi_n \rangle \tag{7.1}$$

$$E_n^{(2)} = \sum_{m \neq n} \frac{|\langle \phi_m | W | \phi_n \rangle|^2}{E_n^{(0)} - E_m^{(0)}}. \tag{7.2}$$

7. Stark Effect

7.1.2. DC Stark shift of energies

In the case of a constant external electric field the perturbation potential W is given by the dipole interaction

$$\lambda W = -\mathbf{F} \cdot \mathbf{d}$$

with electric field \mathbf{F} . The magnitude of \mathbf{F} plays the role of the parameter λ . The atomic or molecular electric dipole moment is given by \mathbf{d} . [111, 112]

According to (7.1) the *first-order* Stark shift is

$$E_n^{(1)} = -\mathbf{F} \cdot \langle \phi_n | \mathbf{d} | \phi_n \rangle.$$

This means that atoms and molecules with a permanent dipole moment $\boldsymbol{\mu} := \langle \phi_n | \mathbf{d} | \phi_n \rangle$ experience a linear Stark shift. Using (7.2) the *second-order* Stark shift can be written as

$$E_n^{(2)} = -\mathbf{F} \cdot \left(-\sum_{m \neq n} \frac{\langle \phi_m | \mathbf{d} | \phi_n \rangle \otimes \langle \phi_n | \mathbf{d} | \phi_m \rangle}{E_n^{(0)} - E_m^{(0)}} \right) \mathbf{F} \quad (7.3)$$

which can be interpreted as the electric field acting on the *induced* dipole moment $\alpha \mathbf{F}$. The *polarizability tensor*

$$\alpha = -2 \sum_{m \neq n} \frac{\langle \phi_m | \mathbf{d} | \phi_n \rangle \otimes \langle \phi_n | \mathbf{d} | \phi_m \rangle}{E_n^{(0)} - E_m^{(0)}} \quad (7.4)$$

contains the information about how the system is polarized when the inducing electric field points in a certain direction. In total the Stark shift of the eigenenergy $E_n^{(0)}$ up to second order reads

$$\begin{aligned} E_n(\mathbf{F}) &= E_n^{(0)} - \boldsymbol{\mu} \cdot \mathbf{F} - \frac{1}{2} \alpha \mathbf{F} \cdot \mathbf{F} + O(\mathbf{F}^3) \\ &= E_n^{(0)} - \sum_i \mu_i F_i - \frac{1}{2} \sum_{ij} \alpha_{ij} F_i F_j + O(F_i F_j F_k) \end{aligned} \quad (7.5)$$

7.1.3. AC Stark shift of energies

If the external electric field is not constant but a monochromatic wave it is possible to consider the *AC Stark shift* (also *dynamic Stark shift*). It takes the frequency of the field into account, i.e. the shifted energies depend not only on the electric field strength but also on its frequency. One can distinguish between the *resonant* and *nonresonant* case depending on whether the frequency matches the transition energy between the respective atomic or molecular states. The shift is time-independent and can be considered as an averaged effect [113].

There are generally two ways to tackle this problem. The first uses a semiclassical approach where the electric field is described classically and the relevant equations are solved via a

Floquet method. The second involves a quantized electric field and is the approach that we choose to discuss in this work. We proceed to follow the derivations published in [114, 115]. Another good reference is [116].

Because the field is quantized the total state of the system is a product of the state of the atom or molecule (henceforth just called atom) and the state of the field. The total Hamiltonian takes the form

$$H = H_0 + H_{\text{int}}.$$

where H_0 includes the Hamiltonians of the atom and the field, without the interaction between the two, which is completely contained in H_{int} and is given by the dipole interaction

$$H_{\text{int}} = -\mathbf{d} \cdot \mathbf{F}(\mathbf{r}).$$

The dipole moment operator is named \mathbf{d} . The electric field $\mathbf{F}(\mathbf{r})$ is taken in plane-wave quantization and as a single mode of frequency ω

$$\mathbf{F}(\mathbf{r}) = i\sqrt{\frac{2\pi\omega}{V}}(ae^{i\mathbf{k}\cdot\mathbf{r}} - a^\dagger e^{-i\mathbf{k}\cdot\mathbf{r}})\mathbf{e}.$$

The creation- and annihilation operators are denoted by a^\dagger and a , respectively, \mathbf{k} is the wave and \mathbf{e} the polarization vector. The quantization volume of the field is given by V .

Let us introduce the atomic states $|m\rangle$ and the photon-number states $|n\rangle$, the product states $|m; n\rangle := |m\rangle \otimes |n\rangle$ give the eigenstates of H_0

$$H_0|m; n\rangle = (E_m + n\omega)|m; n\rangle.$$

The energy of the atomic state $|m\rangle$ is given by E_m and the energy of n photons is simply $n\omega$.

The interaction H_{int} only directly couples atomic states of different symmetry because the dipole moment operator is an odd function in position space. With ‘‘directly’’ it is meant that states of the same symmetry are coupled only by multiple interactions. In case of the atomic states a chain of interactions, each coupling states of different symmetry, is required to give a total coupling of states with the same symmetry. In addition, only photon states that differ by a single photon are directly coupled. This follows from the actions of the ladder operators on the photon states $a^\dagger|n\rangle = \sqrt{n+1}|n+1\rangle$ and $a|n\rangle = \sqrt{n}|n-1\rangle$. In summary, the only nonvanishing matrix elements of H_{int} are

$$\begin{aligned} H_{mm';n}^+ &= \langle m; n+1 | H_{\text{int}} | m'; n \rangle = -i\sqrt{\frac{2\pi(n+1)\omega}{V}} \langle m | \mathbf{d} \cdot \mathbf{e} | m' \rangle e^{-i\mathbf{k}\cdot\mathbf{r}} \\ H_{mm';n}^- &= \langle m; n-1 | H_{\text{int}} | m'; n \rangle = -i\sqrt{\frac{2\pi n\omega}{V}} \langle m | \mathbf{d} \cdot \mathbf{e} | m' \rangle e^{i\mathbf{k}\cdot\mathbf{r}} \end{aligned}$$

where the atomic states corresponding to m and m' have different symmetry.

7. Stark Effect

Nonresonant case Considering H_{int} as a perturbation, we can apply time-independent perturbation theory. The first-order correction (7.1) vanishes because there is no coupling between a state and itself. For the second-order correction (7.2) for the energy $E_{m;n}$ of the state $|m;n\rangle$ holds

$$E_{m;n}^{(2)} = - \sum_{m'} \left[\frac{|H_{m'm;n}^+|^2}{E_{m'} - E_m + \omega} + \frac{|H_{m'm;n}^-|^2}{E_{m'} - E_m - \omega} \right] \quad (7.6)$$

This expression can be a little simplified. For large $n \gg 1$ it holds that $\sqrt{n+1} \approx \sqrt{n}$. This leads to

$$|H_{mm';n}^+|^2 \approx |H_{mm';n}^-|^2 = \frac{2\pi n \omega}{V} |\langle m | \mathbf{d} \cdot \mathbf{e} | m' \rangle|^2 \quad (7.7)$$

$$= \frac{F_0^2}{4} |\langle m | \mathbf{d} \cdot \mathbf{e} | m' \rangle|^2 \quad (7.8)$$

where in the second step $n\omega/V$ was taken to be the energy density of the electric field. In atomic units it equals $F_0^2/8\pi$ with electric field strength F_0 . Expression (7.6) then reduces to

$$E_{m;n}^{(2)} = -\frac{F_0^2}{2} \sum_{m'} |\langle m | \mathbf{d} \cdot \mathbf{e} | m' \rangle|^2 \frac{E_{m'} - E_m}{(E_{m'} - E_m)^2 - \omega^2}. \quad (7.9)$$

It can be seen that (7.9), and also the nonsimplified expression (7.6), cover only nonresonant field frequencies ω . If $\omega \approx E_{m'} - E_m$ the coupling between the states of energy E_m and $E_{m'}$ is no longer a small perturbation and this approach breaks down.

In case of low field frequencies ω , i.e. if $\omega^2 \ll (E_{m'} - E_m)^2$ for all m' , the expression should go over into the DC Stark shift. For $\omega = 0$ and $\mathbf{F}_0 := F_0 \mathbf{e}$

$$E_{m;n}^{(2)} = -\frac{1}{2} \mathbf{F}_0 \cdot \left(\sum_{m'} \frac{\langle m | \mathbf{d} | m' \rangle \otimes \langle m' | \mathbf{d} | m \rangle}{E_{m'} - E_m} \right) \mathbf{F}_0.$$

The sum in parentheses equals half of the polarizability tensor, $\alpha/2$. For this, note that the energies in the difference in the denominator are interchanged compared to (7.4). Accordingly

$$E_{m;n}^{(2)} = -\frac{1}{4} \mathbf{F}_0 \cdot \alpha \mathbf{F}_0, \quad (7.10)$$

which means that we arrive at half of the second-order DC Stark shift (compare expression (7.5)).

Resonant case Let us assume that the field frequency is close to the transition frequency between two atomic states $|1\rangle$ and $|2\rangle$, i.e. $\omega \approx E_2 - E_1$, with $E_2 > E_1$. Other atomic states may also be involved, but their coupling should be negligible in comparison. This holds true as long as their transition energies are not close to ω .

Since perturbation theory is not applicable we have to resort to the direct diagonalization of the total Hamiltonian $H_0 + H_{\text{int}}$. The corresponding matrix in the subspace spanned by $|m;n\rangle$

7. Stark Effect

The Hamiltonian of an electron interacting with two frozen-in-place nuclei with internuclear distance R and linearly polarized electric field of the laser $F(t)$ takes the form

$$H_R = T + V_R(z) + zF(t)$$

where T is the kinetic energy of the electron and V_R the potential due to the nuclei. The motion of the electron is restricted to the direction z along the internuclear axis and the direction of the field $F(t)$ is aligned along that axis as well. This means that we are considering the *parallel* Stark shift where the polarization of the molecule takes place along the internuclear axis. We expand the state $|\psi_R\rangle$ in terms of the two energetically lowest field-free eigenstates $|\psi_g^R\rangle$ and $|\psi_u^R\rangle$

$$|\psi_R\rangle = c_g(R)|\psi_g^R\rangle + c_u(R)|\psi_u^R\rangle.$$

The left side of the Schrödinger equation

$$H_R|\psi_R\rangle = E_R|\psi_R\rangle$$

is

$$H_R|\psi_R\rangle = c_g(R)\left(E_g(R) + zF_0\right)|\psi_g^R\rangle + c_u(R)\left(E_u(R) + zF_0\right)|\psi_u^R\rangle$$

with the field-free BO potentials $E_g(R)$ and $E_u(R)$, i.e. $(T + V_R)|\psi_{g,u}^R\rangle = E_{g,u}(R)|\psi_{g,u}^R\rangle$. Projection onto $|\psi_g^R\rangle$ and $|\psi_u^R\rangle$ yields two coupled equations for the coefficients $c_g(R)$ and $c_u(R)$

$$\begin{aligned} c_g(R)E_g(R) + c_u(R)F(t)\langle\psi_g^R|z|\psi_u^R\rangle &= E_Rc_g(R) \\ c_u(R)E_u(R) + c_g(R)F(t)\langle\psi_u^R|z|\psi_g^R\rangle &= E_Rc_u(R) \end{aligned}$$

which can be written as a vector equation

$$\begin{pmatrix} E_g(R) & F(t)D(R) \\ F(t)D(R)^* & E_u(R) \end{pmatrix} \begin{pmatrix} c_g(R) \\ c_u(R) \end{pmatrix} = E_R \begin{pmatrix} c_g(R) \\ c_u(R) \end{pmatrix}.$$

The dipole-transition matrix element $D(R) := \langle\psi_g^R|z|\psi_u^R\rangle$ is real-valued, i.e. $D(R) = D(R)^*$ where the asterisk denotes the complex-conjugate. The eigenvalues of the above matrix are

$$E_{\pm}^{\text{DC}}(R, F(t)) = \frac{E_g(R) + E_u(R)}{2} \pm \frac{1}{2}\sqrt{(E_g(R) - E_u(R))^2 + 4F(t)^2D(R)^2}. \quad (7.11)$$

This expression gives the Stark-shifted potential energy curves in terms of the field-free potentials $E_g(R)$ and $E_u(R)$, the electric field $F(t)$ and the matrix element $D(R)$. The modulus of the latter can be approximated by the following expression [117]

$$|D(R)| = 0.4e^{-R} + \frac{R}{2}. \quad (7.12)$$

A comparison of this approximation with exact values taken from [118] can be seen in Figure 7.1.

For small values of the electric field strength $F(t)$, specifically

$$F(t)^2 \ll (E_g(R) - E_u(R))^2/4D(R)^2,$$

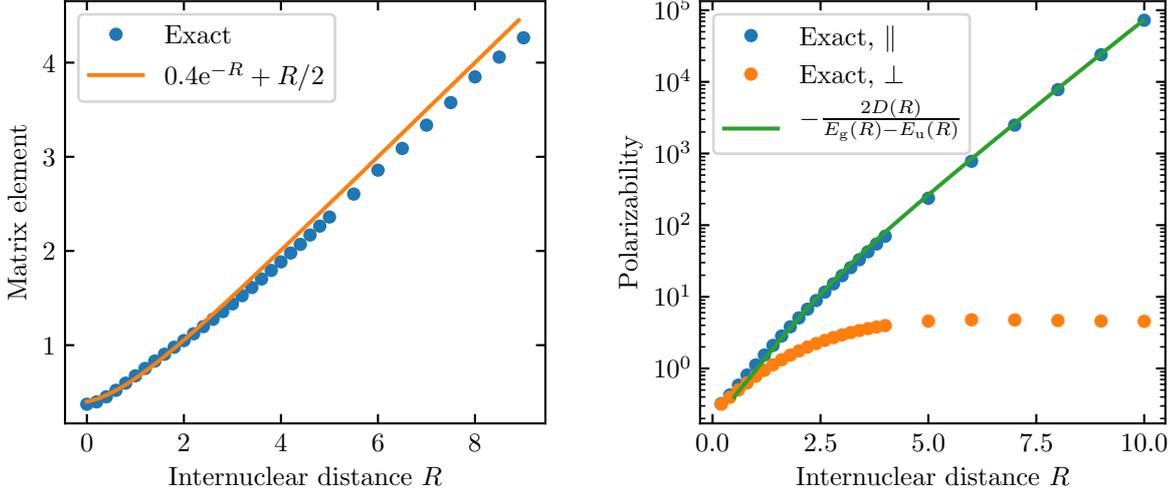


Figure 7.1.: Comparison of **Left:** exact [118] and approximated (7.12) dipole-transition matrix element $D(R)$. **Right:** exact parallel and perpendicular polarizability [119] and $\alpha_{\parallel}^+(R)$ (7.15).

we expect expression (7.11) to approach the results from perturbation theory (7.5) (see section 7.1.1). Expanding the square-root in (7.11) in a Taylor-series to first-order yields

$$\begin{aligned} E_{\pm}^{\text{DC}}(R, F(t)) &\approx \frac{E_g(R) + E_u(R)}{2} \pm \frac{|E_g(R) - E_u(R)|}{2} \left(1 + \frac{2F(t)^2 D(R)^2}{(E_g(R) - E_u(R))^2} \right) \\ &= \frac{E_g(R) + E_u(R) \pm (E_u(R) - E_g(R))}{2} \pm \frac{D(R)^2}{E_u(R) - E_g(R)} F(t)^2. \end{aligned} \quad (7.13)$$

In the second line we made use of the fact that $E_u(R) > E_g(R)$ for all R and therefore $|E_g(R) - E_u(R)| = E_u(R) - E_g(R)$.

From expression (7.13) we see that there is no first order contribution in the electric field. We are interested in the Stark shift of the ground-state potential curve $E_g(R)$

$$E_{-}^{\text{DC}}(R, F(t)) \approx E_g(R) - \frac{1}{2} \alpha_{\parallel}^+(R) F(t)^2 \quad (7.14)$$

with parallel polarizability

$$\alpha_{\parallel}^+(R) = -\frac{2D(R)^2}{E_g(R) - E_u(R)} \quad (7.15)$$

which has the same form as in (7.4). It agrees well with values from [119], see Figure 7.1.

An example of a Stark-shifted potential curve is shown in Figure 7.2 for an electric field strength F_0 that corresponds to an intensity of $1.5 \cdot 10^{14} \text{ W/cm}^2$. It differs significantly from the field-free curve. The asymptotic behaviour for large R is no longer constant and for this particular F_0 the minimum resembles a saddle point. The Taylor-expanded expression (7.14) is accurate only up to approximately 2.5. For larger distances the coupling between the two states becomes

7. Stark Effect

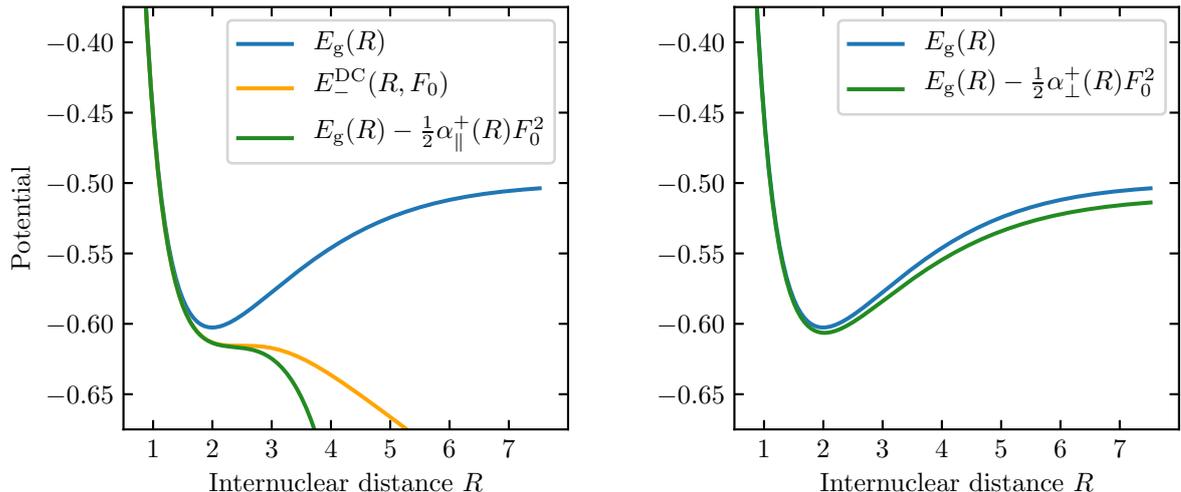


Figure 7.2.: Stark-shifted ground-state potential energy curves of H_2^+ for an electric field strength F_0 corresponding to an intensity of $1.5 \cdot 10^{14} \text{ W/cm}^2$. **Left:** Parallel alignment **Right:** Perpendicular alignment. The values for $\alpha_{\pm}^+(R)$ are taken from [119].

too large (see Figure 7.1) and the dipole interaction is no longer a small perturbation. The matrix-approach is better suited to describe the Stark shift for large internuclear distances.

For lower intensities the minimum survives and is bounded by a tunnel barrier while for larger intensities the potential is practically only a falling slope. Figure 7.3 shows the potentials for different intensities and for a wider range of internuclear distances.

Ionization potential The ionization potential $I_p = V_{\text{BO}}^+(R_0) - E_0$ depends on the potential energy curve of the ion V_{BO}^+ and therefore is dependent on the DC Stark shift. E_0 and R_0 are the ground-state energy and equilibrium distance of the neutral (field-free) molecule H_2 . We will study the influence of the parallel shift on I_p , because the perpendicular shift is negligible in comparison (see next section 7.2.2).

The largest occurring shift during the time-dependent electric field $F(t)$ happens at the field maximum F_0 . Hence, we can use F_0 to determine an upper bound for the shift induced by $F(t)$. In this regard, we define the DC shifted ionization potential analogously to the field-free one

$$I_p^{\text{DC}} = V_{\text{BO}}^{+\text{DC}}(R_0) - E_0. \quad (7.16)$$

The DC shifted ground state potential energy curve of the ion is $V_{\text{BO}}^{+\text{DC}}(R) = E_-^{\text{DC}}(R, F_0)$, expression (7.11). Since both isotopes H_2^+ and D_2^+ have the same potential energy curve, the DC shift, and therefore the change in ionization potential due to it, is independent of the isotope.

In the left panel of Figure 7.4 we plot I_p^{DC} of H_2 as a function of orientation θ and intensity I of the electric field. The picture shows the expected qualitative behaviour. Since we neglect the perpendicular component, the shift is zero at $\theta = \pi/2$ and thus $I_p^{\text{DC}} = I_p$. Trivially, the

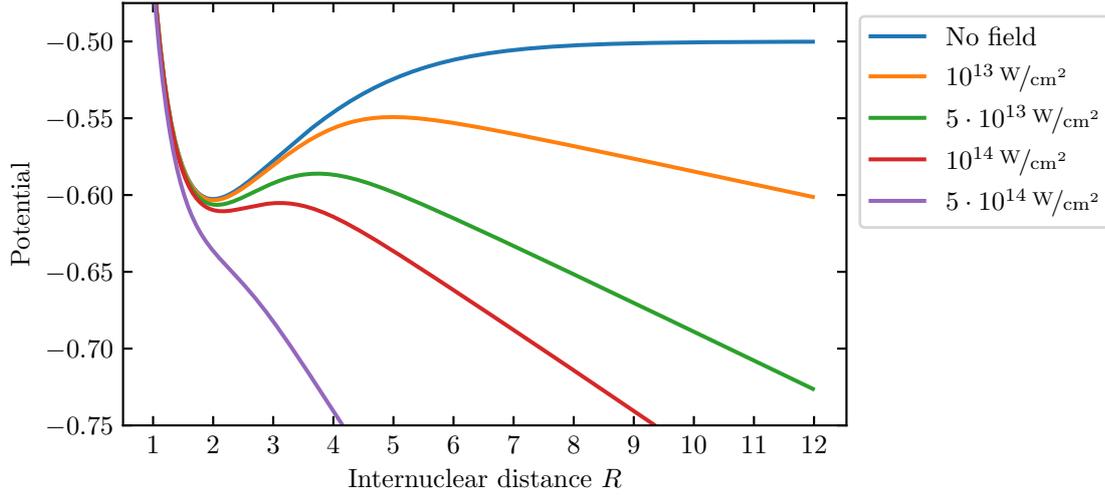


Figure 7.3.: Parallel Stark-shifted ground-state potential energy curves of H_2^+ for a range of different electric field strengths corresponding to the given intensities.

shift vanishes for zero intensity as well. It is only nonzero if the electric field has a parallel component and the greatest deviation of I_p^{DC} from I_p occurs for parallel alignment. It holds that $I_p^{\text{DC}} < I_p$ because the ionic potential curve is distorted downwards. This can be seen for example in Figure 7.3. We highlight the values for the intensities 1.5 and $2 \cdot 10^{14} \text{ W/cm}^2$ for which we have experimental harmonic ratios (see section 8). Additionally, the higher intensity $4 \cdot 10^{14} \text{ W/cm}^2$ is pointed out for comparison as well. The relative change in I_p

$$\delta I_p^{\text{DC}} = \frac{I_p^{\text{DC}} - I_p}{I_p} \quad (7.17)$$

for these three intensities is plotted in the right panel. The relative change is less than 2% and should therefore be negligible even for the high intensity $4 \cdot 10^{14} \text{ W/cm}^2$. But because the shift is approximately quadratic in the electric field strength F_0 , see expression (7.14), it becomes not only greater with increasing F_0 , but also changes more rapidly with it. This means that the change in I_p will quickly become nonnegligible for greater intensities.

7.2.2. Perpendicular DC Stark shift

Figure 7.1 also shows the perpendicular polarizability of H_2^+ , i.e. when the electric field vector is perpendicular to the internuclear axis. It has smaller values than the parallel polarizability, especially for large internuclear distances where the difference between the two amounts to several orders of magnitude.

This different behaviour can be understood by considering the definition of the polarizability as the ratio of the induced dipole moment and the inducing electric field. For parallel alignment it is easy to create a large separation of positive and negative charges within the molecule when the electron density is shifted towards one nuclei. It therefore grows with increasing internuclear

7. Stark Effect

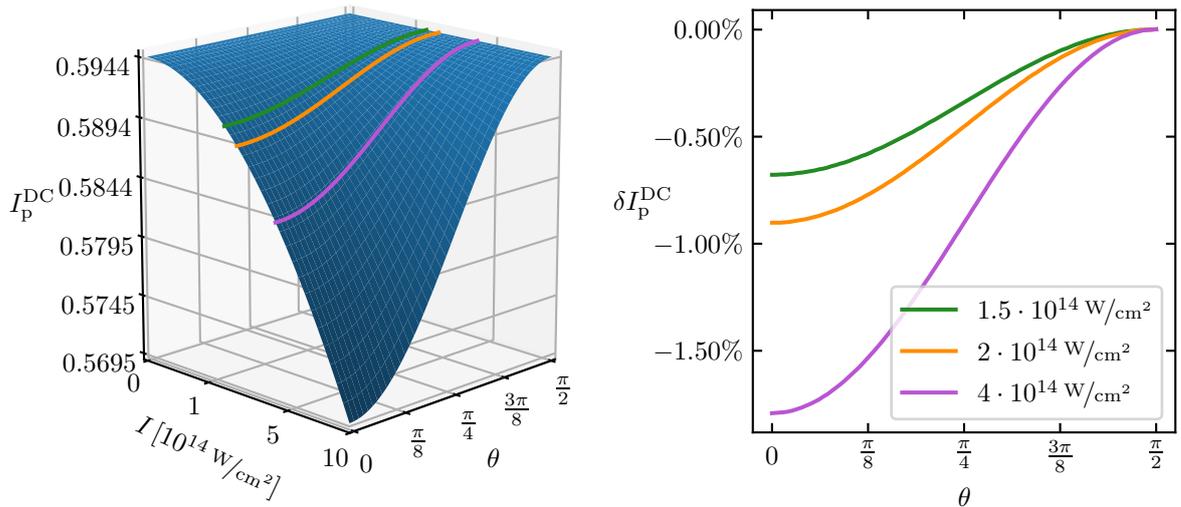


Figure 7.4.: **Left:** Dependence of the DC shifted ionization potential I_p^{DC} of H_2 on the field orientation θ and intensity I . The lines mark the intensities 1.5 (green), 2 (orange) and $4 \cdot 10^{14} \text{ W/cm}^2$ (violet). **Right:** Relative change δI_p^{DC} as a function of θ for the three intensities highlighted in the left panel.

distance. For perpendicular alignment the distance between the nuclei is of less importance for charge separation and a change in distance has less impact the higher that distance is.

An example of the second-order perpendicular Stark shift is shown in Figure 7.2. While the parallel Stark shift changes the overall shape of the potential the perpendicular effect has only little influence. The position of the minimum is slightly shifted to lower energy and larger internuclear distance. The constant asymptotic character for large R of the field-free potential approximately persists with a lower value. This can be seen from the nearly constant value of the perpendicular polarizability as shown in Figure 7.1.

For a specific angle θ between the electric field vector and the internuclear axis the parallel Stark shift will have significantly more influence on the potential than the perpendicular counterpart. For nuclear dynamics taking place within the potential well it should therefore be acceptable to neglect the perpendicular Stark shift. An angle dependence can then be simply taken into account by multiplying the electric field strength $F(t)$ with a factor $\cos(\theta)$ in expression (7.11). Hence, the potential energy curve acquires a time- and angle-dependence.

7.3. Hydrogen molecule

In this section we want to study the influence of the Stark effect on the vibrational ground state of the neutral hydrogen molecule H_2 . This is the initial state for the nuclear dynamics taking place in H_2^+ , see section 2.2.1. In the ion, we calculate the DC Stark shift with a time-dependent electric field to include the specific time-dependence of the potential energy curve that influences the vibrational dynamics. In contrast, we calculate the AC Stark shift for the neutral molecule, because its ground state should be less sensitive to the rapid oscillations of the electric field

that lead to small shifts of the potential minimum in Figure 4.1.

7.3.1. AC Stark shift

First we want to check whether the laser frequency requires a nonresonant matrix diagonalization or if the perturbation expression (7.9) can be used. The typical wavelength of the driving laser in HHG is 800 nm which corresponds to an angular frequency of $\omega_{800} \approx 0.05695$. The lowest electronic singlet state in terms of energy above the ground state is $B^1\Sigma_u^+ 2p\sigma$ (or $1^1\Sigma_u^+ 2p\sigma$ in the notation of [77]). We will denote this state by B and the ground state by X in the following. The minimum energy difference

$$E_{BX} = \min\{E_B(R) - E_X(R) : R \geq 0\} \\ \approx 0.2807$$

lies above ω_{800} . Note that this is the smallest energy difference that can occur between the ground state and a higher singlet state. In particular the ratio

$$\frac{\omega_{800}^2}{E_{BX}^2} \approx 4.1\% \quad (7.18)$$

shows that ω_{800} is nowhere close to the energy differences. It should therefore be adequate to apply the theory for the nonresonant case.

Another consequence of the low ratio in (7.18) is that we can approximate the AC shift by the DC shift, see equation (7.10) and the explanations in that section. This has the advantage that we only need the polarizabilities $\alpha_{\parallel}(R)$ and $\alpha_{\perp}(R)$ which can be found in the literature [120,121]. Otherwise all potential energy curves and dipole-transition matrix elements of excited states giving significant contributions in the sum of (7.9) would need to be known. While this is without difficulty in the ion H_2^+ , where the major contribution comes from the coupling between the ground state $1s\sigma_g$ and only one excited state $2p\sigma_u$, the situation is more complicated in H_2 , as we will see in the following.

In the literature one can find potential energy curves and transition elements with the ground state for some Σ_u and Π_u states [77, 78, 122]. Because of the symmetry of Σ orbitals the only nonvanishing component of the transition element for $X \rightarrow \Sigma_u$ is in the direction parallel to the internuclear axis. If we set the z -axis along the internuclear axis and call the transition element M , this means that only M_z is nonzero. With the same reasoning applied to the symmetry properties of Π orbitals, the only nonvanishing component for $X \rightarrow \Pi_u$ transitions, in case of nonnegative angular momentum projection along z , is $M_+ = (M_x + iM_y)/\sqrt{2}$, while both $M_- = (M_x - iM_y)/\sqrt{2}$ and M_z are equal to zero. The coupling with the Π_u states therefore yields perpendicular contributions. Hence, the parallel and perpendicular polarizabilities can be written as

$$\alpha_{\parallel}^{\text{PT}} = -2 \sum_{\Sigma_u} \frac{|M_z|^2}{E_X - E_{\Sigma_u}} \quad \text{with} \quad M_z = \langle \Sigma_u | d_z | X \rangle \\ \alpha_{\perp}^{\text{PT}} = -2 \sum_{\Pi_u} \frac{|M_x|^2}{E_X - E_{\Pi_u}} \quad \text{with} \quad M_x = \langle \Pi_u | d_x | X \rangle \quad (7.19)$$

7. Stark Effect

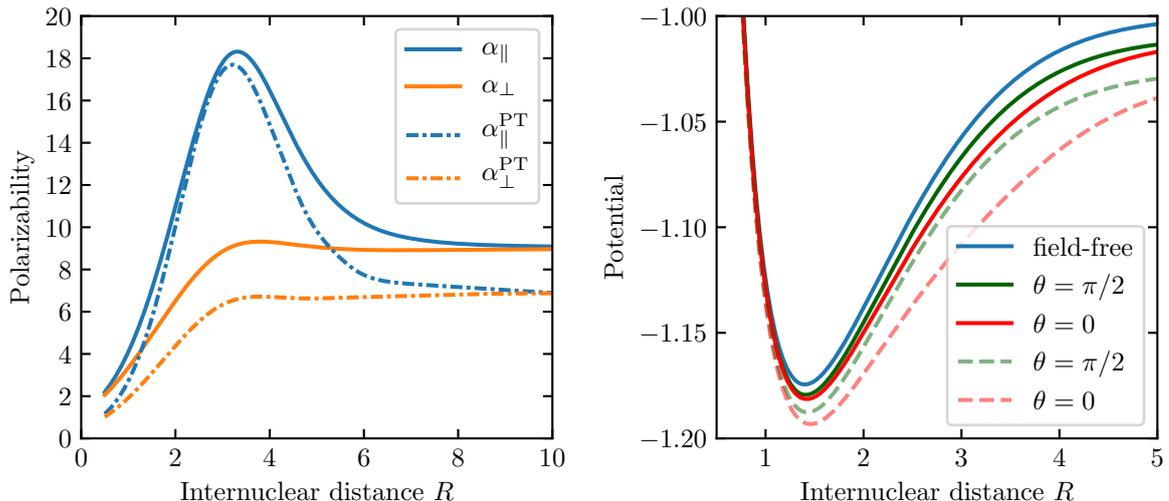


Figure 7.5.: **Left:** Parallel and perpendicular polarizabilities of the hydrogen molecule H_2 . Shown is a comparison between exact values (solid lines) [120,121] and values calculated with expressions (dashed-dotted lines) (7.19). For the parallel case the six lowest Σ_u states are included and for the perpendicular case the lowest four Π_u states. It can be seen that this is insufficient to reproduce the exact values. More states would need to be included. **Right:** AC-shifted ground state potential energy curves for parallel ($\theta = 0$) and perpendicular ($\theta = \pi/2$) orientation of the electric field. The high contrast solid curves correspond to an intensity of $1.5 \cdot 10^{14} \text{ W/cm}^2$ and the low contrast dashed curves to $4 \cdot 10^{14} \text{ W/cm}^2$.

where the respective sum goes over the available states. Since we do not cover all contributing states here, these expressions are not exact and a comparison with exact values for the polarizabilities serves as a benchmark for the accuracy that can be achieved with the states at hand. The left panel of Figure 7.5 shows such a comparison. For the parallel case the six lowest Σ_u states and for the perpendicular case the four lowest Π_u states are included (see Figure 4.1 for the potential energy curves). Apparently these are not sufficient to reproduce the polarizabilities accurately and more states are needed. Compare with the corresponding data for H_2^+ in Figure 7.1 where the coupling with only one excited state reproduces the exact polarizability adequately. It is therefore advantageous that the laser parameters allow us to resort to the known static polarizabilities, because otherwise the calculations would not be as accurate.

As a side note, Π states, and states with higher quantum number $\Lambda = |M_L|$ as well, are twofold degenerate. Values of M_L and $-M_L$ yield the same energy because of the axial symmetry of the molecule, where M_L is the projection of the orbital angular momentum of the electrons about the internuclear axis. This means that for every term in the sum of $\alpha_{\perp}^{\text{PT}}$ there is another with the same value because the two states have the same energy and (again for symmetry reasons) the same modulus of the transition element M_x . Since $M_x = M_+/\sqrt{2}$ for nonnegative M_L , we can calculate $\alpha_{\perp}^{\text{PT}}$ by using M_+ instead of M_x in the formula in (7.19) and only sum over half the states (with $M_L = 1$) because the factors 2 and $1/(\sqrt{2})^2$ cancel each other. We therefore do not distinguish between M_L and $-M_L$ when we talk about the six lowest Σ_u states, for example.

According to expression (7.10) we can write the AC-shifted potential energy curve as

$$V_{\text{BO}}^{\text{AC}}(R) = V_{\text{BO}}(R) - \frac{F_0^2}{4} \left(\alpha_{\parallel}(R) \cos^2(\theta) + \alpha_{\perp}(R) \sin^2(\theta) \right) \quad (7.20)$$

where F_0 is the amplitude of the electric field and θ the angle between the electric field vector and the internuclear axis, as before. V_{BO} is the vibrational ground state potential ($X^1\Sigma_g^+ 1s\sigma$, see again Figures 4.1 and 4.2). For the polarizabilities α_{\parallel} , α_{\perp} we use the exact values from [120,121].

The right panel of Figure 7.5 shows the AC-shifted ground state potential energy curve for parallel ($\theta = 0$) and perpendicular ($\theta = \pi/2$) orientation, for two electric field intensities $1.5 \cdot 10^{14} \text{ W/cm}^2$ and $4 \cdot 10^{14} \text{ W/cm}^2$. For these intensities the potential keeps its overall shape. The potential well is shifted to higher internuclear distances, lower energies and is broadened, which is reflected by the corresponding ground states of H_2 in Figure 7.6. The asymptotic value for large R is shifted down as well. Since the parallel and perpendicular polarizabilities have the same value of $\alpha_{\infty} = 9$ [120, 123] in the limit $R \rightarrow \infty$, the asymptotic shift

$$V_{\text{BO}}^{\text{AC}}(R \rightarrow \infty) = V_{\text{BO},\infty} - \frac{\alpha_{\infty} F_0^2}{4}$$

is independent of the angle θ . The asymptotic value of V_{BO} for $R \rightarrow \infty$ is $V_{\text{BO},\infty} = -1$.

Ionization potential In order to assess the influence of the Stark shift on the saddle-point times, we plot in Figure 7.7 the dependence of the ionization potential I_{p}^{AC} on the electric field intensity and the orientation. We define

$$I_{\text{p}}^{\text{AC}} = V_{\text{BO}}^+(R_0^{\text{AC}}) - E_0^{\text{AC}}$$

in analogy to the field-free I_{p} . R_0^{AC} is the equilibrium distance and E_0^{AC} the ground state energy of the AC-shifted potential. The left panel shows I_{p}^{AC} for H_2 . It grows with increasing field intensity and coincides with the field-free I_{p} for $I = 0$, as expected. Furthermore, the parallel orientation leads to a greater I_{p}^{AC} than the perpendicular orientation and the difference grows with the field intensity (compare with expression (7.20) and Figure 7.5).

We highlight the same three intensities as in Figure 7.4 of the DC shift in H_2^+ , namely $1.5, 2$ and $4 \cdot 10^{14} \text{ W/cm}^2$. In the right panel the relative change

$$\delta I_{\text{p}}^{\text{AC}} = \frac{I_{\text{p}}^{\text{AC}} - I_{\text{p}}}{I_{\text{p}}} \quad (7.21)$$

is shown for both isotopes H_2 (thin lines) and D_2 (thick lines). In contrast to the change in I_{p} due to DC shift of H_2^+ , the AC shifted ionization potential depends on the isotope because the ground-state energy E_0^{AC} does so.

Even for the largest of the three intensities, the relative change amounts to just about 2%. Similar as for the DC shift in section 7.2, the change in I_{p} will grow quickly (i.e. quadratic) with F_0 .

7. Stark Effect

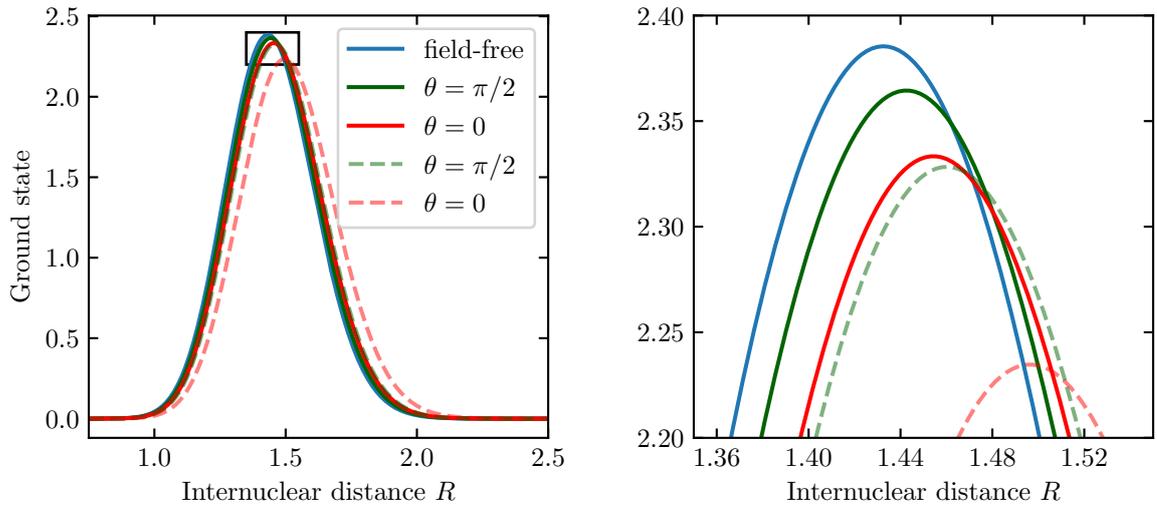


Figure 7.6.: Modulus squared of H_2 ground states of the AC-shifted potential energy curves in the right panel of Figure 7.5. The right panel shows the region enclosed by the rectangle in the left panel.

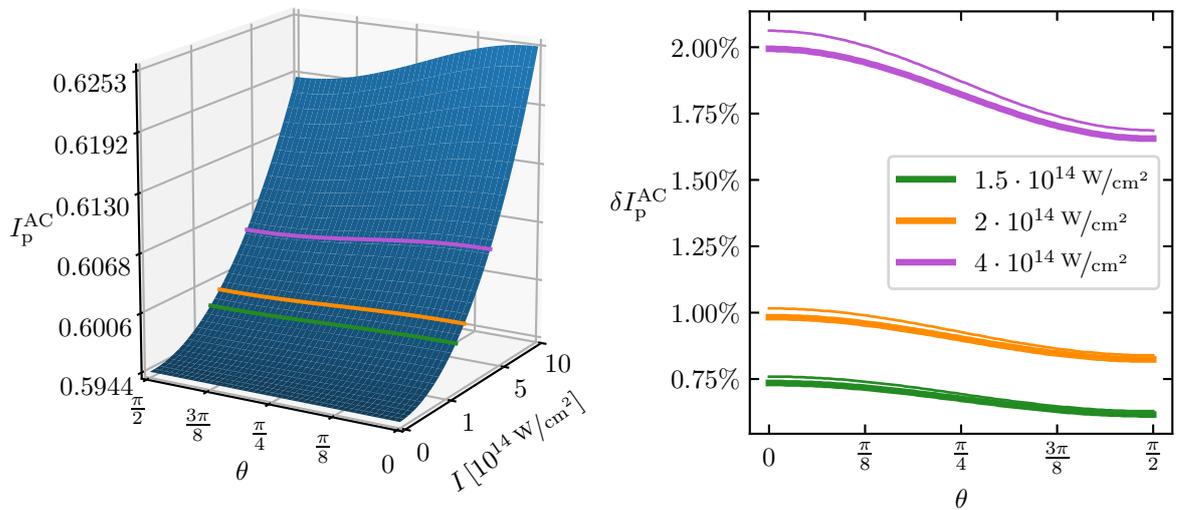


Figure 7.7.: **Left:** Dependence of the AC-shifted ionization potential I_p^{AC} of H_2 on the angle θ and on electric field intensity I . The lines correspond to the intensities 1.5 (green), 2 (orange) and $4 \cdot 10^{14} \text{ W/cm}^2$ (violet). **Right:** Dependence of the relative change in ionization potential δI_p^{AC} for the three different intensities marked in the left panel. Thick lines correspond to D_2 and thin lines to H_2 .

7.4. Ionization potential

In the previous sections about the Stark shifts in the ion and neutral molecules, we considered the changes in the ionization potential I_p separately, i.e. the change caused by the DC shift in the ion or that caused by the AC shift in the neutral molecule. In Figures 7.4 and 7.7 we see that while the DC shift by itself reduces I_p , the AC shift increases it, and they do so by approximately the same amount. This suggests that if both shifts are simultaneously included in the calculations, the net change in I_p

$$\delta I_p^{\text{AC/DC}} = \frac{I_p^{\text{AC/DC}} - I_p}{I_p}$$

with

$$I_p^{\text{AC/DC}} = V_{\text{BO}}^{+\text{DC}}(R_0^{\text{AC}}) - E_0^{\text{AC}}, \quad V_{\text{BO}}^{+\text{DC}}(R) = E_-^{\text{DC}}(R, F_0/\sqrt{2}) \quad (7.22)$$

may be smaller than the individual changes δI_p^{AC} , equation (7.21) and δI_p^{DC} , equation (7.17).

It should be noted here that we use a time-dependent electric field $F(t)$ in the DC shift of the ion, expression (7.11), and not a constant electric field F_0 , as we did in analyzing I_p^{DC} (7.16). This means that every vibrational wave packet evolution on the potential energy curve of the ion is triggered by an ionization event with a different instantaneous value of the ionization potential. To account for this it should be sufficient to consider the average value of the DC shift over one period of the electric field, instead of accounting for the time-dependency explicitly. To this end, the square of a sinusoidal wave has an average value of 1/2, meaning that in equation (7.22) we calculate $V_{\text{BO}}^{+\text{DC}}$ with $F_0/\sqrt{2}$ instead of F_0 . This is analogous to the factor 1/2 that enters the AC shift when it is approximated by the DC shift (7.10). The contribution from the DC shift to $I_p^{\text{AC/DC}}$ is therefore less than that shown in Figure 7.4 where the peak amplitude F_0 was used.

In Figure 7.8 we plot $I_p^{\text{AC/DC}}$ and $\delta I_p^{\text{AC/DC}}$ as before. Since we neglect the perpendicular DC shift in H_2^+ , the value for $\delta I_p^{\text{AC/DC}}$ coincides with δI_p^{AC} at $\theta = \pi/2$. For smaller angles, the two contributions lead to smaller changes than they do individually, as expected. The minimum change occurs for parallel alignment, because here the individual changes had the largest values with opposite signs. This leads to a value of approximately 1% for the large intensity $4 \cdot 10^{14} \text{ W/cm}^2$.

7. Stark Effect

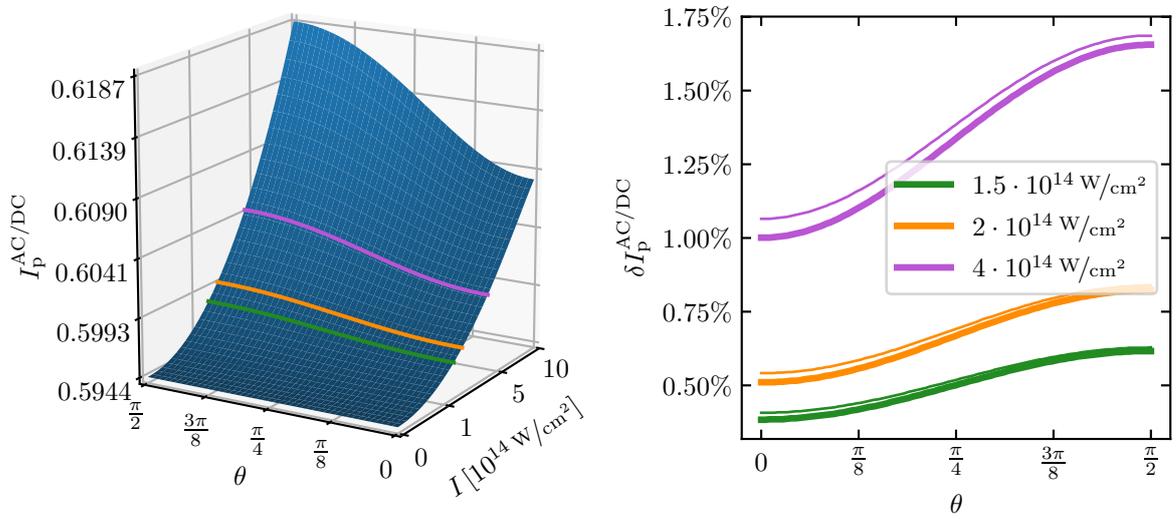


Figure 7.8.: **Left:** Dependence of the ionization potential $I_p^{AC/DC}$ of H₂ on the angle θ and on electric field intensity I . The lines correspond to the intensities 1.5 (green), 2 (orange) and $4 \cdot 10^{14}$ W/cm² (violet). **Right:** Dependence of the relative change in ionization potential $\delta I_p^{AC/DC}$ for the three different intensities marked in the left panel. Thick lines correspond to D₂ and thin lines to H₂.

8. Trajectory-Resolved High-Harmonic Spectroscopy

The group of Pengfei Lan from the Huazhong University of Science and Technology in Wuhan, China, were able to experimentally measure trajectory-resolved HHG spectra of H₂ and D₂, and provided us with their data of harmonic ratios. We are thus able to test the validity of harmonic ratios, calculated by means of saddle-point-time vibrational autocorrelations, against the experiment. The collaboration resulted in a joint publication, see [59].

The experiment exploited the different phase properties of the harmonics initiated by short and long trajectories. The dipole phase of a specific trajectory of order q , approximately given by $\alpha_q^j I(\mathbf{r}, t)$, acquires a temporal and spatial dependence via the laser pulse envelope $I(\mathbf{r}, t)$. The coefficient α_q^j is dependent on the kind of trajectory (labelled by j). The temporal dependence gives rise to a shifted harmonic frequency, $\omega_q = q\omega_0 + \alpha_q^j \frac{\partial I(\mathbf{r}, t)}{\partial t}$. In combination with macroscopic phase-matching effects, one can identify a red-shifted harmonic frequency with short trajectories, because they are phase-matched on falling edge of the pulse envelope. In contrast, the long trajectories are phase-matched on the rising edge and can be identified with a blue-shifted harmonic frequency.

The spatial dependence of I leads to a curved phase-front of the emitted harmonics. The coefficient α_q^j is generally larger for the long trajectory, giving it a larger divergence angle than the short trajectory. Both kinds of trajectories can therefore be distinguished in the spatial domain as well. For the details concerning the experiment, see [59]. Additional literature on the dipole phase of the trajectories can be found in [68–70].

In this chapter we present the theory part of the publication. The experimental data is shown in Tables 8.1 and 8.2 for $1.5 \cdot 10^{14}$ W/cm² and $2 \cdot 10^{14}$ W/cm², respectively, and Figure 8.1 shows the corresponding plots. In both cases the laser pulse is linearly polarized, has a central wavelength of 800 nm and a duration of 30 fs. Also shown in the plots is the angle-averaged autocorrelation ratio, with random alignment and with alignment distribution (see next section), calculated in the field-free BO potential energy curve $\mathcal{V}_{\text{BO}}^+$ (see also section 2.2.4). Although the agreement is reasonable, the comparison suggests that the propagation on the field-free curve is not sufficient to explain the slope of the ratio. The autocorrelation ratio for fixed parallel alignment ($\theta = 0$) does reproduce the slope very well and the overall agreement for the short trajectories is noteworthy. However, the magnitude of the ratio for the long trajectories is too high, in particular for the lower intensity. Additionally, there is likely no perfect parallel alignment of the experimental molecular ensemble. The good agreement might therefore be coincidental.

This leads to the idea of PACER (Probing Attosecond dynamics by Chirp-Encoded Recollision)

8. Trajectory-Resolved High-Harmonic Spectroscopy

Short trajectories			Long trajectories		
Energy	Harm. Order	Ratio	Energy	Harm. Order	Ratio
23.0487	14.8720	0.9695 ± 0.0263	23.4052	15.1020	1.1401 ± 0.0345
26.1671	16.8842	0.9999 ± 0.0290	26.3705	17.0154	1.1700 ± 0.0351
29.1135	18.7853	1.0110 ± 0.0379	29.4768	19.0197	1.1962 ± 0.0362
32.3513	20.8745	1.0553 ± 0.0406	32.5653	21.0126	1.2049 ± 0.0381
35.5373	22.9302	1.0994 ± 0.0495	35.6626	23.0110	1.2699 ± 0.0489
38.6654	24.9486	1.1644 ± 0.0689	38.7539	25.0057	1.5415 ± 0.0896

Table 8.1.: Experimental trajectory-resolved ratios of harmonic intensities, D_2/H_2 , for a wavelength of 800 nm and an intensity of $1.5 \cdot 10^{14} \text{ W/cm}^2$. Note that due to a frequency-shift (see main text) the harmonic orders are not integer values. Short trajectories (left table) are red- and long trajectories (right table) blue-shifted.

Energy	Harm. Order	Ratio, short	Ratio, long
23.2470	15	0.9372 ± 0.0381	1.2183 ± 0.1158
26.3466	17	1.0150 ± 0.0641	1.2370 ± 0.1358
29.4462	19	1.0438 ± 0.0837	1.2863 ± 0.1568
32.5459	21	1.0811 ± 0.1017	1.3046 ± 0.1689
35.6455	23	1.1575 ± 0.1072	1.3895 ± 0.1969
38.7451	25	1.1446 ± 0.0862	1.2920 ± 0.1188

Table 8.2.: Experimental trajectory-resolved ratios of harmonic intensities, D_2/H_2 , for a wavelength of 800 nm and an intensity of $2 \cdot 10^{14} \text{ W/cm}^2$. The frequency-shift is not available for this set of data points, which is why the harmonic orders are given as integers.

[28, 54, 124], which aims to find a potential that more accurately describes the vibrational motion. The ultimate goal is to retrieve the nuclear dynamics of the ion during the continuum excursion of the electron. The details are laid out below.

8.1. Theoretical model

The basis of our considerations is the ratio of the modulus-squared vibrational autocorrelations evaluated at the saddle-point times for D_2 and H_2 (see chapter 3)

$$R_C(t_s, t'_s) = \frac{|C(t_s, t'_s)|^2 \Gamma(I_p, E(\text{Re } t'_s))|_D}{|C(t_s, t'_s)|^2 \Gamma(I_p, E(\text{Re } t'_s))|_H}. \quad (8.1)$$

The times t'_s, t_s and the ionization potential I_p are used for D_2 in the nominator and for H_2 in the denominator. The ADK tunnelling rate is given by $\Gamma(I_p, E) = \exp(-2[2I_p]^{3/2}/(3|E|))$.

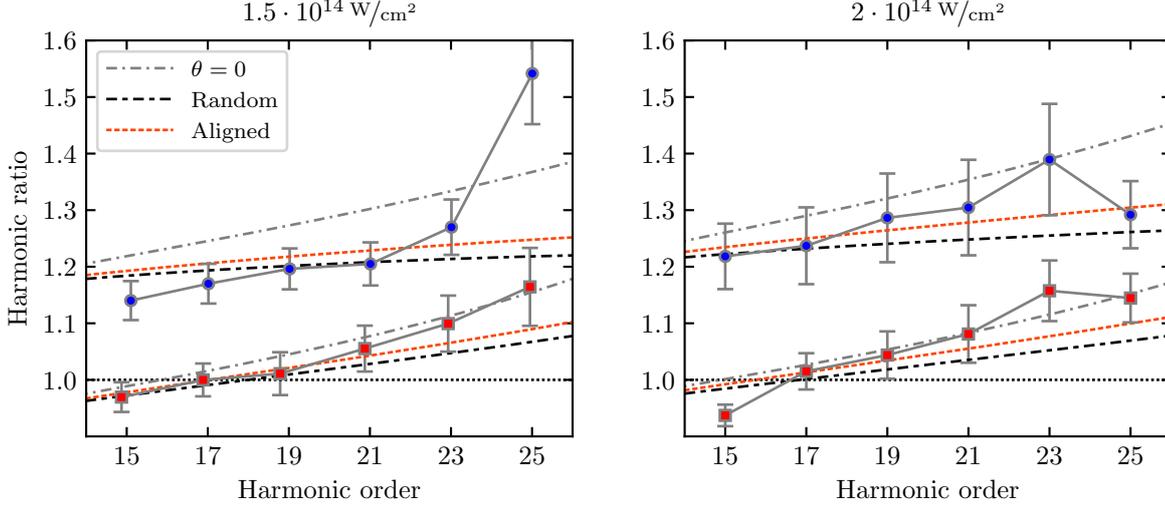


Figure 8.1.: Plots of the experimental trajectory-resolved harmonic ratios listed in Tables 8.1 and 8.2. The wavelength is 800 nm. The dashed lines show the autocorrelation ratio as given in expression (8.5), i.e. angle-averaged with random alignment (expression (6.16)) and with alignment distribution (expression (6.15)), calculated in the exact BO potential energy curve. The agreement between these curves and the experimental data is reasonable, but the slope is underestimated. Including the alignment distribution increases the slope and the agreement with the experimental data. The remaining disagreement is the motivation of the PACER method, as explained in the main text. **Lower curves:** Short trajectories. **Upper curves:** Long trajectories.

For the autocorrelation, we employ the form for a linearly polarized electric field with perpendicular components neglected, equation (3.1). We set the ionization matrix element identically to unity, $d_{\text{ion}} \equiv 1$. It then reads

$$C(t_s, t'_s) = \int dR d_{\text{rec}}^*(p_s(t_s, t'_s) + A(t_s), R) \chi_0^*(R) \mathcal{U}_R^+(t_s - t'_s) \chi_0(R) \quad (8.2)$$

with saddle-point momentum p_s , $A(t) = -\int^t dt' E(t')$ and time-evolution operator \mathcal{U}_R^+ for the shifted ionic BO potential energy curve $\mathcal{V}_{\text{BO}}^+$ (expression (2.22)). For details, refer to section 2.2.1 and chapter 3.

The recombination matrix element d_{rec} can be calculated analytically if the electronic ground state is approximated by a linear combination of hydrogen ground states ψ_h [125, 126]. In velocity form it takes the form (appendix A.1)

$$d_{\text{rec}}(\mathbf{k}, R) = \frac{2}{\sqrt{2(1 + s(R))}} \mathbf{e}_E \cdot \mathbf{k} \cos\left(\frac{kR \cos(\theta)}{2}\right) \tilde{\psi}_h(\mathbf{k}) \quad (8.3)$$

where $\tilde{\psi}_h$ is the hydrogen ground state in momentum space and $s(R)$ is the overlap of two such ground states, separated by a distance of R . The angle between the momentum \mathbf{k} and the internuclear axis is denoted by θ . According to equation (2.25), the return momentum $p_s(t_s, t'_s) + A(t_s)$ of the electron, at which d_{rec} is evaluated in expression (8.2), can be written as a function of harmonic frequency ω , $k_r(\omega) = \sqrt{2(\omega - I_p)}$, and is therefore isotope-dependent via I_p . The difference in I_p between D_2 and H_2 is approximately $2.9 \cdot 10^{-3}$. This is one order of magnitude smaller than the photon energy of a 800 nm laser pulse ($\omega_{800} \approx 5.695 \cdot 10^{-2}$) and

8. Trajectory-Resolved High-Harmonic Spectroscopy

even smaller compared to the generated high harmonics. It is therefore reasonable to neglect the factors \mathbf{k} and $\tilde{\psi}(\mathbf{k})$ in d_{rec} , facilitating the computation. The leading term, although dependent on R via $s(R)$, is neglected as well. This leaves only the cosine expression $\cos(kR \cos(\theta)/2)$, which is then substituted for d_{rec} in (8.2). It accounts for two-center interference effects during recombination [52, 53].

The laser pulse that drives harmonic generation simultaneously aligns the molecular ensemble. The plots in Figure 6.3 in section 6.2.4 show the alignment distribution for the laser parameters used here. It can be seen that there is a significant alignment at the peak of the pulse along the laser polarization direction. We therefore include the alignment distribution in our PACER calculations, see next section. The procedure is laid out in section 6.3. It results in the following expression for the autocorrelation as a function of harmonic energy ω

$$C(\omega) = \int dR \eta(\omega, R) \chi_0^*(R) \mathcal{U}_R^+(\tau_s(\omega)) \chi_0(R) \quad (8.4)$$

with electron travel time $\tau_s(\omega) = t_s(\omega) - t'_s(\omega)$ and the angle-average function $\eta(\omega, R)$, defined in expression (6.15). The ratio R_C in (8.1) as a function of harmonic frequency is then

$$R_C(\omega) = \frac{|C(\omega)|^2 \Gamma(I_p, E(\text{Re } t'_s))|_{\text{D}}}{|C(\omega)|^2 \Gamma(I_p, E(\text{Re } t'_s))|_{\text{H}}}. \quad (8.5)$$

8.2. PACER

What is commonly understood as PACER is the procedure to find a BO potential energy curve that reproduces the experimental data of harmonic ratios. Specifically, the requirement for that energy curve is that the vibrational dynamics evolving on it lead to an autocorrelation ratio that matches the experiment. In our case, that ratio is given by expression (8.5). This effectively serves as a measuring tool for the ionic vibrational potential in the range of internuclear distances that is accessible within the time range of the short and long trajectories. Once it has been determined, the nuclear dynamics (i.e. the vibrational motion) can be retrieved by a time propagation.

The motivation behind modifying the potential energy curve $\mathcal{V}_{\text{BO}}^+$ is that the strong laser field may distort it during HHG, thus influencing the vibrational motion. The modifications that transform $\mathcal{V}_{\text{BO}}^+$ to the new curve $\mathcal{V}_{\text{PACER}}^+$ can then be studied in terms of, for example, Stark effects or alignment distributions to identify the physical mechanism.

We introduce the same parametric set of curves as in [54] to model the potential

$$\mathcal{V}_{\text{PACER}}^+(R) = \frac{1}{R} - \frac{1}{2} + \frac{\alpha_1}{\alpha_2 + R} + \frac{\alpha_3}{\alpha_4 + R^2} + \alpha_5 e^{-\alpha_6 R} + \alpha_7 e^{-\alpha_8 R^2} + V_{\text{BO}}^{\text{shift}}.$$

which by construction has the correct asymptotic behaviour $\lim_{R \rightarrow 0} \mathcal{V}_{\text{PACER}}^+(R) \simeq 1/R$ and $\lim_{R \rightarrow \infty} \mathcal{V}_{\text{PACER}}^+(R) = -1/2 + V_{\text{BO}}^{\text{shift}}$. However, the former needs to be adjusted to match the

correct helium-limit of $\lim_{R \rightarrow 0} \mathcal{V}_{\text{PACER}}^+(R) \simeq 1/R - 2 + V_{\text{BO}}^{\text{shift}}$. The parameter α_7 can be fixed to achieve this

$$\alpha_7 = - \left(\frac{3}{2} + \frac{\alpha_1}{\alpha_2} + \frac{\alpha_3}{\alpha_4} + \alpha_5 \right).$$

See appendix A.4 for more details. Furthermore, we fix α_8 such that $\mathcal{V}_{\text{PACER}}^+$ has the same root as the field-free BO potential $\mathcal{V}_{\text{BO}}^+$, i.e. $\mathcal{V}_{\text{PACER}}^+(R_0) = 0$, with R_0 being the equilibrium distance of H_2 . This guarantees that the (vertical) ionization potential I_p is the same for all sets of parameter values. Otherwise, the saddle-point times would need to be recalculated for every set of parameters that is encountered while optimizing the potential. In principle one could allow for a variable ionization potential to account for a wider range of modifications the laser could have on the vibrational motion, but we do not consider this here. For α_8 the value is

$$\alpha_8 = -\frac{1}{R_0^2} \ln \left(\frac{1}{\alpha_7} \left[-\frac{1}{R_0} + \frac{1}{2} - \frac{\alpha_1}{\alpha_2 + R_0} - \frac{\alpha_3}{\alpha_4 + R_0^2} - \alpha_5 e^{-\alpha_6 R_0} - V_{\text{BO}}^{\text{shift}} \right] \right)$$

with α_7 as above. This leaves us with six parameters $\alpha_1, \dots, \alpha_6$ for optimization. We use a least-squares optimization algorithm [127] to determine them. Specifically, the sum of squared residuals to minimize is

$$\sum_{\substack{n \\ \text{short}}} r_s(\omega_n)^2 + \sum_{\substack{n \\ \text{long}}} r_l(\omega_n)^2$$

with residuals

$$r_{s,l}(\omega_n) = \frac{R_{\text{exp}}^{s,l}(\omega_n) - R_C^{s,l}(\omega_n)}{R_{\text{err}}^{s,l}(\omega_n)}.$$

In this expression, n counts the experimental data points, R_C is given by (8.5), R_{exp} and R_{err} are the experimental ratio and error. The indices s,l stand for short and long trajectories. To increase the sample size, we perform a natural spline interpolation through the original data points and use the interpolated values in the optimization. The energies at which the interpolation is evaluated are given by ω_n .

8.2.1. Results

The resulting potentials of the optimization, together with the corresponding values for $\alpha_1, \dots, \alpha_6$, are shown in Figure 8.2. For the calculation we neglected the small deviation of the harmonic frequencies from their integer values. The dashed line shows the exact ionic BO potential $\mathcal{V}_{\text{BO}}^+$ and the solid lines the optimized PACER potentials. It is important to note that only a relatively small range of internuclear distances is actually probed by the procedure. This range is marked by the transparent thick lines, which indicate how far the expectation value of R evolves for the long trajectory of harmonic order 11 in H_2 . This is approximately the longest long trajectory occurring in this setup. The values of the potentials outside these ranges are therefore not physically relevant. The corresponding harmonic ratios are shown as solid lines in Figure 8.3.

8. Trajectory-Resolved High-Harmonic Spectroscopy

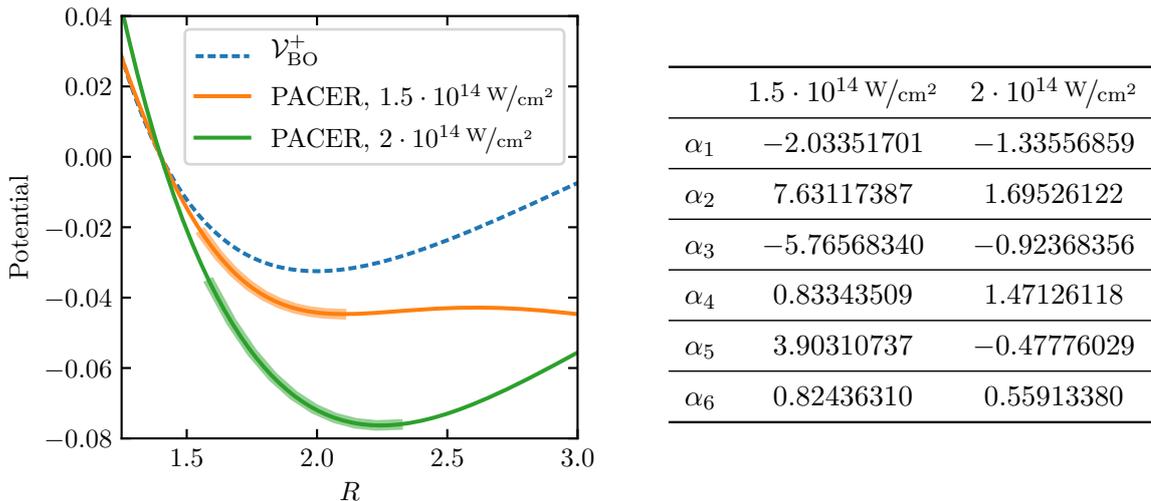


Figure 8.2.: **Left:** Comparison between the field-free BO potential and the PACER potentials for the two different intensities. Shown as transparent thick lines is the range of internuclear distances that the nuclei of the ion cover during the electron excursion of the long trajectory that belongs to the 11th harmonic order of H_2 . This is approximately the full range of R that can be probed with the available experimental data. The values of the potentials smaller and larger than this range are not accessible and therefore technically undetermined. **Right:** The numeric values of the potential parameters $\alpha_1, \dots, \alpha_6$.

One can see that the PACER ratios reflect the experimental ratios much better than the field-free counterparts, in particular with regard to the slope. This is achieved by the steeper gradient of the PACER potentials, see Figure 8.2, which leads to a more pronounced difference of the nuclear motions between the two isotopes. This, in turn, results in a larger slope of the harmonic ratio.

The extracted nuclear motions, i.e. the expectation value of R , for the 19th harmonic and lower intensity, $1.5 \cdot 10^{14} \text{ W/cm}^2$, can be seen in Figure 8.4, determined by a time propagation in the field-free BO and PACER potentials. In the left panel, the time axis is relative to the moment after tunnelling. The dynamics of the nuclei during the tunnelling of the electron (see also section 3.2.2) leads to the initial internuclear distance being dependent on the potential and the isotope. If the classical ionization and recombination times were used (which are real) the vibrational motion during tunnelling would not be included and all curves in the left panel would start at the equilibrium distance of the neutral molecule.

The right panel of Figure 8.4 shows the complete step-wise time evolution of R in the complex plane. One can see that, compared to the field-free BO potential, the nuclei separate more quickly during tunnelling in the PACER potential and the separation is approximately linear. Moreover, the nuclei also separate faster during the real time evolution following the tunnelling, i.e. the solid curves are not just shifted up by the differences in initial internuclear distance but also grow quicker than the dashed curves. This last fact is better seen in the left panel.

The long trajectories allow for a considerably larger time span and consequently for a greater range of internuclear distances to be probed. For the specific example of the 19th harmonic shown here, the time span is approximately doubled. The reached internuclear distance during

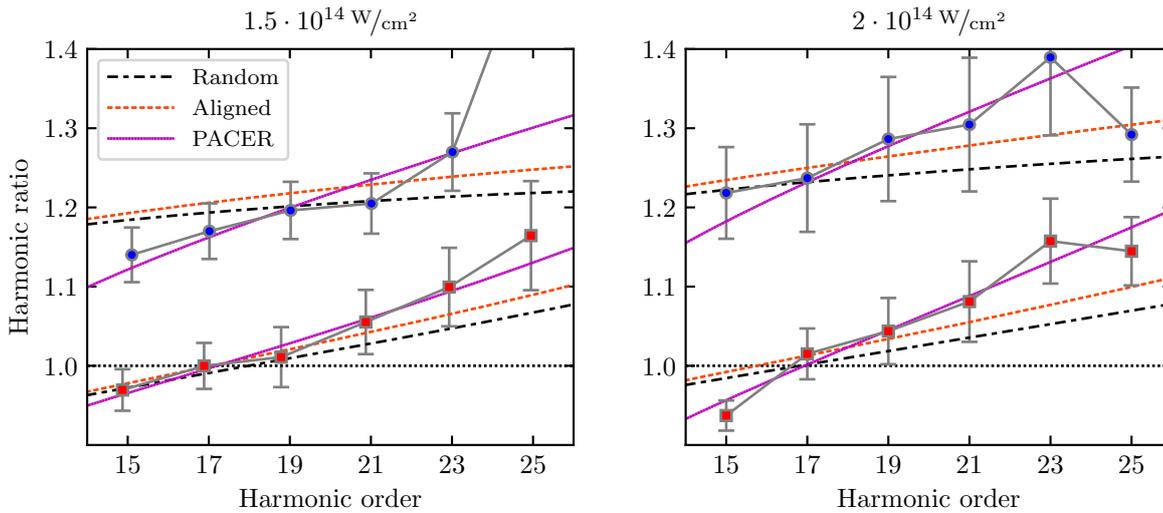


Figure 8.3.: Plots of the autocorrelations ratios resulting from the PACER potentials, together with the experimental data. Also shown are the angle-averaged ratios calculated with the field-free BO potential, i.e. the same curves as in Figure 8.1. The corresponding potentials can be seen in Figure 8.2. The PACER ratios agree significantly better with the experiment. **Lower curves:** Short trajectories. **Upper curves:** Long trajectories.

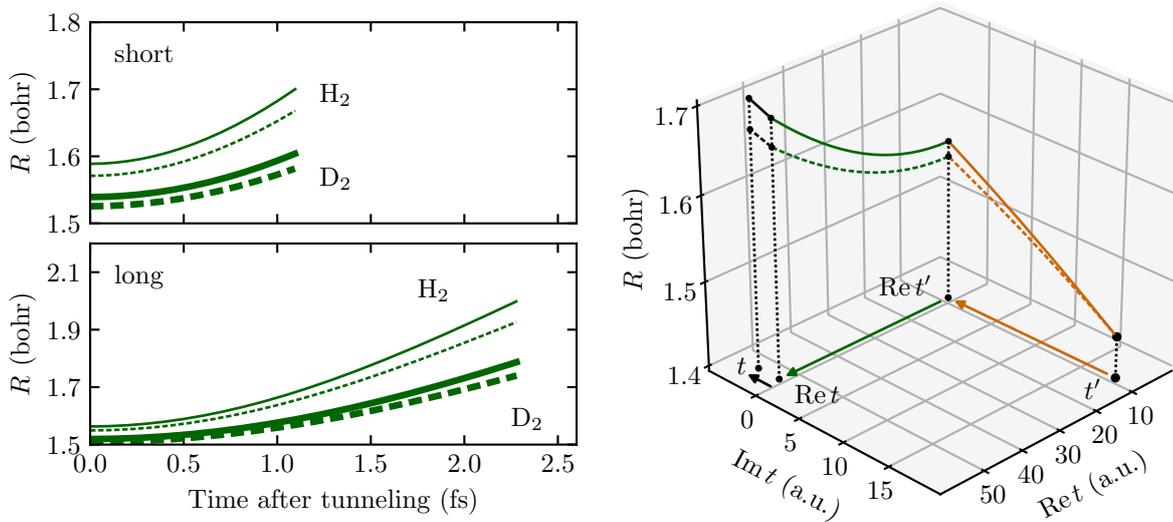


Figure 8.4.: Time evolution of the internuclear distance for the 19th harmonic and intensity $1.5 \cdot 10^{14} \text{ W/cm}^2$. **Left:** Evolution after tunnelling, i.e. from Ret' to Ret . Thick lines are for D_2 and thin lines for H_2 . The origin of the time axis is set to the moment after tunnelling, i.e. to Ret' . The curves start at different R because the tunnelling dynamics is dependent on the isotope and BO potential. The dashed lines are the results for the field-free BO potential and the solid lines for the PACER potential. **Right:** Stepwise time evolution from the ionization time t' to the recombination time t , for the short trajectory of H_2 . Dashed and solid lines are the results for the BO and PACER potential, respectively. The real time evolution between Ret' and Ret is the same as in top-left panel.

8. Trajectory-Resolved High-Harmonic Spectroscopy

that time is about 0.3 larger compared to the short trajectories in H_2 . It should be noted that due to the nonlinear character of the saddle-point times (see Figure 2.8) as a function of harmonic frequency and the overall intricate time evolution, the behaviour of the nuclear dynamics cannot be easily generalized to all harmonic orders or even different laser parameters.

8.3. Stark effect

The shape of the PACER potentials in Figure 8.2 is reminiscent of the Stark shifted potentials in Figures 7.2 and 7.3. The intent of this section is to investigate whether the Stark effect (chapter 7) is sufficient to explain the difference between the PACER potentials and the field-free potential.

In sections 7.2 and 7.3 the change in ionization potential due to the Stark effect was studied. For the two intensities encountered here, it lies at or below 1%, as can be seen in Figures 7.4, 7.7 and 7.8, which show the modifications of the ionization potential when the DC effect in the ion and the AC effect in the neutral molecule are included separately or together. This in turn changes the saddle-point times only marginally, which is shown in Figure 2.10. It is therefore an appropriate approximation to neglect the modifications of the saddle-point times due to the Stark effect. This significantly reduces the effort. We consider two cases, see below.

The ratios shown in this section are calculated via expression (8.5), with the autocorrelation being given by the expressions below.

8.3.1. DC effect in the ion

Including only the DC Stark effect in the ion the BO potential $\mathcal{V}_{\text{BO}}^+$ acquires an angle- and time-dependence. The angle-dependence arises from the orientation-dependence of the polarizability and the time-dependence from the electric field of the laser. The angle-average can then no longer be written in a closed form via $\eta(\omega, R)$. Instead, the time-evolution operator \mathcal{U}_R^+ becomes dependent on θ and $F(t)$

$$C_{\text{DC}}(\omega) = \int_0^\pi d\theta \sin(\theta) \sigma_{\text{max}}(\theta) \int dR \cos\left(\frac{k_r(\omega)R \cos(\theta)}{2}\right) \chi_0^*(R) \mathcal{U}_{R, F(t), \theta}^+(t_s(\omega), t'_s(\omega)) \chi_0(R) \quad (8.6)$$

where σ_{max} is the alignment distribution evaluated at the peak of the laser pulse, see section 6.3. Note that the integration over θ can also be done from 0 to $\pi/2$, because H_2^+ is a symmetric molecule. In particular, the transformation $\theta \rightarrow \pi - \theta$ leaves any θ -dependent components in (8.6) invariant. The constant factor of 2 arising from the full integral from 0 to π is irrelevant in the harmonic ratios.

The harmonic ratios resulting from C_{DC} are shown in Figure 8.5, together with the PACER ratios and the aligned angle-averaged ratios, expression (8.4). The DC ratio does not agree well

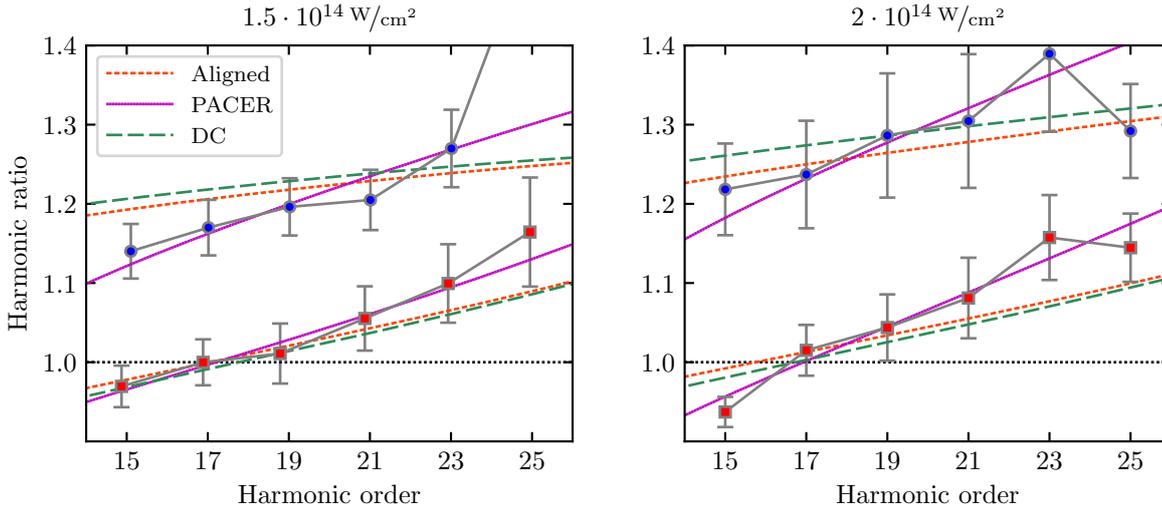


Figure 8.5.: Comparison of the PACER autocorrelation ratios with DC Stark shift ratios, where the autocorrelation is calculated according to expression (8.6). Also shown is the angle-averaged field-free case with alignment distribution. One can see that the (angle-averaged) DC effect does not bring the ratio into agreement with the PACER ratio. With regard to Figure 8.6 one can conclude that the influence of the DC Stark shift mostly vanishes in the angle-average. **Lower curves:** Short trajectories. **Upper curves:** Long trajectories.

with the PACER or experimental ratios. It mostly shifts the field-free ratios down for the long and up for the short trajectories, but does not change the slope significantly. The difference between the DC and aligned ratios is larger for the greater intensity. This is plausible, because a greater intensity leads to a more pronounced distortion of the potential.

Similar to the field-free case, the situation is different if the DC ratio is evaluated for a fixed angle of $\theta = 0$, i.e. parallel alignment, Figure 8.6. The slope is again in very good agreement with the experimental data and the short-trajectory ratio agrees well overall. However, the ratio is too high for the long trajectories.

The large parallel polarizability of H_2^+ means that the DC Stark shift bends down the potential energy curve significantly in that orientation (Figure 7.3). This leads to a more pronounced difference in the vibrational wave packet motions between D_2 and H_2 . The result is an increased slope that is visible in 8.6. The alignment distributions favor the parallel orientation (Figure 6.3), but the factor of $\sin(\theta)$ in the angle-average suppresses it. The large influence of the alignment distribution in parallel orientation therefore does not contribute much and the DC effect mostly averages out.

8.3.2. Including the AC effect in the neutral molecule

When the AC effect in the neutral molecule is included in addition to the DC effect in the ion, the distorted neutral potential leads to a modified vibrational ground state $\chi_{0,\theta}(R)$ (see Figure

8. Trajectory-Resolved High-Harmonic Spectroscopy

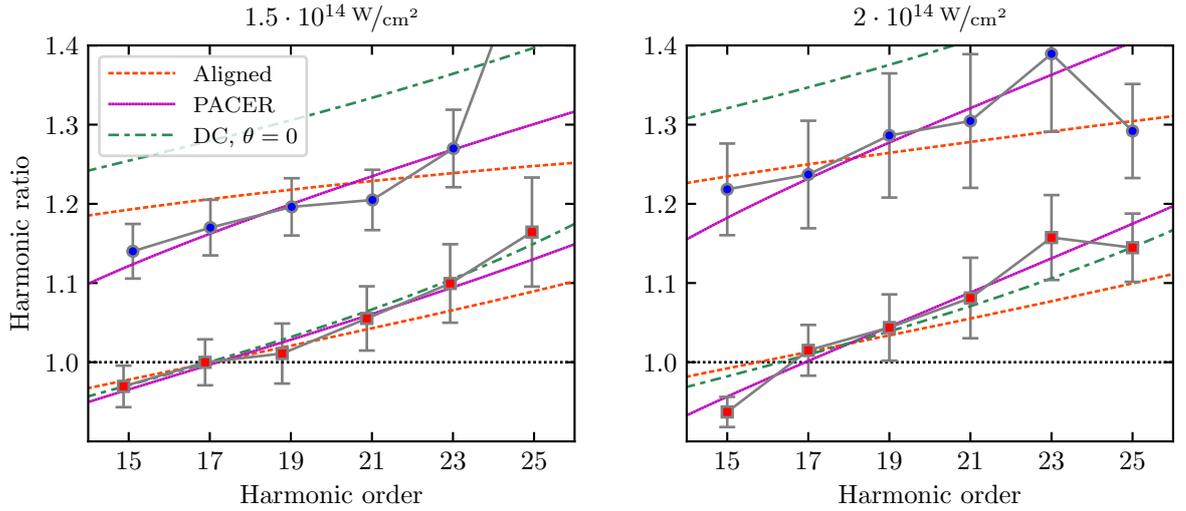


Figure 8.6.: Comparison of the PACER autocorrelation ratios with DC Stark shift ratios at fixed angle $\theta = 0$, i.e. parallel orientation. It is calculated according to expression (8.6), but without the integral over θ . Also shown is the angle-averaged field-free case with alignment distribution. One can see that the parallel DC effect yields a remarkable good agreement in case of the short trajectories. For the long trajectories, the slope is in good agreement, but the ratio is too high. **Lower curves:** Short trajectories. **Upper curves:** Long trajectories.

7.6) that becomes dependent on θ as well. The autocorrelation then reads

$$C_{AC/DC}(\omega) = \int_0^\pi d\theta \sin(\theta) \sigma_{\max}(\theta) \int dR \cos\left(\frac{k_r(\omega) R \cos(\theta)}{2}\right) \times \chi_{0,\theta}^*(R) \mathcal{U}_{R,F(t),\theta}^+(t_s(\omega), t'_s(\omega)) \chi_{0,\theta}(R). \quad (8.7)$$

The resulting ratio is shown in Figure 8.7. It can be seen that the AC effect leads to a shift to lower ratios. The slope is changed only marginally. In particular, it is not sufficient to explain the PACER ratios. The AC distortion of the neutral potential shifts the equilibrium distance and thus the vibrational ground state to larger internuclear distances, in addition to a broadening due to a wider potential well. The nuclei of the ion are therefore farther apart at the time of ionization. Figure 8.7 shows that this does not lead to an increased slope. The down-shift of the ratio happens for all angles θ . This is the reason why it survives the angle-average.

8.4. Orientation dependence of ionization

Another factor that might play a role in the experiment is the dependence of the ionization rate on the orientation relative to the laser. The ratio of ionization rates for parallel and perpendicular alignment varies with internuclear distance of the molecule and intensity of the laser. In order to probe the influence of this anisotropy on the ratio of harmonics calculated via autocorrelations, we introduce a simple model based on results reported in [128, 129]. For

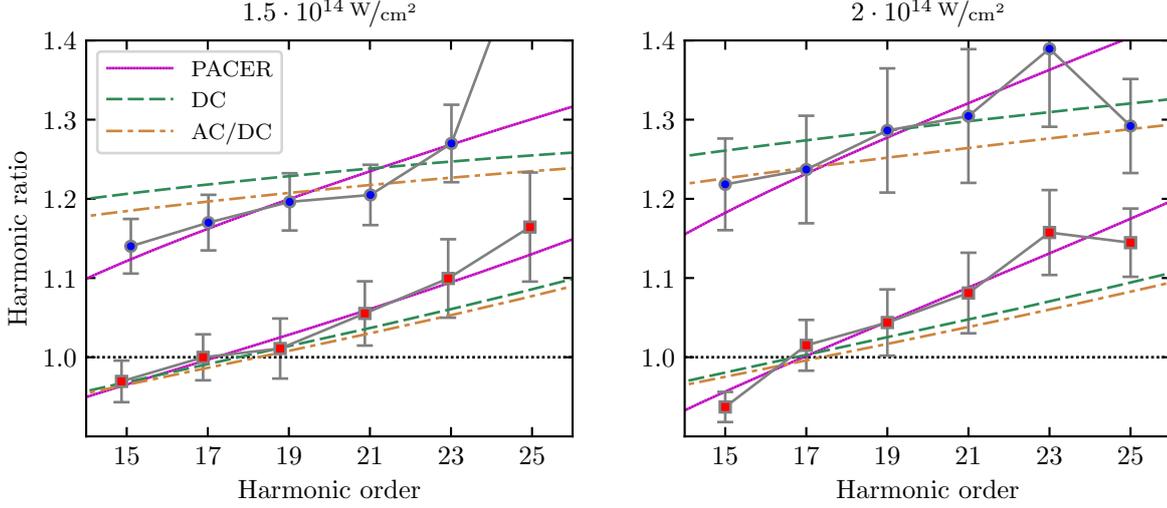


Figure 8.7.: Comparison of autocorrelation ratios with and without the AC effect (expression (8.7)) in the neutral molecule included, in addition to the DC effect in the ion. Also shown are the PACER ratios. The AC effect only shifts the ratios down, affecting their slope negligibly. **Lower curves:** Short trajectories. **Upper curves:** Long trajectories.

the present laser parameters and an internuclear distance of 1.4 the ionization rate of H_2 as a function of the orientation angle θ has a shape close to that of an ellipse with length-ratio of the semiaxes of approximately $F_0 = 1.32$ in favor of parallel orientation. We define the following weight function

$$F_{\text{ion}}(\theta) = F_0^2 \cos^2(\theta) + \sin^2(\theta)$$

which can be used to heuristically include the angle-dependence in the autocorrelation. Similar to angle-average with the alignment distribution $\sigma_{\text{max}}(\theta)$, we write the autocorrelation as

$$C_{\text{ion}}(\omega) = \int_0^\pi d\theta \sin \theta \sqrt{F_{\text{ion}}(\theta)} \int dR \cos\left(\frac{k_{\text{r}}(\omega)R \cos(\theta)}{2}\right) \chi_0^*(R) \mathcal{U}_R^+(\tau_s(\omega)) \chi_0(R). \quad (8.8)$$

Using the same function $F_{\text{ion}}(\theta)$ for both H_2 and D_2 , a comparison of the autocorrelation ratios calculated with (8.8) with F_0 either 1 (isotropy, random alignment) or 1.32 (anisotropy) is shown in Figure 8.8. The difference grows larger with increasing harmonic order but the curves are very close together and can be hardly distinguished in the given scale. Assuming that the angle-dependence does not critically depend on the isotope, we conclude that the orientation dependence of the ionization rate, for the present laser parameters, plays no significant role for the harmonic ratio and can therefore be neglected.

8.5. Ammonia

To demonstrate the general validity of the autocorrelation method, the trajectory-resolved measurements of harmonic ratios were also carried out with methane CD_4/CH_4 and Ammonia ND_3/NH_3 , see the supplemental material of [59]. For the latter, we aim to reproduce the

8. Trajectory-Resolved High-Harmonic Spectroscopy

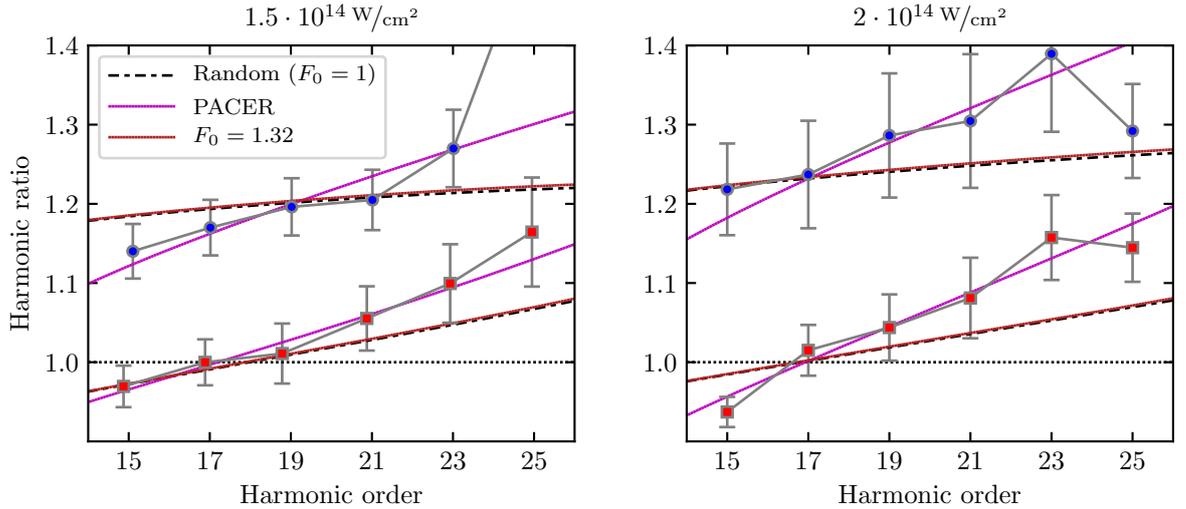


Figure 8.8.: Comparison of autocorrelation ratios calculated with orientation-dependence of the ionization rate ($F_0 = 1.32$). Also shown are the ratios for random alignment ($F_0 = 1$) and for the PACER potential. The influence of the ionization anisotropy is negligible. On this scale it can hardly be distinguished from the random case.

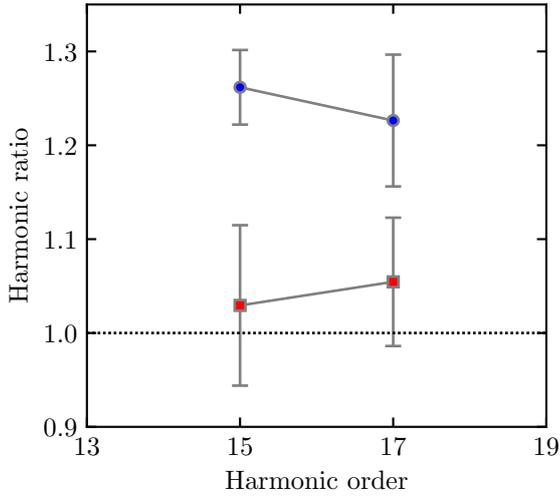
experimental data as was done for D_2/H_2 above. The experimental ratios, for a wavelength of 800 nm and an intensity of $1.3 \cdot 10^{14} \text{ W/cm}^2$ are shown in Figure 8.9. The experimental conditions only allowed for two harmonic orders to be measured. In contrast to H_2 , the ratio of the long trajectories is decreasing with increasing harmonic order. It should be noted, however, that an increase with harmonic order cannot be ruled out, given the size of the error bars.

8.5.1. Model and Results

In the calculations we use the models that also found application in [58, 130]. More detailed investigations of the potentials can be found in [131, 132]. The potentials for the neutral molecule and the ion that we use are shown in Figures 8.10 and 8.11. They are shifted (see below) such that the correct adiabatic ionization potential (i.e. the difference in ground state energies of the ion and neutral molecule) for NH_3 , $I_p^{NH_3, ad} \approx 10.07 \text{ eV} \approx 0.3701$ [133], is reproduced. Due to the different nuclear masses (of the hydrogen atoms) this results in slightly different vertical ionization potentials

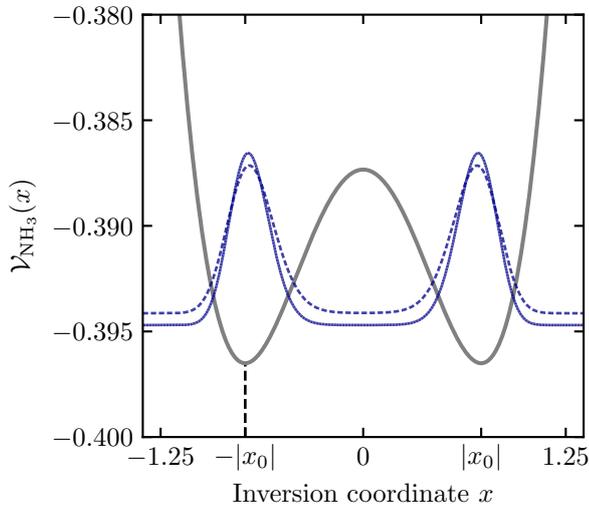
$$\begin{aligned} I_p^{NH_3} &\approx 0.39414 \approx 10.73 \text{ eV} \\ I_p^{ND_3} &\approx 0.3947 \approx 10.74 \text{ eV}. \end{aligned}$$

The 3 hydrogen and the single nitrogen atoms together form a triangular pyramid. The distance of the nitrogen atom to the plane formed by the hydrogen atoms is denoted by the coordinate



HO	Ratio, short	Ratio, long
15	1.0294 ± 0.0855	1.2618 ± 0.0397
17	1.0545 ± 0.0684	1.2264 ± 0.0702

Figure 8.9.: **Left:** Plot of trajectory-resolved harmonic ratios for ND_3 vs. NH_3 . The driving laser has a wavelength of 800 nm and an intensity of $1.3 \cdot 10^{14} \text{ W/cm}^2$. **Upper curves:** Long trajectories. **Lower curves:** Short trajectories. In contrast to D_2/H_2 , the ratio for the long trajectories is decreasing with harmonic order. **Right:** Table of numeric values shown in the left plot.



a_0	-56.554867222	a_6	-0.033241458
a_1	-0.035695180	a_7	0.034812181
a_2	0.036824248	a_8	-0.021077736
a_3	-0.003428001	a_9	0.006806258
a_4	-0.005527547	a_{10}	-0.000907247
a_5	0.018772562		

Figure 8.10.: Shifted potential $\mathcal{V}_{\text{NH}_3}$ for neutral ammonia molecule (left) with corresponding parameters (right), where the functional form is given by expression (8.9). The coordinate x measures the distance of the nitrogen atom to the plane formed by the 3 hydrogen atoms. The nitrogen atom can be located on either side of the plane without changing the potential energy, which is why it is symmetric with respect to $x \rightarrow -x$. The (stable) equilibrium distance is $|x_0| \approx 0.728$. The ground states for NH_3 (dashed) and ND_3 (solid) are shown (scaled by a factor of 0.005) at their respective energies.

8. Trajectory-Resolved High-Harmonic Spectroscopy

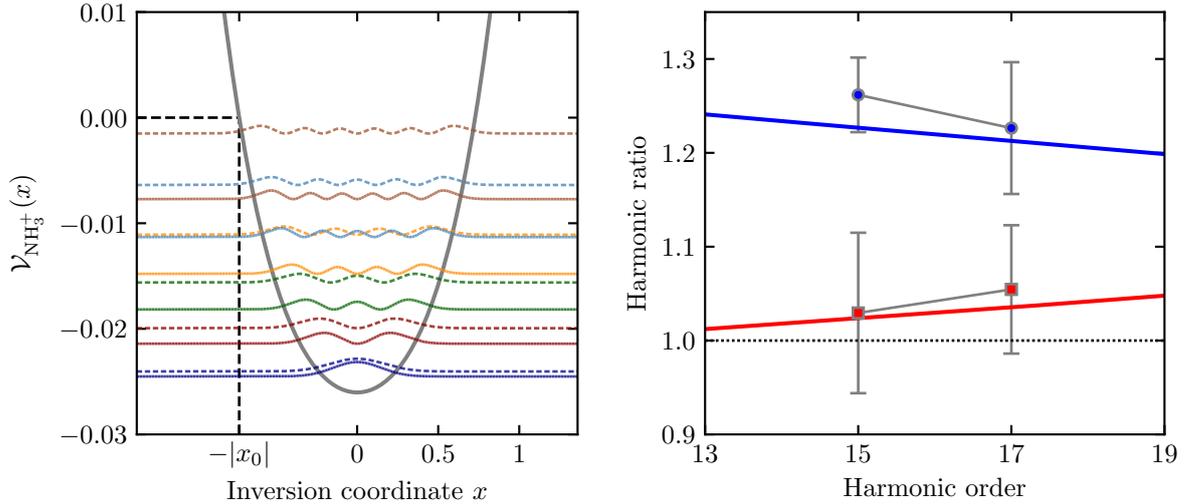


Figure 8.11.: **Left:** Shifted potential $\mathcal{V}_{\text{NH}_3^+}$ for the ammonia cation. The functional dependence is given by expression (8.10), with $K_1 = 0.033386$ and $K_2 = 0.0296437$. Ionization removes the potential barrier of $\mathcal{V}_{\text{NH}_3}$ at $x = 0$ and allows for oscillations of the nitrogen atom through the plane of the hydrogen atoms. The first 6 eigenstates for NH_3^+ (dashed) and ND_3^+ (solid) are shown (scaled by a factor of 0.0005) at their respective energies. Inspired by Figure 1 of [58]. **Right:** Experimental harmonic ratios for ND_3 vs. NH_3 , together with the autocorrelation ratio (solid lines), which reproduces the experimental data well. For the details of the calculations see the main text. Note that the autocorrelation ratio reproduces the decreasing ratio of the long trajectories (upper curves) and the increasing ratio of the short trajectories (lower curves) with harmonic order.

x , called the *inversion coordinate*. The unshifted potentials are given by

$$V_{\text{NH}_3}(x) = \sum_{n=0}^{10} a_n x^{2n}$$

$$V_{\text{NH}_3^+}(x) = K_1 x^2 + K_2 x^4$$

The parameters for the ion are $K_1 = 0.033386$ and $K_2 = 0.0296437$ and the ones for the neutral molecule are given in Figure 8.10. The shifted counterparts (that are used in the calculations) are simply

$$\mathcal{V}_{\text{NH}_3}(x) = V_{\text{NH}_3}(x) + V_{\text{NH}_3}^{\text{shift}} \quad (8.9)$$

$$\mathcal{V}_{\text{NH}_3^+}(x) = V_{\text{NH}_3^+}(x) + V_{\text{NH}_3^+}^{\text{shift}} \quad (8.10)$$

with constant energy shifts

$$V_{\text{NH}_3}^{\text{shift}} = -E_0^{\text{NH}_3} + E_0^{\text{NH}_3^+} - V_{\text{NH}_3^+}(x_0) - I_p^{\text{NH}_3, \text{ad}}$$

$$V_{\text{NH}_3^+}^{\text{shift}} = -V_{\text{NH}_3^+}(x_0).$$

Here, $E_0^{\text{NH}_3}$ and $E_0^{\text{NH}_3^+}$ are the ground state energies of the unshifted potentials. With these shifts, the ionic potential is zero at the Franck-Condon point $|x_0|$, analogue to the potentials of hydrogen.

The distinctive feature of the model for the neutral molecule is a position-dependent reduced mass that mimics changes of the bond-length in the real molecule when the nitrogen atom moves

$$\mu(x) = \mu_0 + \frac{3mx^2}{r_0^2 - x^2} \quad \text{with} \quad \mu_0 = \frac{3mM}{3m + M}.$$

with mass of a ^{14}N atom given by $M \approx 25526.04$ and proton/deuteron mass m . The length r_0 is the distance between the nitrogen and a hydrogen atom at $x = 0$, i.e. when all constituting atoms lie in a plane. Because of the symmetric molecular geometry, the transformation $x \rightarrow -x$ does not change the potential energy. At $x = 0$, the neutral molecule is in an unstable equilibrium and the nitrogen atom can move to either side of the plane for the system to reach a stable equilibrium. The double well potential in the left panel of Figure 8.10 reflects this. The (stable) equilibrium distance is $|x_0| \approx 0.728$.

Once the neutral molecule is ionized, the nitrogen atom can oscillate around $x = 0$, i.e. through the plane of the hydrogen atoms, which no longer corresponds to a potential barrier. The reduced mass of the ion is given by μ_0 .

The autocorrelation function is evaluated as

$$C_{\text{NH}_3}(\omega) = \int dx \chi_{\text{NH}_3}^*(x) \mathcal{U}_{\text{NH}_3^+}(\tau_s(\omega)) \chi_{\text{NH}_3}(x),$$

analogue to the case of hydrogen, but with transition matrix elements set to unity. The ground state of the neutral molecule is given by χ_{NH_3} , the time-evolution operator for the ionic potential $\mathcal{V}_{\text{NH}_3^+}$ by $\mathcal{U}_{\text{NH}_3^+}$ and the saddle-point excursion time by τ_s . The latter is evaluated via equations (2.23), (2.24) and (2.25) with the vertical ionization potentials $I_{\text{p}}^{\text{NH}_3}$ and $I_{\text{p}}^{\text{ND}_3}$ for the two isotopes. Finally the ratio is determined via (8.5).

The experimental ratios, together with the autocorrelation ratio are shown in the right panel of Figure 8.11. There is a good agreement between them. In particular, the decreasing ratio of the long trajectories with increasing harmonic order is reproduced.

8.6. Conclusion

The availability of trajectory-resolved harmonic ratios for D_2 vs. H_2 makes it possible to test the validity of the saddle-point time autocorrelation ratios. Generally, the computed results agree satisfactorily. Even one of the simplest models of random alignment with a LCAO recombination element yields the correct general trend. In Figure 8.1, the dashed black curves reproduce most the experimental data within the error bars and, in particular, shows an increase of the ratio with harmonic order for both short and long trajectories. The principal disagreement lies in the slope of the ratio, which is underestimated by the calculation.

The inclusion of the alignment distribution at the pulse peak as a weighting function in the angle-average increases the slope and improves the agreement. This is an indicator that the

8. Trajectory-Resolved High-Harmonic Spectroscopy

alignment plays a role under the experimental conditions. It should be made clear, that using the alignment distribution at the pulse peak may be questionable. Given that the parallel orientation reproduces the experimental slope quite well (see Figures 8.1 and 8.6), the molecular alignment seems to be an important ingredient in the model and may need closer investigation in the future. Since the time-dependence of the pulse envelope is a crucial part of the experiment, this becomes even more important.

The potentials found via PACER show the expected good agreement with the experimental data points. For both intensities, it reproduces all points within the error bars except for the highest order 25 for the long trajectories. With the potentials at hand, the nuclear dynamics can be calculated easily via propagation of the vibrational wave-packet. Assuming that the form of the PACER potentials is dictated by the influence of the laser on the field-free potential, it is mandatory to investigate if the Stark effect is the physical mechanism. It turns out that is not the case as the calculated ratios including the Stark effect do not lead to a significant increase in slope. This holds for the DC effect in the ion and the additional inclusion of the AC effect in the neutral molecule. Furthermore, a heuristic study of the orientation dependence of the ionization rate does not improve the ratio in this regard either.

Concerning the PACER method, it should be noted that there is no mathematical rigorous argument supporting the uniqueness of the acquired potentials. Apart from numerical accuracy, it is conceivable that qualitatively different potentials exist that result in a similarly good agreement with the experimental data.

To account for experimental uncertainties, we also tested slightly different intensities in order to check if they lead to a better agreement with the experiment. The data points for the lower intensity $1.5 \cdot 10^{14} \text{ W/cm}^2$ are slightly better reproduced by the autocorrelation ratios when the intensity in the calculation is lowered by 10 – 15 % (not shown). This is based on the model that includes the angle-average with alignment distribution. This improvement mainly concerns the long trajectories while the agreement for the short trajectories is still within the error bars. However, the improvement is not significant and, in particular, does not lead to a better agreement of the slope.

As an additional test of the method, the saddle-point time autocorrelation ratios can also be compared with experimental data with other molecules as targets. In our case, we use established models to check the calculated ratios for ammonia. There is a good agreement with the experiment, see the right panel of Figure 8.11.

9. Summary, Conclusion and Outlook

9.1. Summary and Conclusion

The topic of the thesis at hand was HHG of the hydrogen molecule, H_2 . It is a well-known fact that different isotopes of a molecular target exhibit different strengths of the emitted harmonics. The nuclear mass enters the SFA theory via the vibrational autocorrelation function, which also depends on the ionization and recombination times of the participating electron. These times, after employing the saddle-point approximation, turn out to be complex-valued. This led to the central focus of this thesis, namely the calculation of autocorrelation ratios with the complex-valued ionization and recombination times originating from the saddle-point-approximated SFA theory (section 2.2). The motivation for this was the question if it improves the agreement of TDSE ratios (of D_2 vs. H_2) with the corresponding autocorrelation ratios. Of particular interest in this regard was the separate study of the short and long trajectories. To this end we considered the complex-time autocorrelation in detail (chapter 3) and tested its viability in the calculation of harmonic ratios against TDSE solutions (chapter 5). Also considered in this regard were the hitherto used real-valued times from the well-established semiclassical three-step model. Furthermore, we compared the autocorrelation ratios with experimental data (chapter 8).

The comparison with TDSE ratios was done by solving the TDSE numerically and extracting the harmonic ratios from it via the Gabor transform (section 5.2.1), giving rise to the name “Gabor ratio”. Such a short-time Fourier transform allowed us to separate the short and long contributions. A specialty of the saddle-point autocorrelation was the use of an exact dipole-transition recombination matrix element (section 4.5). For this we used numerically exact electronic ground and scattering states as input. The model for these states is the same that also underlies the TDSE calculations. Two such models were used, one for a parallel and one for a perpendicular orientation of the internuclear axis to the linearly polarized electric field vector. The classical autocorrelation made use of an analytical matrix element in LCAO approximation and a heuristically corrected electron return momentum. The results showed that the saddle-point autocorrelation ratio may improve the agreement with TDSE results (see sections 5.3 and 5.4). However, this improvement is not for all laser parameters significant and the classical approach works remarkably well. We found that the first maximum of the Gabor ratio due to two-center interference is better reproduced by the saddle-point autocorrelation and the second maximum is better reproduced by the classical approach. Important in this regard is the finding that there may be a significant discrepancy between the Gabor and autocorrelation ratios. For some laser parameters the agreement is remarkable, but for others the Gabor ratios take on larger values than the autocorrelation counterparts. In particular, the discrepancy seems to grow with intensity. The origin of this behaviour is not clear and requires

9. Summary, Conclusion and Outlook

further investigation. The Gabor ratio behaves differently in this respect for the short and long trajectories. For the tested laser parameters, the short ratio showed an increasing deviation with wavelength while the long ratio exhibits an decreasing deviation with wavelength once the wavelength is large enough (Figures 5.14 and 5.15). As to the qualitative behaviour of the ratio as a function of harmonic energy, the saddle-point approach yields better results. This can be seen in the various Figures in section 5.3 and is also quantified by the deviation measures of the derivatives.

The comparison with experimental data was made possible by a cooperation with the group of Pengfei Lan from the Huazhong University of Science and Technology in Wuhan, China. They provided us with experimental harmonic ratios of D_2 vs. H_2 . This allowed the direct comparison of the saddle-point autocorrelation ratios with the experiment. It turns out that even a very simple model, with a LCAO-approximated recombination matrix element and random alignment of the molecular ensemble, is able to satisfactorily predict the ratios and their positive slope as a function of harmonic energy. The discrepancy lies in the value of the that slope, which was underestimated by the autocorrelation ratio. Investigations showed that parallel alignment of the molecular ensemble increases the slope and the agreement with the experimental data. This motivated the calculation of alignment distributions (chapter 6) and their inclusion in the autocorrelation calculations. The increased slope that resulted from this approach still underestimates the slope of the experimental data. In order to determine what is necessary to correctly reproduce the experiment, we resorted to the PACER method that aims at finding BO potential energy surfaces such that the theoretical ratios match the experimental ones. This can be seen as a measuring tool of the nuclear potential. The resulting autocorrelation ratios fit the experiment very well and the corresponding potentials enabled us to reconstruct the nuclear dynamics during the continuum excursion of the electron, including what the motion looks like in complex time. Furthermore, having the correct potential at hand prompted us to investigate the Stark effect (chapter 7) to see if it suffices to explain the differences between the PACER potentials and the exact BO potential. It turns out that it has surprisingly little influence on the harmonic ratios as its effect is reduced by the angle-average. We extended our studies to the ammonia molecule, NH_3 , for which harmonic ratios could also be measured in an experiment (carried out by Pengfei Lan et al. as well). The suitability of the saddle-point autocorrelation ratios was further confirmed by reproducing the experimental data very well.

All things considered, is it beneficial to use the complex-valued saddle-point times over their classical counterparts? There is no definite answer to this question; it depends on the purpose. The saddle-point autocorrelation yields viable results and we observed that it often better reproduces the qualitative behaviour of the Gabor ratios as a function of harmonic energy than its classical counterpart. It offers, however, not a universal improvement over the classical approach and a case study of both models is the best course. An inherent difficulty of the saddle-point approach is the need to evaluate time-dependent quantities at complex values, an example being the molecular alignment distribution. The classical model does not pose such a problem and has the considerable advantage that it is computationally simpler to calculate. The ionization and recombination times can be determined from a simple classical simulation of a Newtonian point particle. In contrast, finding the complex-valued solutions to the saddle-point equations requires more initial effort, as does the complex-time time evolution itself, depending on the numerical propagation scheme. To discuss the general properties of harmonic ratios, the

classical approach is sufficient. For a more in-depth analysis, the benefits of the saddle-point approach may be worth the additional effort.

9.2. Outlook

Regarding the results of chapter 5, there are still open questions. Why are the Gabor ratios for some laser parameters significantly higher than the autocorrelation ratios? Physically this means that the strengths of the emitted harmonics by D_2 are underestimated by the autocorrelation ratios (or H_2 is overestimated), by both the saddle-point as well as classical approach. The only major component of the autocorrelation not included in our results is the *ionization* matrix element. The reason for not including it is that it diverges in the standard version of the saddle-point approximation (for the relevant internuclear distances). Is it possible that the ratio of autocorrelations does not deviate from the Gabor ratios when the ionization element is included? According to the saddle-point equations, the kinetic electron momentum at the moment of ionization is given by $\sqrt{-2I_p}$, i.e. dependent on the isotope. This introduces an additional asymmetry between the isotopes into the ratio. Another possibility of including the ionization element would be to not apply the saddle-point approximation to the ionization time.

The investigation of the autocorrelation ratios in H_2 could also be extended to tritium, T_2 , at least in theory. Comparison of ratios of D_2 vs. H_2 and T_2 vs. H_2 might give more insight into why the TDSE sometimes predicts a significantly higher ratio than the autocorrelations.

Investigating the contributions of the short and long trajectories separately could also be done with the help of a two-color laser field. It has been shown [134] that such a setting can be used to prevent either the short or long trajectories from returning to the parent ion, via control of the phase between the two perpendicularly oriented fields. This could potentially make the low-energy region of the long contributions accessible.

The Eikonal-Volkov approximation [43, 44], that includes the influence of parent ions potential on the continuum electron, can be used to introduce corrections to the saddle-point times, as was shown in [45]. It would be interesting to investigate if these corrections improve the agreement between the saddle-point autocorrelation and TDSE ratios.

Concerning the comparison of autocorrelation and trajectory-resolved experimental ratios, the experiment exploited the different phase properties of the short and long trajectories. These properties depend on the time-dependent pulse envelope. However, the envelope was not included in the saddle-point times, which were always calculated for a sinusoidal single-cycle field. Given that the molecular alignment plays a nonnegligible role, this appears questionable. It would be more correct to include the envelope into the autocorrelation calculations by using different, envelope-dependent saddle-point times for the short and long trajectories. It is not straightforward how one should approach this “envelope-resolved” HHG, however. A similar argument can be made for the alignment distribution, which was taken to give the dominant contributions at the maximum field strength.

A. Additional Information

A.1. H₂ LCAO dipole transition matrix elements with plane waves

The ground state of a H₂ molecule can be approximated by a linear combination of hydrogen ground states $\psi_{\text{h}}(\mathbf{r}) = \frac{1}{\sqrt{\pi}}e^{-|\mathbf{r}|}$

$$\psi_{\text{H}_2}^{\text{LCAO}}(\mathbf{r}) = \frac{1}{\sqrt{2(1+s(R))}} \left[\psi_{\text{h}}\left(\mathbf{r} + \frac{\mathbf{R}}{2}\right) + \psi_{\text{h}}\left(\mathbf{r} - \frac{\mathbf{R}}{2}\right) \right]$$

with $s(R)$ being the overlap between hydrogen ground states separated by a distance \mathbf{R}

$$\begin{aligned} s(R) &= \langle \psi_{\text{h}}(\mathbf{r} - \mathbf{R}/2) | \psi_{\text{h}}(\mathbf{r} + \mathbf{R}/2) \rangle \\ &= e^{-R}(3 + 3R + R^2)/3. \end{aligned}$$

A.1.1. Velocity form

In velocity form the dipole transition matrix element can be calculated as follows (the continuum states $|\mathbf{k}\rangle$ are given by plane waves)

$$\begin{aligned} \mathbf{d}_{\text{V}}^{\text{LCAO}}(\mathbf{k}, \mathbf{R}) &= \langle \mathbf{k} | \mathbf{p} | \psi_{\text{H}_2}^{\text{LCAO}} \rangle \\ &= \int d^3r e^{-i\mathbf{k}\cdot\mathbf{r}} (-i\nabla) \psi_{\text{H}_2}^{\text{LCAO}}(\mathbf{r}) \\ &= -i \left[e^{-i\mathbf{k}\cdot\mathbf{r}} \psi_{\text{H}_2}^{\text{LCAO}}(\mathbf{r}) \Big|_{-\infty}^{\infty} - \int d^3r (\nabla e^{-i\mathbf{k}\cdot\mathbf{r}}) \psi_{\text{H}_2}^{\text{LCAO}}(\mathbf{r}) \right] \quad \text{Partial integration} \\ &= i(-i\mathbf{k}) \int d^3r e^{-i\mathbf{k}\cdot\mathbf{r}} \psi_{\text{H}_2}^{\text{LCAO}}(\mathbf{r}) \quad \text{Boundary term vanishes} \\ &= \mathbf{k} \tilde{\psi}_{\text{H}_2}^{\text{LCAO}}(\mathbf{k}) \\ &= \frac{1}{\sqrt{2(1+s(R))}} \mathbf{k} \left[e^{i\mathbf{k}\cdot\mathbf{R}/2} \tilde{\psi}_{\text{h}}(\mathbf{k}) + e^{-i\mathbf{k}\cdot\mathbf{R}/2} \tilde{\psi}_{\text{h}}(\mathbf{k}) \right] \quad \text{Shifted FT of } \psi_{\text{h}} \\ &= \sqrt{\frac{2}{1+s(R)}} \mathbf{k} \cos\left(\frac{\mathbf{k}\cdot\mathbf{R}}{2}\right) \tilde{\psi}_{\text{h}}(\mathbf{k}) \quad (\text{A.1}) \end{aligned}$$

A. Additional Information

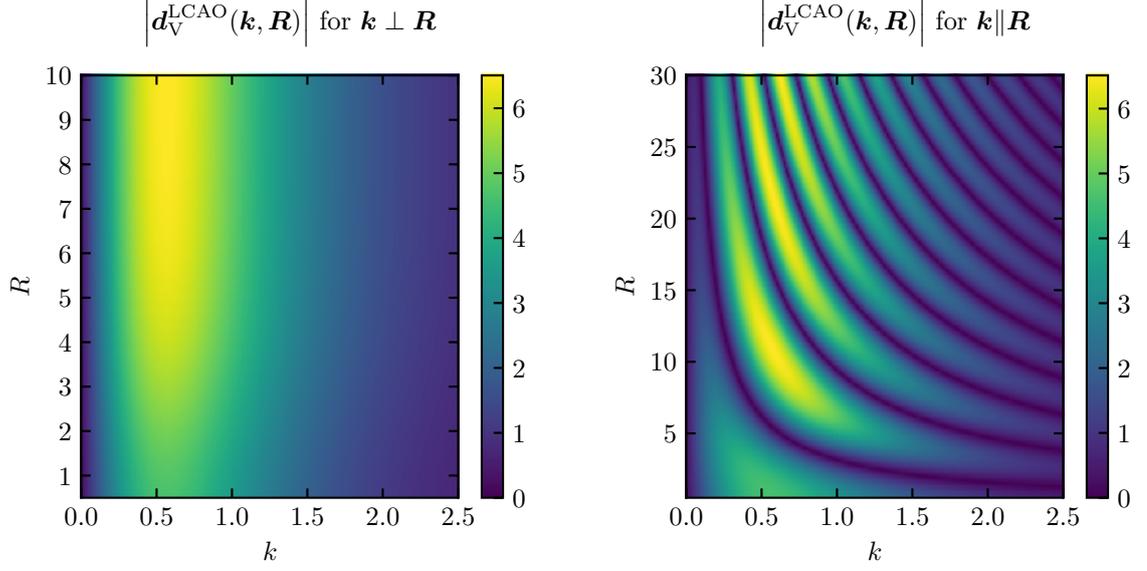


Figure A.1.: Modulus-squared velocity-form LCAO dipole-transition matrix element for perpendicular and parallel orientation.

with the Fourier-transformed hydrogen ground state

$$\begin{aligned}
 \tilde{\psi}_h(\mathbf{k}) &= \int d^3r e^{-i\mathbf{k}\cdot\mathbf{r}} \psi_h(\mathbf{r}) \\
 &= \frac{2\pi}{\sqrt{\pi}} \int_0^\infty dr r^2 \int_0^\pi d\theta \sin(\theta) e^{-(ik \cos(\theta)+1)r} \\
 &= \frac{8\sqrt{\pi}}{(k^2 + 1)^2}
 \end{aligned} \tag{A.2}$$

For perpendicular orientation

$$\begin{aligned}
 \mathbf{k} \perp \mathbf{R}: \quad |d_V^{\text{LCAO}}(\mathbf{k}, \mathbf{R})| &= \sqrt{\frac{2}{1+s(R)}} |\mathbf{k} \tilde{\psi}_h(\mathbf{k})| \\
 &= 8\sqrt{\pi} \sqrt{\frac{2}{1+s(R)}} \frac{k}{(k^2 + 1)^2}.
 \end{aligned}$$

The maximum is independent of R at $k_{\text{max}} = 1/\sqrt{3} \approx 0.58$.

A.1.2. Length form

In length form the matrix element is

$$\begin{aligned}
d_L^{\text{LCAO}}(\mathbf{k}, \mathbf{R}) &= \langle \mathbf{k} | \mathbf{r} | \psi_{\text{H}_2}^{\text{LCAO}} \rangle \\
&= \int d^3r e^{-i\mathbf{k}\cdot\mathbf{r}} \mathbf{r} \psi_{\text{H}_2}^{\text{LCAO}}(\mathbf{r}) \\
&= i \nabla_{\mathbf{k}} \int d^3r e^{-i\mathbf{k}\cdot\mathbf{r}} \psi_{\text{H}_2}^{\text{LCAO}}(\mathbf{r}) \\
&= i \nabla_{\mathbf{k}} \tilde{\psi}_{\text{H}_2}^{\text{LCAO}}(\mathbf{k}) \\
&= i \sqrt{\frac{2}{1+s(R)}} \left[-\frac{\mathbf{R}}{2} \sin\left(\frac{\mathbf{k}\cdot\mathbf{R}}{2}\right) \tilde{\psi}_{\text{h}}(\mathbf{k}) + \cos\left(\frac{\mathbf{k}\cdot\mathbf{R}}{2}\right) \nabla_{\mathbf{k}} \tilde{\psi}_{\text{h}}(\mathbf{k}) \right] \quad (\text{A.3})
\end{aligned}$$

with the Fourier-transformed hydrogen ground state $\tilde{\psi}_{\text{h}}(\mathbf{k})$ as in (A.2) and its derivative

$$\nabla_{\mathbf{k}} \tilde{\psi}_{\text{h}}(\mathbf{k}) = \frac{-32\sqrt{\pi}}{(k^2+1)^3} \mathbf{k}.$$

For perpendicular orientation

$$\begin{aligned}
\mathbf{k} \perp \mathbf{R}: \quad |d_L^{\text{LCAO}}(\mathbf{k}, \mathbf{R})| &= \sqrt{\frac{2}{1+s(R)}} |\nabla_{\mathbf{k}} \tilde{\psi}_{\text{h}}(\mathbf{k})| \\
&= 32\sqrt{\pi} \sqrt{\frac{2}{1+s(R)}} \frac{k}{(k^2+1)^3}.
\end{aligned}$$

The maximum is independent of R at $k_{\text{max}} = 1/\sqrt{5} \approx 0.45$.

A.2. WKB approximation

A.2.1. Proof of WKB phase integral for the Coulomb potential

In order to show that

$$\int_0^x dx' \sqrt{k^2 + \frac{2}{|x'|}} = x \sqrt{k^2 + \frac{2}{|x|}} + \frac{\text{sgn}(x)}{|k|} \ln \left(1 + k^2|x| + |kx| \sqrt{k^2 + \frac{2}{|x|}} \right) \quad (\text{A.4})$$

one can take the derivation of the right hand side for $x \neq 0$

$$\frac{\partial(\text{A.4})}{\partial x} = \sqrt{k^2 + \frac{2}{|x|}} + x \frac{-\frac{\text{sgn}(x)}{|x|^2}}{\sqrt{k^2 + \frac{2}{|x|}}} + \frac{\text{sgn}(x)}{|k|} \underbrace{\left(\frac{k^2 \text{sgn}(x) + |k| \text{sgn}(x) \sqrt{k^2 + \frac{2}{|x|}} + |kx| \frac{-\frac{\text{sgn}(x)}{|x|^2}}{\sqrt{k^2 + \frac{2}{|x|}}}}{1 + k^2|x| + |kx| \sqrt{k^2 + \frac{2}{|x|}}} \right)}_{(*)}$$

A. Additional Information

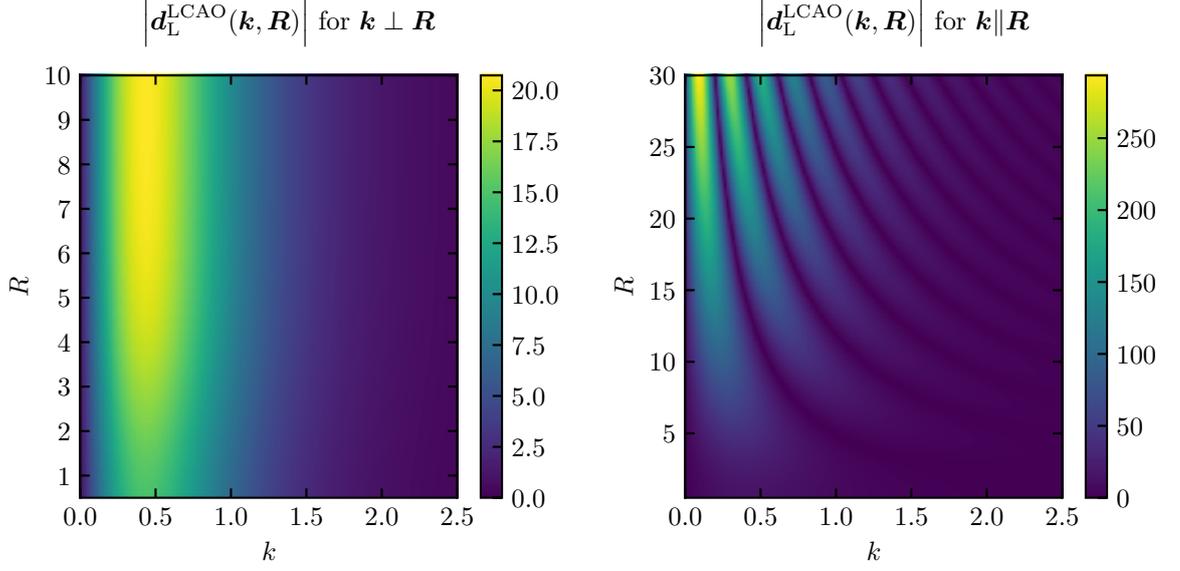


Figure A.2.: Modulus-squared length-form LCAO dipole-transition matrix element for perpendicular and parallel orientation.

The first term is the original integrand. Therefore the remaining terms (*) have to sum to zero. Set $w = \sqrt{k^2 + \frac{2}{|x|}}$ for convenience

$$\begin{aligned}
 (*) &= -\frac{1}{|x|w} + \frac{k^2 + |k|w - \frac{|k|}{|x|} \frac{1}{w}}{|k|(1 + k^2|x| + |kx|w)} \\
 &= -\frac{1}{|x|w} + \frac{k^2w + |k|w^2 - \frac{|k|}{|x|}}{|k|w(1 + k^2|x| + |kx|w)} \\
 &= \frac{-(|k| + k^2|kx| + k^2|x|w) + k^2|x|w + |kx|w^2 - |k|}{|kx|w(1 + k^2|x| + |kx|w)}
 \end{aligned}$$

With w^2 expanded to $k^2 + 2/|x|$ one sees that the numerator sums to zero. q.e.d.

A.2.2. Eikonal approximation of WKB phase integral

Asymptotically one can invoke the Eikonal approximation, assuming that the potential is sufficiently small compared to k^2 . The square root expression occurring in the WKB integral (4.14) can then be expanded to first order

$$\sqrt{k^2 + \frac{2}{|x|}} = |k| \sqrt{1 + \frac{2}{k^2|x|}} \approx |k| \left(1 + \frac{1}{k^2|x|} \right) + \mathcal{O}\left(\frac{1}{k^4|x|^2}\right).$$

This then gives for the whole integral

$$\begin{aligned}
 \phi_k^{\text{WKB}}(x) &\approx kx \left(1 + \frac{1}{k^2|x|} \right) + \frac{\text{sgn}(x)}{k} \ln \left(1 + k^2|x| + k^2|x| \left(1 + \frac{1}{k^2|x|} \right) \right) \\
 &\approx kx + \frac{\text{sgn}(x)}{k} + \frac{\text{sgn}(x)}{k} \ln(2 + 2k^2|x|) \\
 &\approx \underbrace{kx + \frac{\text{sgn}(x)}{k} \ln(2|kx|)}_{:=\phi_k^{\text{Coulomb}}(x)} + \underbrace{\text{sgn}(x) \frac{1}{k} [1 + \ln(|k|)]}_{:=\phi_{\text{shift}}(k)}.
 \end{aligned}$$

In the last line the constant term 2 was neglected in the logarithm.

A.3. Angle Average of LCAO dipole-transition matrix element in velocity form

For the ratio of autocorrelations the relevant factor of the LCAO dipole-transition matrix element in (A.1) is the cosine. Averaging this expression over all angle $(\phi, \theta) \in [0, 2\pi] \times [0, \pi]$ between the momentum \mathbf{k} and the internuclear axis \mathbf{R} yields

$$\begin{aligned}
 \left\langle \cos\left(\frac{\mathbf{k} \cdot \mathbf{R}}{2}\right) \right\rangle &= \frac{1}{4\pi} \int_0^{2\pi} d\phi \int_0^\pi d\theta \sin(\theta) \cos\left(\frac{kR \cos(\theta)}{2}\right) & \mathbf{k} \cdot \mathbf{R} = kR \cos(\theta) \\
 &= \frac{1}{4\pi} 2\pi \left(-\sin\left(\frac{kR \cos(\theta)}{2}\right) \frac{2}{kR} \right) \Big|_0^\pi \\
 &= \frac{\sin(kR/2)}{kR/2}
 \end{aligned}$$

A.4. Fixed parameters of PACER potential

The parametric set of curves for modelling the vibrational potential of H_2^+ reads

$$\mathcal{V}_{\text{PACER}}^+(R) = \frac{1}{R} - \frac{1}{2} + \frac{\alpha_1}{\alpha_2 + R} + \frac{\alpha_3}{\alpha_4 + R^2} + \alpha_5 e^{-\alpha_6 R} + \alpha_7 e^{-\alpha_8 R^2} + V_{\text{BO}}^{\text{shift}}.$$

In order to ensure the correct limit for $R \rightarrow 0$ we fix α_7 to get the limit of $\frac{1}{R} - 2$ for the helium ion He^+ (which is a hydrogen-like atom with a nuclear charge of 2 and ground-state energy of -2)

$$\begin{aligned}
 \mathcal{V}_{\text{PACER}}^+(R \rightarrow 0) &\approx \frac{1}{R} - \frac{1}{2} + \underbrace{\frac{\alpha_1}{\alpha_2} + \frac{\alpha_3}{\alpha_4} + \alpha_5 + \alpha_7 + V_{\text{BO}}^{\text{shift}}}_{\stackrel{!}{=} -2 + V_{\text{BO}}^{\text{shift}}} \\
 \Rightarrow \alpha_7 &= - \left(\frac{3}{2} + \frac{\alpha_1}{\alpha_2} + \frac{\alpha_3}{\alpha_4} + \alpha_5 \right)
 \end{aligned}$$

A. Additional Information

With α_7 fixed we enforce $\mathcal{V}_{\text{PACER}}^+(R_0) = 0$ and solve for α_8

$$\alpha_8 = -\frac{1}{R_0^2} \ln \left(\frac{1}{\alpha_7} \left[-\frac{1}{R_0} + \frac{1}{2} - \frac{\alpha_1}{\alpha_2 + R_0} - \frac{\alpha_3}{\alpha_4 + R_0^2} - \alpha_5 e^{-\alpha_6 R_0} - V_{\text{BO}}^{\text{shift}} \right] \right)$$

A.5. Fit of H₂ alignment distribution

In order to find an analytical expression of the numerically known alignment distribution $\sigma(\theta)$ we introduce the following truncated Fourier series for $\eta(\theta) := \sin(\theta)\sigma(\theta)$

$$\eta(\theta) = \eta_0 + \sum_{n=1}^N \lambda_n \sin(n\theta) + \sum_{n=1}^N \mu_n \cos(n\theta). \quad (\text{A.5})$$

Since H₂ is a homonuclear molecule we can impose that $\eta(\theta) \stackrel{!}{=} \eta(\pi - \theta)$. This gives

$$\begin{aligned} \lambda_n \sin(n\theta) &\stackrel{!}{=} \lambda_n \sin(n(\pi - \theta)) = -\lambda_n \sin(n\theta - n\pi) &\Rightarrow \lambda_n = 0 \text{ for } n \text{ even} \\ \mu_n \cos(n\theta) &\stackrel{!}{=} \mu_n \cos(n(\pi - \theta)) = \mu_n \cos(n\theta - n\pi) &\Rightarrow \mu_n = 0 \text{ for } n \text{ odd.} \end{aligned}$$

Additionally we know that $\eta(0) = \eta(\pi) = 0$ because of the factor $\sin(\theta)$ in $\eta(\theta)$. This immediately tells us that the sum of all nonzero cosine coefficients μ_n and η_0 must be zero:

$$\eta_0 + \sum_{\substack{n=1 \\ n \text{ even}}}^N \mu_n = 0$$

This reduces (A.5) to

$$\eta(\theta) = \sum_{\substack{n=1 \\ n \text{ odd}}}^N \lambda_n \sin(n\theta) + \sum_{\substack{n=1 \\ n \text{ even}}}^N \mu_n \cos(n\theta) - \sum_{\substack{n=1 \\ n \text{ even}}}^N \mu_n.$$

In practice a number of $N = 3$ is sufficient to adequately reproduce the numerical data. Figure A.3 shows an example.

For the evaluation of the autocorrelation the angle average is important. The relevant integral expression (see section 6.3) is

$$\eta(\omega, R) = \int_0^\pi d\theta \sin(\theta) \sigma_{\text{max}}(\theta) \cos\left(\frac{k(\omega)R \cos(\theta)}{2}\right).$$

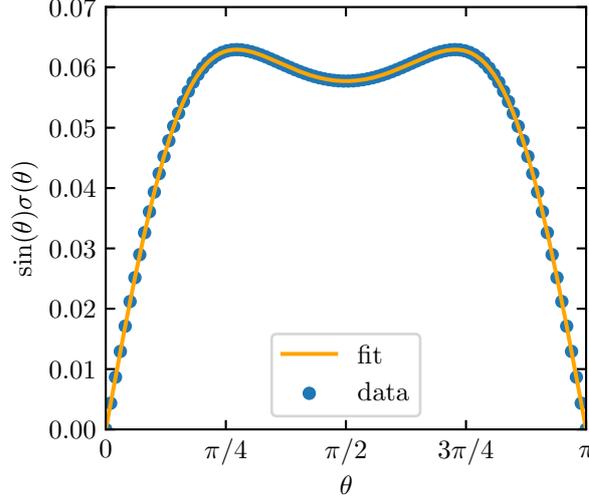


Figure A.3.: Comparison of numerical alignment data $\eta(\theta)$ and corresponding fit ($N = 3$) for an intensity of $2 \cdot 10^{14} \text{ W/cm}^2$ and a temperature of 293.15 K.

With the help of *Mathematica*, this expression, with $N = 3$, evaluates to

$$\begin{aligned} \eta(\omega, R) = & \frac{1}{k(\omega)^5 R^5} \times \\ & \times \left[4 \left(k(\omega)^4 R^4 (\lambda_1 + 3\lambda_3 + 5\lambda_5) - 32k(\omega)^2 R^2 (\lambda_3 + 21\lambda_5) + 6144\lambda_5 \right) \sin\left(\frac{k(\omega)R}{2}\right) \right. \\ & - 4\pi \left(k(\omega)^4 R^4 (\mu_2 + 4\mu_4 + 9\mu_6) - 96k(\omega)^2 R^2 (\mu_4 + 16\mu_6) + 30720\mu_6 \right) J_1\left(\frac{k(\omega)R}{2}\right) \\ & + 64k(\omega)R \left(k(\omega)^2 R^2 (\lambda_3 + 5\lambda_5) - 192\lambda_5 \right) \cos\left(\frac{k(\omega)R}{2}\right) \\ & \left. - 96\pi k(\omega)R \left(k(\omega)^2 R^2 (\mu_4 + 6\mu_6) - 320\mu_6 \right) J_0\left(\frac{k(\omega)R}{2}\right) \right]. \end{aligned}$$

where J_α are the *Bessel functions of the first kind*.

A.6. Values of potential energy curves for small internuclear distances

The extrapolation of potential energy curves presented in this section was not needed after all. There are, in fact, publications where the data spans a sufficient range of internuclear distances. [77, 78, 122, 135]. The results shown here are therefore not relevant for the main part of this thesis and the reader may skip this section. Nevertheless, the instructions may be useful for future work.

A. Additional Information

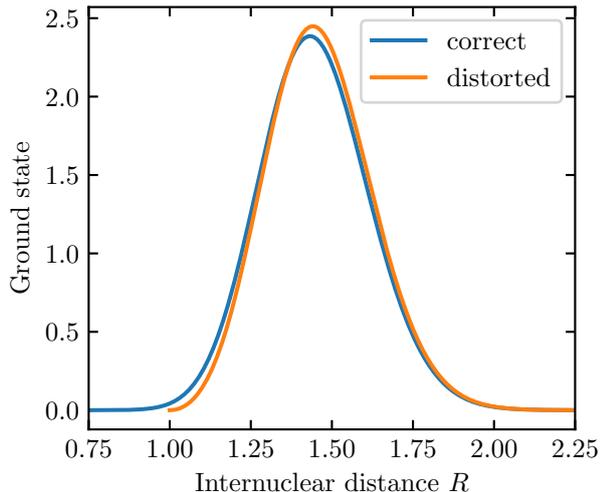


Figure A.4.: Comparison between the modules-squared correct and distorted vibrational ground state of H_2 when the corresponding potential energy curve is only given for $R \geq 1$.

Molecular state	United atom state	United atom energy $E_0^{\text{u.a.}}$
$\text{X}^1\Sigma_g^+$	1s	-2.903
$\text{B}^1\Sigma_u^+$	4p	-2.031
$\text{C}^1\Pi_u$	2p	-2.123

Table A.1.: Correlation between molecular states of H_2 and united atom states of He where one electron is in the given state while the other remains in the ground state, taken from [136]. The united atom energies are from [137, 138].

For the electronic ground state the BO potential energy curves for H_2 and H_2^+ are readily available in the literature and also given for a usually sufficient range of internuclear distances. The probably most comprehensive collection in this regard is given in [135]. However, the energy curves for the excited states, if available at all, might not be given for the internuclear distances needed. As an example, the lowest two singlet states with odd parity in H_2 (namely $\text{B}^1\Sigma_u^+$ and $\text{C}^1\Pi_u$) are, as far as is known to us, only given for $R \geq 1$. Although this is sufficient to adequately calculate the vibrational ground states in these potentials, it causes problems when combining them with the ground state curve ($\text{X}^1\Sigma_g^+$) to determine a AC Stark shifted potential. When restricting to $R \geq 1$, the ground state curve is not suitable to determine a vibrational state, as can be seen in Figure A.4.

Since recalculating the curves by ourselves would be too demanding it might be better to extend the existing data for $R < 1$. For this we subtract the $1/R$ -term describing the interaction between the two bare nuclei. Our primary interest lies on the two already mentioned electronic states $\text{B}^1\Sigma_u^+$ and $\text{C}^1\Pi_u$ of H_2 . The original data is shown in Figure A.5. The correlation between the molecular and united atom states can be retrieved from tables as given in [136]. For the states at hand the correlation can be seen in Table A.1.

A.6. Values of potential energy curves for small internuclear distances

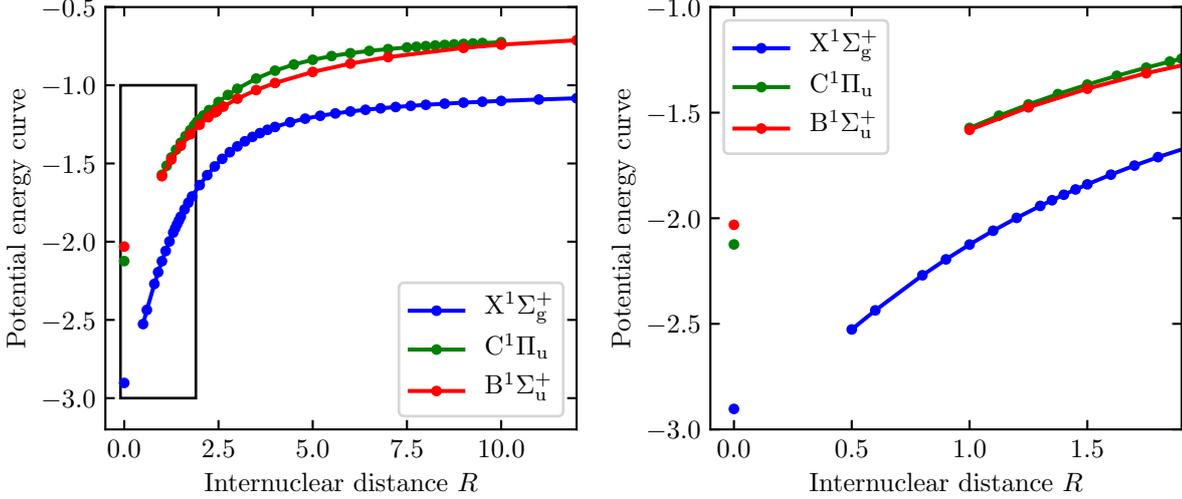


Figure A.5.: Initial data for potential energy curves without the $1/R$ interaction term. We wish to extend the curves for $B^1\Sigma_u^+$ and $C^1\Pi_u$ to at least $R = 0.5$ to match the range of the curve for $X^1\Sigma_g^+$. The single points at $R = 0$ are the corresponding united atom (Helium) energies, see Table A.1. The right panel shows the region indicated by the rectangle in the left panel.

For the purpose of this work and because of the $1/R$ -term, the accuracy of the potentials for $R \rightarrow 0$ might not be as critical as for $R \geq 1$. It is therefore probably sufficient to approximately determine the potential for $R \rightarrow 0$ and connect the resulting data smoothly to the data for $R \geq 1$, i.e. fill the gap for $0 < R < 1$ shown in Figure A.5. A theory for short-range atomic interactions is given in [139]. In the following we show the procedure we employ based on this theory. For a detailed description the reader is encouraged to read the original work.

The potential energy curve of a system of two atoms of equal kind a small distance R apart can be given as

$$E(R) = E_0^{\text{u.a.}} + \mu W(R) + O(\mu^2) \quad \text{with} \quad \mu = \frac{Z^2}{(2Z)^2} = \frac{1}{4}$$

where $E_0^{\text{u.a.}}$ is the united atom energy and Z the nuclear charge. The first order coefficient is given by

$$W(R) = Z \int d^3\mathbf{r} \left(\frac{1}{r} - \frac{1}{|\mathbf{r} - \mathbf{R}|} \right) \rho(\mathbf{r}) \quad (\text{A.6})$$

with $R = |\mathbf{R}|$ and the electron density

$$\rho(\mathbf{r}) = \sum_{i=1}^{N_{\text{el}}} \langle \psi_{\text{u.a.}} | \delta^3(\mathbf{r} - \mathbf{r}_i) | \psi_{\text{u.a.}} \rangle.$$

N_{el} is the number of electrons and $|\psi_{\text{u.a.}}\rangle$ is the united atom state. The scalar product is taken with respect to the electron coordinates \mathbf{r}_i .

Expression (A.6) can be simplified when considering a united atom state with specific principal quantum number N , total orbital angular momentum quantum number L and its projection

A. Additional Information

along the internuclear axis M . The internuclear axis is formed when the atoms are separated to form a diatomic molecule. Its electron density $\rho^{N,L,M}(\mathbf{r})$ is independent of ϕ and can be expanded in *Legendre polynomials* $P_k(\cos \theta)$ with even k

$$\rho^{N,L,M}(\mathbf{r}) = \sum_{l=0}^L P_{2l}(\cos \theta) \rho_{2l}^{N,L,M}(r).$$

Since the M -dependence can be explicitly written in terms of *Clebsch-Gordon coefficients* $\langle L_1 L_2 M_1 M_2 | LM \rangle$

$$\rho_{2l}^{N,L,M}(r) = \frac{\langle L, 2l, M, 0 | L, M \rangle}{\langle L, 2l, L, 0 | L, L \rangle} \rho_{2l}^{N,L,L}(r)$$

the electron density needs to be known only for different N and L . This allows for writing $W(R)$ in terms of the r -dependent expansion coefficients $\rho_{2l}^{N,L,L}(r)$

$$W(R)(N, L, M; R) = W_0(N, L; R) + \sum_{l=1}^L \frac{\langle L, 2l, M, 0 | L, M \rangle}{\langle L, 2l, L, 0 | L, L \rangle} W_{2l}(N, L; R) \quad (\text{A.7a})$$

$$W_0(N, L; R) = 4\pi Z R^2 \int_0^1 \rho_0^{N,L,L}(Rt)(1-t)t dt \quad (\text{A.7b})$$

$$W_{2l}(N, L; R) = \frac{4\pi Z R^{2l}}{4l+1} \left[- \int_0^\infty \frac{\rho_{2l}^{N,L,L}(r)}{r^{2l}} r dr + R^2 \int_0^1 \frac{\rho_{2l}^{N,L,L}(Rt)}{(Rt)^{2l}} (1-t^{4l+1})t dt \right] \quad (\text{A.7c})$$

For H_2 the united atom is He. The states of He necessary for our calculations are given in Table A.1. Because of the lack of exact analytical wave functions approximations are needed. The easiest approach is to neglect the interaction between the two electrons and use hydrogen-like orbitals for $Z > 1$ in a Slater-type expression

$$\psi_{nlm}^{\text{He}}(\mathbf{r}_1, \mathbf{r}_2) = \frac{1}{\sqrt{2}} \left(\psi_{100}(\mathbf{r}_1) \psi_{nlm}(\mathbf{r}_2) - \psi_{100}(\mathbf{r}_2) \psi_{nlm}(\mathbf{r}_1) \right).$$

The wave function for a hydrogen-like atom (with reduced mass of the core and electron set to 1) reads [140]

$$\psi_{nlm}(\mathbf{r}) = R_{nl}(r) Y_{lm}(\theta, \phi)$$

$$R_{nl} = \sqrt{\left(\frac{2Z}{na_0} \right)^3 \frac{(n-l-1)!}{2n[(n+l)!]}} e^{-Zr/na_0} \left(\frac{2Zr}{na_0} \right)^l L_{n-l-1}^{2l+1} \left(\frac{2Zr}{na_0} \right)$$

with the *generalized Laguerre polynomials* L_n^α , the *spherical harmonics* Y_{lm} and the Bohr radius a_0 . Because of orthonormality the electron density takes the simple form

$$\rho(\mathbf{r}) = |\psi_{100}(\mathbf{r})|^2 + |\psi_{nlm}(\mathbf{r})|^2. \quad (\text{A.8})$$

A.6. Values of potential energy curves for small internuclear distances

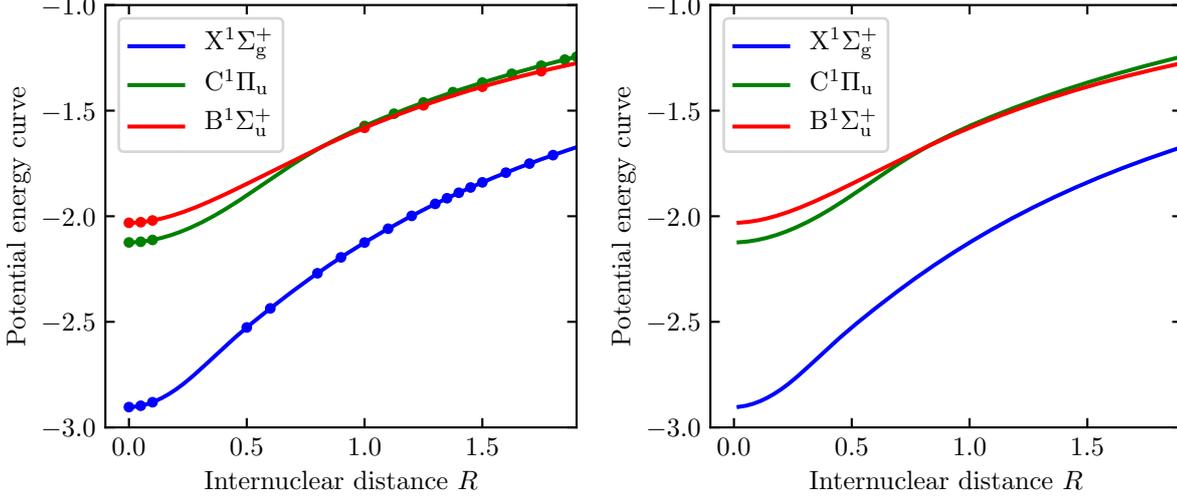


Figure A.6.: Extended potential energy curves. Both the left and the right panel show the same data but in the right panel the sample points are not shown to get a better view of the curve.

Taking the electron density in (A.8) the only nonvanishing expansion coefficients $\rho_{2l}^{N,L,M}(r)$ for $(N, L, M) = (2, 1, 1)$ and $(4, 1, 1)$ are

$$\rho_0^{2,1,1}(r) = \frac{Z^3}{96\pi a_0^5} e^{-\frac{2rZ}{a_0}} \left(96a_0^2 + r^2 Z^2 e^{\frac{rZ}{a_0}} \right)$$

$$\rho_2^{2,1,1}(r) = -\frac{r^2 Z^5}{96\pi a_0^5} e^{-\frac{rZ}{a_0}}$$

$$\rho_0^{4,1,1}(r) = \frac{1}{5242880\pi a_0^9} e^{-\frac{2rZ}{a_0}} \left(5242880a_0^6 Z^3 + \frac{4}{3} r^2 Z^5 e^{\frac{3rZ}{2a_0}} (80a_0^2 - 20a_0 r Z + r^2 Z^2)^2 \right)$$

$$\rho_2^{4,1,1}(r) = -\frac{r^2 Z^5}{3932160\pi a_0^9} e^{-\frac{rZ}{2a_0}} (80a_0^2 - 20a_0 r Z + r^2 Z^2)^2.$$

The value for the nuclear charge Z may be chosen less than 2 to accommodate for the screening effect the electrons have on one another. The typical value for Helium is $Z = 1.69$ [141] which we choose for the present calculations.

Figure A.6 shows the completed potential energy curves, determined with equations (A.7). Specifically, in the left panel, the points around $R = 0$ are the calculated values at $R = 0.05$ and $R = 0.1$. These points, together with the original data, are interpolated with cubic splines. The interpolation was done on an extended set of points, where the values for $R > 0$ are duplicated for $R < 0$ to arrive at symmetric data. This is reasonable because negative values for R correspond to interchanging the nuclei which should be the physically equivalent to $R > 0$. It has the convenient effect that the curve is continuously differentiable with zero slope at $R = 0$.

A. Additional Information

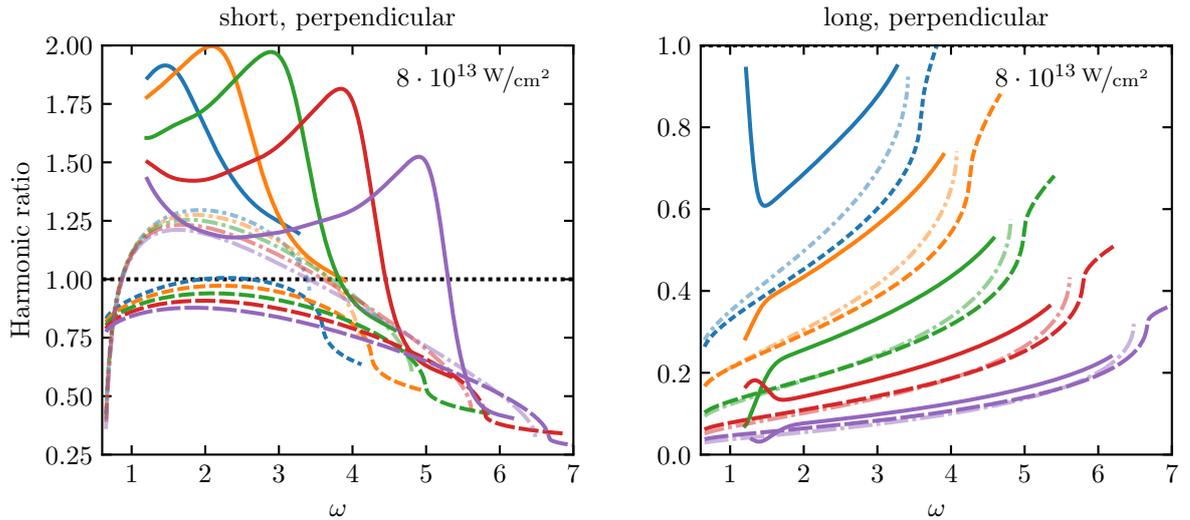


Figure A.7.: Harmonic ratios for the *perpendicular* orientation, a fixed intensity of $8 \cdot 10^{13} \text{ W/cm}^2$ and wavelengths of 1800 nm, 2000 nm, 2200 nm, 2400 nm and 2600 nm. Shown are \mathcal{R}_G (high-contrast solid line), $\mathcal{R}_c[C_{\text{SPA}}]$ (high-contrast dashed line) and $\mathcal{R}_c[C_{\text{SM}}]$ (low-contrast dotted-dashed line). Same-color curves belong to the same wavelengths; additionally, the length of the dashes indicate the wavelength. The short-trajectory ratio \mathcal{R}_G exhibits an interference-related maximum, the position of which increases with wavelength. This hampers a comparison with the autocorrelation ratios for this and also other intensities (see main text in section 5.3.1). The long-trajectory ratio \mathcal{R}_G is free from such features and agrees well with the autocorrelation ratios for increasing wavelength (apart from the LER interference that is generally present and appears here below $\omega \approx 1.5$).

A.7. Harmonic ratios

This section contains additional pictures of autocorrelation and Gabor ratios (Figures A.7 and A.8) as presented in chapter 5.

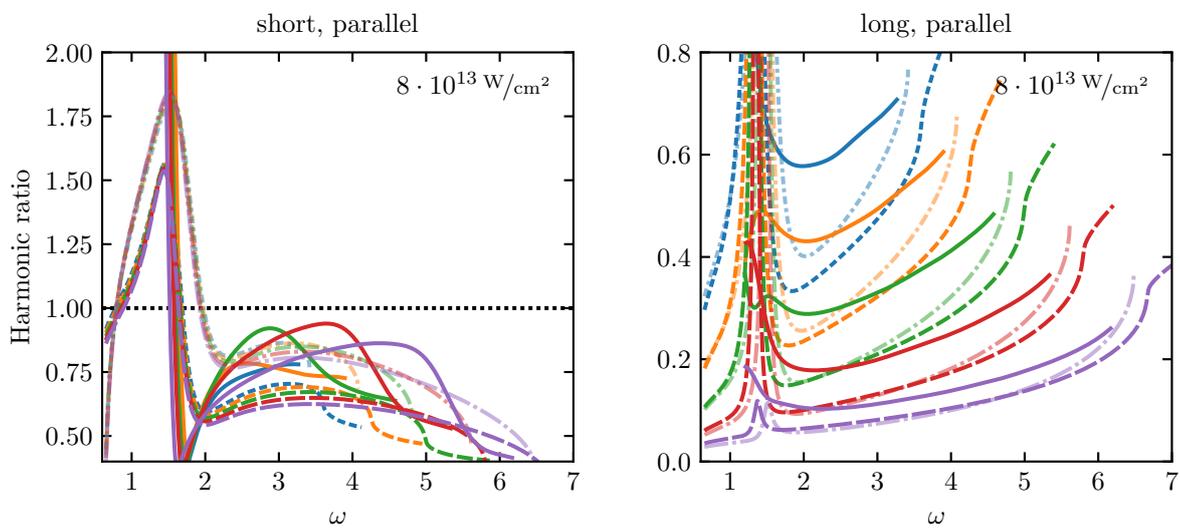


Figure A.8.: Harmonic ratios for the *parallel* orientation with the same laser parameters as in Figure A.7.

B. Numerical Implementation

This chapter is dedicated to the numerical implementations that underlie the results of this thesis. The computationally intensive tasks such as time evolutions and eigenstate determinations were done with the following algorithms implemented with the C programming language and compiled with the C compiler from the GNU Compiler Collection [142]. For some basic operations, in particular one-dimensional spline interpolation, but also the evaluation of functions such as spherical harmonics and Bessel functions, the GNU Scientific Library (GSL) was used [143].

Most of the data analysis was done with the Python programming language, in particular with the help of the libraries NumPy [144] and SciPy [145] for data structures and manipulation, Matplotlib [146, 147] for the creation of the pictures and also SymPy [148, 149] for some small analytical calculations. These and more libraries can be found packaged in (among others) the Anaconda distribution for Python [150], which was used for this work. Furthermore, for some data inspections and manipulations Gnuplot [151] was used, in addition to the GNU implementations of the well-known Unix tools such as sed, gawk, grep and many others. The whole thesis was written with the VIM text editor [152] and typeset with the TeX Live distribution [153]. For version control Git was used [154]. All machines involved were running GNU/Linux operating systems, primarily Ubuntu [155].

B.1. Numerical algorithms

In this section the algorithms used in the numerical calculations of this thesis are briefly outlined. In the following the position-dependence of the wave function and operators is omitted where possible for clarity.

B.1.1. Solving the time-dependent Schrödinger equation

Given a state $\psi(t_0)$ at time t_0 which evolves according to the TDSE with time-dependent Hamiltonian $H(t)$

$$i\frac{\partial\psi(t)}{\partial t} = H(t)\psi(t), \quad (\text{B.1})$$

the state of the system at any later time $t > t_0$ can be formally written with the help of the unitary (if H is hermitian) time-evolution operator $U(t, t_0)$

$$\psi(t) = U(t, t_0)\psi(t_0).$$

B. Numerical Implementation

Defining $t_n = t_0 + n\Delta t$ with $n = 0, 1, \dots, N-1$ and $\Delta t = (t - t_0)/(N-1)$, the above can be written [156]

$$\psi(t) = U(t_{N-1}, t_{N-2})U(t_{N-2}, t_{N-3}) \dots U(t_2, t_1)U(t_1, t_0)\psi(t_0) \quad (\text{B.2})$$

The operator U satisfies the same equation (B.1) as ψ and is therefore in general just as difficult to acquire. If the Hamiltonian is time-independent, however, it takes the form

$$U(t, t_0) = \exp(-iH(t - t_0)).$$

Choosing Δt in (B.2) small, compared to the timescale on which $H(t)$ changes, motivates

$$\begin{aligned} U(t_{n+1}, t_n) &\approx \exp\left(-iH\left(t_n + \frac{\Delta t}{2}\right)\Delta t\right) \\ &=: U_n. \end{aligned}$$

U_n is also called the short-time propagator. Equation (B.2) can then be approximated by

$$\psi(t) \approx U_{N-2}U_{N-3} \dots U_1U_0\psi(t_0).$$

Split-operator method

The split-operator method [157] is a special type of implementation of U_n . In this thesis it is used in the form

$$\begin{aligned} U_n &= \exp(-i(T + V_n)\Delta t) \\ &= \exp\left(-iV_n \frac{\Delta t}{2}\right) \exp(-iT\Delta t) \exp\left(-iV_n \frac{\Delta t}{2}\right) + O(\Delta t^3) \end{aligned}$$

with kinetic momentum operator T and

$$V_n = V\left(t_n + \frac{\Delta t}{2}\right),$$

where V is the potential of the system. The exponential terms containing V_n act as a multiplication in position space while T does so in momentum space. The split-operator propagation scheme then implements the action of U_n as follows:

1. Apply $\exp(-iV_n \frac{\Delta t}{2})$ in position space to $\psi(t_n)$.
2. Fourier transform to momentum space.
3. Apply $\exp(-iT\Delta t)$.
4. Inverse Fourier transform back to position space.
5. Apply $\exp(-iV_n \frac{\Delta t}{2})$ again.

What makes this scheme viable is the use of a Fast-Fourier transform implementation [158].

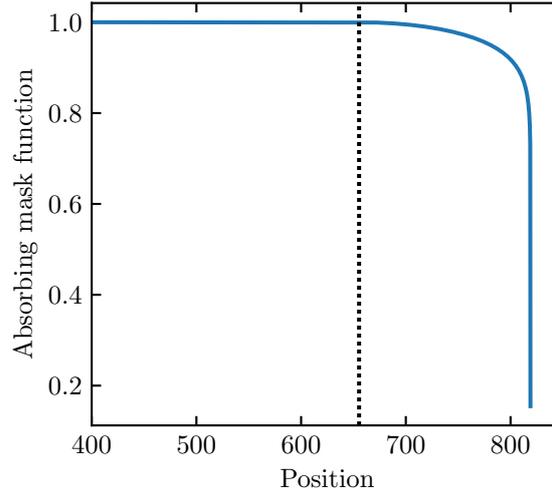


Figure B.1.: Example of the absorbing mask function used in the numerical TDSE calculations. Here the grid covers the interval $[-819.2, 819.2]$. The vertical dotted line indicates the beginning of the masking area. To the left of it the function is 1, and to the right it falls off as $\cos^{1/n}$ with $n = 20$ between 0 and $\pi/2$.

B.1.2. Absorbing mask at grid boundary

In the two-dimensional TDSE calculations of the parallel and perpendicular model an absorbing mask is employed at the appropriate grid boundaries to avoid spurious effects in the wave function. The wave function is multiplied, after every timestep, by a function that takes on the value 1 in the center of the grid and decreases toward the grid boundary in the last 10% of the total grid points. Specifically, this is done for both boundaries of the electron dimension and at the high boundary of the nuclear dimension (i.e. large internuclear distance). The low boundary of the nuclear dimension does not need to be masked because the high values of the BO potential energy curves prevents the wave function from reaching this boundary. On the last 10%, the function used is equal to $\cos(x)^{1/n}$ with $n = 20$. An example is shown in Figure B.1 for clarity.

B.1.3. Solving the time-independent Schrödinger equation

Stationary states with imaginary time evolution

Once a propagation scheme is implemented to solve the TDSE, it can also be used to find stationary states of a system. The TDSE with time-independent Hamiltonian H

$$i \frac{\partial \psi(t)}{\partial t} = H \psi(t)$$

can be rewritten with $t = -i\tau$ and $\phi(\tau) = \psi(-i\tau)$ as

$$-\frac{\partial \phi(\tau)}{\partial \tau} = H \phi(\tau).$$

B. Numerical Implementation

The time-evolution operator, that propagates forward a time range of τ , is exactly given by

$$U(\tau) = \exp(-H\tau).$$

Let $\{\phi_j\}$ be the eigenstates of H with eigenenergies E_j

$$H\phi_j = E_j\phi_j.$$

Some initial state ϕ_{ini} can be expanded in $\{\phi_j\}$

$$\phi_{\text{ini}} = \sum_j c_j \phi_j \tag{B.3}$$

with $c_j = \langle \phi_j | \phi_{\text{ini}} \rangle$. Application of $U(\tau)$ gives

$$\begin{aligned} \phi(\tau) &= U(\tau)\phi_{\text{ini}} \\ &= \sum_j c_j \phi_j \exp(-E_j\tau). \end{aligned}$$

Assuming that $E_j < E_{j+1}$ (for a nondegenerate system), it follows for sufficiently large τ

$$\phi(\tau) \stackrel{\tau \gg 0}{\approx} c_0 \phi_0 \exp(-E_0\tau),$$

which gives the ground state of the system, ϕ_0 , after normalizing $\phi(\tau)$. The eigenenergy E_0 can be determined by propagating $\phi(\tau) = \phi_0$ one more timestep $\Delta\tau$

$$\phi(\tau + \Delta\tau) = \exp(-E_0\Delta\tau)\phi(\tau),$$

hence

$$E_0 = -\frac{1}{2\Delta\tau} \ln(\langle \phi(\tau + \Delta\tau) | \phi(\tau + \Delta\tau) \rangle).$$

In order to determine the first excited state, ϕ_1 , one can subtract the ground state portion from the expansion (B.3) and repeat the procedure. In principle this subtraction has to be done only once, but numerical inaccuracies require to do it repeatedly. In general, to calculate the state ϕ_j , all coefficients c_i with $i < j$ have to vanish and c_j needs to be nonzero.

Numerov's method

The time-independent Schrödinger equation

$$E\psi(x) = -\frac{1}{2m}\psi''(x) + V(x)\psi(x)$$

can be rewritten as

$$\psi''(x) = -k(x)\psi(x) \tag{B.4}$$

with

$$k(x) = 2m(E - V(x))$$

and mass m . Sampling at equidistant points x_n with stepsize Δx , Numerov's method gives with $\psi_n = \psi(x_n)$ and $k_n = k(x_n)$

$$\psi_n = \frac{\left(2 - \frac{5\Delta x^2}{6}k_{n-1}\right)\psi_{n-1} - \left(1 + \frac{\Delta x^2}{12}k_{n-2}\right)\psi_{n-2}}{\left(1 + \frac{\Delta x^2}{12}k_n\right)}.$$

Hence, knowing the wave function at two grid points x_{n-2} and x_{n-1} enables one to calculate it at x_n . This formula can be derived by Taylor-expansion of $\psi_{n\pm 1}$ around the point x_n up to fourth order, adding both results and simplifying the second and fourth derivative via equation (B.4) and the three-point formula for the second derivative.

Shooting method

Given the *one-dimensional* Schrödinger equation

$$E\psi(x) = H\psi(x),$$

the calculation of a bound state $\psi(x)$ constitutes a boundary-value problem, with boundary conditions $\psi(x \rightarrow \pm\infty) = 0$. This problem can be approached with the shooting method by treating it as an initial value problem. Starting on one side of the grid with an initial guess for the energy E , say at $-x_b$ with $x_b \gg 0$, $\psi(-x_b) = 0$ and $\psi'(-x_b) \neq 0$, the solution is numerically integrated over the whole grid to find $\psi(E; x)$. If the energy E is not the correct eigenenergy of the bound state, the solution diverges, i.e. $|\psi(x_b)| \gg 0$. The eigenenergy E can be found by calculating the root of the function $f(E) = \psi(E; x_b)$. This is done with a bisection algorithm. Once the energy E is found, it can be used to find ψ , again by numerical integration from the starting values. Here, it is convenient to integrate from the left and right grid boundaries, matching both solutions in the middle and normalizing.

In this work the shooting method is implemented via Numerov's method shown above, where the initial conditions are given by the value of ψ at two grid points.

B.1.4. Integration

Integrals of functions $f(x, \psi(x))$, sampled at grid points x_n , are approximated by

$$\int dx f(x, \psi(x)) = \sum_n f(x_n, \psi(x_n))\Delta x.$$

An example is the norm of ψ . Any spurious contributions at the grid boundary are typically irrelevant because in practice f is often a product containing ψ . In ψ , values at the grid boundary

B. Numerical Implementation

are suppressed by the aforementioned mask function. The grid spacing Δx is generally chosen small enough to resolve oscillations of $\psi(x)$.

For integrals not containing $\psi(x)$, over an interval $[x_0, x_{N-1}]$ sampled at N points x_n , the following integration formula [159] is used

$$\int_{x_0}^{x_{N-1}} dx f(x) = \Delta x \left[\frac{3}{8} f_0 + \frac{7}{6} f_1 + \frac{23}{24} f_2 + f_3 + \cdots + \right. \\ \left. + f_{N-4} + \frac{23}{24} f_{N-3} + \frac{7}{6} f_{N-2} + \frac{3}{8} f_{N-1} \right] + O(N^{-4}),$$

with $f_n = f(x_n)$.

B.2. Numerical implementations and parameters

In this section it is outlined which numerical algorithm is used for a particular calculation, together with the numerical parameters used. Convergence of the numerical results is generally tested by varying the numerical parameters and observing that the physical results are independent of them.

B.2.1. Autocorrelation

Here the numerical implementation of the vibrational autocorrelation is outlined.

Numerical grid

The autocorrelation $C(p, t, t')$ as in expression (3.1) depends on a one-dimensional wave function $\chi(R, t)$. All such wave functions (for H₂ and D₂) in this work are represented on a numerical grid with parameters

$$R_a = 0.5, \\ \Delta R = 0.005, \\ N_R = 6144,$$

where R_a is the low boundary of the grid, ΔR the grid spacing and N_R the number of grid points. The grid correspondingly extends to 31.215.

Time evolution

For the time evolution, two different methods are used. They are applicable for real-valued as well as complex-valued time propagations.

If $\chi(R, t)$ evolves on the (shifted) BO potential energy curve $\mathcal{V}_{\text{BO}}^+(R)$, it is efficient to calculate $C(p, t, t')$ via expansion in vibrational eigenstates χ_ν^+ of $\mathcal{V}_{\text{BO}}^+$, as in expression (3.2). Since the ionization matrix element d_{ion} is set to unity, the corresponding set of expansion coefficients is constant, $c'_{\text{ion}} = \langle \chi_\nu^+ | \chi_0 \rangle$, also called Franck-Condon factors.

If the BO potential is time-dependent, for example when including the Stark shift, or changes in every iteration of the PACER method, the split-operator propagation is used. For these propagations the real-valued timestep is chosen as $\Delta t = 0.1$. From this a complex-valued timestep Δt_c is calculated for a given complex-valued excursion time τ of the electron as follows

$$\Delta t_c = \frac{\tau}{N_t} \quad \text{with} \quad N_t = \left\lceil \frac{|\tau|}{\Delta t} \right\rceil,$$

i.e.

$$|\Delta t_c| \leq \Delta t.$$

For every set of ionization and recombination times, the time evolution is calculated anew, i.e. starting from the ground vibrational state of the neutral molecule.

Vibrational states

The vibrational ground state χ_0 of V_{BO} is calculated with the shooting method (see above). The ionic vibrational states χ_ν^+ of V_{BO}^+ are calculated via imaginary time propagation (see also above). The shifted potentials, such as $\mathcal{V}_{\text{BO}}^+$, have the same eigenstates. Only the energies are affected by the shift.

Ammonia

The calculations for NH_3 and ND_3 are done on a numerical grid with parameters

$$\begin{aligned} x_a &= -1.36, \\ \Delta x &= 0.002125, \\ N_x &= 1280, \end{aligned}$$

where x_a is the low boundary of the grid, Δx the grid spacing and N_x the number of grid points. The numerical algorithms are the same as for H_2 and D_2 .

B. Numerical Implementation

B.2.2. Saddle-point times

The real-valued times from the semiclassical three-step model (section 2.1) as well as the complex-valued solutions to the saddle-point equations (2.23), (2.24), (2.25) were calculated with Mathematica via its root-finding algorithms.

B.2.3. TDSE

This section outlines the numerical implementation of the two-dimensional TDSE calculations underlying the Gabor ratios of chapter 5.

Numerical grid

The numerical grid parameters for the electron dimension x and the nuclear dimension R are

$$\begin{aligned}x_a &= -819.2, & R_a &= 0.5, \\ \Delta x &= 0.2, & \Delta R &= 0.05, \\ N_x &= 8192, & N_R &= 256,\end{aligned}$$

where x_a , R_a are the lower boundaries of the grid; Δx , ΔR are the grid spacings and N_x , N_R are the number of grid points. The electron grid therefore extends to 819.2 and the nuclear grid to 13.25.

Time evolution

The time evolution is done with split-operator propagation (see above). The timestep is $\Delta t = 0.02$. The number of timesteps is chosen large enough to accommodate the length of the laser pulse. For the mostly single-cycle pulses of chapter 5, this corresponds to the period of one cycle.

Ground state

The ground states of the parallel and perpendicular potentials of chapter 4 are calculated with imaginary time evolution (see above).

B.2.4. Dipole-transition matrix element

This sections outlines the numerical implementation of the dipole-transition matrix elements in section 4.5. The evaluation of the matrix elements in the autocorrelation function is done via a

two-dimensional spline interpolation [160] of the previously calculated values.

Numerical grid

The matrix element is, for both orientations, calculated on a numerical grid with the following parameters for the electron dimension

$$\begin{aligned}x_a &= -2048, \\ \Delta x &= 0.01, \\ N_x &= 409600,\end{aligned}$$

where x_a is the lower boundary of the grid, Δx the grid spacing and N_x the number of grid points. The grid therefore extends to 2047.99. The grid is noticeably larger and finer than the grid of the 2D TDSE calculations. This is because of the difficulties of resolving both low and high electron momenta as explained in section 4.5.

For the perpendicular orientation, the parameters for the nuclear dimension are

$$\begin{aligned}R_a &= 0.5, \\ \Delta R &= 0.04, \\ N_R &= 500,\end{aligned}$$

with R_a being the lower boundary, ΔR the grid spacing and N_R the number of grid points. The grid extends to 20.46. The autocorrelation is calculated on a larger grid and in order to evaluate the matrix element for larger R , it is constantly continued with the value at $R = 20.46$. This is appropriate since for the perpendicular orientation the matrix element changes very slowly for large R (compare Figures 4.7, 4.10 and 4.11).

For the parallel orientation, the parameters are

$$\begin{aligned}R_a &= 0.5, \\ \Delta R &= 0.04, \\ N_R &= 800,\end{aligned}$$

and the grid therefore extends to 32.46, which covers the entire grid of the autocorrelation above.

Electronic ground and scattering states

The electronic ground state ψ_R for fixed internuclear distance R is calculated via the shooting method (see above). The exact scattering states ψ_k^c do not require the determination of an eigenenergy since their energy E is continuous and given as input, $E = k^2/2$. They are calculated with Numerov's method (see also above), with initial conditions as explained in section 4.5.2.

B.2.5. Alignment distribution

The calculation of alignment distributions and related quantities requires solving the set of coupled differential equations (6.6) for the coefficient functions $F_{J_i J}(t)$. For this the ODE-system implementation provided by the GSL [143] is used. In particular, the used algorithm is the explicit embedded Runge-Kutta Prince-Dormand (8, 9) method, with an absolute error of 10^{-6} and a relative error of 0 (see the GSL documentation). The values of $\Lambda_{J,\pm}^M$ and Λ_J^M are calculated with Mathematica. When dealing with spherical harmonics between different implementations, one needs to make sure that the same conventions are used.

Bibliography

- [1] G. W. F. Drake, *Handbook of Atomic, Molecular and Optical Physics*, page 5 (Springer 2006).
- [2] T. Brabec and F. Krausz, *Intense few-cycle laser fields: Frontiers of nonlinear optics*, Rev. Mod. Phys. **72**, 545 (2000).
- [3] P. A. Franken, A. E. Hill, C. W. Peters and G. Weinreich, *Generation of Optical Harmonics*, Phys. Rev. Lett. **7**, 118 (1961).
- [4] G. H. C. New and J. F. Ward, *Optical Third-Harmonic Generation in Gases*, Phys. Rev. Lett. **19**, 556 (1967).
- [5] K. Zhao, Q. Zhang, M. Chini, Y. Wu, X. Wang and Z. Chang, *Tailoring a 67 attosecond pulse through advantageous phase-mismatch*, Opt. Lett. **37**, 18, 3891 (2012).
- [6] Y. Pan, S.-F. Zhao and X.-X. Zhou, *Generation of isolated sub-40-as pulses from gas-phase CO molecules using an intense few-cycle chirped laser and a unipolar pulse*, Phys. Rev. A **87**, 035805 (2013).
- [7] F. Krausz and M. Ivanov, *Attosecond physics*, Rev. Mod. Phys. **81**, 163 (2009).
- [8] G. S. Voronov and N. B. Delone, *Ionization of the xenon atom by the electric field of ruby laser emission*, JETP Letters **1**, 66 (1965).
- [9] F. Fabre, G. Petite, P. Agostini and M. Clement, *Multiphoton above-threshold ionisation of xenon at 0.53 and 1.06 μ m*, J. Phys. B **15**, 9, 1353 (1982).
- [10] G. Petite, F. Fabre, P. Agostini, M. Crance and M. Aymar, *Nonresonant multiphoton ionization of cesium in strong fields: Angular distributions and above-threshold ionization*, Phys. Rev. A **29**, 2677 (1984).
- [11] P. Agostini, F. Fabre, G. Mainfray, G. Petite and N. K. Rahman, *Free-Free Transitions Following Six-Photon Ionization of Xenon Atoms*, Phys. Rev. Lett. **42**, 1127 (1979).
- [12] U. Mohideen, M. H. Sher, H. W. K. Tom, G. D. Aumiller, O. R. Wood, R. R. Freeman, J. Boker and P. H. Bucksbaum, *High intensity above-threshold ionization of He*, Phys. Rev. Lett. **71**, 509 (1993).

- [13] B. Yang, K. J. Schafer, B. Walker, K. C. Kulander, P. Agostini and L. F. DiMauro, *Intensity-dependent scattering rings in high order above-threshold ionization*, Phys. Rev. Lett. **71**, 3770 (1993).
- [14] D. N. Fittinghoff, P. R. Bolton, B. Chang and K. C. Kulander, *Observation of nonsequential double ionization of helium with optical tunneling*, Phys. Rev. Lett. **69**, 2642 (1992).
- [15] B. Walker, B. Sheehy, L. F. DiMauro, P. Agostini, K. J. Schafer and K. C. Kulander, *Precision Measurement of Strong Field Double Ionization of Helium*, Phys. Rev. Lett. **73**, 1227 (1994).
- [16] N. H. Burnett, H. A. Baldis, M. C. Richardson and G. D. Enright, *Harmonic generation in CO₂ laser target interaction*, Applied Physics Letters **31**, 3, 172 (1977).
- [17] A. McPherson, G. Gibson, H. Jara, U. Johann, T. S. Luk, I. A. McIntyre, K. Boyer and C. K. Rhodes, *Studies of multiphoton production of vacuum-ultraviolet radiation in the rare gases*, J. Opt. Soc. Am. B **4**, 4, 595 (1987).
- [18] M. Ferray, A. L'Huillier, X. F. Li, L. A. Lompre, G. Mainfray and C. Manus, *Multiple-harmonic conversion of 1064 nm radiation in rare gases*, J. Phys. B: At. Mol. Phys. **21**, 3, L31 (1988).
- [19] J. L. Krause, K. J. Schafer and K. C. Kulander, *High-order harmonic generation from atoms and ions in the high intensity regime*, Phys. Rev. Lett. **68**, 3535 (1992).
- [20] K. J. Schafer, B. Yang, L. F. DiMauro and K. C. Kulander, *Above threshold ionization beyond the high harmonic cutoff*, Phys. Rev. Lett. **70**, 1599 (1993).
- [21] P. B. Corkum, *Plasma perspective on strong field multiphoton ionization*, Phys. Rev. Lett. **71**, 1994 (1993).
- [22] M. Lewenstein, P. Balcou, M. Y. Ivanov, A. L'Huillier and P. B. Corkum, *Theory of high-harmonic generation by low-frequency laser fields*, Phys. Rev. A **49**, 2117 (1994).
- [23] P. M. Paul, E. S. Toma, P. Breger, G. Mullot, F. Augé, P. Balcou, H. G. Muller and P. Agostini, *Observation of a Train of Attosecond Pulses from High Harmonic Generation*, Science **292**, 5522, 1689 (2001).
- [24] N. A. Papadogiannis, B. Witzel, C. Kalpouzos and D. Charalambidis, *Observation of Attosecond Light Localization in Higher Order Harmonic Generation*, Phys. Rev. Lett. **83**, 4289 (1999).
- [25] M. Chini, K. Zhao and Z. Chang, *The generation, characterization and applications of broadband isolated attosecond pulses*, Nature Photonics **8**, 178 EP (2014).
- [26] T. Popmintchev, M.-C. Chen, P. Arpin, M. M. Murnane and H. C. Kapteyn, *The*

- attosecond nonlinear optics of bright coherent X-ray generation*, Nature Photonics **4**, 822 EP (2010).
- [27] J. Itatani, J. Levesque, D. Zeidler, H. Niikura, H. Pépin, J. C. Kieffer, P. B. Corkum and D. M. Villeneuve, *Tomographic imaging of molecular orbitals*, Nature **432**, 867 EP (2004).
- [28] S. Baker, J. S. Robinson, C. A. Haworth, H. Teng, R. A. Smith, C. C. Chirilă, M. Lein, J. W. G. Tisch and J. P. Marangos, *Probing Proton Dynamics in Molecules on an Attosecond Time Scale*, Science **312**, 424 (2006).
- [29] S. Baker, J. S. Robinson, M. Lein, C. C. Chirilă, R. Torres, H. C. Bandulet, D. Comtois, J. C. Kieffer, D. M. Villeneuve, J. W. G. Tisch and J. P. Marangos, *Dynamic Two-Center Interference in High-Order Harmonic Generation from Molecules with Attosecond Nuclear Motion*, Phys. Rev. Lett. **101**, 053901 (2008).
- [30] S. Haessler, J. Caillat and P. Salières, *Self-probing of molecules with high harmonic generation*, J. Phys. B: At. Mol. Phys. **44**, 20, 203001 (2011).
- [31] G. G. Paulus, W. Nicklich, H. Xu, P. Lambropoulos and H. Walther, *Plateau in above threshold ionization spectra*, Phys. Rev. Lett. **72**, 2851 (1994).
- [32] P. B. Corkum, N. H. Burnett and F. Brunel, *Above-threshold ionization in the long-wavelength limit*, Phys. Rev. Lett. **62**, 1259 (1989).
- [33] T. F. Gallagher, *Above-Threshold Ionization in Low-Frequency Limit*, Phys. Rev. Lett. **61**, 2304 (1988).
- [34] G. G. Paulus, W. Becker, W. Nicklich and H. Walther, *Rescattering effects in above-threshold ionization: a classical model*, J. Phys. B: At. Mol. Phys. **27**, 21, L703 (1994).
- [35] D. B. Milošević, G. G. Paulus, D. Bauer and W. Becker, *Above-threshold ionization by few-cycle pulses*, J. Phys. B: At. Mol. Phys. **39**, 14, R203 (2006).
- [36] L. Keldysh, *Ionization in the Field of a Strong Electromagnetic Wave*, JETP **20**, 1307 (1965).
- [37] F. H. M. Faisal, *Multiple absorption of laser photons by atoms*, J. Phys. B **6**, 4, L89 (1973).
- [38] H. R. Reiss, *Effect of an intense electromagnetic field on a weakly bound system*, Phys. Rev. A **22**, 1786 (1980).
- [39] M. Y. Ivanov, M. Spanner and O. Smirnova, *Anatomy of strong field ionization*, J. Mod. Opt. **52**, 2-3, 165 (2005).

- [40] O. Smirnova, M. Spanner and M. Ivanov, *Coulomb and polarization effects in sub-cycle dynamics of strong-field ionization*, J. Phys. B: At. Mol. Phys. **39**, 13, S307 (2006).
- [41] O. Smirnova, A. S. Mouritzen, S. Patchkovskii and M. Y. Ivanov, *Coulomb–laser coupling in laser-assisted photoionization and molecular tomography*, J. Phys. B: At. Mol. Phys. **40**, 13, F197 (2007).
- [42] O. Smirnova, M. Spanner and M. Ivanov, *Analytical solutions for strong field-driven atomic and molecular one- and two-electron continua and applications to strong-field problems*, Phys. Rev. A **77**, 033407 (2008).
- [43] L. Torlina and O. Smirnova, *Time-dependent analytical R-matrix approach for strong-field dynamics. I. One-electron systems*, Phys. Rev. A **86**, 043408 (2012).
- [44] L. Torlina, M. Ivanov, Z. B. Walters and O. Smirnova, *Time-dependent analytical R-matrix approach for strong-field dynamics. II. Many-electron systems*, Phys. Rev. A **86**, 043409 (2012).
- [45] L. Torlina and O. Smirnova, *Coulomb time delays in high harmonic generation*, New J. Phys. **19**, 2, 023012 (2017).
- [46] J. L. Krause, K. J. Schafer and K. C. Kulander, *Optical harmonic generation in atomic and molecular hydrogen*, Chem. Phys. Lett. **178**, 5, 573 (1991).
- [47] T. Zuo, S. Chelkowski and A. D. Bandrauk, *Harmonic generation by the H_2^+ molecular ion in intense laser fields*, Phys. Rev. A **48**, 3837 (1993).
- [48] M. Y. Ivanov and P. B. Corkum, *Generation of high-order harmonics from inertially confined molecular ions*, Phys. Rev. A **48**, 580 (1993).
- [49] R. Kopold, W. Becker and M. Kleber, *Model calculations of high-harmonic generation in molecular ions*, Phys. Rev. A **58**, 4022 (1998).
- [50] A. D. Bandrauk and H. Yu, *High-order harmonic generation by one- and two-electron molecular ions with intense laser pulses*, Phys. Rev. A **59**, 539 (1999).
- [51] T. Kreibich, M. Lein, V. Engel and E. K. U. Gross, *Even-Harmonic Generation due to Beyond-Born-Oppenheimer Dynamics*, Phys. Rev. Lett. **87**, 103901 (2001).
- [52] M. Lein, N. Hay, R. Velotta, J. P. Marangos and P. L. Knight, *Role of the Intramolecular Phase in High-Harmonic Generation*, Phys. Rev. Lett. **88**, 18 (2002).
- [53] M. Lein, N. Hay, R. Velotta, J. P. Marangos and P. L. Knight, *Interference effects in high-order harmonic generation with molecules*, Phys. Rev. A **66**, 023805 (2002).
- [54] M. Lein, *Attosecond Probing of Vibrational Dynamics with High-Harmonic Generation*, Phys. Rev. Lett. **94**, 053004 (2005).

- [55] C. C. Chirilă and M. Lein, *Influence of nuclear vibration on harmonic generation in molecules*, J. Phys. B: At. Mol. Phys. **39**, 13, S437 (2006).
- [56] J. P. Farrell, S. Petretti, J. Förster, B. K. McFarland, L. S. Spector, Y. V. Vanne, P. Decleva, P. H. Bucksbaum, A. Saenz, and M. Gühr, *Strong Field Ionization to Multiple Electronic States in Water*, Phys. Rev. Lett. **107**, 083001 (2011).
- [57] P. M. Kraus and H. J. Wörner, *Attosecond Nuclear Dynamics in the Ammonia Cation: Relation between High-Harmonic and Photoelectron Spectroscopies*, Chem Phys Chem **14**, 1445 (2013).
- [58] J. Förster and A. Saenz, *Theoretical Study of the Inversion Motion of the Ammonia Cation with Subfemtosecond Resolution for High-Harmonic Spectroscopy*, Chem Phys Chem **14**, 1438 (2013).
- [59] P. Lan, M. Ruhmann, L. He, C. Zhai, F. Wang, X. Zhu, Q. Zhang, Y. Zhou, M. Li, M. Lein and P. Lu, *Attosecond Probing of Nuclear Dynamics with Trajectory-Resolved High-Harmonic Spectroscopy*, Phys. Rev. Lett. **119**, 033201 (2017).
- [60] M. Ammosov, N. Delone and V. Krainov, *Tunnel ionization of complex atoms and of atomic ions in an alternating electromagnetic field*, Journal of Experimental and Theoretical Physics **91**, 1191 (1986).
- [61] M. Lewenstein, P. Salières and A. L'Huillier, *Phase of the atomic polarization in high-order harmonic generation*, Phys. Rev. A **52**, 4747 (1995).
- [62] L. Ballentine, *Quantum Mechanics: A Modern Development* (World Scientific 1998).
- [63] B. Sundaram and P. W. Milonni, *High-order harmonic generation: Simplified model and relevance of single-atom theories to experiment*, Phys. Rev. A **41**, 6571 (1990).
- [64] K. Burnett, V. C. Reed, J. Cooper and P. L. Knight, *Calculation of the background emitted during high-harmonic generation*, Phys. Rev. A **45**, 3347 (1992).
- [65] P. Ehrenfest, *Bemerkung über die angenäherte Gültigkeit der klassischen Mechanik innerhalb der Quantenmechanik*, Zeitschrift für Physik **45**, 7, 455 (1927).
- [66] C. C. Chirilă and M. Lein, *Assessing different forms of the strong-field approximation for harmonic generation in molecules*, J. Mod. Opt. **54**, 7, 1039 (2007).
- [67] M. B. Gaarde, F. Salin, E. Constant, P. Balcou, K. J. Schafer, K. C. Kulander and A. L'Huillier, *Spatiotemporal separation of high harmonic radiation into two quantum path components*, Phys. Rev. A **59**, 1367 (1999).
- [68] L. He, P. Lan, Q. Zhang, C. Zhai, F. Wang, W. Shi and P. Lu, *Spectrally resolved spatiotemporal features of quantum paths in high-order-harmonic generation*, Phys. Rev. A **92**, 043403 (2015).

- [69] P. Salières, A. L’Huillier and M. Lewenstein, *Coherence Control of High-Order Harmonics*, Phys. Rev. Lett. **74**, 3776 (1995).
- [70] P. Balcou, P. Salières, A. L’Huillier and M. Lewenstein, *Generalized phase-matching conditions for high harmonics: The role of field-gradient forces*, Phys. Rev. A **55**, 3204 (1997).
- [71] T. Auguste, P. Salières, A. S. Wyatt, A. Monmayrant, I. A. Walmsley, E. Cormier, A. Zair, M. Holler, A. Guandalini, F. Schapper, J. Biegert, L. Gallmann and U. Keller, *Theoretical and experimental analysis of quantum path interferences in high-order harmonic generation*, Phys. Rev. A **80**, 033817 (2009).
- [72] A. Zair, M. Holler, A. Guandalini, F. Schapper, J. Biegert, L. Gallmann, U. Keller, A. S. Wyatt, A. Monmayrant, I. A. Walmsley, E. Cormier, T. Auguste, J. P. Caumes and P. Salières, *Quantum Path Interferences in High-Order Harmonic Generation*, Phys. Rev. Lett. **100**, 143902 (2008).
- [73] D. Shafir, H. Soifer, B. D. Bruner, M. Dagan, Y. Mairesse, S. Patchkovskii, M. Y. Ivanov, O. Smirnova and N. Dudovich, *Resolving the time when an electron exits a tunnelling barrier*, *Supplementary Information*, Nature **485**, 343 (2012).
- [74] C. R. McDonald, G. Orlando, G. Vampa and T. Brabec, *Tunnel Ionization Dynamics of Bound Systems in Laser Fields: How Long Does It Take for a Bound Electron to Tunnel?*, Phys. Rev. Lett. **111**, 090405 (2013).
- [75] X. Urbain, B. Fabre, E. M. Staicu-Casagrande, N. de Ruelle, V. M. Andrianarijaona, J. Jureta, J. H. Posthumus, A. Saenz, E. Baldit, and C. Cornaggia, *Intense-Laser-Field Ionization of Molecular Hydrogen in the Tunneling Regime and Its Effect on the Vibrational Excitation of H_2^+* , Phys. Rev. Lett. **92**, 16 (2004).
- [76] P. J. Mohr, D. B. Newell and B. N. Taylor, *CODATA recommended values of the fundamental physical constants: 2014*, Rev. Mod. Phys. **88**, 035009 (2016).
- [77] G. Staszewska and L. Wolniewicz, *Adiabatic Energies of Excited $^1\Sigma_u$ States of the Hydrogen Molecule*, J. Mol. Spectrosc. **212**, 2, 208 (2002).
- [78] L. Wolniewicz and G. Staszewska, *Excited $^1\Pi_u$ states and the $^1\Pi_u \rightarrow X^1\Sigma_g^+$ transition moments of the hydrogen molecule*, J. Mol. Spectrosc. **220**, 1, 45 (2003).
- [79] J. Wisdom and M. Holman, *Symplectic maps for the n-body problem*, Astronomical Journal **102**, 1528 (1991).
- [80] S. Pieper, *Non-Born-Oppenheimer Dynamics of Hydrogen Molecules in Strong Laser-Fields*, Ph.D. thesis, Universität Kassel, 2009.
- [81] S. C. Rae, X. Chen and K. Burnett, *Saturation of harmonic generation in one- and three-dimensional atoms*, Phys. Rev. A **50**, 1946 (1994).

- [82] M. F. Ciappina, C. C. Chirilă and M. Lein, *Influence of Coulomb continuum wave functions in the description of high-order harmonic generation with H_2^+* , Phys. Rev. A **75**, 043405 (2007).
- [83] A.-T. Le, R. R. Lucchese, S. Tonzani, T. Morishita and C. D. Lin, *Quantitative rescattering theory for high-order harmonic generation from molecules*, Phys. Rev. A **80**, 013401 (2009).
- [84] E. V. van der Zwan and M. Lein, *Molecular Imaging Using High-Order Harmonic Generation and Above-Threshold Ionization*, Phys. Rev. Lett. **108**, 043004 (2012).
- [85] A. Chacon, M. Lein and C. Ruiz, *Asymmetry of Wigner's time delay in a small molecule*, Phys. Rev. A **89**, 053427 (2014).
- [86] D. J. Griffith, *Introduction To Quantum Mechanics* (Prentice-Hall 1995).
- [87] L. D. Landau and E. M. Lifshitz, *Motion in a Coulomb field (spherical polar co-ordinates)*, page 121 (Pergamon Press Ltd. 1965).
- [88] L. D. Landau and E. M. Lifshitz, *The theory of elastic scattering*, page 469 (Pergamon Press Ltd. 1965).
- [89] H. R. Sadeghpour, J. L. Bohn, M. J. Cavagnero, B. D. Esry, I. I. Fabrikant, J. H. Macek and A. R. P. Rau, *Collisions near threshold in atomic and molecular physics*, J. Phys. B: At. Mol. Phys. **33**, 5, R93 (2000).
- [90] K. J. Reed, A. H. Zimmerman, H. C. Andersen and J. I. Brauman, *Cross sections for photodetachment of electrons from negative ions near threshold*, J. Chem. Phys. **64**, 4, 1368 (1976).
- [91] K. Gröchenig, *The Short-Time Fourier Transform*, pages 37–58 (Birkhäuser Boston 2001).
- [92] K. Gröchenig, *Time-Frequency Analysis and the Uncertainty Principle*, pages 21–36 (Birkhäuser Boston 2001).
- [93] V. V. Strelkov, M. A. Khokhlova, A. A. Gonoskov, I. A. Gonoskov and M. Y. Ryabikin, *High-order harmonic generation by atoms in an elliptically polarized laser field: Harmonic polarization properties and laser threshold ellipticity*, Phys. Rev. A **86**, 013404 (2012).
- [94] C. Chirilă and M. Lein, *High-order harmonic generation in vibrating two-electron molecules*, Chemical Physics **366**, 1, 54 (2009).
- [95] H. J. Loesch and A. Remscheid, *Brute force in molecular reaction dynamics: A novel technique for measuring steric effects*, J. Chem. Phys. **93**, 7, 4779 (1990).
- [96] W. Demtröder, *Rotation, Vibration, and Potential Curves of Diatomic Molecules*, pages 79–119 (Wiley-VCH Verlag GmbH 2007).

- [97] B. P. Stoicheff, *High resolution raman spectroscopy of gases: ix. spectra of H₂, HD, and D₂*, Canadian Journal of Physics **35**, 6, 730 (1957).
- [98] R. Torres, R. de Nalda and J. P. Marangos, *Dynamics of laser-induced molecular alignment in the impulsive and adiabatic regimes: A direct comparison*, Phys. Rev. A **72**, 023420 (2005).
- [99] H. Haken and C. Wolf, *Molekülphysik und Quantenchemie: Einführung in die experimentellen und theoretischen Grundlagen*, pages 159–177 (Springer Berlin Heidelberg 2006).
- [100] B. Friedrich and D. Herschbach, *Polarization of Molecules Induced by Intense Nonresonant Laser Fields*, The Journal of Physical Chemistry **99**, 42, 15686 (1995).
- [101] T. Seideman, *Rotational excitation and molecular alignment in intense laser fields*, J. Chem. Phys. **103**, 18, 7887 (1995).
- [102] B. Friedrich and D. Herschbach, *Alignment and Trapping of Molecules in Intense Laser Fields*, Phys. Rev. Lett. **74**, 4623 (1995).
- [103] T. Seideman, *The analysis of magnetic-state-selected angular distributions: a quantum mechanical form and an asymptotic approximation*, Chem. Phys. Lett. **253**, 3, 279 (1996).
- [104] T. Seideman, *Revival Structure of Aligned Rotational Wave Packets*, Phys. Rev. Lett. **83**, 4971 (1999).
- [105] T. Seideman, *New means of spatially manipulating molecules with light*, J. Chem. Phys. **111**, 10, 4397 (1999).
- [106] T. Seideman, *On the dynamics of rotationally broad, spatially aligned wave packets*, J. Chem. Phys. **115**, 13, 5965 (2001).
- [107] H. Stapelfeldt and T. Seideman, *Colloquium*, Rev. Mod. Phys. **75**, 543 (2003).
- [108] J. Ortigoso, M. Rodriguez, M. Gupta and B. Friedrich, *Time evolution of pendular states created by the interaction of molecular polarizability with a pulsed nonresonant laser field*, J. Chem. Phys. **110**, 8, 3870 (1999).
- [109] H. Haken and C. Wolf, *Molekülphysik und Quantenchemie: Einführung in die experimentellen und theoretischen Grundlagen*, pages 239–253 (Springer Berlin Heidelberg 2006).
- [110] C. Cohen-Tannoudji, B. Diu and F. Laloe, *Quantum Mechanics, 2 Volume Set* (Wiley 1992).
- [111] G. W. F. Drake, *Handbook of Atomic, Molecular and Optical Physics*, pages 231–233 (Springer 2006).

- [112] H. Haken and H. C. Wolf, *Atome im elektrischen Feld*, pages 269–302 (Springer Berlin Heidelberg 2004).
- [113] R. W. Heather and F. H. Mies, *Intense-field photodissociation of H_2^+ : Comparison of time-dependent and time-independent calculations*, Phys. Rev. A **44**, 7560 (1991).
- [114] A. M. Bonch-Bruевич and V. A. Khodovoi, *Current methods for the study of the stark effect in atoms*, Soviet Physics Uspekhi **10**, 5, 637 (1968).
- [115] B. Girard, G. O. Sitz, R. N. Zare, N. Billy and J. Vigué, *Polarization dependence of the ac Stark effect in multiphoton transitions of diatomic molecules*, J. Chem. Phys. **97**, 1, 26 (1992).
- [116] E. T. Jaynes and F. W. Cummings, *Comparison of quantum and semiclassical radiation theories with application to the beam maser*, Proceedings of the IEEE **51**, 1, 89 (1963).
- [117] C. C. Chirilă and M. Lein, *Effect of dressing on high-order harmonic generation in vibrating H_2 molecules*, Phys. Rev. A **77**, 043403 (2008).
- [118] D. R. Bates, *The Oscillator Strength of H_2^+* , J. Chem. Phys. **19**, 9, 1122 (1951).
- [119] D. M. Bishop and L. M. Cheung, *Moment functions (including static dipole polarisabilities) and radiative corrections for H_2^+* , J. Phys. B **11**, 18, 3133 (1978).
- [120] J. Rychlewski, *An accurate calculation of the polarizability of the hydrogen molecule and its dependence on rotation, vibration and isotopic substitution*, Molecular Physics **41**, 4, 833 (1980).
- [121] W. Kolos and L. Wolniewicz, *Polarizability of the Hydrogen Molecule*, J. Chem. Phys. **46**, 4, 1426 (1967).
- [122] L. Wolniewicz and G. Staszewska, *$^1\Sigma_u^+ \rightarrow X^1\Sigma_g^+$ transition moments for the hydrogen molecule*, J. Mol. Spectrosc. **217**, 2, 181 (2003).
- [123] L. I. Schiff, *Quantum Mechanics, Third Edition* (McGraw-Hill 1968).
- [124] C. C. Chirilă, and M. Lein, *High-order harmonic generation in vibrating molecules*, J. Mod. Opt. **53**, 1-2, 113 (2006).
- [125] S. Baker, J. S. Robinson, C. A. Haworth, H. Teng, R. A. Smith, C. C. Chirilă, M. Lein, J. W. G. Tisch and J. P. Marangos, *Probing Proton Dynamics in Molecules on an Attosecond Time Scale*, Science **312**, 424 (2006), supporting Material.
- [126] C. C. Chirilă and M. Lein, *Strong-field approximation for harmonic generation in diatomic molecules*, Phys. Rev. A **73**, 023410 (2006).
- [127] C. B. Markwardt, *Non-linear Least-squares Fitting in IDL with MPFIT*, in *Astronomical*

Bibliography

- Data Analysis Software and Systems XVIII, Astronomical Society of the Pacific Conference Series*, volume 411 (edited by D. A. Bohlender, D. Durand and P. Dowler), page 251 (2009).
- [128] A. Staudte, S. Patchkovskii, D. Pavičić, H. Akagi, O. Smirnova, D. Zeidler, M. Meckel, D. M. Villeneuve, R. Dörner, M. Y. Ivanov and P. B. Corkum, *Angular Tunneling Ionization Probability of Fixed-in-Space H_2 Molecules in Intense Laser Pulses*, Phys. Rev. Lett. **102**, 033004 (2009).
- [129] X. Chu, *Time-dependent density-functional-theory calculation of strong-field ionization rates of H_2* , Phys. Rev. A **82**, 023407 (2010).
- [130] N. Aquino, G. Campoy and H. Yee-Madeira, *The inversion potential for NH_3 using a DFT approach*, Chem. Phys. Lett. **296**, 1, 111 (1998).
- [131] V. Špirko and W. Kraemer, *Anharmonic potential function and effective geometries for the NH_3 molecule*, J. Mol. Spectrosc. **133**, 2, 331 (1989).
- [132] W. Kraemer and V. Špirko, *Potential energy function and rotation-vibration energy levels of NH_3^+* , J. Mol. Spectrosc. **153**, 1, 276 (1992).
- [133] H. Ågren, I. Reineck, H. Veenhuizen, R. Maripuu, R. Arneberg and L. Karlsson, *A theoretical investigation of the U.V. excited $^1A_1 \rightarrow ^2A_1$ photoelectron spectra of NH_3 and ND_3* , Molecular Physics **45**, 2, 477 (1982).
- [134] L. Brugnera, D. J. Hoffmann, T. Siegel, F. Frank, A. Zaïr, J. W. G. Tisch and J. P. Marangos, *Trajectory Selection in High Harmonic Generation by Controlling the Phase between Orthogonal Two-Color Fields*, Phys. Rev. Lett. **107**, 153902 (2011).
- [135] T. Sharp, *Potential-energy curves for molecular hydrogen and its ions*, Atomic Data and Nuclear Data Tables **2**, 119 (1970).
- [136] G. Herzberg, *Molecular Spectra and Molecular Structure* (Read Books 2008).
- [137] K. Pachucki, *Born-Oppenheimer potential for HeH^+* , Phys. Rev. A **85**, 042511 (2012).
- [138] W. C. Martin, *Energy levels of neutral helium (4He I)*, Journal of Physical and Chemical Reference Data **2**, 2, 257 (1973).
- [139] W. Byers-Brown and J. D. Power, *Perturbation Theory of Short-Range Atomic Interactions*, Proceedings of the Royal Society of London A: Mathematical, Physical and Engineering Sciences **317**, 1531, 545 (1970).
- [140] R. F. Nalewajski, *Hydrogen-Like Atom*, pages 93–109 (Springer Berlin Heidelberg 2012).
- [141] B. H. Bransden, A. Dalgarno and N. M. King, *Electron Capture - IV: Capture from*

Helium Atoms by Fast Protons, Proceedings of the Physical Society. Section A **67**, 12, 1075 (1954).

- [142] *GNU Compiler Collection*, <https://gcc.gnu.org>.
- [143] *GNU Scientific Library*, <http://www.gnu.org/software/gsl>.
- [144] T. Oliphant, *NumPy*, <http://www.numpy.org>.
- [145] E. Jones, T. Oliphant, P. Peterson et al., *SciPy: Open source scientific tools for Python*, <http://www.scipy.org>, 2001–.
- [146] J. D. Hunter, *Matplotlib: A 2D graphics environment*, Computing In Science & Engineering **9**, 3, 90 (2007).
- [147] *Matplotlib*, <https://matplotlib.org>.
- [148] A. Meurer, C. P. Smith, M. Paprocki, O. Čertík, S. B. Kirpichev, M. Rocklin, A. Kumar, S. Ivanov, J. K. Moore, S. Singh, T. Rathnayake, S. Vig, B. E. Granger, R. P. Muller, F. Bonazzi, H. Gupta, S. Vats, F. Johansson, F. Pedregosa, M. J. Curry, A. R. Terrel, v. Roučka, A. Saboo, I. Fernando, S. Kulal, R. Cimrman and A. Scopatz, *SymPy: symbolic computing in Python*, PeerJ Computer Science **3**, e103 (2017).
- [149] *SymPy*, <https://www.sympy.org>.
- [150] *Anaconda Software Distribution*, <https://www.anaconda.com>.
- [151] *Gnuplot*, <http://www.gnuplot.info>.
- [152] *VIM*, <https://www.vim.org>.
- [153] *TeX Live*, <https://www.tug.org/texlive>.
- [154] *Git*, <https://git-scm.com>.
- [155] *Ubuntu*, <https://www.ubuntu.com>.
- [156] I. Peterson, *Photoelectron Momentum Distributions from Recollision-Free Strong-Field Ionization of Atoms and Molecules*, Ph.D. thesis, Leibniz Universität Hannover, 2014.
- [157] J. A. Fleck, J. R. Morris and M. D. Feit, *Time-dependent propagation of high energy laser beams through the atmosphere*, Applied physics **10**, 2, 129 (1976).
- [158] M. Frigo and S. G. Johnson, *FFTW*, <http://www.fftw.org>.
- [159] W. H. Press, S. A. Teukolsky, W. T. Vetterling and B. P. Flannery, *Numerical Recipes - The Art of Scientific Computing* (Cambridge University Press 2007).

Bibliography

[160] K. P. Esler, *einspline*, <http://einspline.sourceforge.net>.

Curriculum Vitae

Persönliche Daten

Name: Marc Ruhmann
Geburtstag und -ort: 15.06.1989, Hannover
Staatsangehörigkeit: deutsch
Familienstand: ledig

Schule und Studium

1999 – 2008: Abitur an der Integrierten Gesamtschule Hannover
Mühlenberg. Abschlussnote 2,0
2008 – 2011: Bachelorstudium Physik an der Leibniz Universität Hannover.
Abschlussnote 1,4
2011 – 2014: Masterstudium Physik an der Leibniz Universität Hannover.
Abschlussnote 1,2
Seit 2014: Doktorand am Institut für Theoretische Physik der Leibniz
Universität Hannover

List of Publications

- P. Lan, M. Ruhmann, L. He, C. Zhai, F. Wang, X. Zhu, Q. Zhang, Y. Zhou, M. Li, M. Lein and P. Lu, *Attosecond Probing of Nuclear Dynamics with Trajectory-Resolved High-Harmonic Spectroscopy*, Phys. Rev. Lett. **119**, 033201 (2017).